8-8-2005

Spectral Line Synthesis for Hot stars

Wenjin Huang

NOTICE TO BORROWERS

The author of this dissertation is

Wenjin Huang
Department of Physics and Astronomy
Georgia State University, P. O. Box 4106
Atlanta, Georgia 30302-4106

The director of this dissertation is

Douglas R. Gies
Department of Physics and Astronomy
College of Arts and Sciences

Spectral Line Synthesis
for Hot Stars

A Dissertation

Presented in Partial Fulfillment of the Requirements for the
Degree of Doctor of Philosophy
in the College of Arts and Sciences
Georgia State University

2005

by

Wenjin Huang

Committee:

Douglas R. Gies, Chair

William G. Bagnuolo, Jr., Member

Xiaochun He, Member

H. Richard Miller, Member

Richard H. D. Townsend, Member

Paul J. Wiita, Member

Date

H. Richard Miller, Chair
Department of Physics and Astronomy

Abstract

I developed a spectrum synthesis method to investigate the physical properties of hot OB main sequence (MS) stars, which are often rapid rotators. The code realistically simulates the surface conditions of rapidly rotating stars, considering the rotationally-deformed stellar shape and gravity darkening effect. Comparing the synthesized absorption line profiles with the observed spectra of the member stars of 19 young Galactic clusters, I determined the projected rotational velocities of 496 stars. The average surface temperature and gravity for most of these objects were then derived from Hγ line fits. The polar gravity of each star was estimated as a good indicator of the evolutionary status of the star. The derived parameters show that massive rotators spin down during their MS phase. The He abundance data (measured by fitting the He I lines) also favor the theoretical prediction that rotationally-induced mixing can gradually enrich the surface helium abundance through the MS phase. A quicker spin-down is evident in the lower mass star group where a large portion of helium peculiar stars are found. This correlation implies that strong stellar magnetic fields may exist on the surface of these lower mass stars.

The same method is also applied to interferometric observations from the CHARA Array of a nearby rapid rotator, Regulus. By combining results from spectroscopic and interferometric analysis, the shape, space orientation, mass, and surface temperature distribution

of Regulus are firmly determined. This analysis provides the first evidence of the gravity darkening phenomenon among stars that are not components of an eclipsing binary system. The surprisingly high luminosity determined for Regulus appears to agree with the theoretical prediction that rapid rotator can become more luminous as rotationally-induced mixing brings fresh hydrogen down to the core.

Finally I present an extension of the model that simulates the shape, velocity, and temperature variations of a star experiencing nonradial pulsation. I simulated and analyzed the line profile variations in the spectra of ϵ Per, a B0.7 III star with strong evidence of nonradial pulsation (NRP). A comparison of the model simulations and observations indicates that the pulsations of ϵ Per have a corresponding local temperature variation that is out of phase with the radial oscillation (a non-adiabatic phase lag).

INDEX WORDS: Non-Radial Pulsation, Spectral Line Profiles, Spectrum Synthesis,
Stellar Rotation, Massive Stars, Stellar Abundances, Galactic Clusters

Dedication

I dedicate my dissertation, and the time and effort that when into it,

to my wife, Lufeng Zhuang,

who is always by my side, encouraging and supporting me

throughout the long journey,

to my parents,

who not only helped me to choose my direction

but also motivated me to fulfill my goal.

Wenjin Huang

July 22, 2005

Acknowledgments

First, I must thank all members of my family, my wife, parents, and sister. It is their endless support and encouragement that allowed me to pursue my goals without distraction. They share my joy when I have a success. They stayed with me and encouraged me not to give up when I encountered difficulties and frustration. I feel that without their encouragement and motivation, I would be like a sail without wind and would not have come this far.

Second, I must thank my adviser, Douglas Gies, not only for his guidance and critical advice on my research work and his long-term influence on my growth as a good researcher, but also for all kinds of help that he offered to me not as an adviser but as a close friend, that are very precious to a foreign student like me.

Third, I would like to thank all the other members of my committee: Richard H. D. Townsend, Paul J. Wiita, William G. Bagnuolo, Jr., Xiaochun He, and H. Richard Miller. Their comments and suggestions were very helpful and greatly improved my dissertation in both science and language. What I have learned from them during my defense will definitely benefit me in my future research career.

I must thank Hal McAlister, who offered me a great opportunity to take part in the first science project of the CHARA Array on the rapid rotating star, Regulus. I also thank the other co-researchers for their great efforts in this project. This project opened my eyes to

a new technical area of observational astronomy, deepened my understanding about rapidly rotating stars, and as a result, led to the addition of a wonderful chapter on Regulus in my dissertation.

I must mention the help from Ivan Hubeny and Thierry Lanz, the authors of TLUSTY and SYNSPEC, not only because they are the authors of these two wonderful programs that were used throughout my dissertation, but also because they took their precious time to answer all my questions on how to use the programs. Without their help, I would not have been able to finish my research in time.

I would like thank James Harvin (Rusty), Wei-Chun Jao, and John McFarland. They helped me a lot on preparing my dissertation in the LaTeX format. Rusty even kindly offered me his dissertation template, which saved me a lot of editing time. I would also like to thank our department's computer support team, Dave Berger, John McFarland, Rajesh Deo, and Duke Windsor, for their very hard maintenance work. I cannot remember how many times they helped me solve the computer problems. Without them, it is hard to imagine that I could have completed my research during my time at GSU.

Looking back at the years since I started my astronomy career, there are so many people who helped me that it is impossible to list all their names here. They include professors, who taught me courses and gave me an education, or other staff at Georgia State University, who helped me have an easier life at campus, and technical assistants at the observatories I visited (Kitt Peak National Observatory and the University of Texas McDonald Observatory), who helped me during observing runs. I want to say thank you to all of them.

This research made use of data and references obtained from the on-line database of

observational data on stars in galactic open clusters (WEBDA)[1], NASA's Astrophysics Data System Abstract Service (ADS)[2], and the SIMBAD Astronomical Database of the Centre de Données astronomiques de Strasbourg (CDS)[3].

Wenjin Huang

July 22, 2005

[1] Available at http://obswww.unige.ch/webda/
[2] Available at http://adsabs.harvard.edu/abstract_service.html
[3] Available at http://simbad.harvard.edu/sim-fid.pl

Contents

List of Tables **xi**

List of Figures **xii**

Abbreviations **xiii**

1 Stellar Spectrum Synthesis **1**
1.1 Why Spectrum Synthesis? 1
1.2 Local Flux on the Stellar Surface 3
1.2.1 Model Atmospheres 4
1.2.2 Intensity Line Profiles 10
1.3 Surface Conditions of Rotating Stars 13
1.3.1 Geometric Shape 13
1.3.2 Surface Temperature and Gravity 15
1.4 Final Step: Integration 16

2 Stellar Rotation in Young Galactic Clusters **21**
2.1 Introduction 21
2.2 Observations 24
2.3 Projected Rotational Velocities 27
2.3.1 Measuring Projected Rotational Velocities 27
2.3.2 Results and Discussion of the $V \sin i$ Measurements 35
2.4 Effective Temperature and Gravity from Hγ 52
2.5 Polar Gravity of Rotating Stars 61
2.5.1 The Meaning of Derived Temperature and Gravity 61
2.5.2 Estimation of Polar Gravity 71
2.6 Evolution of Stellar Rotation 73
2.7 Helium Abundance 80
2.7.1 Measuring Helium Abundance 81
2.7.2 Evolution of Helium Abundance 90

2.7.3 Rotational Effects on the Helium Abundance . . . 93
2.8 Conclusions . . . 97

3 Regulus **100**
3.1 Introduction . . . 100
3.1.1 The Star Regulus . . . 100
3.1.2 Interferometric Principles . . . 101
3.1.3 The Challenge of the Spectroscopic and Interferometric Analysis on Regulus . . . 103
3.2 Constraints from Spectroscopic Analysis . . . 106
3.2.1 $V \sin i$ Measurements . . . 106
3.2.2 The Hγ Line and the K-Band Flux . . . 109
3.2.3 Parameters from Spectroscopy . . . 111
3.3 Parameters from Interferometry . . . 114
3.3.1 The Geometric Model Fits . . . 114
3.3.2 The Physical Model Fits . . . 116
3.4 Summary and Discussion . . . 122

4 Non–Radial Pulsation in ϵ Per **128**
4.1 Introduction . . . 128
4.2 Line Synthesis Methods . . . 130
4.3 Variations of Local Temperature and Non-adiabatic Phase Lag . . . 134
4.4 Multimode NRP . . . 141
4.5 Comparison with Observations . . . 144
4.6 Conclusions . . . 148

5 Conclusions **150**
5.1 Methodology . . . 150
5.2 Stellar Physics . . . 151
5.3 Future Work . . . 153

A Programs **156**
A.1 Spectral Line Synthesis . . . 156
A.1.1 Associated Programs . . . 156
A.1.2 Synthesis Programs . . . 157
A.2 Interferometric Related Programs . . . 166
A.2.1 Make Images . . . 166

A.2.2 2D Fourier Transformation (Not FFT) 171

B Data Tables **174**

B.1 $V \sin i$ Measurements 174

B.2 Physical Parameters of Cluster Stars 185

References **194**

List of Tables

2.1 Hydra Observing Runs 26
2.2 ZAMS Model Star Parameters 31
2.3 Projected Rotational Velocities of B Stars in 19 Open Clusters 36
2.4 Summary of $V \sin i$ Data for 19 Open Clusters 39
2.5 Physical Parameters of Sample Stars 60
2.6 Physical Parameters of Model Stars 62
2.7 Test Results for Models 65
2.7 Test Results for Models (Cont.) 66
2.7 Test Results for Models (Cont.) 67
2.7 Test Results for Models (Cont.) 68
2.7 Test Results for Models (Cont.) 69
2.7 Test Results for Models (Cont.) 70
2.8 Polar Gravity Corrections 74
2.8 Polar Gravity Corrections (Cont.) 75

3.1 $V \sin i$ Fit Results for Different β Values 109
3.2 Spectroscopic Fit Results 113
3.3 Geometric Model Fit Results 115
3.4 Interferometric Fit Results 119

4.1 Physical Parameters of ϵ Per 136

List of Figures

1.1 Roche Geometry 14
1.2 Surface Grid 17

2.1 Rotational Broadening Line Profile Fitting 32
2.2 Comparing $V \sin i$ Measurements 34
2.3 $V_{\rm eq}$ Distribution 38
2.4 Histogram of $< V \sin i >$ vs. Spectral Subtype 40
2.5 CDFs of $V \sin i$ for 3 Spectral Subtype Groups 41
2.6 $V \sin i$ Histogram for Cluster and Field Stars 42
2.7 CDFs for Single and Binary Stars 44
2.8 CDFs for Different Age and Mass Groups 47
2.9 Evolution of $< V \sin i >$ of Stars Earlier Than B3 49
2.10 Rapid Rotators in the H–R Diagram 51
2.11 Hγ Equivalent Width vs. Temperature at Various Gravities 54
2.12 Hγ Profiles with Common Equivalent Width 55
2.13 Examples of Hγ Fits 57
2.14 Best Fits and Error Contours 58
2.15 Sample Stars (All) in $T_{\rm eff}$–$\log g_{\rm polar}$ Plane 77
2.16 Rapid Rotators in $T_{\rm eff}$–$\log g_{\rm polar}$ Plane 78
2.17 $V \sin i$ vs. $\log g_{\rm polar}$ (Whole Sample) 80
2.18 $V \sin i$ vs. $\log g_{\rm polar}$ (High Mass Group) 81
2.19 $V \sin i$ vs. $\log g_{\rm polar}$ (Mid–Mass Group) 82
2.20 $V \sin i$ vs. $\log g_{\rm polar}$ (Low Mass Group) 83
2.21 $V \sin i$ vs. $\log g_{\rm polar}$ (Binary Sample) 84
2.22 Examples of He I Line Fits 86
2.23 He–Weak Star Example 87
2.24 He–Strong Star Example 88
2.25 Line–to–Line He Abundance Differences 89
2.26 He Abundance vs. $\log g_{\rm polar}$ 91

2.27 He Abundance vs. $T_{\rm eff}$ 92
2.28 He Abundance vs. $\log g_{\rm polar}$ for the High Mass Group 93
2.29 He Abundance vs. $V \sin i$ for 3 Groups at Different Ages 95

3.1 uv coverage 103
3.2 $V \sin i$ fit 108
3.3 Hγ line and K–band Fit 112
3.4 K–band image and its Fourier transformation 118
3.5 Visibility Models A B C 120
3.6 Alpha Chi2 121
3.7 Beta Incl Chi2 122
3.8 A Helium–Weak Star? 123
3.9 Geometric versus Physical 125
3.10 Regulus in the H–R Diagram 126

4.1 Model Line Profiles at Different Temperatures 135
4.2 LPVs with and without Local Temperature Variation 137
4.3 LPVs with Different Non–adiabatic Phase Lag 140
4.4 Multi–mode vs. Mono–mode 142
4.5 Fourier Amplitude Distribution 143
4.6 LVPs at Different Inclinations 144
4.7 Comparison of model LPVs at $i = 70°$ with Observations 145
4.8 Comparison of model LPVs at $i = 40°$ with Observations 146

Abbreviations

A&A ..... Astronomy & Astrophysics
AJ ..... Astronomical Journal
ApJ ..... Astrophysical Journal
ApJS ..... Astrophysical Journal Supplement Series
ARA&A ..... Annual Review of Astronomy & Astrophysics
CCD ..... charge coupled device
CHARA ..... Center for High Angular Resolution Astronomy
CPU ..... Central Process Unit
CTIO ..... Cerro Tololo Inter-American Observatory
EW ..... Equivalent Width
FWHM ..... Full-Width at Half-Maximum
HR, H-R ..... Hertzsprung-Russell
HRD ..... Hertzsprung-Russell Diagram
IR ..... Infrared
KPNO ..... Kitt Peak National Observatory
KS ..... Kolmogorov-Smirnov test
IUE ..... International Ultraviolet Explorer
LPV ..... Line Profile Variation
LTE ..... Local Thermodynamic Equilibrim
MNRAS ..... Monthly Notices of the Royal Astronomical Society
McD ..... McDonald Observatory
MS ..... Main-Sequence
NLTE ..... Non-Local Thermodynamic Equilibrium
NOAO ..... National Optical Astronomy Observatory
NRP ..... Non-Radial Pulsation
ODF ..... Opacity Distribution Function
OPD ..... Optical Pathlength Difference
OS ..... Operating System
RMS ..... Root Mean Square

PASP ..... Publications of the Astronomical Society of the Pacific
S/N ..... Signal-to-Noise ratio
TAMS ..... Terminal-Age Main Sequence
TE ..... Thermodynamic Equilibrium
UD ..... Uniform Disk
UT ..... Universal Time
UV ..... ultraviolet
WIYN ..... Wisconsin Indiana Yale NOAO
ZAMS ..... Zero-Age Main Sequence

Chapter 1

Stellar Spectrum Synthesis

1.1 Why Spectrum Synthesis?

Why do we need stellar spectrum synthesis in studies of stellar physics? The answer to this question may not be immediately clear until we consider the legacy of spectroscopic analysis methods in astrophysics. Here I offer a short introduction to the history of studies of stellar radiation, the one direct physical connection between the stars and us, and I describe how the analysis of stellar radiation has deepened our understanding of the physics of stars.

The first recorded information about stars was limited to only very basic data, such as their positions, apparent brightness (or magnitude), and color. This situation continued until the early 1700s when Newton discovered in his prism refraction experiment that light from the Sun is actually a mixture of different color components. This discovery opened an opportunity to investigate the properties of a distant light source through a study of its radiation, a vital criterion for astronomical research. The first important observation of a stellar spectrum came in 1817 with Fraunhofer's discovery of "dark lines" in the spectrum of our Sun. In 1866 Fr. Angelo Secchi, a Jesuit astronomer in Italy, made visual observations of prism spectra of about 4000 stars, and he divided the stars into four broad spectral cat-

egories based upon the presence of common spectral absorption features. A huge advance came with the introduction of photography in the late 19th century. This meant that high quality spectra recorded on photographic plates could be archived for careful classification and comparison with theoretical work. Astronomers at Harvard Observatory launched the Henry Draper Memorial Survey between 1886 and 1897 to carry out a systematic photographic study of stellar spectra of more than 220,000 stars over the entire sky. In 1890, Edward Pickering and Williamina Fleming made a first attempt at spectral classification based upon the strength of hydrogen lines. In 1901, Annie Jump Cannon noted for first time that stellar temperature was the principal distinguishing feature among different spectra, and she came up with seven primary classes that we still use today: types O, B, A, F, G, K, and M. William Morgan and Phillip Keenan (1943) later added luminosity as a second classification parameter for stellar spectra, running from class I for supergiants to class V for dwarfs (main sequence stars). All of these major historical spectral investigations built the basis of our knowledge about stars, and allowed us to estimate basic stellar physical properties and to test theories of stellar evolution within a simple framework. Today, with more reliable theories and more refined instruments, spectroscopic investigations are found at the core of every branch of stellar astrophysics, and we are coming to understand almost every aspect of stellar physics by analyzing stellar spectra in detail.

The parameters characterizing the surface of a star, such as temperature, gravity, rotational velocity, and chemical abundance, are all tightly connected with specific features in the stellar spectrum. The best way to extract such information from observed spectra is to construct synthetic spectra for model stars that, with the right choice of input parameters,

can successfully match the observed spectra. If the models can provide a reliable description of physical laws that govern the emergence of radiation from a stellar atmosphere, then the stellar parameters derived by matching the observed and model spectra will be a good representation of those for the real star. Hence we see how spectrum synthesis is a critical step in spectroscopic analysis methods.

The idea behind spectrum synthesis is quite simple. The observed stellar spectrum is formed from flux contributions from over the entire visible surface of the star. Thus, spectrum synthesis can be done in two steps. The first step is to evaluate the radiation from every small patch on the stellar surface (local specific intensity times the projected area), and then sum these contributions together to form the spectrum. In next section, I will focus on the evaluation of the local flux, and in Sections 1.3 and 1.4 I will discuss the issues related to the surface integration.

1.2 Local Flux on the Stellar Surface

The evaluation of the local radiation field at the stellar surface requires first an accurate description of the local physical conditions of the stellar atmosphere, which are generally obtained by calculating theoretical model atmospheres. Once we have the proper model atmosphere in hand, the solution of the radiative transfer equation can then provide us the local radiative energy distribution for any desired frequency window. The focus of this work will often be on one spectral absorption line that we will call the intrinsic or specific intensity line profile.

1.2.1 Model Atmospheres

The first step toward our final goal of obtaining the synthesized stellar spectrum is to derive a model stellar atmosphere appropriate to the star of interest. The construction of model atmospheres is another very large topic in stellar astrophysics that is too complicated to be covered in detail here. Thus, beginning with only a short and very schematic outline, this subsection will focus more on the programs used in this work for constructing model atmospheres.

What is a model atmosphere? What parameters does it use to describe the physical conditions of the top layers of stars? In order to calculate the radiation from the photosphere of a star, we need to determine the distributions of temperature, pressure, and various particle densities within the photosphere. A model atmosphere is a listing of these quantities as a function of depth in the atmosphere. It tabulates not only the geometrical depth but also the optical depth that photons of some wavelength will encounter as they pass through the stellar atmosphere.

The numerical calculation of model atmospheres generally involves some built-in assumptions that can dramatically simplify the models in some aspects. The first of the important assumptions is the adoption of hydrostatic equilibrium. This is the concept that the atmosphere is static with a balance existing between the gravitational force inwards and a pressure gradient outwards. We further assume that any macroscopic motions in the stellar atmosphere are small compared to thermal motions of the particles within it. In other words, there are no large-scale accelerations comparable to the surface gravity. This static view about stars holds quite well except for a few special types of stars, such as very hot

O-type stars that have strong stellar winds. The second assumption is that of plane parallel geometry, i.e., that the atmosphere can be fully described by one depth parameter (ignoring two other spatial dimensions). This is generally valid, except in the case of supergiant stars, because the geometric depth of stellar atmosphere is much smaller than the stellar radius, and therefore we can safely ignore the spherical curvature of the stellar surface.

Another important assumption is that of local thermodynamic equilibrium (LTE). The beauty of the idea of thermodynamic equilibrium (TE) is that we only need two variables in the macroscopic world, temperature and pressure, to characterize materials in a TE state (i.e., their particle velocity distributions, population distributions among energy levels, and ionization degree). However, because of the radiation loss from the stellar surface, a temperature gradient must exist in a stellar atmosphere and leave no possibility for strict TE there. In order to take advantage of the properties of TE and at the same time acknowledge the energy leakage in a stellar atmosphere, the LTE assumption is introduced. The idea is that the two parameters, temperature and pressure, may be applied locally to help estimate the physical distributions of the gas. Again, this assumption is widely reliable, except for cases such as the very hot O-type stars and the more evolved giant/supergiant stars, where the radiation field is so dominant and/or the outer layers are so tenuous that the LTE assumption eventually breaks down. In these cases, non-LTE (NLTE) treatments are needed.

The atmospheric structure of any given star is mainly determined by two physical parameters, effective temperature ($T_{\rm eff}$) and logarithm of the surface gravity ($\log g$), combined with other less important factors, such as chemical composition and microturbulent velocity. $T_{\rm eff}$ is the temperature of an equivalent black-body source that has the same integrated radiant

flux as that passing through stellar atmosphere, i.e., it measures the bolometric brightness of the star, and it is the major factor controlling the temperature structure in the stellar atmosphere. On the other hand, the surface gravity ($\log g = \log[GM/R^2]$) directly affects the surface gas pressure and, consequently, the densities of the gas components, including electrons, protons, H I, He I, He II, and other metallic atoms and ions. The local temperature and particle densities then dictate the opacity of materials at that depth, which controls the radiative flux passing through the gas. Here we can see that all stratifications in a stellar atmosphere, such as the temperature structure, density distribution of various particles, and ionization status in different layers, must attain values for which hydrostatic equilibrium, radiative equilibrium (constant flux in all layers), and some thermodynamic equilibrium (LTE and/or NLTE, which controls the ionization states and particle populations at different energy levels) are maintained throughout. In real computations the final equilibrium state (the model atmosphere) can be obtained through a complex iteration procedure, which generally starts with a simple model (such as the gray atmosphere in which opacity is wavelength independent) and then adjusts the distributions of temperature and other variables in each iteration with corrections based upon the difference of total flux between the computed model and that set by $T_{\rm eff}$ (Kurucz 1979).

There have been significant advances in detailing stellar opacity sources (more and more accurate atomic and molecular data) and in improving algorithms, so that modern stellar model atmosphere programs can offer us accurate and reliable simulations of stellar atmospheric conditions. They can be used to derive key parameters of stars and to investigate stellar physics problems through a comparison of predictions from models and observa-

tional data. There are many wonderful programs available for modeling stellar atmospheres, such as ATLAS (R. L. Kurucz), TLUSTY (I. Hubeny and T. Lanz), and PHOENIX (P. H. Hauschildt). The code ATLAS is among the most widely used (the current version is called ATLAS9). It was developed by R. L. Kurucz at the Harvard-Smithsonian Center for Astrophysics, and it calculates fully line blanketed LTE model atmospheres based upon a library of about 60 million lines used in the calculation of opacities (including those from diatomic molecules). ATLAS9 can generate realistic models for mid-range temperature stars. Other more recent programs, such as TLUSTY and PHOENIX, have improved algorithms and parallelization methods that can be applied to difficult NLTE problems. TLUSTY, for example, can treat the NLTE populations of H, He, and many other atoms, and is useful in studies of very hot stars. The PHOENIX code can even deal with the non-hydrostatic equilibrium cases, such as stars with strong stellar winds and supernovae. The work in this dissertation relies upon model atmospheres generated by ATLAS and TLUSTY, and the following paragraphs cover some of their key features and applications.

The official FORTRAN source code for ATLAS9 can be downloaded from Kurucz's webpage[1]. However, the ATLAS9 codes I used in this work are from different sources: (1) a revised UNIX version by M. Lemke that can be compiled only by f77 under UNIX OS, and (2) a revised LINUX version by A. Reiners[2] that can be compiled using the free GNU compiler g77 under any Linux OS. The program comes with two sets of Opacity Distribution Functions (ODF), one with a coarse wavelength spacing (328 points) and one with a finer spacing (1213 points). Each set is available for different microturbulent velocities and metallicities.

[1] http://kurucz.harvard.edu/programs/atlas9/
[2] http://www.hs.uni-hamburg.de/DE/Ins/Per/Reiners/package.htm

Some model atmospheres of quite wide coverage in temperature, gravity, and metallicity are already calculated for direct use (Kurucz CD13, 16, 17, and 19[3]). However, the existing model grid is not dense enough for accurate interpolation, and therefore ATLAS9 is needed to prepare the specific models required for research purposes.

The two versions of ATLAS9 are run using slightly different syntax to issue the commands, but the procedure is basically the same. The user specifies the effective temperature, surface gravity, microturbulent velocity, metallicity, and the ODF file, and then the program will generally converge to a final result after several iterations. It generally requires only a couple of minutes to obtain a converged model atmosphere on a modern PC (with a CPU such as a Pentium 4 running at 2.8 GHz). In addition to the parameters listed above, an input file is used to specify other controls on the computing procedure, such as the optical depth grid, included opacity sources, and use of convection. The program may fail to converge in some circumstances (for example, in cases where the temperature is very high and the surface gravity is very low), and in these situations it is helpful to include an existing calculated model atmosphere in the input file for use as the starting point for the iterations.

The TLUSTY program is maintained by I. Hubeny and T. Lanz[4]. The most significant difference from ATLAS9 is that TLUSTY is capable of calculating a fully consistent, NLTE line blanketed model. The current version is TLUSTY200. The program is still under active development in many aspects. Earlier versions of TLUSTY could only be compiled by using commercial FORTRAN compilers or f77 under UNIX OS. However, the newer version, TLUSTY200, can also be compiled using the free GNU compiler, g77. The TLUSTY

[3]http://kurucz.harvard.edu/cdroms.html
[4]http://tlusty.gsfc.nasa.gov/

NLTE code is far more computationally intensive than LTE programs such as ATLAS. The program can evaluate the contributions to the opacity from all elements (atoms/ions) with atomic number 1 – 30, and the populations at each energy level in these model atoms can be evaluated by solving the NLTE equations of statistical equilibrium. A calculation of a NLTE, metal line blanketed model that considers all the available 30 elements requires hours or even days on a modern PC with more than 1 GB of memory. Fortunately, Hubeny and Lanz published a grid of 690 metal line-blanketed, NLTE, plane-parallel, hydrostatic models prepared using TLUSTY200[5] (Lanz & Hubeny 2003), which are very useful for studies of hot early-type stars.

The convenient aspects of TLUSTY are its versatility and flexibility. TLUSTY was designed to produce full NLTE, line blanketed models, but the code can also generate much simpler models, such as those for H and He atoms alone. The user can decide if the populations of an element should be calculated by LTE or NLTE treatments or whether it should not be considered at all. The code can also calculate LTE models with various line blanketing options. The abundances of all elements other than H are user-adjustable. Although these simplified models may not represent the real stellar atmosphere as well as the fully NLTE, metal line blanketed models do, they can save a lot of computing time and they are very useful for some work that does not require accurate atmospheric structure. The authors have produced an informative User's Guide[6]. I caution that, like ATLAS, TLUSTY uses either a gray model or an existing model as the initial seed for the iterative procedure, and for difficult cases of high temperature and low gravity, convergence is aided by using an existing

[5]http://tlusty.gsfc.nasa.gov/Tlusty2002/tlusty-frames-models.html
[6]http://tlusty.gsfc.nasa.gov/Tlusty2002/pdf/tlguide200.pdf

model for the starting point.

The work described in this dissertation is based upon the creation of a large grid of model atmospheres that spans the full range of temperature and gravity of the stars that I will investigate. Most of the models were calculated for solar metallicity and a small microturbulent velocity (2 km s^{-1}), which are appropriate choices for the young and massive stars that form the focus of this work. These models form the basis for the subsequent spectrum synthesis calculations.

1.2.2 Intensity Line Profiles

Spectral line synthesis is an easier task compared to the calculation of stellar model atmospheres. We can use the given model atmosphere to solve the radiative transfer equation (accounting for both continuum and line opacity) and obtain the emergent radiation at any wavelength. The radiation from any small patch on the stellar surface is mainly controlled by the local temperature, gravity, and the cosine of the angle between the surface normal and the line of sight to the observer, μ. The latter quantity establishes the area projection factor and the "limb darkened" appearance of the surface element. For stars with spherical shape, the total flux integrated over the visible hemisphere is equal to the integral of the product of the specific intensity and μ over all viewing angles ($\mu = 0$ to 1) multiplied by the square of the angular radius, so it is a relatively simple calculation to obtain the predicted flux profile from the specific intensity profiles.

However, there are many situations in which the shapes of stars are non-spherical and the physical conditions vary with position on the stellar surface. Stellar rotation, tidal

deformation in close binaries, and nonradial pulsation are all examples of these more complex integration problems. A simple integration of specific intensity based on the radiation data at one surface location would not represent a true picture of the full emergent flux. Instead, we must calculate the flux contribution from every small patch on the visible stellar surface, according to its local temperature, gravity, and viewing angle of the observer.

I used the radiative transfer code SYNSPEC (current version SYNSPEC43) to obtain the specific intensity line profiles. This code was also developed by I. Hubeny and T. Lanz, and it is designed as a general spectrum synthesis tool, with many choices available to users for output related to spectral analysis and synthesis. SYNSPEC has several modes for spectrum synthesis. The standard mode allows the user to include thousands of lines into the computation, and the program will automatically check the opacity of each line to determine if is large enough to be included in the calculation. I adopted the few-lines mode which is used for cases where only one or several lines are required. There is also a continuum mode that calculates spectra using only continuous sources and the broad hydrogen lines for opacity.

A full description of how to use SYNSPEC can be found at the SYNSPEC webpage[7]. Only a few relatively important points are mentioned here. SYNSPEC can use input model atmospheres generated by both TLUSTY and ATLAS. If the input model is an LTE model, then the intensity profiles are calculated assuming LTE (i.e., the Boltzmann and Saha equations define the populations). If the input model is a NLTE model (from TLUSTY), then the line synthesis is done by exact NLTE, approximate NLTE, or forced LTE schemes (ignoring

[7]http://tlusty.gsfc.nasa.gov/Tlusty2002/pdf/syn43guide.pdf

NLTE populations). The NLTE populations for each energy level from the input NLTE model atmosphere are used in the exact NLTE approach. The approximate NLTE scheme uses a second-order escape probability method to estimate NLTE populations (Hubeny et al. 1986). The calculation of intensity profiles for all lines other than hydrogen and helium assume a line opacity profile given by the Voigt function, which includes the effects of natural, Stark, Van der Waals, and thermal Doppler broadening. For those lines having no individual broadening parameters, SYNSPEC can use the values from the classical expressions (Kurucz 1979) or use broadening data from Griem's book (Griem 1974). For hydrogen and helium, the Stark effect is so big that the broadening properties of these lines are dramatically different from the lines of the heavier elements. SYNSPEC uses broadening data for the H and He transitions from many published sources (see Section 1.5 in SYNSPEC43 User's Guide for details). SYNSPEC has several output files that are assigned to numerical units. The most important output file for this work is unit 10 (fort.10), which contains the specific intensity data. The user can set up a grid of μ values as input parameters, and SYNSPEC will output the specific intensities for each value in the μ grid. Readers should note that the output wavelength grid generally does not have a uniform wavelength spacing.

Thanks to the SYNSPEC program, we are able to prepare the specific intensity profiles required for the integration of flux profiles. This final integration depends on the physical conditions on the surface of the star, in particular: (1) the three dimensional shape of the star; (2) the temperature at each surface position; and (3) the gravity at each surface position. These can be easily established for non-rotating stars (which are spherical and have a constant temperature and gravity), but for rotating stars the situation becomes more

complicated, as we will see in the next section.

1.3 Surface Conditions of Rotating Stars

1.3.1 Geometric Shape

The shape of a rotating star departs from a perfect sphere because of centrifugal forces. The radius in the equatorial direction will grow as the rotation velocity increases (see Figure 1.1). The most widely used theoretical model to describe the geometry of a rotating star is the Roche model, which assumes that all the mass of the star is located at the central point and that the star rotates as a rigid body. Under these assumptions, the total potential field in the frame corotating with the star would include the central gravitational potential term and the rotational potential term,

$$\psi \equiv \frac{GM}{r} + \frac{\omega^2(x^2+y^2)}{2}. \tag{1.1}$$

The surface of the rotating star then forms an equipotential surface, i.e., one on which $\psi =$ a constant. We can derive the surface equation from (1.1),

$$\frac{GM}{r(\theta)} + \frac{1}{2}\omega^2 r(\theta)^2 \sin^2\theta = \frac{GM}{r_p} \tag{1.2}$$

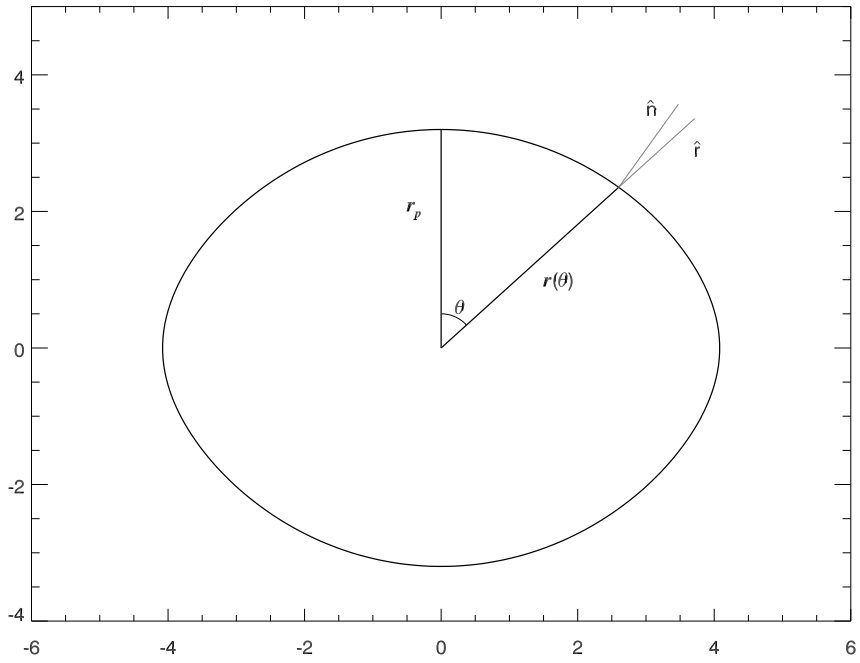

Figure 1.1: The Roche profile of a rotating star with $r_p = 3.2R_\odot$, $M = 3.5M_\odot$, and $V_{\rm eq} = 300$ km s^{-1}. Notice that the normal ($\hat{n}$) and the radial direction ($\hat{r}$) are different at any surface location other than the equator and the poles.

where M is stellar mass, ω is the angular velocity, and r_p is the polar radius. The formal solution of the equation (1.2) is given by (van Belle et al. 2001):

$$x(\theta) = \frac{r(\theta)}{r_p} = \frac{3}{u \sin\theta} \cos\Big[\frac{\cos^{-1}(-u \sin\theta) + 4\pi}{3}\Big] \tag{1.3}$$

where u is a dimensionless quantity, defined as

$$u^2 = \frac{27}{8}\frac{r_p^3 \omega^2}{GM}. \tag{1.4}$$

In real calculations, I use a different numerical algorithm to obtain $x(\theta)$ (Appendix A.1.1). Because r increases from the poles to the equator, the normal of any location on the surface except the poles and the equator no longer points radially. The tangent of the angle between the normal and the radial direction ($\hat{r}$) at any location on the surface can be calculated by:

$$\frac{1}{x(\theta)}\frac{dx(\theta)}{d\theta} = \frac{b\sin 2\theta\, x(\theta)^2}{1 - 3b\sin^2\theta} \tag{1.5}$$

where $b = 4u^2/27$. This formula (1.5) is very useful for calculating the projected area of each surface patch.

1.3.2 Surface Temperature and Gravity

The von Zeipel (1924) theorem states that the local bolometric flux F on the surface of a rotating star is proportional to the local effective gravity $g_{\rm eff}$, which is the sum of the gravitational and centrifugal forces. This theorem strictly holds only for the conservative cases, which basically assume no differential rotation. Because the local flux is related to the local effective temperature by $F = \sigma T_{\rm eff}^4$, the von Zeipel theorem actually tells us the relationship between the local effective temperature and effective gravity: $T_{\rm eff} \propto g_{\rm eff}^{0.25}$. If a star has a convective envelope, then the relation becomes $T_{\rm eff} \propto g_{\rm eff}^{0.08}$ (Lucy 1967). More generally, we can write the effective temperature – colatitude distribution of a rotating star as:

$$T_{\rm eff}(\theta) = T_p\left(\frac{g(\theta)}{g_p}\right)^{\beta} \tag{1.6}$$

where T_p and g_p $(= GM/R_p^2)$ are the polar temperature and the polar gravity, respectively. Theoretical calculations by Claret (1998, 2000) suggest that the transition of the β value from 0.08 (convection predominant) to 0.25 (radiation predominant) happens roughly in the temperature interval $3.81 \leq \log T_{\rm eff} \leq 3.86$. The hot OB stars that I will consider in this dissertation all have a surface temperature greater than 10000 K, so the adoption of $\beta = 0.25$ is a safe assumption (see also Chapter 3).

The effective gravity distribution can be derived from equation (1.1) (Collins 1963):

$$g_{\rm eff}(\theta) = g_p \left\{ \left[\frac{1}{x(\theta)^2} - 2b\, x(\theta) \sin^2\theta \right]^2 + [b\, x(\theta) \sin 2\theta]^2 \right\}^{1/2} \tag{1.7}$$

where b has the same meaning as in (1.5).

1.4 Final Step: Integration

I have outlined above the details of how to prepare all the material required for the final integration step of spectrum synthesis. In this section, I discuss the methodology and numerical techniques that finally turn those materials into synthetic stellar spectra.

First we need to divide the surface into small pieces for a numerical realization of the surface integration. Each piece is so small that it can be treated as free of curvature, and all the physical parameters, such as temperature and gravity, are assumed to be constant within its boundaries. There are many ways to divide a stellar surface into small patches. The easiest way is to make uniform divisions in both the θ and ϕ directions. However, such division will result in patches of unequal area, and the scheme is inconvenient for

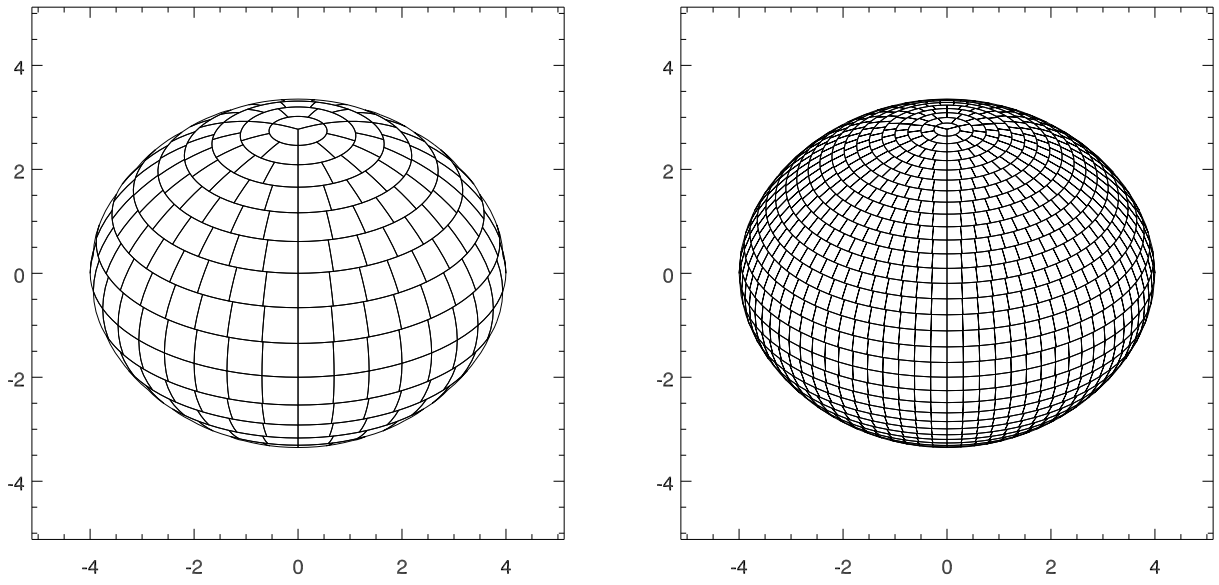

Figure 1.2: The two different surface partition layouts: The left panel shows a rough cut case ($N = 412$), and the right panel shows a fine cut case ($N = 2038$). The inclination angle $i = 60°$.

numerical integration (since many patches contribute very little). Here we use a better surface division strategy: we cut uniformly in the θ direction, but assign intervals in the ϕ direction for each θ that result in nearly equal patch areas. The entire surface is divided into N small patches with approximately equal area. The area of each patch is approximately $\Delta\theta\Delta\phi\sin\theta \simeq 4\pi/N$ steradians. Figure 1.2 shows two examples with approximately 400 and 2000 surface elements, respectively. A typical value of N in real calculations is between 10000 and 40000, which makes each patch so small that the numerical errors induced by this tiling method are negligible.

We can find the local temperature and gravity for each small surface element using (1.6) and (1.7), and we can calculate the μ value (the cosine of the angle between the normal and

the line of sight to the observer) according to the element's surface location (θ, ϕ) and the inclination angle of the spin axis i. In principle, we could feed the parameters associated with the individual surface elements directly into the atmosphere codes (ATLAS/TLUSTY) and the spectrum synthesis codes (SYNSPEC) to get its flux contribution. However, given the large number of surface elements, it is impractical to apply this procedure in a computationally efficient way. Instead, we first precalculate a grid of intensity line profiles, which covers the parameter space of interest ($T_{\rm eff}$, $\log g$, and μ). Then the specific intensity profile of each surface element is interpolated from the grid.

The integrated spectrum is obtained by summing the specific intensity profiles $f(\lambda')$ of all the visible surface elements, weighted by their projected area:

$$F(\lambda) = \int f\left[\lambda\left(1 + \frac{v_r}{c}\right)^{-1}\right] \mu dS \tag{1.8}$$

where the factor $1 + v_r/c$ takes care of the wavelength shift caused by the Doppler effect. For a rotating star having an inclination angle i, the radial velocity of a surface element (θ, ϕ) is given by:

$$v_r = r(\theta)\omega \sin\theta \sin\phi \sin i \tag{1.9}$$

where ω is the angular velocity of rotation. We can see from the formula (1.9) that the absolute value of v_r never exceeds $r(90^\circ)\omega \sin i$, or $v_{\rm eq} \sin i$, which approximately defines the spectral line width caused by rotational broadening.

The final goal of synthesizing stellar spectra is to compare them with the observations and to derive basic physical parameters of stars. The synthesized spectra generated from

equation (1.8) need one more step, convolution with the instrumental broadening profile, before they can be compared with the observations. All observed stellar spectra contain unavoidable broadening due primarily to diffraction by the entrance slit of the spectrograph, and the form of this distribution is called the instrumental broadening function. The net result for the incoming spectrum is a smoothing that is expressed mathematically as a convolution:

$$F_{\rm obs}(\lambda) = \int F(\lambda')w(\lambda - \lambda')d\lambda' \tag{1.10}$$

where $F_{\rm obs}$ is the final "observed" spectrum, F is the synthesized spectrum from (1.8), and $w(x)$ is the instrumental broadening function. Generally, $w(x)$ is assumed to have a Gaussian shape:

$$w(x) = \frac{1}{a\sqrt{\pi}}\, e^{-x^2/a^2} \tag{1.11}$$

where the value of a is related to the widely used quantity for spectral resolution, the full width at half maximum (FWHM), by

$$a = \frac{\rm FWHM}{2\sqrt{\ln 2}}. \tag{1.12}$$

This concludes my review of the all the common aspects of the spectrum synthesis methods used in this dissertation. In following chapters, I will describe several applications of this method in stellar astrophysical research. I will focus in Chapter 2 on stellar rotation in young Galactic clusters and show how synthesized spectra can help us to measure the stellar rotation of the cluster member stars and study their spin evolution. I will describe

in Chapter 3 a method that combines interferometric and spectroscopic data to determine the properties of the famous rapidly rotating B-star, Regulus. I will show in Chapter 4 how the spectrum synthesis method helps in the analysis of spectral data of ϵ Per, a B star with strong nonradial pulsation (NRP) signatures in its spectrum. The main conclusions will then be summarized in Chapter 5, where I also describe new directions for future study.

Chapter 2

Stellar Rotation in Young Galactic Clusters

2.1 Introduction

Unlike low mass stars that can lose their angular momentum early in their main sequence phase, massive OB stars are usually born with a large initial angular momentum that can last throughout their relatively short, core hydrogen-burning phase. Thus, we need to consider all the ways that stellar rotation could influence the properties and evolution of massive stars.

The first thing is the rotation rate itself. How does stellar rotation change with time in these massive stars? Theoretical models of massive rotating stars were recently developed independently by Heger & Langer (2000) and Meynet & Meader (2000). Their studies show that the spin evolution of a single, non-magnetic, massive star is driven by angular momentum loss in the stellar wind, a net increase in the moment of inertia, and an increase in stellar radius. One of the predictions of the models is that massive stars spin down during core H-burning at a rate that is larger for more massive stars and for those with higher initial rotational speeds. These models predict that a spin-up episode can occur very close to the terminal age main sequence (TAMS) when the core contracts prior to H-shell

burning. In some situations this increase may lead to near critical rotational velocities and induce enhanced equatorial mass outflows such as are observed in rapidly rotating Be stars (Maeder et al. 1999; Zorec 2004). Fabregat & Torrejón (2000) found that the incidence of Be stars tends to peak in open clusters with ages between 13 and 25 Myr, approximately when early B-type stars are close to the TAMS. A similar conclusion was also found by McSwain & Gies (2005) based upon a study of the frequency of Be stars in some 48 southern sky clusters. However, the positions of the Be stars in the Hertzsprung–Russell diagram (HRD) cover the entire range between the zero-age main sequence (ZAMS) and the TAMS (Mermilliod 1982; Zorec 2004; McSwain & Gies 2005) so it is doubtful that many Be stars are actually TAMS objects. Another possible process causing spin-up in massive stars is mass transfer in close binary systems. There are many examples of rapid rotation of the mass gainer in close binaries (van den Heuvel 1970; Etzel & Olson 1993; Šimon 1999; Barai et al. 2004). Even moderate mass transfer can cause a significant spin up of the mass gainer star (Langer et al. 2004). One extreme example of this spin up process is found in the classical Be star, ϕ Persei, which was probably spun up by an earlier stage of mass transfer to attain the observed projected rotational velocity of $V \sin i = 450$ km s^{-1} (about 97% of the critical velocity) (Gies et al. 1998).

The second thing is that the evolutionary paths of rapidly rotating massive stars can be very different from those for non–rotating stars (Heger & Langer 2000; Meynet & Maeder 2000). At the ZAMS, rapid rotating stars are generally less luminous and cooler than their non–rotating counterparts because the centrifugal force partially cancels gravitational force. However, rapid rotation can trigger strong mixing inside massive stars that will bring fresh

hydrogen from the envelope down to the core, thereby extending the core hydrogen-burning lifetime and significantly increasing the luminosity. Thus, massive rapid rotators are expected to be hotter and more luminous than non–rotating stars. The mixing process will also bring the core matter up into the surface layers and change the chemical composition of the stellar surface with time.

By providing us with examples of stellar populations at various well-defined ages and probably the same chemical compositions, a collection of young clusters offers us the means to examine various mechanisms affecting rotation evolution and to detect the unique signatures of rotation–altered stellar evolution. However, the direct comparison of the observational data with theoretical predictions is difficult because rotation causes the stellar flux to become dependent on orientation with respect to the spin axis. Rotation changes a star in two fundamental ways: the photospheric shape is altered by the centrifugal force (Collins 1963) and the local effective temperature drops from pole to equator, resulting in a flux reduction near the equator called gravity darkening (von Zeipel 1924). Consequently, the physical parameters of temperature and gravity (and perhaps microturbulent velocity) become functions of the colatitude angle from the pole. The brightness and color of the star will then depend on the orientation of its spin axis to the observer (Collins & Sonneborn 1977; Collins et al. 1991). Evidence of gravity darkening is found in observational studies of eclipsing binary systems (Claret 1998; Claret 2003), and more recently, in the direct angular resolution of the rapid rotating star, α Leo (B7 V), with the CHARA Array, an optical long-baseline interferometer (McAlister et al. 2005). These rotation–induced effects make it more difficult for us to derive the surface parameters from observations and to compare

them with the theoretical predictions.

In this chapter, I present an investigation on the rotation properties and stellar evolution of the brighter stars in 19 open clusters with an age range between 3 and 60 Myr. A spectroscopic analysis method, developed to deal with the difficulties in studying rotating stars, is also introduced here. In Section 2.2, I describe the observing runs and data reduction procedures. Section 2.3 focuses on determining the projected rotational velocity, including the method, the statistical results and some implications purely from the $V \sin i$ measurements. Section 2.3 shows some evidence of changes in the rotational velocity distribution with cluster age, but because of the wide range in stellar mass within the samples for each cluster, it is difficult to study evolutionary effects due to the mixture of unevolved and evolved stars present. To characterize sample stars more accurately, their effective temperature ($T_{\rm eff}$) and surface gravity ($\log g$) are derived in Section 2.4, and then their polar gravity ($\log g_{\rm polar}$, a better indicator of the evolutionary state of rotating stars) is estimated in Section 2.5. With these new key stellar parameters determined, I discuss the evolution of stellar rotation and surface helium abundance in Section 2.6 and 2.7, respectively. A short summary of all the findings is given in Section 2.8.

2.2 Observations

Moderate dispersion, blue spectra of B-type stars in 19 Galactic clusters were obtained during the observing runs in 2000 and 2001. The WEBDA open cluster database (Mermilliod & Paunzen 2003) was used to select clusters for this study based on the following criteria: (1) age < 60 Myr, (2) distance modulus $m - M < 15$, (3) angular diameter 10 – 60 arcmin,

and (4) $>$ 20 main sequence and/or giant star members with MK classifications of B9 or earlier. The spectra of the northern sky clusters were obtained with the Wisconsin-Indiana-Yale-NOAO (WIYN) 3.5-m telescope at Kitt Peak National Observatory while the southern clusters were observed with the Cerro Tololo Interamerican Observatory (CTIO) 4-m telescope. Both telescopes are equipped with Hydra multiple-object spectrographs (Barden & Armandroff 1995) that use micropositioners and fiber optics to obtain spectra of many targets simultaneously. The main goal was to record the absorption line profiles of He I $\lambda\lambda 4026, 4387, 4471$, Mg II $\lambda 4481$, and Hγ $\lambda 4340$ that are relatively strong throughout the B-type spectral class. Each cluster field was generally observed on at least two nights, so that I could make a preliminary identification of the radial velocity variable stars (candidate spectroscopic binaries).

The details of the spectrograph set up for each run are summarized in Table 2.1. The Hydra spectra from the two runs are comparable but the WIYN spectra have better resolving power than those from CTIO. All the targets in a particular cluster were observed in a single fiber configuration using multiple exposures of 10 minutes (CTIO) or 20 minutes (WIYN) duration. Additional fibers were set on the blank sky to estimate the sky background. In addition to nightly bias and dark frames, we also obtained flat field spectra for every fiber configuration and telescope pointing. Typically, spectra of 30 – 80 stars were obtained in each observation, but I report here only on the brighter OB type stars that are identified in each field.

All the spectra and calibration frames were reduced using standard routines in IRAF[1].

[1]IRAF is distributed by the National Optical Astronomy Observatory, which is operated by the Association of Universities for Research in Astronomy, Inc., under cooperative agreement with the National Science

Parameter	WIYN 3.5 m	CTIO 4.0 m
UT Dates	2000 Nov. 13 – 16	2001 Feb. 9 – 12
Fiber diameter (μm)	310	300
Camera name	Simmons	Bench Schmidt
Camera focal length (mm)	381	400
Grating name	1200@28.7	KPGLD
Grating grooves mm^{-1}	1200	790
Grating blaze angle (deg)	28.7	19.6
Order	2	2
Order sorting filter	CuSO4	BG-39
CCD detector	SITe 2 × 2K	SITe 2 × 4K
CCD pixel size (μm)	24	15
Reciprocal dispersion (Å pixel^{-1})	0.252	0.440
Wavelength range (Å)	3983 – 4501	3878 – 4781
Comparison source	CuAr	He-Ne-Ar
FWHM at 4026 Å (Å)	0.74	1.74
FWHM at 4387 Å (Å)	0.83	1.44
FWHM at 4471 Å (Å)	0.85	1.42

Table 2.1: Hydra Observing Runs

The extraction and calibration of the individual spectra from the images was done using the *dohydra* package (Valdes 1995), in which flat fielding is accomplished by dividing the stellar spectrum by the flat field spectrum after extraction. The individual sub-exposures were extracted separately and then co-added to improve the S/N ratio. All the spectra were transformed to a heliocentric wavelength scale and rectified to a unit continuum, and most have a S/N = 50 – 400 pixel^{-1} (depending on the star's brightness). The focus of each spectrograph varied slightly across the spectrum, and I used width measurements of the unresolved comparison lines to estimate the FWHM of the resolution element (yielding the instrumental spectral line broadening) at the positions of the important spectral features. These are listed in the last three rows of Table 2.1.

Foundation.

2.3 Projected Rotational Velocities

Rotational broadening is the process that dominates the apparent shapes of photospheric absorption lines in rapid rotating stars. As mentioned in the previous chapter (see Equation (1.9)), when we study stellar rotation spectroscopically, we encounter an unavoidable projection effect that all spectral lines are rotationally broadened by the projected equatorial rotational velocity ($V_{\rm eq} \sin i$ or simplified as $V \sin i$), not by the true rotation velocity ($V_{\rm eq}$).

2.3.1 Measuring Projected Rotational Velocities

The derivation of the projected rotational velocity ($V \sin i$) from the rotationally broadened lines is the first step to study stellar rotation. One simple way to characterize these broadened line profiles is by measuring a line width (such as FWHM). The $V \sin i$ value can be directly determined if the relation between the line width and $V \sin i$ is carefully calibrated (Slettebak et al. 1975; Howarth et al. 1997). This method has been developed and improved over many decades, and it has become the dominant method in this field because of its simplicity and efficiency for processing large amounts of spectral data. However, since this method is based only upon one quantity, the line width, to gauge the effects of rotation on the line profile, the accuracy of the results may suffer. Furthermore, in the case of fast stellar rotation line width measurements become less useful due to the reduction in wing strength caused by strong gravity darkening of the equatorial flux in the stellar atmosphere (**?**).

One way to solve this problem and to obtain more reliable and accurate $V \sin i$ measurements is by fitting the entire observed line profile with a grid of the theoretical calculations (Howarth & Smith 2001; Mathys et al. 2002; **?**). Because this method uses all the avail-

able line data, we can derive a secure value for $V \sin i$ and help establish other physical properties such as effective temperature, gravity, and chemical abundance. The key to the success of this method is to begin by constructing reliable theoretical line profiles. It is often assumed for the sake of simplicity that the local intensity profiles have a Gaussian or Lorentzian shape, and then flux profiles are calculated by integrating these shapes over the visible, limb-darkened stellar surface. However, here I will mainly examine He I lines that have specific intensity profiles that are too complicated to be described by Gaussian or Lorentzian functions. Therefore, I decided to calculate realistic intensity profiles using the modern stellar atmosphere code TLUSTY and the radiative transfer code SYNSPEC (Hubeny & Lanz 1995).

For hotter stars ($T_{\rm eff} > 13000$ K), I choose to fit the He I lines with the synthesized profiles based on intensity profiles calculated by TLUSTY and SYNSPEC, while I modeled and fit the Mg II λ4481 line for the cooler, late-type B stars. I first calculated a set of simple H-He LTE model atmospheres using TLUSTY, assuming solar abundances and a constant microturbulent velocity (2 km s^{-1}). Note that these are not line-blanketed model atmospheres, so that our assigned effective temperatures will be somewhat hotter than the actual values. Nevertheless, for the purpose of determining $V \sin i$ from the line profiles, these simple LTE models and assumptions are fully adequate to calculate model profiles with appropriate strengths and shapes. I then constructed a grid of specific intensity profiles using SYNSPEC that was based on a three dimensional parameterization using μ, the cosine of the angle between the surface normal and line of sight, $T_{\rm eff}$, the local effective temperature, and $\log g$, the logarithm of the surface gravity. The effective temperature ranges from $T_{\rm eff} =$

12000 K to 34000 K in steps of 2000° for the He I lines (and from 8000 K to 20000 K for the Mg II line); the surface gravity spans the range from $\log g = 3.2$ to 4.2 in steps of 0.2 dex; and the orientation cosine ranges from $\mu = 0.1$ to 1.0 in steps of 0.1.

I then integrated the flux contributions over the visible hemisphere of the model star to obtain the synthesized line profiles. The synthesis procedure included: (1) dividing the stellar surface into a large number of facets with approximately equal area (10000 - 20000 facets); (2) finding $T_{\rm eff}$ and $\log g$ at the center of each facet, by considering the Roche geometry for a point-like (condensed) mass distribution and the consequent gravity darkening caused by stellar rotation (Collins & Harrington 1966); (3) calculating the specific intensity as a function of wavelength across the profile for each facet by interpolating within the grid of specific intensity profiles described above; (4) integrating the contribution from all visible facets, Doppler-shifted properly and weighted by the projected area; (5) finally rectifying the final output to a unit continuum.

I compared the model He I and Mg II profiles directly with those in the observed spectrum to estimate the appropriate temperature model that I parameterized by a spectral subtype index. Table 2.3.1 lists the physical parameters (effective temperature, mass, radius) for these stellar models that were adopted from ZAMS evolutionary calculations for non-rotating stars (Schaller et al. 1992). The 21 temperatures in the grid were selected to correspond approximately to a pseudo-spectral subtype according to the spectral subtype – temperature calibrations given by Hanson et al. (1997) (for the hotter subtypes) and by Gray (1992) (for the cooler subtypes) (Note: some pseudo-spectral subtypes were added by interpolation). The He I lines increase in strength to a maximum near subtype B2 and then begin to decline,

but I can distinguish between the hot and cool portions of the He I curve by the appearance of Mg II, which declines monotonically with increasing temperature. I found the best fit profile from the grid for each available line, and I adopted the average spectral subtype index for models used in the rotational broadening analysis. I caution that these indices may not correspond to an actual MK subtype for a number of reasons: (1) the theoretical line profiles are based on simple H-He LTE, unblanketed atmosphere models that may yield a slightly different spectral subtype – temperature relation than adopted elsewhere; (2) line blending problems in spectroscopic binaries; and (3) the assumption of a He solar abundance will not be accurate for the He-peculiar B-stars.

I constructed rotational line profiles for each line and for each spectral subtype index over a grid of projected rotational velocities ($V \sin i$ = 0, 50, 100, 150, 200, 250, 300, 350, and 400 km s^{-1}) with a fixed inclination angle of $i = 90°$ (corresponding to a line of sight in the equatorial plane of the star). Finally, all the synthesized profiles were convolved with proper instrumental broadening profiles (Table 2.1) before comparison with the observations. For each spectrum I first estimated the spectral subtype index, determined an approximate projected rotational velocity, and then made a final fit after application of small corrections for the radial velocity shift and continuum placement. I found solutions for $V \sin i$ that minimized the χ^2 difference between the observed and calculated profiles for the adopted spectral subtype, and then formed an average based on all the available lines. Examples of the fitting procedure are illustrated in Figure 2.1 for a fast rotator (*top panels*) and a slow rotator (*bottom panels*) in the cluster NGC 884 (χ Per).

The measurement errors varied among our sample stars, depending on their magnitude,

Index	Pseudo–Spectral Subtype	$T_{\rm eff}$ (kK)	M ($M_\odot$)	R ($R_\odot$)
0...	O9.5 V	34.9	20.0	5.8
1...	O9.8 V	32.6	17.0	5.3
2...	B0.0 V	31.1	15.0	5.0
3...	B0.3 V	29.1	12.6	4.6
4...	B0.5 V	27.8	11.0	4.3
5...	B1.0 V	25.5	9.5	4.0
6...	B1.5 V	23.7	8.3	3.7
7...	B2.0 V	22.0	7.0	3.3
8...	B2.5 V	20.3	6.3	3.1
9...	B3.0 V	18.7	5.5	2.9
10...	B3.5 V	17.8	5.1	2.9
11...	B4.0 V	17.0	4.8	2.8
12...	B4.5 V	16.2	4.4	2.8
13...	B5.0 V	15.4	4.0	2.7
14...	B5.5 V	14.9	3.8	2.6
15...	B6.0 V	14.4	3.6	2.5
16...	B6.5 V	13.9	3.4	2.5
17...	B7.0 V	13.5	3.3	2.4
18...	B7.5 V	13.0	3.2	2.3
19...	B8.0 V	12.6	2.9	2.2
20...	B8.5 V	11.8	1.8	2.1

Table 2.2: ZAMS Model Star Parameters

spectral subtype, and observing set up. Measurements of the He I lines in spectra of stars of subtypes later than B7 are difficult because the lines are weaker and often blended with nearby metallic transitions. For the cooler B stars ($T_{\rm eff} \leq 13000$ K) I relied on fits of the Mg II λ4481 spectral region (which included Ti II λ4468, He I λ4471, Fe II λ4473, and Fe I λ4476). The average inter-line error on $V \sin i$ is about 10% for the CTIO data and about 5% for the WIYN data. The systematic errors introduced by our choice of spectral subtype index are similar in size. The difference in the derived $V \sin i$ measurement is generally $< 5\%$ when I compare results obtained using two adjacent spectral subtypes (see Table 2.3.1) and

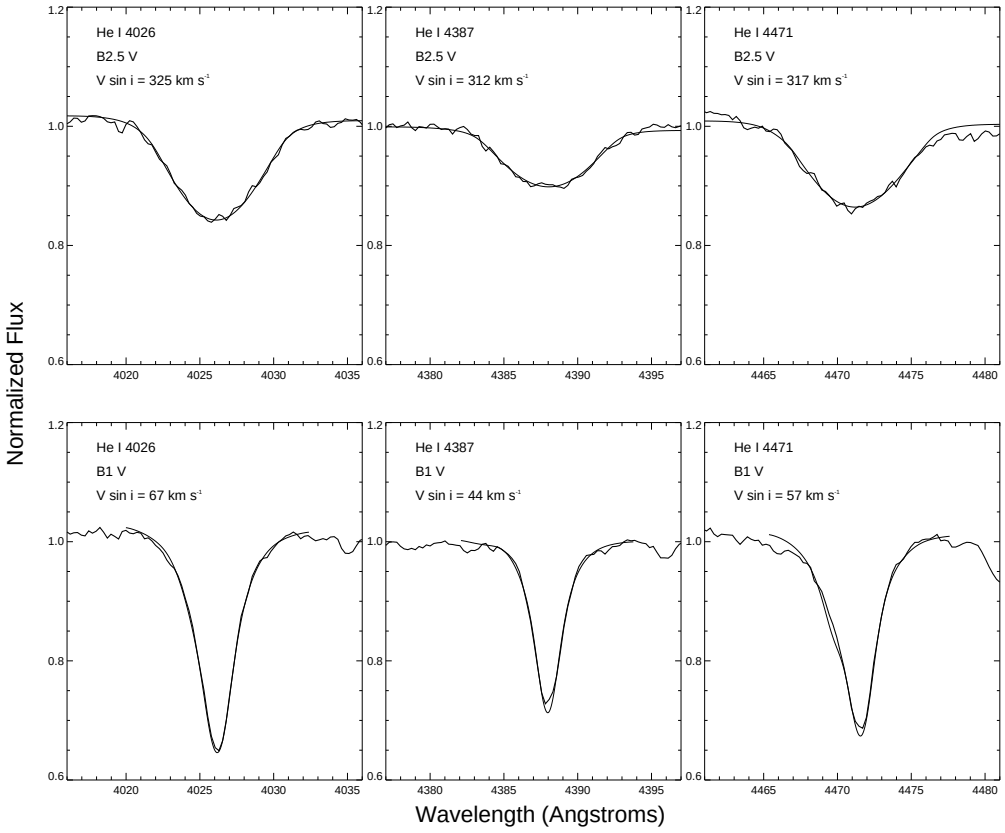

Figure 2.1: Fitting results for the He I lines (*thin lines*) compared with observed profiles (*thick lines*). The top panels show fits for a fast rotator, NGC 884 #2255, while the bottom panel shows the same for a slow rotator, NGC 884 #1983.

in fact decreases to zero around the B2 stars where the strength of the He I lines reaches a maximum and becomes insensitive to temperature.

I found $V \sin i$ measurements in the WEBDA database on open clusters (Mermilliod & Paunzen 2003) for 69 stars in common with our sample (Slettebak 1965; Slettebak 1968; Slettebak 1985; Hill 1967; Balona 1975a; Dworetsky 1975; Wolff 1981; Arnal et al. 1988; Verschueren 1991; Penny 1996; Mathys et al. 2002). Some 90% of these published

$V \sin i$ values were obtained by simple visual estimates or by measuring line widths, but Mathys et al. (2002) measured $V \sin i$ in 6 stellar spectra using line profile fitting and a simple convolution scheme for rotational broadening. Our $V \sin i$ values are generally in good agreement with these results (Figure 2.2), which can be fit by a linear relation $V \sin i$ [Published]=$(0.91 \pm 0.05) V \sin i$ [Ours]+(26.25 ± 7.97) km s^{-1}. A large scatter is not unexpected in such a comparison because of the heterogeneity of the $V \sin i$ data sources and measurement techniques. Our results are systematically larger than the published ones by about 9%, which is probably due to our treatment of gravity darkening effects for fast rotators that accounts for the weaker line wings. The larger $V \sin i$ measurements for the published results in the low $V \sin i$ regime probably reflect the lower resolving power of the observations used in earlier studies.

I offer a few cautionary remarks before consideration of our results in the next section. The run of stellar parameters as a function of temperature or spectral subtype in Table 2.3.1 is probably reliable for slow rotators. However, for fast rotators the physical conditions on the stellar surface can be quite different from non-rotating models due to the rotational effects. For example, Meynet & Maeder (1997) point out that the polar temperature of a fast rotator may be much higher than its effective temperature as derived from either the integrated luminosity and surface area or from the integrated spectrum of its visible hemisphere. Our scheme relies on a temperature estimate from the average line properties formed over the visible hemisphere, and I then adopt this temperature as the polar temperature in the calculation of a sequence of rotating star profiles. This inconsistency will have only a minor affect on our derived $V \sin i$ values because the profile shapes are much more dependent on the

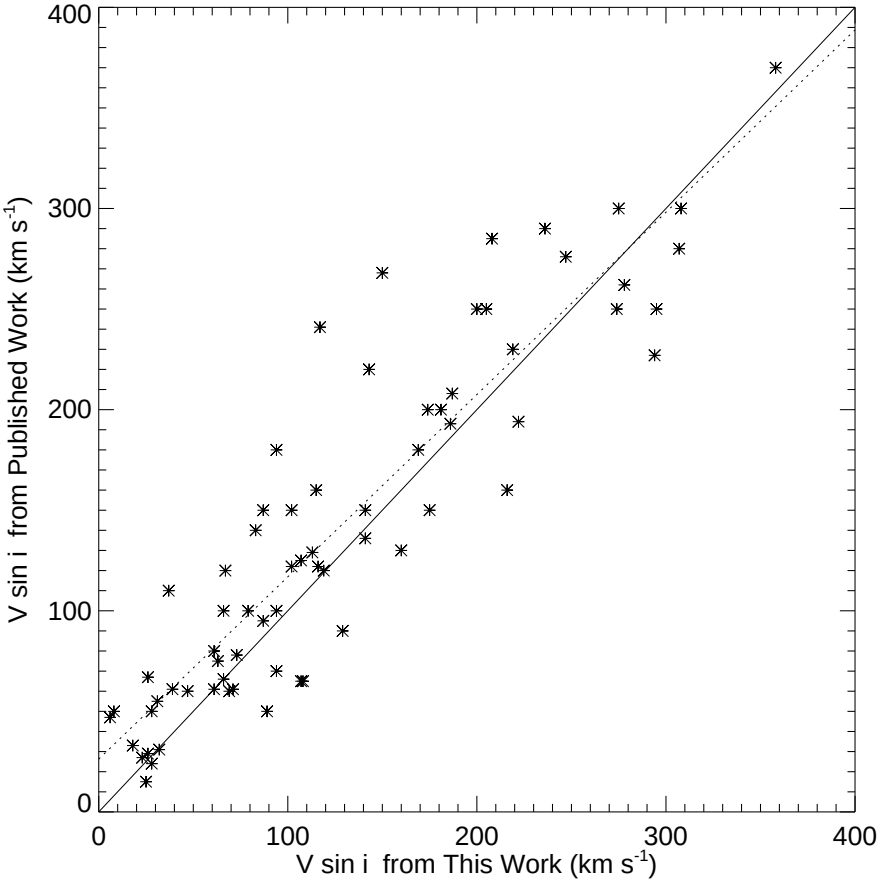

Figure 2.2: A comparison of our measured $V \sin i$ values with published work. The solid line shows the one-to-one relationship while the dotted line is the result of a linear least-squares fit.

Doppler shifts caused by rotation than on the adopted temperature of the local atmosphere.

A similar problem may arise because of our assumption of solar abundances. Many He-strong and He-weak stars are known to exist among the B-stars (Mathys 2004), and since our temperature estimation scheme is based on He I line strengths, some of our derived spectral subtype estimates may be incorrect. However, even in these cases the assumed profile shapes will probably be satisfactory because the Doppler broadening due to rotation is much more important for line shape than is the assumed chemical abundance. I found only one extreme

case (NGC 6193, #17) for which the He I line strengths were so extreme that none of the solar abundance models made a satisfactory fit.

Finally, I note that the assumption about the spin axis orientation angle has a negligible impact on the results. I calculated the line profiles assuming a fixed inclination angle of $i = 90°$, but the actual spin axes of the stars point randomly in space. In order to determine the consequences of this simplification for the final results, I tested the fitting code using rotationally broadened line profiles made assuming different inclination angles. I found that the line profiles change very little from $i = 90°$ to $i = 30°$ for a fixed geometric value of $V \sin i$, and for the infrequent cases of smaller inclination angle ($i < 30°$) the fitting code can still find the correct $V \sin i$ using a slightly different spectral type.

2.3.2 Results and Discussion of the $V \sin i$ Measurements

I obtained $V \sin i$ measurements of total 496 stars in 19 young clusters. The results for the individual stars in each cluster are listed in Table 2.3, which is given in full only in the Appendix B.1. The columns list: (1) the cluster name; (2) WEBDA identification number of the star (coordinates are given in the last column for stars with no WEBDA identification); (3) derived $V \sin i$ averaged over the values obtained from He I $\lambda\lambda 4026, 4387, 4471$, and/or Mg II $\lambda 4481$; (4) the RMS of residuals of the $V \sin i$ measurements; (5), (6), (7) the radial velocity for each observing night, based on measurements of the positions of the He I lines (note that the targets were observed on three nights for NGC 2244 and IC 2944, only one night for Trumpler 14 and 16, and on 2 nights for the rest); (8) the assigned index for spectral subtype of the star (Table 2.3.1); and (9) notes for interesting stars, such as double-

lined spectroscopic binaries (SB2) or stars having unusual line profiles, where the $V \sin i$ measurement may not be reliable. For double-lined spectroscopic binary systems, the $V \sin i$ values are determined by fitting the dominant component in the double-peak line profiles. The full version of Table 2.3 also gives the mid-exposure heliocentric Julian dates of each observation.

Cluster Name	WEBDA Number	$V \sin i$ (km s^{-1})	$\delta V \sin i$ (km s^{-1})	$V_r(N1)$ (km s^{-1})	$V_r(N2)$ (km s^{-1})	$V_r(N3)$ (km s^{-1})	Spectral Subtype Index	Notes
Ber 86	1	184	1	30.3	30.8	···	1.3	···
Ber 86	3	192	9	−24.6	7.5	···	4.0	SB2
Ber 86	4	178	10	17.2	45.2	···	1.0	SB2
Ber 86	9	362	3	−7.6	−15.7	···	3.3	···
Ber 86	12	309	23	−6.8	8.0	···	10.0	···
Ber 86	13	182	28	49.9	48.3	···	0.7	···
Ber 86	14	133	5	−131.7	−142.5	···	1.3	SB2
Ber 86	15	23	8	-13.9	−15.8	···	5.0	···
···	···	···	···	···	···	···	···	···

Table 2.3: Projected Rotational Velocities of B Stars in 19 Open Clusters
(a full version of this table is given in Appendix B.1)

The radial velocities were obtained by measuring the shift required to match the model and observed profiles. The measurement errors depend on the S/N of the individual spectrum but are typically ± 10 km s^{-1}. However, there are systematic radial velocity errors present in several clusters that are at least this large and that are manifested in overall differences in cluster mean velocity between nights. Our main interest in the velocity data is to identify the radial velocity variable stars that are candidate short period spectroscopic binaries. I adopted a limit of a radial velocity shift greater than 30 km s^{-1} between two nights as the criterion for detection of possible binaries. However, to avoid any systematic shifts in radial velocity between nights, I did not directly use the raw measurements of radial velocity listed

in Table 2.3 to estimate such variations. Instead, I calculated the mean radial velocity of each night for every cluster first, and then compared the residuals (the radial velocity minus the mean) between different nights to find the binaries using the 30 km s^{-1} criterion. This step was done in an iterative way for each cluster: once I found the binary candidates, I removed them from the list and recalculated the mean using the rest of stars and I repeated this isolation of the binary candidates and calculation of the mean until no more stars met the binary star criterion. The velocity variable stars are identified in Table 2.3 by the notation SB1 in the final column. The stars that I found to be double-lined spectroscopic binaries were also usually velocity variable, but these are simply noted as SB2 in Table 2.3.

The cumulative distribution function of $V \sin i$ for whole sample is plotted in Figure 2.3 (*top panel*). I did not build the $V \sin i$ distribution directly on statistical counts from the data. Instead, I first made a 4th order polynomial fit to the cumulative function (*dotted line* in top panel), and then obtained the $V \sin i$ distribution from the derivative of the fit curve (*dotted line* in bottom panel). Also I derived the $V_{\rm eq}$ distribution (*dashed line* in bottom panel) from the $V \sin i$ distribution using the deconvolution algorithm given in the paper by Lucy (1974).

I summarize in Table 2.4 the results for each of the 19 clusters, which are listed in order of increasing age. The columns here indicate: (1) the common name for the cluster; (2) the logarithm of the cluster age as listed in the WEBDA database (Mermilliod & Paunzen 2003); (3) the number of stars measured; (4) the mean projected rotational velocity of the whole sample; (5) the mean projected rotational velocity of the subsample of those stars of type B3 or earlier (according to the assigned spectral subtype index); (6) the percentage of

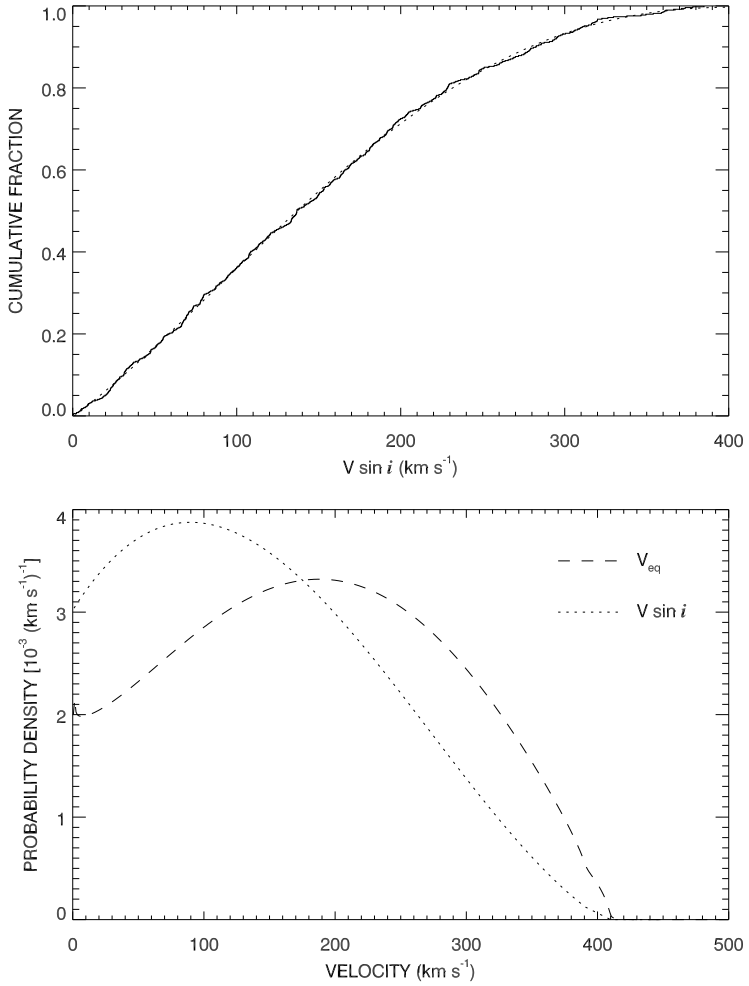

Figure 2.3: Top panel: the cumulative curve of 496 sample stars (*solid line*) and its polynomial fit (*dotted line*). Bottom panel: the $V \sin i$ distribution based on the polynomial fit (*dotted line*) and the $V_{\rm eq}$ distribution (*dashed line*).

very rapid rotators, i.e., stars with a projected rotational velocity greater than 300 km s^{-1}; (7) the percentage of candidate spectroscopic binary stars; and (8) the observatory where the spectra were obtained (see Table 2.1). Note that no binary estimates appear for Trumpler 14 and 16 since I have only single observations available for these clusters.

Name	log age (yr)	N	$< V \sin i >$ (All) (km s^{-1})	$< V \sin i >$ ($\leq$ B3) (km s^{-1})	$V \sin i >$ 300 km s^{-1} (%)	Candidate Binary (%)	Obs.
Trumpler 16	6.43	36	135	148	6	···	CTIO
IC 1805 ...	6.67	30	145	150	3	30	WIYN
Trumpler 14	6.67	5	103	178	0	···	CTIO
NGC 6193 .	6.72	19	156	134	10	21	CTIO
IC 2944 ...	6.73	38	136	125	5	13	CTIO
NGC 2362 .	6.77	28	161	141	4	14	CTIO
NGC 2244 .	6.80	41	169	165	12	39	WIYN
NGC 2384 .	6.90	15	91	83	0	7	CTIO
NGC 1502 .	7.03	18	172	183	11	28	WIYN
NGC 3293 .	7.03	23	184	173	22	9	CTIO
Berkeley 86	7.05	17	194	181	18	6	WIYN
NGC 869 ..	7.10	55	121	116	4	25	WIYN
NGC 457 ..	7.15	19	153	173	5	32	WIYN
NGC 884 ..	7.15	57	149	142	7	25	WIYN
NGC 2467 .	7.24	14	150	165	7	14	CTIO
NGC 4755 .	7.26	33	141	161	3	9	CTIO
IC 2395 ...	7.35	16	110	94	0	13	CTIO
NGC 7160 .	7.37	16	183	185	13	25	WIYN
NGC 2422 .	7.78	15	143	245	7	13	WIYN

Table 2.4: Summary of $V \sin i$ Data for 19 Open Clusters

I begin my review of these results by considering the properties of all the stars in full sample of clusters. The stars of our sample correspond mainly to MK spectral types from O9.5 to B8.5, and to luminosity classes from III to V. I plot in Figure 2.4 the mean $V \sin i$ versus spectral subtype with the total number of stars in each subtype bin given below. These numbers show that my sample is biased towards earlier subtypes (luminosity biased).

The distribution of $V \sin i$ for cluster stars is basically flat over this range and appears to similar the classical diagram for nearby B-type stars presented by Slettebak (1970). There is a slight indication that there are more fast rotators among the late–B subgroups (B5 – B8), which is similar to what Brown & Verschueren (1997) found for stars an in Sco OB2 and to what Abt et al. (2002) found for nearby field stars. However, the differences between the subtype groups are modest. I plot in Figure 2.5 the cumulative distribution functions of $V \sin i$ for three subgroups, [O9.5, B1.5], (B1.5, B5.0], and (B5.0, B9.0]. The three curves are all similar to each other and their mean $V \sin i$ values are almost same: 146.6 km s^{-1}, 143.4 km s^{-1}, and 153.8 km s^{-1} for these three groups, respectively.

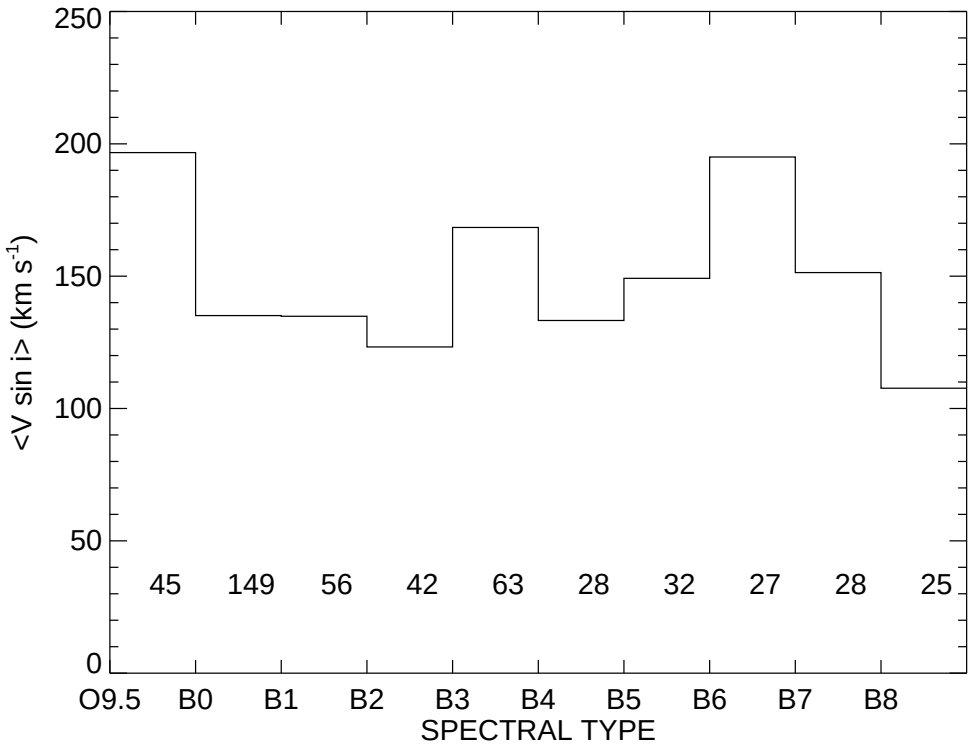

Figure 2.4: Mean $V \sin i$ as a function of spectral subtype. The number of stars in each subtype bin is give at the bottom.

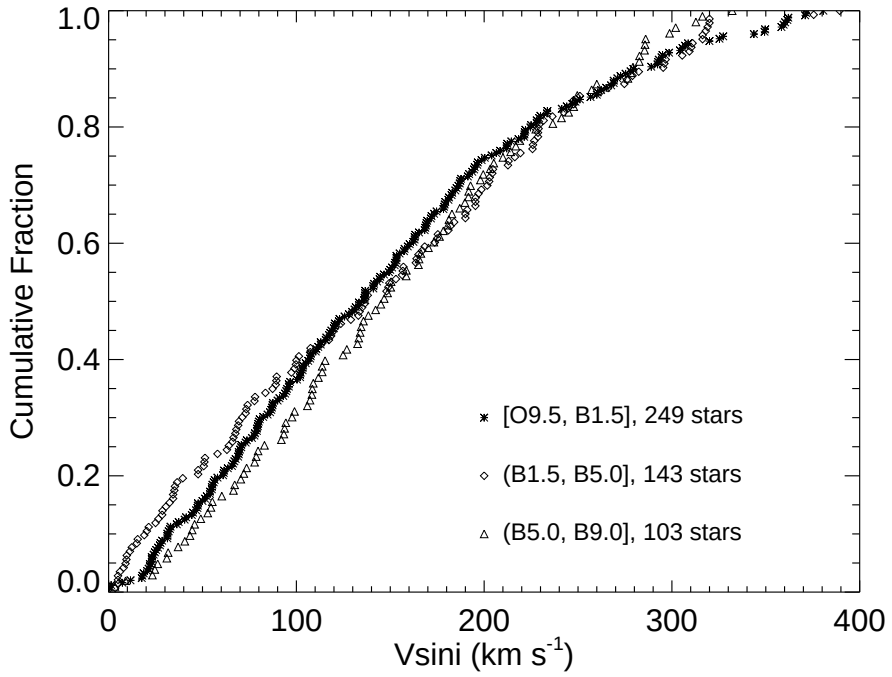

Figure 2.5: The cumulative distribution functions of $V \sin i$ for the stars gathered into three groupings of spectral subtype. Here we follow the mathematic tradition in which "[" means the boundary is included while "(" means the boundary is not included.

I next compare the projected rotational velocity distributions of cluster and field B stars. A histogram of the distribution of $V \sin i$ for all the measured stars (subtypes O9.5 to B8.5) is plotted in Figure 2.6 (*solid line*). I also extracted a subset of similar data for field stars from Abt et al. (2002) for stars with subtypes of B8.5 or earlier and luminosity classes between III and V (737 stars), and we plot the field star histogram also in Figure 2.6 (*dashed line*). The comparison shows that there are more slow rotators among the field B stars than is the case for the cluster stars. The mean projected rotational velocities are 113 ± 3 km s^{-1} and 148 ± 4 km s^{-1} for the field and cluster stars, respectively (where the quoted errors are the standard deviation of the mean). Part of this difference may be due to the better spectral resolution

of the spectra used by Abt et al. (2002) (better able to discern the sharpest-lined stars) and due to the presence of unrecognized binaries in our sample (with blended and broadened line profiles). It is also possible that the field stars represent a somewhat older population (stars from dispersed clusters) so that the difference reflects evolutionary spin-down (see below).

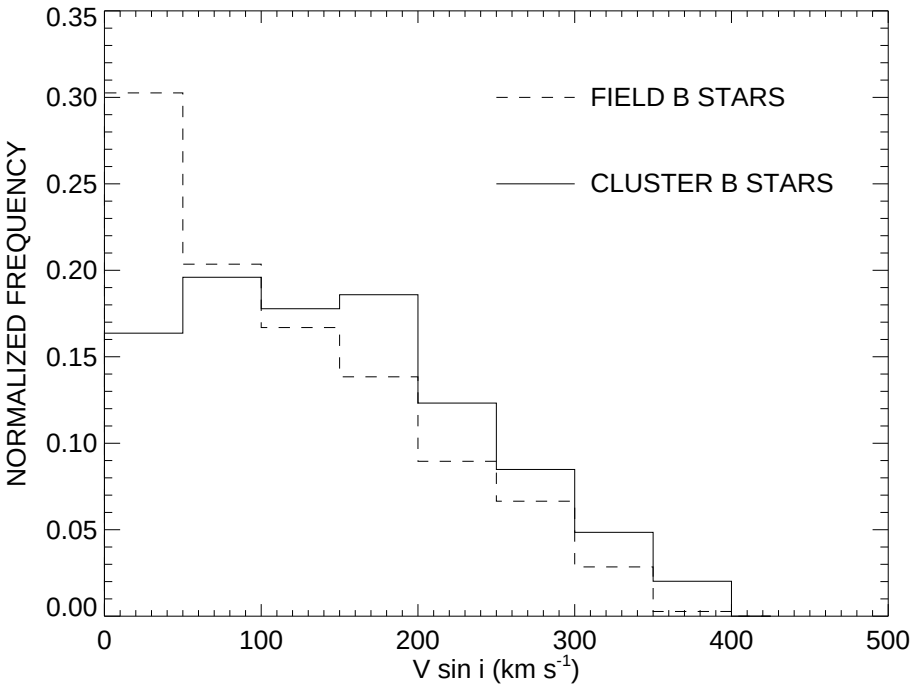

Figure 2.6: Histograms of $V \sin i$ for field stars (Abt et al. 2002) (*dashed line*) and for cluster stars (*solid line*).

I expect that the rotational velocity distributions of single and close binary stars may differ, since binary systems may experience either spin-down through tidal braking or a spin-up from mass transfer. There is evidence of rotational and orbital synchronization among binaries in the field population (Wolff et al. 1982; Abt et al. 2002). There are 94 variable radial velocity stars (21%) among the 454 stars in our sample with more than one radial velocity measurement that meet the spectroscopic binary criterion I adopted

($\Delta V_r >$ 30 km s^{-1}). The mean $V \sin i$ of the candidate binary group is 165 ± 9 km s^{-1} compared to a mean of 144 ± 5 km s^{-1} for the remaining radial velocity constant stars. This is a somewhat surprising result since synchronously rotating binary stars among the field population have a lower mean $V \sin i$ than single stars (Abt et al. 2002). I wondered if the larger radial velocity measurement errors associated with the rapid rotators (which have broad and shallow lines) led to the accidental inclusion of some rapid rotators in the candidate binary group. Consequently, I selected a second group of binary candidates using a more stringent radial velocity variation criterion ($\Delta V_r >$ 50 km s^{-1}). The adoption of this criterion reduces the number of candidate binaries to 49, and the mean $V \sin i$ for this group is even higher, 173 ± 15 km s^{-1}. The cumulative distribution functions for all three groups of stars (single stars, binary stars from the 30 km s^{-1} criterion, and binary stars from the 50 km s^{-1} criterion) are plotted in Figure 2.7. The Kolmogorov-Smirnov test (KS, hereafter) indicates that there is a 1% probability that the the single and binary star ($\Delta V_r >$ 30 km s^{-1}) data are drawn from the same distribution (or a 3% probability for the binary group selected using the tighter constraint, $\Delta V_r >$ 50 km s^{-1}). Thus, the difference appears to be significant. One possible explanation could be that our binary group includes many cases in which a faint or only partially resolved spectral line from the companion causes the composite profile to appear broader and to lead to a higher value of $V \sin i$ for such binaries. On the other hand, it may be attributed to some real physical mechanism, such as mass transfer happening in a binary system that causes a spin–up. Follow up spectroscopic investigations of the candidate binaries will be required to determine the precise nature of their projected rotational velocities.

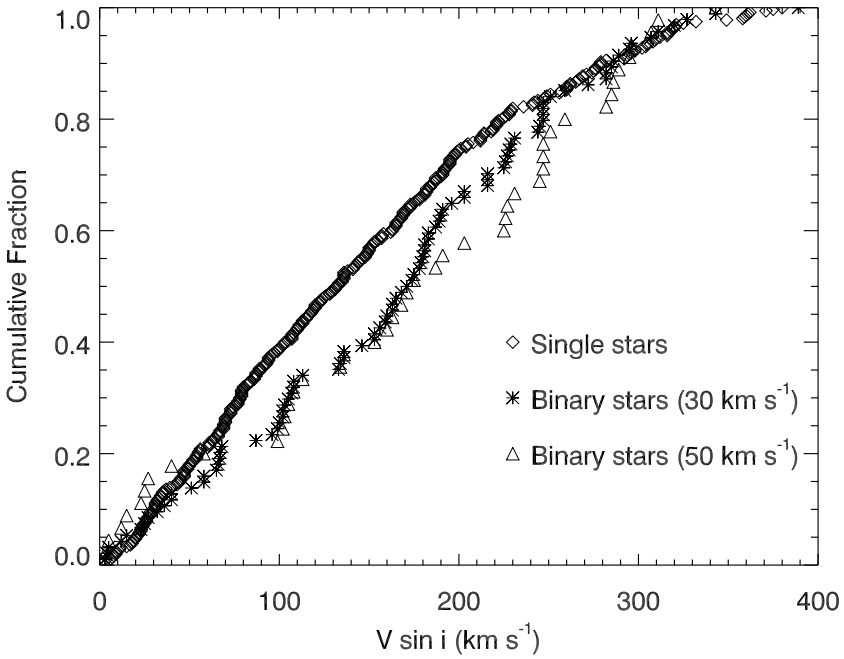

Figure 2.7: The cumulative distribution functions of $V \sin i$ for single and candidate binary stars (according to two criteria for the minimum radial velocity range).

I next turn to the question of temporal changes in the rotational velocity distributions by considering the cluster ages. One way to show the possible evolutionary effects of rotation for B-stars in these clusters is by plotting the $V \sin i$ cumulative distribution functions for clusters of different ages. Since the effects of rotation are expected to occur on time scales comparable to the main sequence lifetime (Heger & Langer 2000; Meynet & Maeder 2000) and since the lifetimes increase among later-type stars, I chose to divide the sample into three groups based upon spectral subtypes: [O9.5, B1.0) (194 stars), [B1.0, B4.0) (161 stars), and [B4.0, B9] (140 stars). Ideally, I would like to have a sufficient number of stars of each group in every cluster for statistical analysis, but since about half of the clusters contain only 20 or fewer stars, this kind of division is impractical. Thus, I grouped clusters with similar

ages together in order to have adequate numbers of stars in each age and spectral type category. The cumulative distribution functions of $V \sin i$ for these different age and spectral type bins are shown in Figure 2.8. The panels of Figure 2.8 are arranged in 3 columns for spectral subtype and in 5 rows for various age groups. Every panel shows two distributions, the cumulative function for all the stars in the spectral subtype group (*filled dots*), which appears the same in each respective subtype column, and the cumulative function for the specific age group in this spectral subtype bin (*diamonds*). I also list in each panel the KS probability that the all-age and specific-age binned $V \sin i$ data are drawn from the same distribution. I note that although the bottom row in Figure 2.8 is labeled with a log age range of 7.2 to 7.8, all but NGC 2422 fall in the log age range of 7.2 to 7.4 (Table 2.4).

Based on the stellar parameters adopted in Table 2.3.1, I can assume that the stars shown in the first spectral subtype column in Figure 2.8 have an average mass of approximately 12 $M_{\odot}$, while the representative masses are approximately 6 $M_{\odot}$ and 3 $M_{\odot}$ for the second and third columns, respectively. Meynet & Meader (2000) present evolutionary sequences for rotating stars that demonstrate that massive stars ($M > 9M_{\odot}$) experience a spin down over their entire MS phase that lasts until just before the TAMS when they experience a short spin-up episode due to core contraction. For a star with 12 $M_{\odot}$, their study predicts that the spin up will occur at log age = 7.2 after an extended period of spin down. This predicted trend is very similar to what we see in the first column in Figure 2.8. We see that in the fourth age bin (log age = 7.1 to 7.2) the specific-age distribution function falls above the all-age function, which indicates that specific-age projected rotational velocities are somewhat smaller than those for the all-age sample. On the other hand, the data for the

final specific-age bin (log age = 7.2 to 7.8) has a distribution lower than that of the all-age sample, which suggests that these older clusters host more rapid rotators. The KS probability that the these last two specific-age binned samples are drawn from the same distribution is 8%, which again suggests that the stars in the greatest age bin are characterized by faster rotation.

The main sequence lifetimes for the second and third spectral subtype groups correspond approximately to log age = 7.8 and 8.5, respectively (Schaller et al. 1992), both larger than the ages of the clusters in our sample (Table 2.4). Unfortunately, there are no modern evolutionary sequences available for intermediate mass rotating stars, but it is reasonable to assume that any spin-down they may experience will also occur on main sequence time scales (neglecting magnetic braking). Thus, we would not expect to see evolutionary effects among the lower mass stars in our sample given the relative youth of the clusters in our sample. The cumulative distribution functions illustrated in Figure 2.8 for columns 2 and 3 are mainly consistent with this expectation that the rotational properties of the lower mass stars do not change significantly over the time span sampled by these clusters. The main exception appears in the top, right panel for the lower mass stars in the very young clusters, Trumpler 14, Trumpler 16, and IC 1805, where the distribution indicates a predominance of slow rotators. However, I do not attach any special significance to this result since there are only 11 stars in this particular sub-sample.

It is difficult to make a direct comparison of the predictions for evolutionary spin down with the cluster data because the spin down rates are related to both stellar mass and initial rotational velocity. I have made a simplified analysis by restricting the sample to single stars

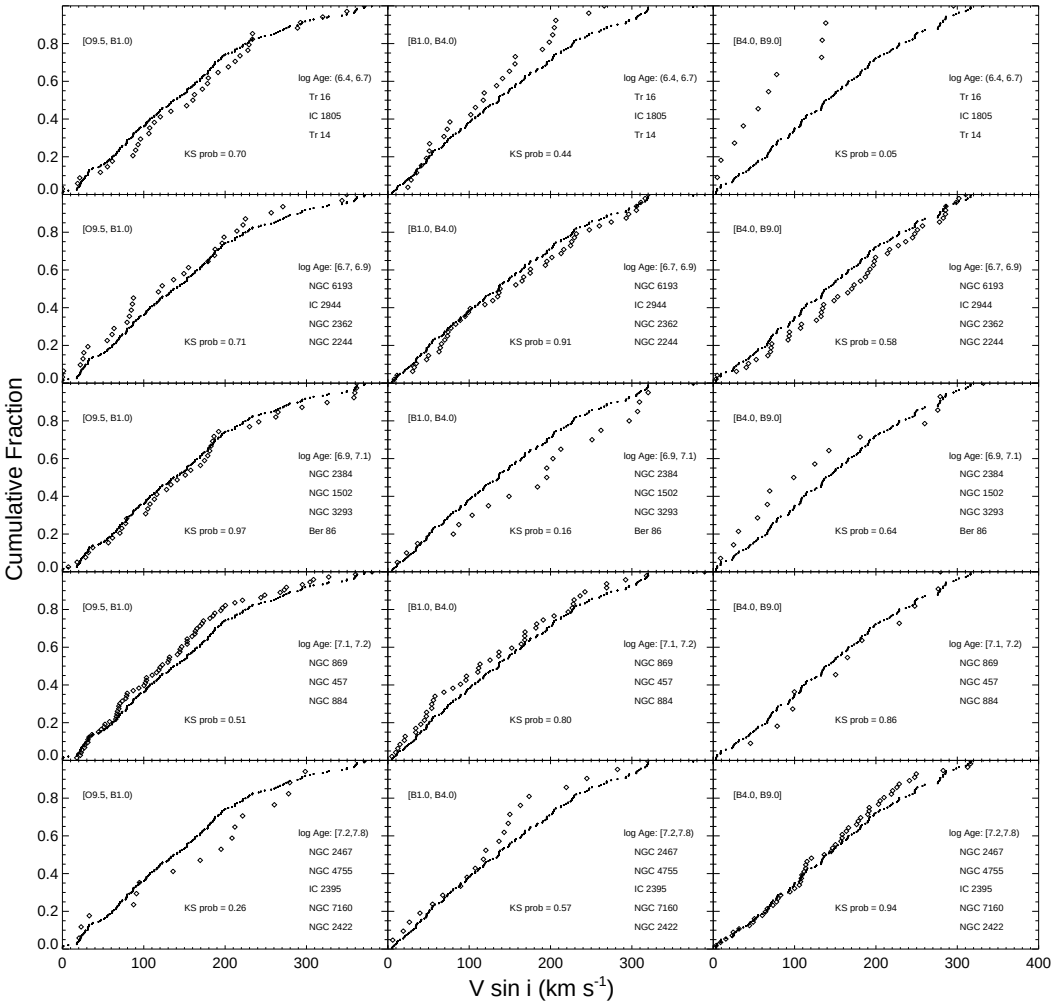

Figure 2.8: The cumulative distribution functions of $V \sin i$ for sample subgroups having certain age and spectral subtype ranges. The panels are arranged in three columns of early- to late-type stars and in five rows corresponding to clusters of increasing age. Each panel has two curves: one is for the specific-age subgroup (*diamonds*) and the other is for all stars of a spectral subtype range (*filled circles*). The KS probability that the two samples are drawn from the same parent distribution is listed in each case.

of subtype B3 and earlier where we expect the spin down rates to be largest. These cluster mean $V \sin i$ values are listed in Table 2.4, and I plot the means in Figure 2.9 for those clusters with log age < 7.5 and with more than 7 measurements. The mean spectral subtype in this limited sample corresponds approximately to a star of mass between 9 and $12 M_{\odot}$, so I used models for this mass range from Meynet & Maeder (2000) to estimate the predicted spin down between ZAMS and TAMS. I assumed that all clusters begin with a distribution of stellar rotational velocities given by our histogram in Figure 2.6. Then, I used the Meynet & Maeder (2000) model results to calculate how each 50 km s^{-1} bin is transformed to a lower velocity at each time step in order to determine a new mean $V \sin i$ for that time step. This predicted decline is shown as the solid line in Figure 2.9. Note that this basic calculation ignores the fact that the global distribution is actually based upon stars with a mixture of ages and that I have underestimated the actual velocity distribution by neglecting projection effects (i.e., by using a distribution of $V \sin i$ instead of V). I attempted to correct for these deficiencies by applying a normalization factor of 1.03 to the predicted mean $V \sin i$ curve in order to better match the observed means in the youngest clusters. The predicted slow decline in $V \sin i$ with time is consistent with the data for clusters younger than 10 Myr, but there appears to be a surplus of clusters with rapid rotators in the age range 10 to 20 Myr (see also the percentage of fast rotators in column 6 of Table 2.4). It is possible that these specific clusters have a large mean $V \sin i$ because of larger spin rates at birth or because their samples contain relatively more lower mass stars (with slower spin down rates), but taken at face value, these results suggest that some spin up processes become important in this time span.

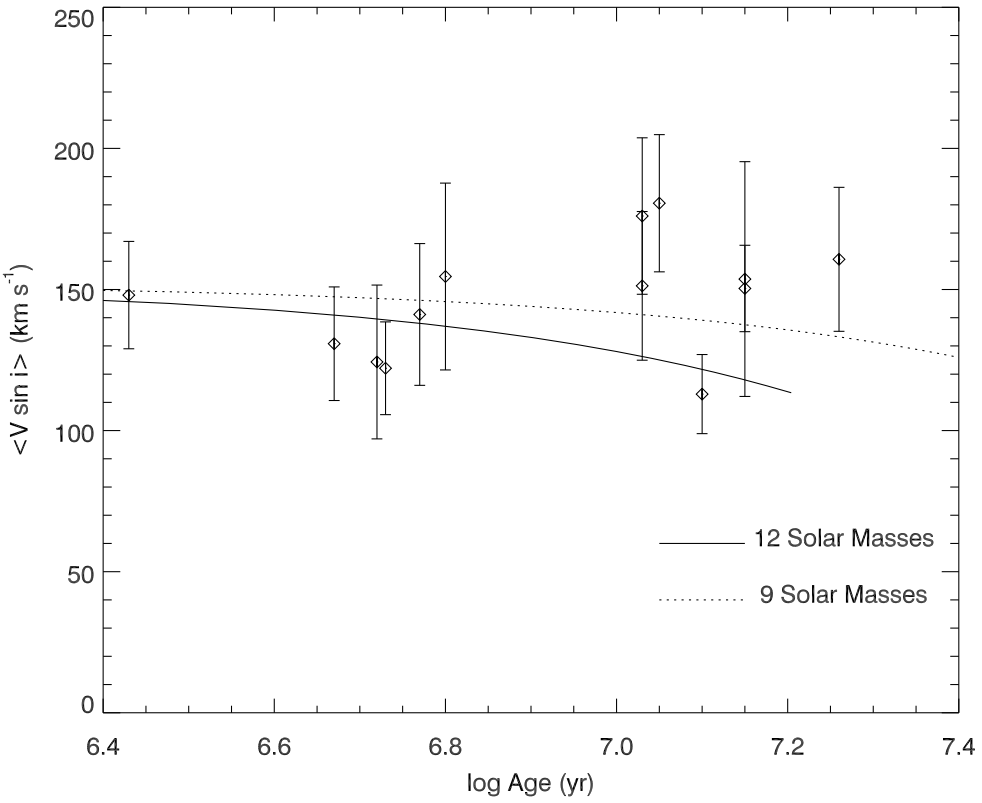

Figure 2.9: Mean $V \sin i$ for stars earlier than or equal to spectral subtype B3 in young clusters plotted against logarithm of cluster age. The solid line and dotted line show the predictions from Meynet & Maeder (2000) for an ensemble of $12 M_{\odot}$ and $9 M_{\odot}$ stars, respectively, which was normalized to the observed means for the youngest clusters.

Models of the evolution of massive rotating stars (Heger & Langer 2000; Meynet & Maeder 2000) predict that stars experience a short duration spin up episode caused by interior core contraction as the star approaches the TAMS. If correct, then I might expect to find these fast rotators located near the TAMS region in the HRD. The two observed clusters that have the fastest mean $V \sin i$ are NGC 3293 and Berkeley 86, and both of these have an age near 10 Myr. I found that 9 of the 23 stars we observed in NGC 3293 have $V \sin i > 260$ km s^{-1}, and one additional fast rotator was found by Balona (1975b). I found

4 of 17 stars with $V \sin i > 260$ km s^{-1} for the cluster Berkeley 86. I plot the positions of all these fast rotators in color-magnitude diagrams in Figure 2.10. Only two of these stars are found near the TAMS in the region where single star models predict that the spin up may occur. I caution that even the positions of these two stars may be artificially shifted to redder colors by rotation and gravity darkening and so may not actually be in the TAMS region. The rapid rotators appear to be located throughout the band from the ZAMS to the TAMS in the HRD much as are the rapidly rotating Be stars (Zorec 2004; McSwain & Gies 2005). This suggests that the spin up observed in these clusters is not generally related to the predicted core adjustment that occurs at TAMS.

However, clusters with an age of ≈ 10 Myr probably contain close binary systems that are old enough for the evolutionary expansion and Roche lobe overflow to occur, and the mass gainers could be spun up to become rapid rotators (see, for example, the study of the Algol binary RY Per by Barai et al. (2004)). I find evidence for only one candidate binary among these rapid rotators (NGC 3293 #83 = CPD$-57°3501$), but post-mass transfer binaries are probably not easily detected in our survey since they probably have long orbital periods and small radial velocity semi-amplitudes (see, for example, the study of the Be binary ϕ Per by Gies et al. (1998)). Models of the binary spin up process (Pols et al. 1991; Van Bever & Vanbeveren 1997) suggest that most of the mass gainer stars will appear among the more massive stars near the top of the main sequence. It will be important to compare our results on the rotational velocities of the brighter cluster members with investigations of the rotational properties of the fainter, lower mass population in order to test this prediction.

The approach in this section was to group individual stars according to cluster member-

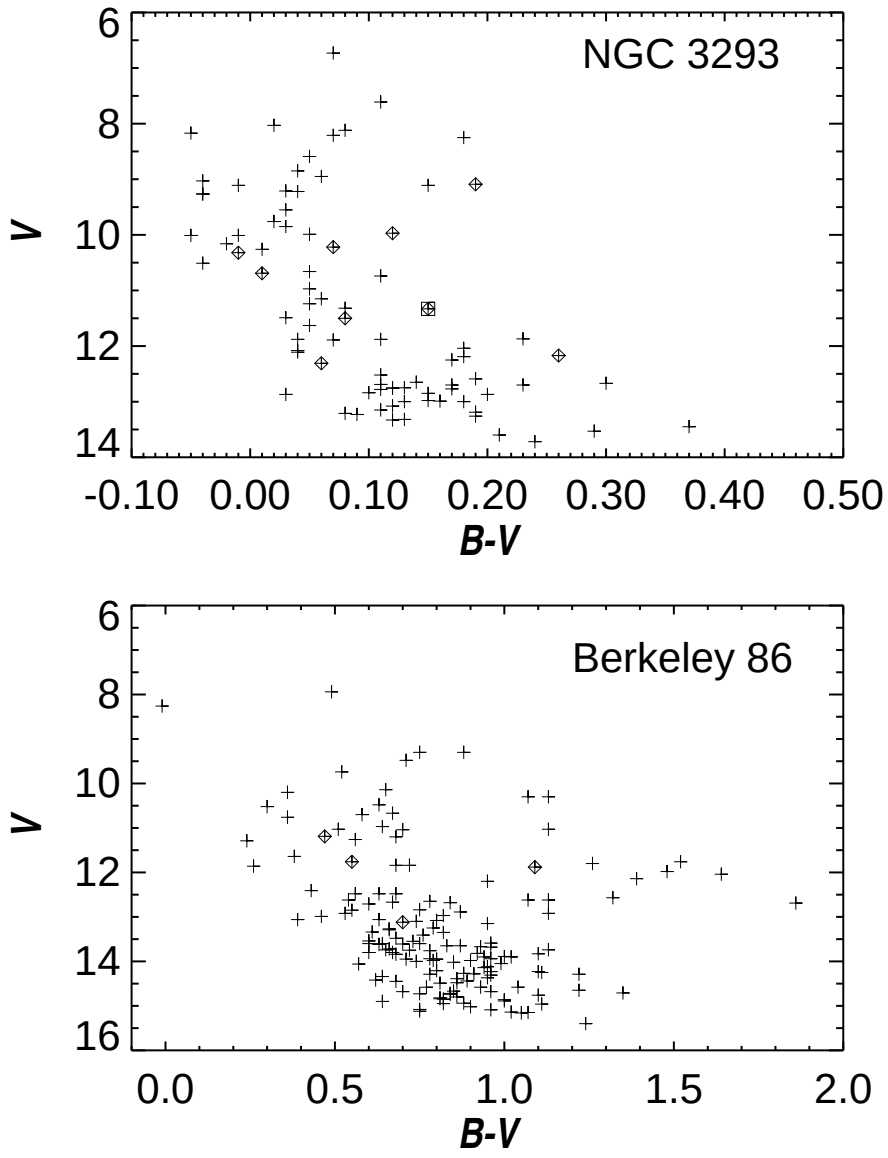

Figure 2.10: Color-magnitude diagrams for NGC 3293 (from photometry by Turner et al. (1980) and Berkeley 86 (photometry by Forbes et al. (1992) and Massey et al. (1995)). The crosses enclosed in diamonds mark the fast rotators ($V \sin i >$ 260 km s^{-1}). The only candidate binary star identified among the fast rotators is NGC 3293 #83, which is marked by an enclosing square in the upper panel.

ship and age groupings to study how the rotational velocity distribution varies with time. However, since the predicted evolutionary time scales vary with stellar mass, some information on the rotational evolution is probably lost by averaging over groups with a significant range in stellar mass. In the following sections, I present a scheme I have developed to determine the effective temperature, gravity, and helium abundance for each of the targets in this survey. With more derived stellar parameters some additional evidence is found for the evolutionary spin down that is predicted to occur for massive rotating stars.

2.4 Effective Temperature and Gravity from Hγ

The stellar spectra of B-stars contain many line features that are sensitive to temperature, $T_{\rm eff}$, and gravity, $\log g$. The hydrogen Balmer lines in the optical are particularly useful diagnostic features throughout the B-type and late O-type spectral classes. Gies & Lambert (1992), for example, used fits of the Hγ profile to derive gravities of stars while temperatures were obtained independently from a reddening-free Strömgren photometric index. Unfortunately, the available Strömgren photometric data for our sample are far from complete and have a wide range in accuracy. Thus, I decided to develop a procedure to derive both temperature and gravity based solely upon a fit of the Hγ line profile that is recorded in all our spectra (see Section 2.2). I show in Figure 2.11 how the equivalent width of Hγ varies as a function of temperature and gravity. The line increases in strength with decreasing temperature (to a maximum in the A-stars), and for a given temperature it also increases in strength with increasing gravity due to the increase in the pressure broadening (linear Stark effect) of the line wings. This dependence on gravity is shown in Figure 2.12 where I plot a

series of model profiles that all have the same equivalent width but differ significantly in line width. Thus, the combination of line strength and width essentially offer two parameters that lead to a unique model fit dependent on specific values of temperature and gravity. This method of matching the Balmer line profiles to derive both parameters was presented by Leone & Manfre (1997) in their study of the chemical abundances in three He-weak stars. The only prerequisite for the application of this method is an accurate estimate of the star's projected rotational velocity, $V \sin i$, which I have already obtained in Section 2.3. The Hγ profile is the best single choice among the Balmer sequence for our purpose, because it is much less affected by incipient emission that often appears in the Hα and Hβ lines among the Be stars (often rapid rotators) and it is better isolated from other transitions in the series compared to the higher order Balmer lines so that only one hydrogen line needs to be considered in our synthetic spectra.

The synthetic Hγ spectra were calculated using a grid of line blanketed LTE model atmospheres derived from the ATLAS9 program written by Robert Kurucz. These models assume solar abundances and a microturbulent velocity of 2 km s^{-1}, and they were made over a grid of effective temperature from $T_{\rm eff}$ = 10000 K to 30000 K at intervals of 2000 K and over a grid of surface gravity from $\log g = 2.6$ to 4.4 at increments of 0.2 dex. Then a series of specific intensity spectra were calculated using the code SYNSPEC (Hubeny & Lanz 1995) for each of these models for a cosine of the angle between the surface normal and line of sight between 0.05 and 1.00 at steps of 0.05. Finally I used our surface integration code for a rotating star (usually with 20000 – 40000 discrete surface area elements; see Section 2.3) to calculate the flux spectra from the visible hemisphere of the star, and these spectra were

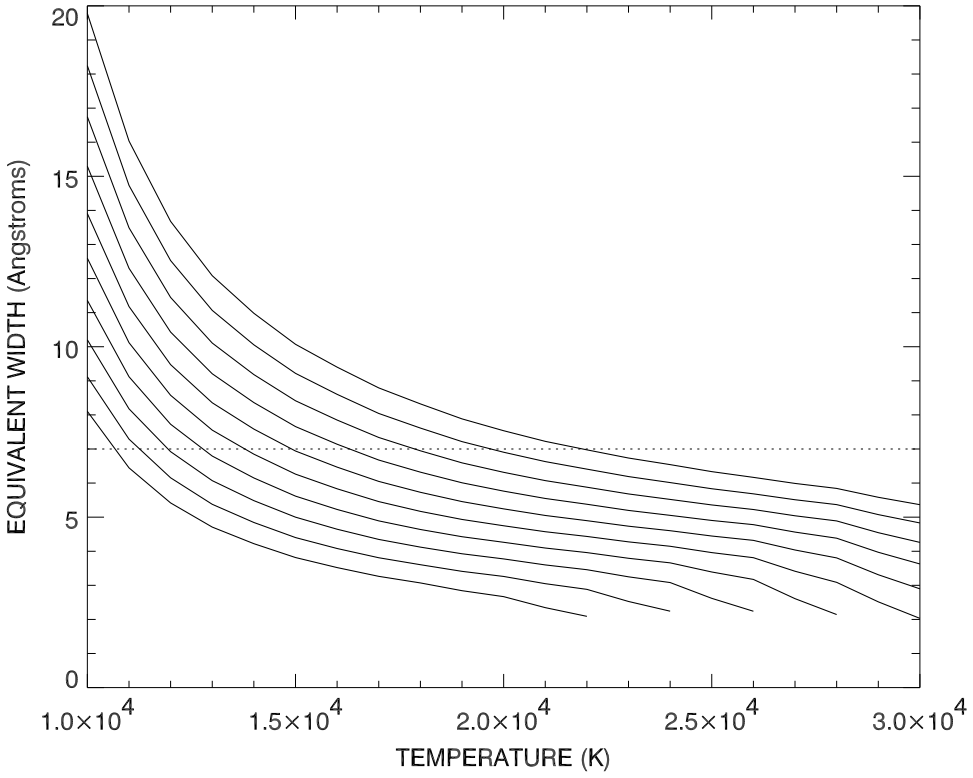

Figure 2.11: The equivalent width of the Hγ line (including all strong metallic lines in the vicinity) plotted as a function of $T_{\rm eff}$. Each line corresponds to a specific value of $\log g$ that ranges from $\log g = 2.6$ (*bottom*) to $\log g = 4.4$ (*top*) in increments of 0.2 dex. The Hγ profiles for the intersection points of the curves and the dotted line ($W_\lambda = 7$ Å) are plotted in Figure 2.12.

convolved with the appropriate instrumental broadening function for direct comparison with the observed profiles.

One key issue that needs to be considered in this procedure is the line blending in the Hγ region. Our sample includes stars with effective temperatures ranging from 10000 K to 30000 K, and the spectral region surrounding Hγ for such stars will include other metallic lines from species such as Ti II, Fe I, Fe II, and Mg II (in spectra of stars cooler than 12000 K) and from species like O II, S III, and Si III (in spectra of stars hotter than 22000 K). Many

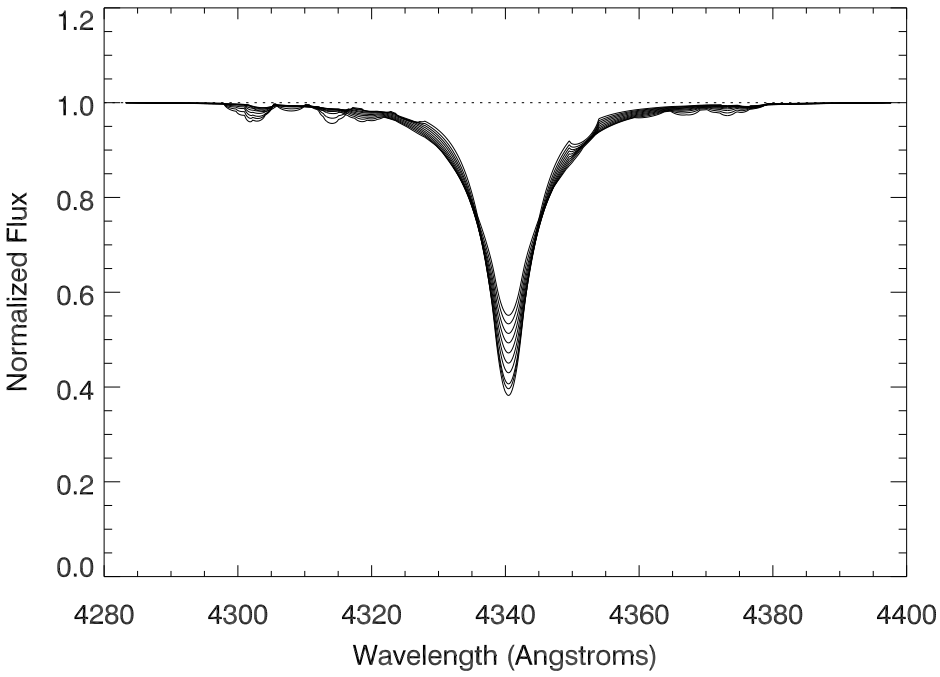

Figure 2.12: A series of model Hγ profiles ($V \sin i$ = 150 km s^{-1}) with constant equivalent width (7 Å) for a locus of ($T_{\rm eff}, \log g$) points (defined in Figure 2.11, $T_{\rm eff}$ = 10666, 11255, 11937, 12778, 13786, 14908, 16300, 17865, 19696, 21897 K for $\log g$ = 2.6, 2.8, ..., 4.4, respectively). The profiles vary from narrow at low gravity to broad-winged at high gravity due to collisional broadening (linear Stark effect).

of these lines will be completely blended with Hγ, particularly among the spectra of the rapid rotators whose metallic profiles are shallow and broad. Neglecting these blends would lead to the introduction of systemic errors in the estimates of temperature and gravity (at least in some temperature domains). I consulted the Web library of B-type synthetic spectra produced by Gummersbach and Kaufer[2] (Gummersbach et al. 1998), and I included in the input line list all the transitions shown in their spectra that attain an equivalent width > 30 mÅ in the Hγ region (4300 – 4380Å). I assumed a solar abundance for these metal lines in

[2]http://www.lsw.uni-heidelberg.de/cgi-bin/websynspec.cgi

each case, and any profile errors introduced by deviations from solar abundances for these weak lines in the actual spectra will be small in comparison to those errors associated with the observational noise and with the $V \sin i$ measurement.

I begin by considering the predicted Hγ profiles for a so–called "virtual star" by which I mean a star having a spherical shape, an equatorial rotating velocity equal to a given $V \sin i$, and constant gravity and temperature everywhere on its surface. Obviously, the concept of a "virtual star" does not correspond to reality (see Section 2.5), but the application of this concept allows us to describe a star using only three parameters: $T_{\rm eff}$, $\log g$, and $V \sin i$. These fitting parameters will correspond to some hemispheric average in the real case, and can therefore be used as starting points for detailed analyses. The procedure for the derivation of temperature and gravity begins by assigning a $V \sin i$ to the virtual star model, and then comparing the observed Hγ line profile with a set of synthesized, rotationally broadened profiles for the entire temperature-gravity grid. In practice, I start by measuring the equivalent width of the observed Hγ feature, and then construct a series of interpolated temperature-gravity models with this Hγ equivalent width and a range in line broadening (see Figure 2.13). I find the χ^2 minimum in the residuals between the observed and model profile sequence, and then make a detailed search in the vicinity of this minimum for the best fit values of temperature and gravity that correspond to the global minimum of the χ^2 statistic.

I was able to obtain estimates of $T_{\rm eff}$ and $\log g$ for 461 stars from the sample of cluster stars described in Section 2.3. The results are listed in Table 2.5, which is available in complete form in Appendix B.2. The columns here correspond to: (1) cluster name; (2) WEBDA

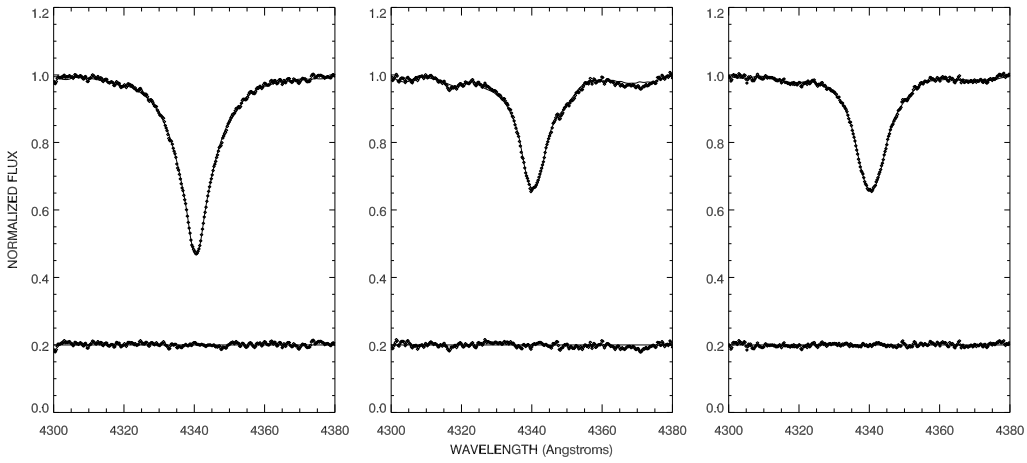

Figure 2.13: The Hγ line fitting results for the stars (*from left to right*) NGC 1502 #23 ($T_{\rm eff} = 15286 \pm 113$ K, $\log g = 3.951 \pm 0.019$), NGC 869 #803 ($T_{\rm eff} = 24838 \pm 354$ K, $\log g = 3.891 \pm 0.033$), and NGC 884 #2255 ($T_{\rm eff} = 20360 \pm 178$ K, $\log g = 3.560 \pm 0.022$). The thin solid lines show the fits while the diamonds indicate the observed profiles. The residuals from the fit are shown at the bottom of each plot.

index number (Mermilliod & Paunzen 2003) (where some blank entries corresponds to the stars which do not have WEBDA index number; these stars can be indentified using their $V \sin i$ values and their positional information in Table 2.3); (3) $T_{\rm eff}$; (4) error in $T_{\rm eff}$; (5) $\log g$; (6) error in $\log g$; (7) $V \sin i$ (from Table 2.3); (8) estimated polar gravity $\log g_{\rm polar}$ (Section 2.5); (9 – 11) log of the He abundance relative to the solar value as derived from He I $\lambda\lambda$4026, 4387, 4471, respectively (Section 2.7); (12) mean He abundance; and (13) inter-line standard deviation of the He abundance. Examples of the final line profile fits for three stars (#23 in NGC 1502, #803 in NGC 869, and #2255 in NGC 884) are shown in Figure 2.13. Their corresponding χ^2 contour plots are plotted in Figure 2.14, where we can clearly see that the temperature - gravity fitting scheme leads to unambiguous parameter estimates and errors. Each contour interval represents an increase in the residuals from the

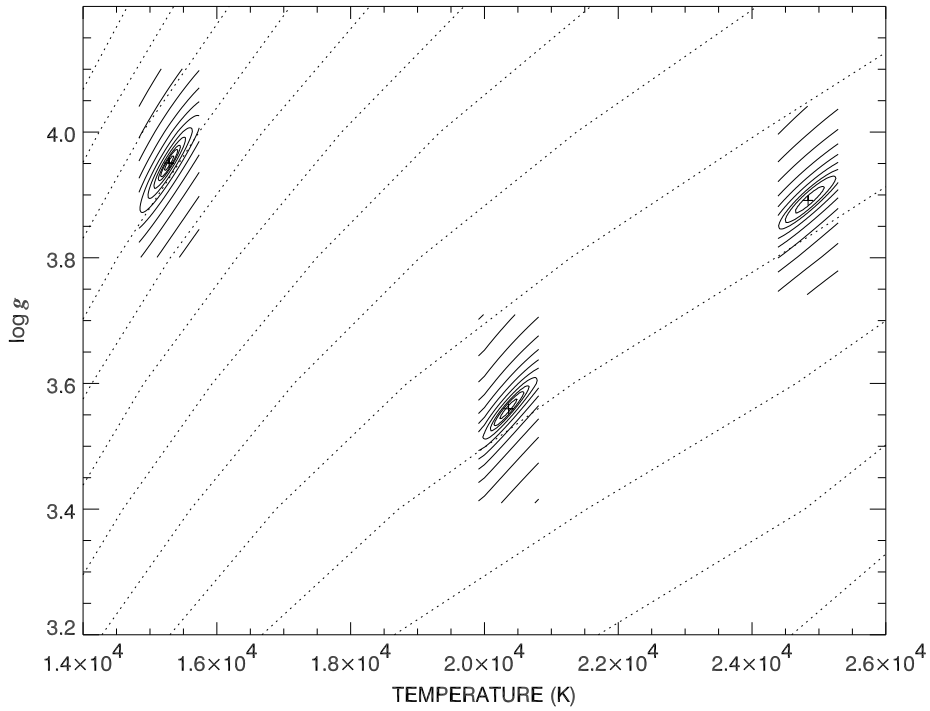

Figure 2.14: χ^2 residual contour plots for the same stars shown in Fig. 2.13 (*from left to right*: NGC 1502 #23, NGC 884 #2255, and NGC 869 #803). The solid lines show contours of increasing error residuals relative to the minimum value (at the center of the contours), while the the dotted lines are loci of constant equivalent width (see Figure 2.11).

best fit as the ratio

$$\frac{\chi^2_\nu - \chi^2_{\nu\ \mathrm{min}}}{\chi^2_{\nu\ \mathrm{min}}/N} \tag{2.1}$$

where N represents the number of wavelength points used in making the fit ($N \approx 180$), and the specific contours plotted from close to far from each minimum correspond to ratio values of 1, 3, 5, 10, 20, 40, 80, 160, 320, 640, and 1280. The contours reflect only the errors introduced by the observed noise in the spectrum, but I must also account for the propagation of errors in the T_{eff} and $\log g$ estimates due to errors in our $V \sin i$ estimate from Table 2.3. The average error for $V \sin i$ is about 10 km s^{-1}, so I artificially increased and

decreased the $V \sin i$ measurements by this value and used the same procedure to derive new temperature and gravity estimates and hence the propagated errors in these quantities. I found that the $V \sin i$ related errors depend on $T_{\rm eff}$, $\log g$, and $V \sin i$, and the mean values of these $V \sin i$ related errors are about ± 200 K for $T_{\rm eff}$ and ± 0.02 for $\log g$. Our final estimated errors for temperature and $\log g$ (Table 2.5) are based upon the quadratic sum of the $V \sin i$ propagated errors and the errors due to intrinsic noise in the observed spectrum.

Cluster Name	WEBDA Index	$T_{\rm eff}$ (K)	$\Delta T_{\rm eff}$ (K)	$\log g$	$\Delta \log g$	$V \sin i$ (km s^{-1})	$\log g_{polar}$	$\log[\frac{\epsilon}{\epsilon_\odot}]$ (4026Å)	$\log[\frac{\epsilon}{\epsilon_\odot}]$ (4387Å)	$\log[\frac{\epsilon}{\epsilon_\odot}]$ (4471Å)	$\overline{\log[\frac{\epsilon}{\epsilon_\odot}]}$	$\Delta \log[\frac{\epsilon}{\epsilon_\odot}]$
Ber86 .	1	26878	406	3.84	0.04	185	3.93	−0.02	−0.05	0.22	0.05	0.12
Ber86 .	12	15440	232	4.05	0.04	309	4.29	−0.30	−0.09	−0.39	−0.26	0.12
Ber86 .	13	28711	191	3.59	0.02	183	3.73	−0.11	−0.19	0.26	−0.02	0.20
Ber86 .	15	23049	316	4.10	0.03	23	4.10	0.04	0.01	0.10	0.05	0.04
Ber86 .	17	26357	415	4.08	0.04	79	4.10	−0.03	−0.04	0.11	0.01	0.07
Ber86 .	30	16513	322	3.92	0.05	104	3.97	0.32	0.46	0.40	0.39	0.06
Ber86 .	149	20354	241	4.21	0.03	181	4.29	−0.40	−0.32	−0.36	−0.36	0.03
Ber86 .	214	15737	405	4.00	0.06	276	4.22	−0.15	0.07	−0.35	−0.14	0.17
...	...	...	...	...	...	...	...	...	...	...	...	...

Table 2.5: Physical Parameters of Sample Stars
(a full version of this table is given in Appendix B.2)

2.5 Polar Gravity of Rotating Stars

The surface temperature and gravity of a rotating star vary as functions of the polar co-latitude because of the shape changes due to centrifugal forces and the associated gravity darkening. Thus, the estimates of temperature and gravity I obtained from the Hγ profile (Seciton 2.4) represent an average of these parameters over the visible hemisphere of a given star. Several questions need to be answered before we can use these derived values for further analyses: (1) What is the meaning of the stellar temperature and gravity derived from the Hγ fitting method for the case of a rotating star? (2) What is the relationship between our derived temperature/gravity values and the distribution of temperature/gravity on the surface of a real rotating star? In other words, what kind of average will the derived values represent? (3) Can we determine the evolutionary status of rotating stars from the derived temperatures and gravities as we do in the analysis of non-rotating stars?

2.5.1 The Meaning of Derived Temperature and Gravity

We can attempt to answer the first two questions by creating synthetic profiles that use realistic models for rotating stars (see the example of the study of α Leo: Chapter 3 and McAlister et al. (2005)). The key parameters to describe a model of a real rotating star include the polar temperature, stellar mass, polar radius, inclination angle, and $V \sin i$. The surface of the model star is then calculated based on Roche geometry (i.e., assuming that the interior mass is concentrated like a point source) and the surface temperature distribution is determined by the von Zeipel theorem ($T \propto g_{\rm eff}^{1/4}$; von Zeipel (1924)). Thus, I can use the surface integration code (which accounts for limb darkening, gravity darkening,

and rotational changes in the projected area and orientation of the surface elements) to synthesize the Hγ line profile for a given inclination angle and $V \sin i$, and I can compare the temperature and gravity estimates from the "virtual star" approach with the actual run of temperature and gravity on the surface of the model rotating star.

Model Number	Mass ($M_\odot$)	R_{polar} ($R_\odot$)	T_{polar} (K)	$\log g_{polar}$	V_c (km s^{-1})
1	9.5	4.0	25500	4.211	549
2	9.5	5.0	25500	4.018	491
3	9.5	6.4	25500	3.803	434
4	5.5	2.9	18700	4.253	491
5	5.5	3.9	18700	3.996	423
6	5.5	4.9	18700	3.798	378
7	4.0	2.7	15400	4.177	434
8	4.0	3.4	15400	3.977	387
9	4.0	4.1	15400	3.814	352

Table 2.6: Physical Parameters of Model Stars

The physical parameters of the nine models I have chosen for this test are listed in Table 2.6. They are representative of high-mass (models 1, 2, 3), mid-mass (models 4, 5, 6), and low-mass (models 7, 8, 9) stars in our sample at different evolutionary stages between the zero age main sequence (ZAMS) and terminal age main sequence (TAMS). The evolutionary stage is closely related to the value of the polar gravity $\log g_{\rm polar}$ (see below). Table 2.6 gives the model number, stellar mass, polar radius, polar temperature, polar gravity, and critical velocity, V_c, (at which centripetal and gravitation accelerations are equal at the equator). I examined the predicted Hγ profiles for each model assuming a range of different combinations of inclination angle and $V \sin i$. Theoretical studies of the interiors of rotating stars show that the polar radius of a rotating star depends only weakly on angular velocity (at least

for the case of uniform rotation) and usually is $< 3\%$ different from its value in the case of a non-rotating star (Sackmann & Anand 1970; Jackson et al. 2005). Thus, I assume a constant polar radius for each model. I show the test results for all models listed in Table 2.7 where I list various temperature and gravity estimates for a range in assumed inclination angle (between the spin axis and line of sight) and projected rotational velocity. The $T_{\rm eff}$ and and $\log g$ derived from fits of the model Hγ profile (the "virtual star" approach outlined in Section 2.3) are given in columns 8 and 9, respectively, and labeled by the subscript *msr*. These are compared with two kinds of averages of physical values made by integrations over the visible hemisphere of the model star. The first set is a geometrical mean given by

$$< x >= \int x\hat{r} \cdot d\vec{s} \Big/ \int \hat{r} \cdot d\vec{s} \tag{2.2}$$

where x represents either T or $\log g$ and the integral is over the projected area elements given by the dot product of the unit line of sight vector $\hat{r}$ and the area element surface normal vector $\vec{s}$. These geometrically defined averages are given in columns 4 and 5 and denoted by a subscript *geo*. The next set is a flux weighted mean given by

$$< x >= \int xF_\lambda\hat{r} \cdot d\vec{s} \Big/ \int F_\lambda\hat{r} \cdot d\vec{s} \tag{2.3}$$

where F_λ is the monochromatic flux from the area element, and these averages are listed in columns 6 and 7 with the subscript *flux*. Finally I provide an average model temperature (Meynet & Maeder 1997) that is independent of inclination and based on the stellar

luminosity

$$< T_L >= (\int T^4 ds \Big/ \int ds)^{1/4} \tag{2.4}$$

that is given in column 10. The final column 11 gives the difference between the model polar gravity and the measured average gravity, $\delta \log g = \log g_{\rm polar} - \log g_{\rm msr}$. There is reasonably good agreement between the temperature and gravity estimates from our "virtual star" Hγ fit measurements and those from the different model averages, which provides some assurance that our method does offer the meaningful measurements of the temperatures and gravities of rotating stars. The listings in Table 2.7 show the expected trend that as the rotation speed increases, the equatorial regions becomes more extended and cooler, resulting in lower overall temperatures and gravities. These effects are largest at an inclination of 90° where the equatorial zone presents the largest projected area.

Model Number	i (deg)	$V \sin i$ (km s^{-1})	$T_{\rm geo}$ (K)	$\log g_{\rm geo}$	$T_{\rm flux}$ (K)	$\log g_{\rm flux}$	$T_{\rm msr}$ (K)	$\log g_{\rm msr}$	T_L (K)	$\delta \log g$
1	90	50	25447	4.208	25446	4.208	25437	4.208	25453	0.004
1	90	100	25288	4.197	25284	4.197	25282	4.195	25312	0.016
1	90	200	24635	4.151	24625	4.151	24656	4.143	24744	0.068
1	90	300	23489	4.068	23487	4.068	23555	4.046	23790	0.165
1	90	400	21747	3.931	21834	3.938	21927	3.885	22462	0.327
1	70	50	25443	4.207	25442	4.207	25432	4.207	25447	0.004
1	70	100	25269	4.196	25267	4.195	25262	4.195	25287	0.017
1	70	200	24559	4.146	24558	4.146	24562	4.139	24644	0.072
1	70	300	23314	4.054	23350	4.057	23392	4.044	23562	0.167
1	70	400	21423	3.902	21661	3.921	21489	3.867	22072	0.344
1	50	50	25422	4.206	25423	4.206	25407	4.206	25420	0.005
1	50	100	25188	4.190	25191	4.190	25173	4.191	25179	0.020
1	50	200	24229	4.122	24267	4.125	24232	4.126	24207	0.085
1	50	300	22540	3.992	22773	4.010	22549	4.007	22586	0.204
1	30	50	25341	4.200	25346	4.201	25323	4.203	25312	0.008
1	30	100	24859	4.167	24888	4.169	24823	4.180	24744	0.032
1	30	200	22820	4.014	23117	4.037	22631	4.052	22462	0.159
2	90	50	25434	4.013	25433	4.013	25422	4.013	25441	0.005
2	90	100	25234	3.999	25230	3.999	25247	3.999	25265	0.018
2	90	200	24411	3.941	24401	3.941	24435	3.930	24554	0.087
2	90	300	22947	3.833	22961	3.834	22977	3.803	23360	0.215
2	90	400	20673	3.645	20898	3.664	20694	3.570	21734	0.448
2	70	50	25428	4.013	25427	4.013	25417	4.012	25434	0.005

Table 2.7: Test Results for All Models in Table 2.6

Model Number	i (deg)	$V \sin i$ (km s^{-1})	$T_{\rm geo}$ (K)	$\log g_{\rm geo}$	$T_{\rm flux}$ (K)	$\log g_{\rm flux}$	$T_{\rm msr}$ (K)	$\log g_{\rm msr}$	T_L (K)	$\delta \log g$
2	70	100	25211	3.998	25208	3.998	25206	3.997	25234	0.021
2	70	200	24316	3.935	24318	3.935	24341	3.928	24428	0.090
2	70	300	22727	3.815	22801	3.821	22772	3.796	23076	0.222
2	70	400	20257	3.603	20789	3.648	20386	3.566	21282	0.451
2	50	50	25403	4.011	25404	4.011	25388	4.011	25400	0.006
2	50	100	25109	3.991	25114	3.991	25100	3.993	25099	0.024
2	50	200	23901	3.904	23962	3.908	23929	3.912	23882	0.106
2	50	300	21737	3.731	22156	3.765	21921	3.763	21882	0.254
2	30	50	25301	4.004	25308	4.004	25283	4.008	25265	0.010
2	30	100	24697	3.962	24736	3.964	24625	3.973	24554	0.044
2	30	200	22083	3.759	22571	3.798	22120	3.827	21734	0.191
3	90	50	25415	3.797	25414	3.797	25411	3.798	25425	0.006
3	90	100	25159	3.780	25154	3.779	25154	3.777	25199	0.026
3	90	200	24094	3.704	24084	3.703	24170	3.693	24287	0.110
3	90	300	22160	3.556	22212	3.560	22246	3.515	22762	0.288
3	90	400	19084	3.277	19792	3.342	18899	3.159	20827	0.644
3	70	50	25408	3.797	25407	3.797	25405	3.797	25415	0.006
3	70	100	25129	3.778	25126	3.777	25121	3.776	25159	0.027
3	70	200	23972	3.695	23980	3.696	24030	3.687	24125	0.116
3	70	300	21872	3.532	22040	3.545	22005	3.508	22405	0.295
3	50	50	25376	3.795	25377	3.795	25371	3.796	25372	0.007
3	50	100	24999	3.769	25006	3.769	24964	3.769	24986	0.034
3	50	200	23433	3.654	23540	3.662	23346	3.658	23426	0.145
3	50	300	20561	3.408	21434	3.484	20782	3.466	20983	0.337

Table 2.7: Test Results for All Models in Table 2.6 (cont.)

Model Number	i (deg)	$V \sin i$ (km s^{-1})	$T_{\rm geo}$ (K)	$\log g_{\rm geo}$	$T_{\rm flux}$ (K)	$\log g_{\rm flux}$	$T_{\rm msr}$ (K)	$\log g_{\rm msr}$	T_L (K)	$\delta \log g$
3	30	50	25246	3.786	25255	3.786	25267	3.794	25199	0.009
3	30	100	24467	3.731	24526	3.735	24365	3.743	24287	0.060
3	30	200	20962	3.442	21886	3.522	21091	3.546	20827	0.257
4	90	50	18651	4.249	18651	4.249	18635	4.249	18657	0.005
4	90	100	18505	4.235	18501	4.235	18495	4.233	18527	0.020
4	90	200	17900	4.177	17890	4.176	17964	4.171	18005	0.082
4	90	300	16824	4.068	16826	4.068	16967	4.062	17128	0.191
4	90	400	15153	3.880	15299	3.896	15355	3.854	15934	0.400
4	70	50	18647	4.248	18647	4.248	18617	4.247	18651	0.007
4	70	100	18488	4.233	18485	4.233	18484	4.233	18504	0.020
4	70	200	17830	4.170	17829	4.170	17928	4.173	17912	0.080
4	70	300	16662	4.051	16708	4.055	16740	4.045	16919	0.208
4	70	400	14847	3.838	15222	3.881	14915	3.820	15601	0.433
4	50	50	18629	4.247	18629	4.247	18604	4.247	18627	0.007
4	50	100	18413	4.226	18417	4.227	18388	4.227	18405	0.027
4	50	200	17525	4.140	17567	4.144	17446	4.138	17511	0.116
4	50	300	15935	3.967	16232	3.999	15831	3.970	16042	0.283
4	30	50	18554	4.240	18559	4.240	18495	4.238	18527	0.015
4	30	100	18110	4.197	18140	4.200	18012	4.199	18005	0.055
4	30	200	16189	3.994	16544	4.033	15849	4.006	15934	0.247
5	90	50	18635	3.990	18633	3.980	18621	3.990	18642	0.006
5	90	100	18437	3.971	18432	3.971	18447	3.971	18468	0.025
5	90	200	17612	3.891	17602	3.890	17744	3.892	17763	0.104

Table 2.7: Test Results for All Models in Table 2.6 (cont.)

Model Number	i (deg)	$V \sin i$ (km s^{-1})	$T_{\rm geo}$ (K)	$\log g_{\rm geo}$	$T_{\rm flux}$ (K)	$\log g_{\rm flux}$	$T_{\rm msr}$ (K)	$\log g_{\rm msr}$	T_L (K)	$\delta \log g$
5	90	300	16108	3.734	16144	3.737	16337	3.723	16588	0.273
5	90	400	13713	3.428	14388	3.515	13914	3.396	15141	0.600
5	70	50	18629	3.989	18628	3.989	18608	3.989	18634	0.007
5	70	100	18413	3.969	18411	3.969	18416	3.969	18437	0.027
5	70	200	17518	3.882	17522	3.882	17601	3.882	17638	0.114
5	70	300	15885	3.707	16016	3.721	16111	3.709	16314	0.287
5	50	50	18604	3.987	18605	3.987	18582	3.987	18601	0.009
5	50	100	18313	3.960	18319	3.960	18279	3.958	18303	0.038
5	50	200	17101	3.839	17184	3.847	17007	3.841	17099	0.155
5	50	300	14865	3.572	15616	3.662	14741	3.607	15250	0.389
5	30	50	18504	3.978	18511	3.978	18448	3.978	18468	0.018
5	30	100	17902	3.920	17949	3.924	17743	3.920	17763	0.076
5	30	200	15156	3.605	15949	3.702	14803	3.655	15141	0.341
6	90	50	18618	3.790	18616	3.790	18602	3.790	18627	0.008
6	90	100	18368	3.767	18363	3.766	18385	3.766	18408	0.032
6	90	200	17318	3.664	17309	3.663	17448	3.661	17521	0.137
6	90	300	15352	3.448	15467	3.461	15654	3.436	16063	0.362
6	90	350	13928	3.262	14472	3.330	14179	3.233	15241	0.565
6	70	50	18611	3.789	18609	3.789	18589	3.788	18618	0.009
6	70	100	18339	3.764	18336	3.763	18345	3.763	18369	0.035
6	70	200	17198	3.651	17213	3.653	17269	3.649	17364	0.149
6	70	300	15063	3.410	15374	3.445	15234	3.408	15740	0.390
6	50	50	18579	3.786	18580	3.787	18555	3.786	18576	0.011
6	50	100	18213	3.752	18221	3.752	18198	3.753	18201	0.045

Table 2.7: Test Results for All Models in Table 2.6 (cont.)

Model Number	i (deg)	$V \sin i$ (km s^{-1})	$T_{\rm geo}$ (K)	$\log g_{\rm geo}$	$T_{\rm flux}$ (K)	$\log g_{\rm flux}$	$T_{\rm msr}$ (K)	$\log g_{\rm msr}$	T_L (K)	$\delta \log g$
6	50	200	16667	3.594	16810	3.609	16586	3.599	16689	0.199
6	30	50	18453	3.775	18463	3.775	18399	3.776	18408	0.022
6	30	100	17691	3.700	17760	3.707	17474	3.701	17521	0.097
7	90	50	15349	4.171	15348	4.171	15321	4.171	15355	0.006
7	90	100	15194	4.154	15190	4.153	15182	4.154	15218	0.023
7	90	200	14549	4.078	14539	4.077	14578	4.075	14666	0.103
7	90	300	13379	3.930	13399	3.933	13486	3.926	13743	0.251
7	90	350	12545	3.813	12658	3.829	12774	3.844	13165	0.333
7	70	50	15344	4.171	15344	4.171	15315	4.170	15349	0.007
7	70	100	15175	4.152	15173	4.151	15155	4.151	15194	0.026
7	70	200	14475	4.069	14477	4.069	14482	4.065	14568	0.112
7	70	300	13204	3.905	13299	3.917	13233	3.899	13527	0.278
7	70	350	12299	3.773	12604	3.816	12580	3.852	12894	0.325
7	50	50	15325	4.169	15325	4.169	15290	4.168	15323	0.009
7	50	100	15097	4.142	15101	4.143	15055	4.142	15089	0.035
7	50	200	14149	4.028	14213	4.036	14162	4.040	14145	0.137
7	50	300	12411	3.781	12973	3.862	12525	3.880	12668	0.297
7	30	50	15246	4.160	15252	4.160	15190	4.160	15218	0.018
7	30	100	14775	4.105	14813	4.109	14627	4.099	14666	0.078
8	90	50	15336	3.970	15334	3.969	15315	3.970	15343	0.007
8	90	100	15139	3.947	15135	3.947	15136	3.948	15170	0.029
8	90	200	14317	3.850	14308	3.848	14386	3.849	14474	0.128
8	90	300	12786	3.648	12863	3.658	12929	3.652	13324	0.325
8	90	350	11677	3.477	12055	3.533	12054	3.561	12655	0.416
8	70	50	15330	3.969	15329	3.969	15303	3.969	15335	0.008

Table 2.7: Test Results for All Models in Table 2.6 (cont.)

Model Number	i (deg)	$V \sin i$ (km s^{-1})	$T_{\rm geo}$ (K)	$\log g_{\rm geo}$	$T_{\rm flux}$ (K)	$\log g_{\rm flux}$	$T_{\rm msr}$ (K)	$\log g_{\rm msr}$	T_L (K)	$\delta \log g$
8	70	100	15116	3.945	15114	3.944	15115	3.947	15140	0.030
8	70	200	14223	3.838	14233	3.839	14279	3.839	14351	0.138
8	70	300	12560	3.613	12784	3.643	12745	3.655	13065	0.322
8	50	50	15305	3.966	15306	3.966	15254	3.963	15302	0.014
8	50	100	15017	3.933	15024	3.934	14998	3.938	15008	0.039
8	50	200	13807	3.784	13916	3.797	13783	3.792	13819	0.185
8	30	50	15206	3.955	15214	3.956	15138	3.954	15170	0.023
8	30	100	14608	3.884	14664	3.891	14466	3.884	14474	0.093
9	90	50	15322	3.805	15321	3.805	15298	3.805	15331	0.009
9	90	100	15085	3.778	15079	3.778	15086	3.779	15123	0.035
9	90	200	14079	3.657	14073	3.657	14192	3.658	14282	0.156
9	90	300	12163	3.393	12360	3.421	12475	3.445	12927	0.370
9	70	50	15315	3.805	15314	3.805	15288	3.804	15322	0.010
9	70	100	15057	3.775	15054	3.775	15049	3.775	15086	0.039
9	70	200	13965	3.643	13987	3.645	14068	3.647	14133	0.167
9	70	300	11886	3.343	12384	3.416	12183	3.429	12647	0.385
9	50	50	15286	3.801	15287	3.801	15250	3.801	15282	0.013
9	50	100	14937	3.761	14946	3.762	14890	3.761	14927	0.053
9	50	200	13455	3.574	13633	3.597	13368	3.579	13499	0.235
9	30	50	15166	3.788	15176	3.789	15095	3.787	15123	0.027
9	30	100	14440	3.701	14516	3.710	14293	3.703	14282	0.112

Table 2.7: Test Results for All Models in Table 2.6 (cont.)

2.5.2 Estimation of Polar Gravity

We can estimate reliably the evolutionary status of a non-rotating star by plotting its position in a color-magnitude diagram or in its spectroscopic equivalent of a temperature-gravity diagram. However, the introduction of rotation makes many of these observed quantities dependent on the inclination of the spin axis (Collins et al. 1991) so that position in the HRD is no longer uniquely related to a star of specific mass, age, and rotation. Furthermore, theoretical models suggest that very rapid rotators might have dramatically different evolutionary paths than those of non-rotating stars (Heger & Langer 2000; Meynet & Maeder 2000), and for some mass ranges there are no available theoretical predictions at all for the evolutionary tracks of rapid rotators. Without a reliable observational parameter for stellar evolutionary status, it is very difficult to investigate the evolution of rotating stars systematically.

The one parameter of a rotating star that is not greatly affected by its rotation is the polar gravity. During the entire MS phase, the change of polar gravity for a rotating star can be attributed to evolutionary effects almost exclusively. For example, models of non-rotating stars (Schaller et al. 1992) indicate that the surface gravity varies from $\log g = 4.3$ at the ZAMS to $\log g = 3.5$ at the TAMS for a mass range from 2 to 15 $M_{\odot}$, i.e., the majority of MS B-type stars, and similar results are found for the available rotating stellar models (Heger & Langer 2000; Meynet & Maeder 2000). Thus, the polar gravity is a good indicator for the evolutionary status and it is almost independent of stellar mass among the B-stars. Rotating stars with different masses but similar polar gravity can be treated as a group with a common evolutionary status. This can dramatically increase the significance of statistical results related to stellar evolutionary effects when the size of a sample is limited.

We can use the model results given above to help estimate the polar gravity for each of the stars in our survey. The measured quantities are $V \sin i$ (Section 2.3) and $T_{\rm eff}$ and $\log g$ as derived from the Hγ line fit. It is clear from the model results in Table 2.7 that the measured $\log g$ values for a given model will generally be lower than the actual polar gravity (see final column in Table 2.7) by an amount that depends on $V \sin i$ and inclination angle. Unfortunately I cannot derive the true value of the polar gravity for an individual star from the available data without knowing its spin inclination angle. Thus, I need to find an alternative way to estimate the polar gravity within acceptable errors. The last column of Table 2.7 shows that the difference $\delta \log g = \log g_{\rm pol} - \log g_{\rm msr}$ for a specific value of $V \sin i$ changes slowly with inclination angle until the angle is so low that the equatorial velocity $(V \sin i)/\sin i$ approaches the critical rotation speed (corresponding to an equatorially extended star with a mean gravity significantly lower than the polar value). This suggests that I can average the corrections $\delta \log g$ over all possible inclination angles for a model at a given $V \sin i$, and then just apply this mean correction to our results on individual stars with the same $V \sin i$ value to obtain their polar gravity. As shown in Table 2.7, this simplification of ignoring the specific inclination of stars to estimate their $\log g_{\rm polar}$ values will lead to small errors in most cases (< 0.03 dex). The exceptional cases are those for model stars with equatorial velocities close to the critical value, and such situations are probably rare in our sample.

I gathered the model results for $T_{\rm msr}$, $\log g_{\rm msr}$, and $\delta \log g$ as a function of inclination i for each model (Table 2.6) and each grid value of $V \sin i$. I then formed averages of each of these three quantities by calculating weighted means over the grid values of inclination. The

intergrating weight includes two factors: (1) the factor $\propto \sin i$ to account for the probability of the random distribution of spin axes in space; (2) the associated probability for the frequency of the implied equatorial velocity among our sample of B-stars. Under these considerations, the mean of a variable x with a specific value of $V \sin i$ would be

$$< x > \Big|_{V \sin i} = \frac{\int_{i_{\min}}^{\pi/2} x|_{V \sin i} P_v(\frac{V \sin i}{\sin i}) \cot i \, di}{\int_{i_{\min}}^{\pi/2} P_v(\frac{V \sin i}{\sin i}) \cot i \, di}, \tag{2.5}$$

where P_v is the equatorial velocity distribution of our sample, deconvolved from $V \sin i$ distribution (see Figure 2.3). The final inclination-averaged means are listed in Table 2.8 for each model and $V \sin i$ pair. I applied these corrections to each star in the sample by interpolating in each of these models to the observed value of $V \sin i$ and then by making a bilinear interpolation in the resulting $V \sin i$ specific pairs of $(T_{\rm msr}, \log g_{\rm msr})$ to find the appropriate correction term $\delta \log g$ needed to estimate the polar gravity. The resulting polar gravities are listed in column 8 of Table 2.5.

2.6 Evolution of Stellar Rotation

Theoretical models (Heger & Langer 2000; Meynet & Maeder 2000) indicate that single rotating stars experience a long-term spin down during their MS phase due to angular momentum loss by stellar wind and a net increase of the moment of inertia. The spin down rate is generally larger in the more massive stars and those born with faster rotational velocities. A spin down may also occur in close binaries due to tidal forces acting to bring the stars into synchronous rotation (Abt et al. 2002). On the other hand, these models also predict that a

Model Number	$V \sin i$ (km s^{-1})	$T_{\rm msr}$ (K)	$\log g_{\rm msr}$	$\delta \log g$
1	50	25300	4.203	0.009
1	100	24900	4.182	0.029
1	200	23970	4.114	0.098
1	300	23120	4.032	0.180
1	400	21760	3.878	0.333
2	50	25260	4.008	0.011
2	100	24740	3.978	0.040
2	200	23650	3.898	0.120
2	300	22500	3.786	0.232
2	400	20580	3.568	0.449
3	50	25240	3.793	0.011
3	100	24500	3.749	0.054
3	200	23050	3.642	0.161
3	300	21610	3.494	0.309
3	400	18900	3.159	0.644
4	50	18466	4.236	0.018
4	100	18100	4.205	0.048
4	200	17240	4.119	0.135
4	300	16450	4.021	0.232
4	400	15190	3.841	0.412
5	50	18413	3.975	0.021
5	100	17860	3.929	0.067
5	200	16680	3.811	0.185
5	300	15660	3.675	0.321
5	400	13910	3.396	0.600
6	50	18361	3.773	0.024
6	100	17640	3.713	0.085
6	200	16660	3.604	0.194
6	300	15170	3.403	0.395
6	350	14180	3.233	0.565

Table 2.8: Polar Gravity Corrections

Model Number	$V \sin i$ km s^{-1}	$T_{\rm msr}$ (K)	$\log g_{\rm msr}$	$\delta \log g$
7	50	15160	4.157	0.020
7	100	14720	4.109	0.069
7	200	14190	4.042	0.135
7	300	13020	3.895	0.282
7	350	12600	3.851	0.326
8	50	15110	3.952	0.025
8	100	14590	3.896	0.081
8	200	13830	3.796	0.181
8	300	12710	3.656	0.321
8	350	12050	3.561	0.416
9	50	15060	3.784	0.030
9	100	14450	3.718	0.096
9	200	13470	3.589	0.225
9	300	12180	3.429	0.385

Table 2.8: Polar Gravity Corrections (cont.)

rapid increase of rotation velocity can occur at the TAMS caused by an overall contraction of the stellar core. In some cases where the wind mass loss rate is low, this increase may bring stars close to the critical velocity.

Here I examine the changes in the rotational velocity distribution with evolution by considering how these distributions vary with polar gravity. Since my primary goal is to compare the observed distributions with the predictions about stellar rotation evolution for single stars, I need to restrict the numbers of binary systems in the working sample. I began by excluding all stars that have double-line features in their spectra, since these systems have neither reliable $V \sin i$ measurements nor reliable temperature and gravity estimates. I then divided the rest of the sample into two groups, single stars (336 objects) and single-lined binaries (79 objects, identified using the same criterion adopted in Section 2.3.2, $\Delta V_r > 30$ km s^{-1}). The stars in these two groups are plotted in the $\log T_{\rm eff} - \log g_{\rm polar}$

plane in Figure 2.15 (using asterisks for single stars and triangles for binaries). I also show a set of evolutionary tracks for non-rotating stellar models with masses from 2.5 $M_{\odot}$ to 15 $M_{\odot}$ (Schaller et al. 1992) as indicators of evolutionary status. The current published data on similar evolutionary tracks for rotating stars are restricted to the high mass end of this diagram. However, since the differences between the evolutionary tracks for rotating and non-rotating models are small except for cases close to critical, the use of non-rotating stellar evolutionary tracks should be adequate for the statistical analysis that follows. Figure 2.15 shows that most of the sample stars are located between the ZAMS ($\log g_{\rm polar} = 4.3 \pm 0.1$) and the TAMS ($\log g_{\rm polar} = 3.5 \pm 0.1$), and the low mass stars appear to be less evolved. This is the kind of distribution that we would expect for stars selected from young Galactic clusters.

I show a similar plot for all rapid rotators in our sample ($V \sin i > 200$ km s^{-1}) in Figure 2.16. These rapid rotators are almost all concentrated in a band close to the ZAMS. This immediately suggests that stars form as rapid rotators and spin down through the MS phase as predicted by the theoretical models. Note that there are three rapid rotators found near the TAMS (from cool to hot, the stars are NGC 7160 #940, NGC 2422 #125, NGC 457 #128), and a few more such outliers appear in the TAMS region if we lower the boundary on the rapid rotator group to $V \sin i > 180$ km s^{-1}. Why are these three stars separated from all other rapid rotators? One possibility is that they were born as extremely rapid rotators, so they still have a relatively large amount of angular momentum at the TAMS compared to other stars. However, this argument cannot explain why there is a such a clear gap in Figure 2.16 between these few evolved rapid rotators and the large number of young rapid

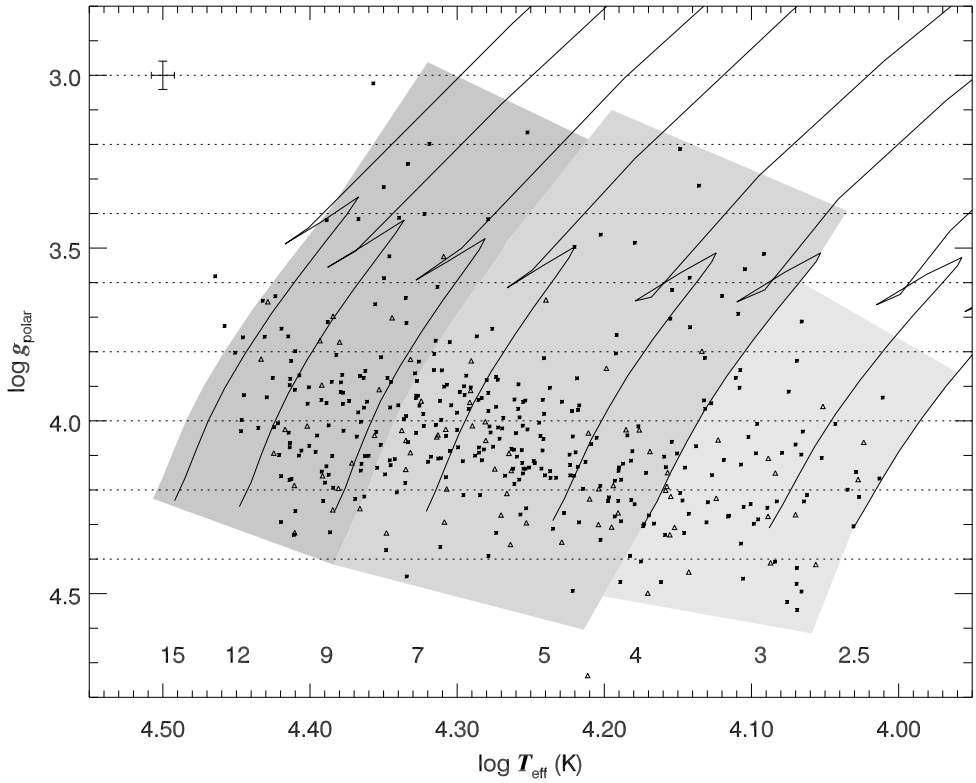

Figure 2.15: The distribution of the stars in the $\log T_{\rm eff} - \log g_{\rm polar}$ plane. Asterisks are assigned to single stars ($N = 336$) while triangles are used for binary systems ($N = 79$). The average errors in $\log T_{\rm eff}$ and $\log g_{\rm polar}$ are indicated in the upper-left corner. The solid lines are the evolutionary tracks for non-rotating stellar models (Schaller et al. 1992), marked by their mass (in $M_{\odot}$) at the bottom. The three shaded areas outline the three mass groups selected for Figures 2.18, 2.19, and 2.20.

rotators. Perhaps these stars are examples of those experiencing a spin up during the core contraction that happens near the TAMS. The scarcity of such objects is consistent with the predicted short duration of the spin up phase.

I next consider the statistics of the rotational velocity distribution as a function of evolutionary state by plotting diagrams of $V \sin i$ versus $\log g_{\rm polar}$. Figure 2.17 shows the distribution of the single stars in our sample in the $V \sin i - \log g_{\rm polar}$ plane. These stars were grouped into 0.2 dex bins of $\log g_{\rm polar}$, and the mean and the range within one standard devi-

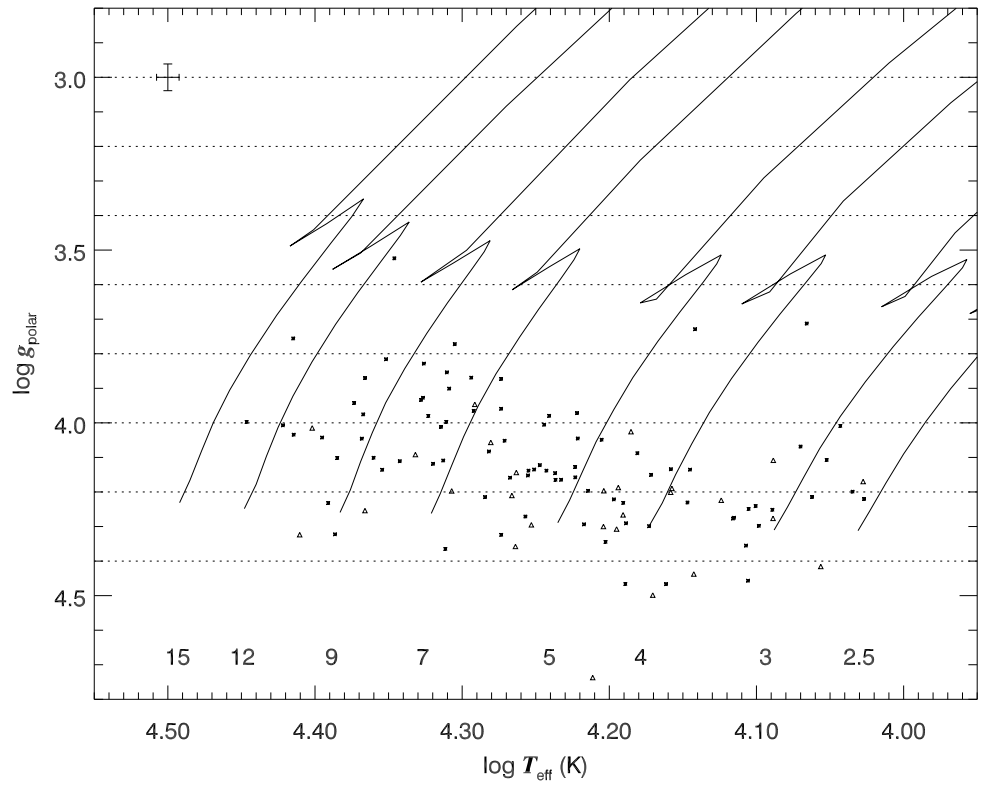

Figure 2.16: The distribution of the stars with $V \sin i > 200$ km s^{-1} in the $\log T_{\rm eff} - \log g_{\rm polar}$ plane in the same format as as Figure 2.15.

ation of the mean for each bin are plotted as a solid line and gray-shaded zone, respectively. The mean $V \sin i$ decreases from 189 km s^{-1} near the ZAMS to 85 km s^{-1} near the TAMS. This subsample of single stars was further divided into three mass categories (shown by the three shaded areas in Figure 2.15): the high mass group (98 stars, $8.5M_{\odot} < M \leq 16M_{\odot}$) is shown in Figure 2.18; the middle mass group (179 stars, $4M_{\odot} < M \leq 8.5M_{\odot}$) in Figure 2.19 and the low mass group (59 stars, $2.5M_{\odot} < M \leq 4M_{\odot}$) in Figure 2.20. All three groups show a spin down trend with decreasing polar gravity, but their slopes differ. The high mass group has a shallow spin down beginning from a relatively small initial mean of $V \sin i = 137$

km s^{-1}. There are three stars with high $V \sin i$ values (around 200 km s^{-1}) in the low gravity bin ($\log g = 3.5$) which raises the mean there to $V \sin i = 106$ km s^{-1}. This group has an average mass of 11 $M_{\odot}$, and it is the only mass range covered by current theoretical studies of rotating stars. The theoretical calculations (Heger & Langer 2000; Meynet & Maeder 2000) of the spin down rate agrees with our statistical results for the high mass group. However, the middle mass and low mass groups show much steeper spin down slopes (with the interesting exception of the rapid rotator, NGC 7160 #940, at $\log g_{\rm polar} = 3.7$ in Figure 2.20). This difference may imply that an additional angular momentum loss mechanism, perhaps involving magnetic fields, becomes important in these middle and lower mass B-type stars. Similar spin down differences among these mass groups were found for the field B-stars by Abt et al. (2002).

Our sample of 79 single-lined binary stars is too small to divide into different mass groups, so I plot them all in one diagram in Figure 2.21. The binary systems appear to experience more spin down than the single B-stars (compare with Figure 2.17). Abt et al. (2002) found that synchronization processes in short-period binary systems can dramatically reduce the rotational velocity of the components. If this is the major reason for the decline in $V \sin i$ in our binary sample, then it appears that tidal synchronization becomes significant in many close binaries when the more massive component attains a polar gravity of $\log g_{\rm polar} = 3.9$, i.e., at a point when the star's larger radius makes the tidal interaction more effective in driving the rotation toward orbital synchronization.

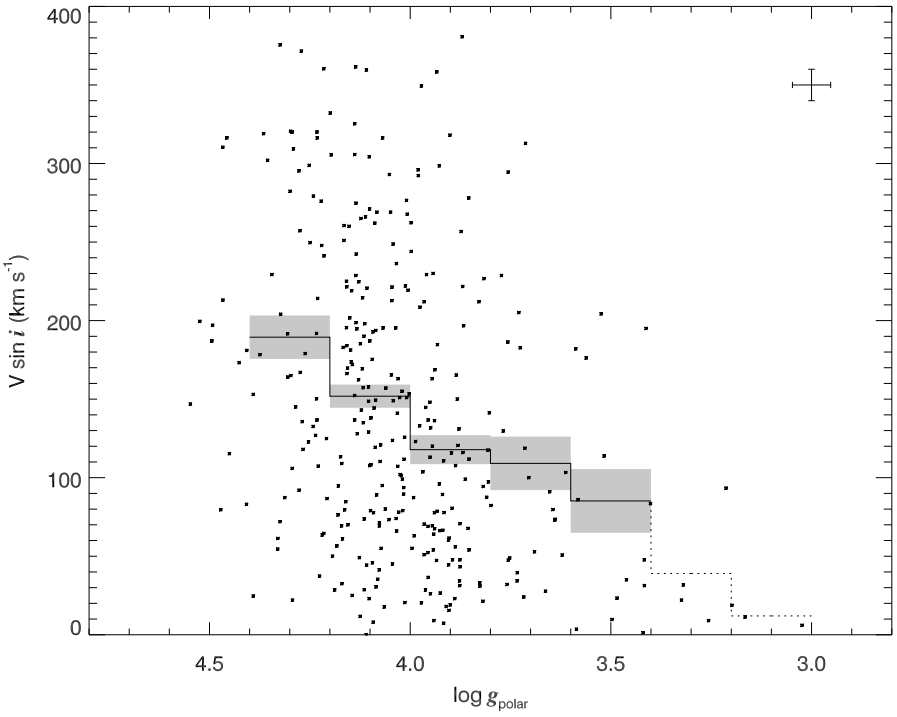

Figure 2.17: The distribution of the single stars in our sample in the $(V \sin i, \log g_{\rm polar})$ plane. The average errors in $V \sin i$ and $\log g_{\rm polar}$ are plotted in the upper-right corner. The solid line shows the mean $V \sin i$ of each 0.2 dex bin of $\log g_{\rm polar}$ that contains 6 or more measurements while the dotted line shows the same for the rest of bins. The shaded areas enclose the associated error of the mean in each bin.

2.7 Helium Abundance

Rotation influences the shape and temperature of a star's outer layers, but it also affects a star's interior structure. Rotation will promote internal mixing processes which cause an exchange of gas between the core and the envelope, so that fresh hydrogen can migrate down to the core and fusion products can be dredged up to the surface. The consequence of this mixing is a gradual abundance change of some elements on surface during the MS phase (He and N become enriched while C and O decrease). The magnitude of the abundance

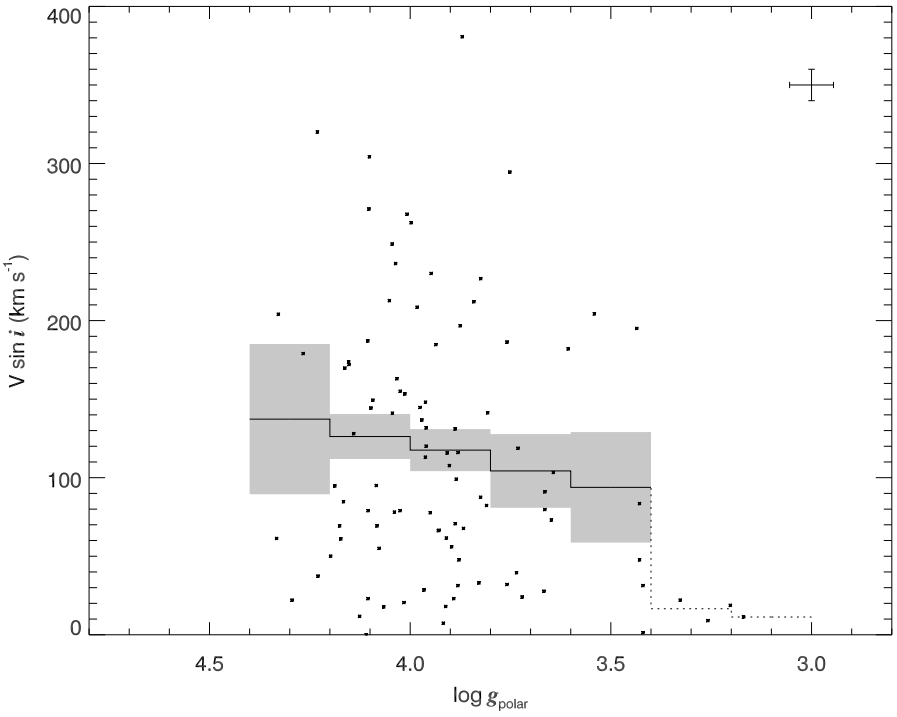

Figure 2.18: A similar plot to Figure 2.17, but only for the single stars in the high mass shaded region ($8.5M_{\odot} < M \leq 16M_{\odot}$) of Figure 2.15

change is predicted to be related to stellar rotational velocity because faster rotation will trigger stronger mixing (Heger & Langer 2000; Meynet & Maeder 2000). In this section, I present He abundance measurements from our spectra that I analyze to test the expected correlations with evolutionary state and rotational velocity.

2.7.1 Measuring Helium Abundance

We can obtain a helium abundance by comparing the observed and model profiles provided we have reliable estimates of $T_{\rm eff}$, $\log g$, and the microturbulent velocity V_t. I already have mean values for the first two parameters ($T_{\rm eff}$ and $\log g$) from Hγ line fitting (Section 2.4). I adopted a constant value for the microturbulent velocity, $V_t = 2$ km s^{-1}, that is comparable

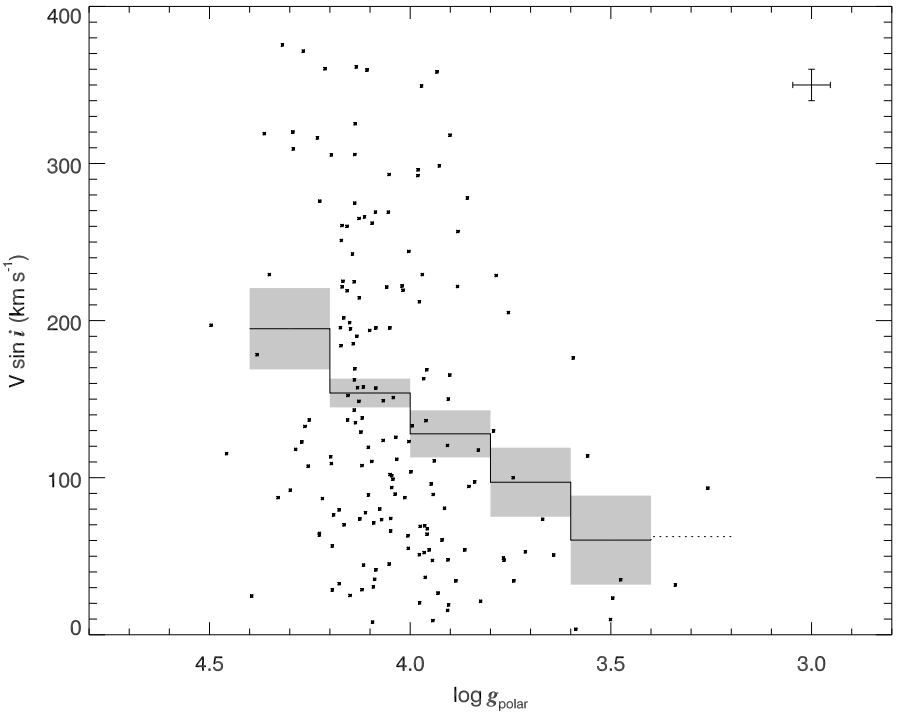

Figure 2.19: A similar plot to Figure 2.17, but only for the single stars in the middle mass shaded region ($4M_{\odot} < M \leq 8.5M_{\odot}$) of Figure 2.15.

to the value found in multi-line studies of similar field B-stars (Lyubimkov et al. 2004). The consequences of this simplification for our He abundance measurements are relatively minor. For example, I calculated the equivalent widths of He I $\lambda\lambda 4026, 4387, 4471$ using a range of assumed $V_t = 0-8$ km s^{-1} for cases of $T_{\rm eff} = 16000$ and 20000 K and $\log g = 3.5$ and 4.0. The largest difference in the resulting equivalent width is $\approx 2.5\%$ between $V_t = 0$ and 8 km s^{-1} for the case of the He I $\lambda 4387$ line at $T_{\rm eff} = 20000$ K and $\log g = 3.5$. These He I strength changes with microturbulent velocity are similar to the case presented by Lyubimkov et al. (2004) for $T_{\rm eff} = 25000$ K and $\log g = 4.0$. All of these results demonstrate that the changes in equivalent width of He I $\lambda\lambda 4026, 4387, 4471$ that result from a different choice of V_t are

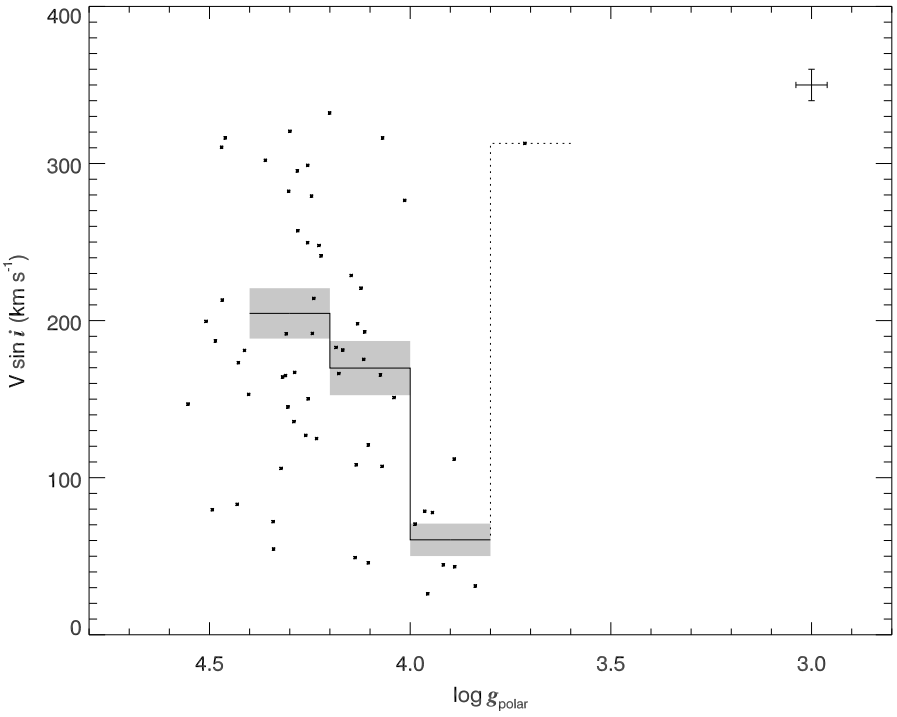

Figure 2.20: A similar plot to Figure 2.17, but only for the single stars in the middle mass shaded region ($2.5M_{\odot} < M \leq 4M_{\odot}$) of Figure 2.15.

small compared to observational errors for MS B-type stars. The V_t measurements of field B stars by Lyubimkov et al. (2004) are mainly lower than 8 km s^{-1} with a few exceptions of hot and evolved stars, which are rare in our sample. Thus, our assumption of constant $V_t = 2$ km s^{-1} for all the sample stars will have a negligible impact on our derived helium abundances.

The theoretical He I $\lambda\lambda 4026, 4387, 4471$ profiles were calculated using the SYNSPEC code and Kurucz line blanketed LTE atmosphere models in the same way as I did for the Hγ line (Section 2.4) to include rotational and instrumental broadening. I derived five template spectra for each line corresponding to helium abundances of 1/4, 1/2, 1, 2, and 4 times

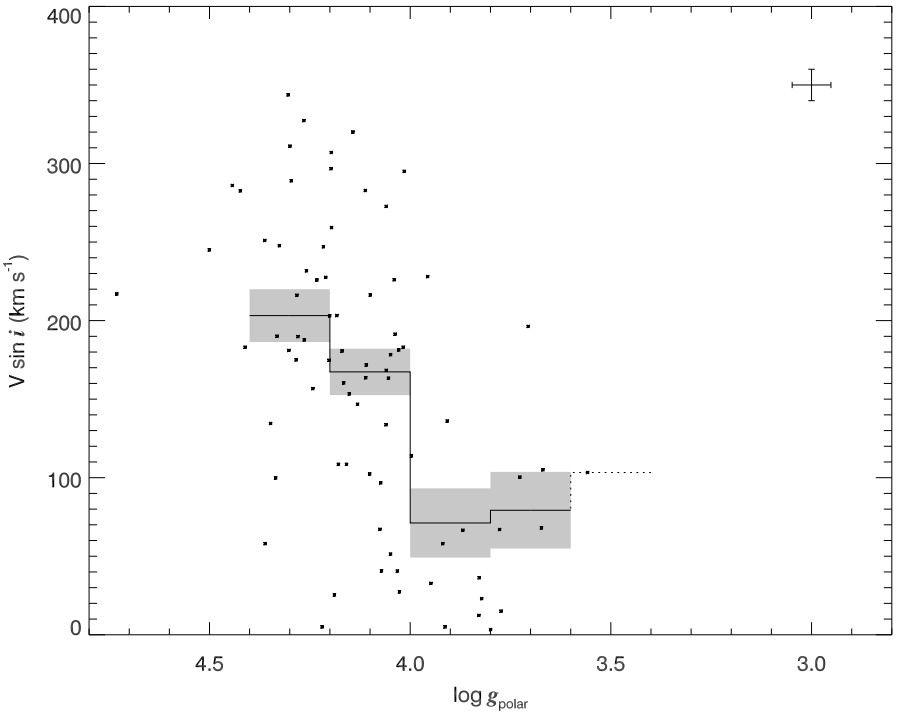

Figure 2.21: A similar plot to Figure 2.17, but restricted to the binary systems.

the solar value. I then made a bilinear interpolation in our $(T_{\rm eff}, \log g)$ grid to estimate the profiles over the run of He abundance for the specific temperature and gravity of each star. The χ^2 residuals of the differences between each of the five template and observed spectra were fitted with a polynomial curve to locate the minimum residual position and hence the He abundance measurement for the particular line. Examples of the fits are illustrated in Figure 2.22. Generally each star has three abundance measurements from the three He I lines, and these are listed in Table 2.5 (columns 9 – 11) together with the mean and standard deviation of the He abundance (columns 12 – 13). However, one or more measurements may be missing for some stars due to: (1) line blending in double-lined spectroscopic binaries; (2) excess noise in the spectral regions of interest; (3) severe line blending with nearby metallic

transitions; (4) extreme weakness of the He I lines in the cooler stars ($T_{\rm eff} < 11500$ K); (5) those few cases where the He abundance appears to be either extremely high ($\gg 4\times$ solar) or low ($\ll 1/4\times$ solar) and beyond the scope of our abundance analysis. I show examples of a He weak spectrum and of a He strong spectrum in Figures 2.23 and 2.24, respectively.

The He abundances I derive are based on LTE models for H and He which may not be accurate for hot and more evolved B giant stars ($T_{\rm eff} > 25000$ K, $\log g < 3.5$). I made a first order correction of the abundances to account for non-LTE effects by comparing the LTE and non-LTE (for H and He) model He I profiles calculated by Auer & Mihalas (1973). I used the equivalent width data for both the LTE and non-LTE cases in their Table 1 to derive corrections based upon stellar temperature and gravity. The corrections for the He abundances ϵ are small in most cases ($\Delta \log(\epsilon) < 0.1$ dex) and are only significant among the hotter and and more evolved stars. Note that I used the derived temperatures based upon line blanketed atmospheres in order to select the non-LTE abundance correction from the temperature grid of Auer & Mihalas (1973). However, Auer & Mihalas (1973) calculated their profiles using pure H–He atmospheres with no line blanketing, and these models assign a slightly higher effective temperature to B-stars of a given spectral subtype. Thus, I may have slightly underestimated the non-LTE corrections in some cases by interpolating in their grid at lower temperature than required for consistency of the temperature scales, but this discrepancy will have no significant consequences for our derived abundances except perhaps for the hottest stars.

The He abundances derived from each of the three He I lines should lead to a consistent result in principle. However, Lyubimkov et al. (2004) found that line-to-line differences do

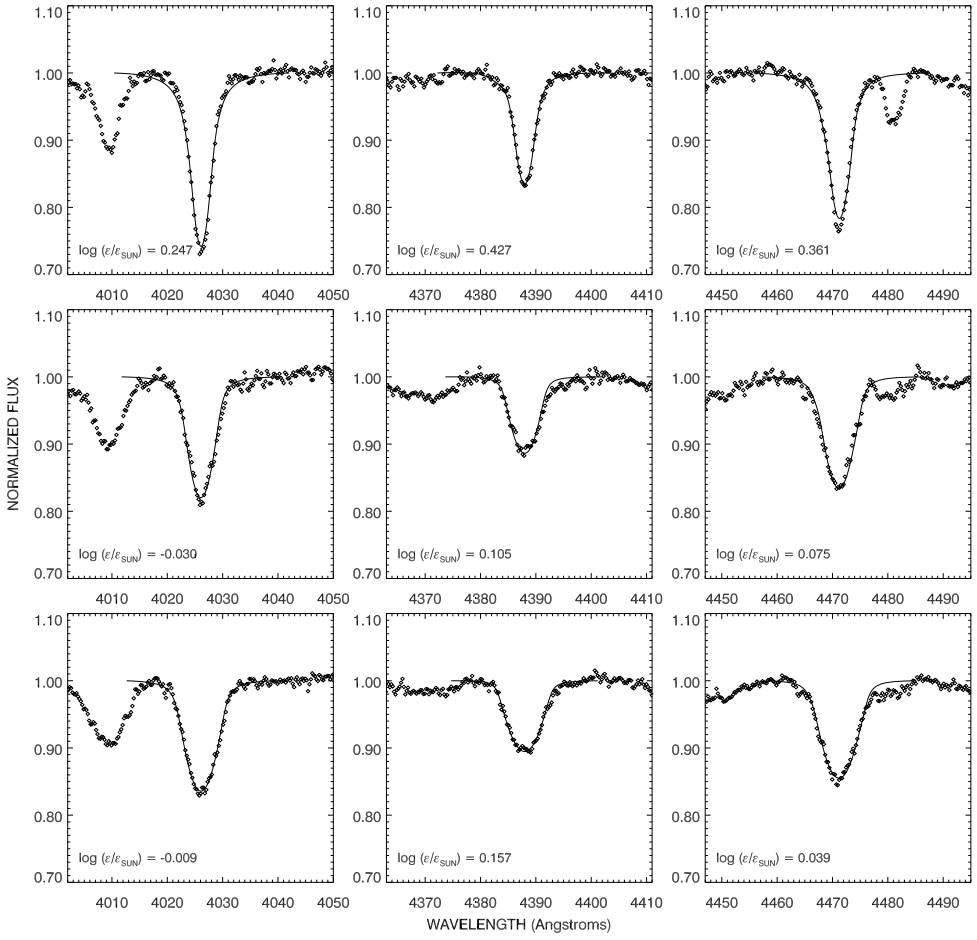

Figure 2.22: Line profile fitting results made to determine the He abundance for the same three stars used in Figure 2.13 and 2.14. Each panel lists the derived He abundance relative to the solar value for He I λ4026 (*left column*), He I λ4387 (*middle column*), and He I λ4471 (*right column*). The stars are (*from top to bottom rows*) NGC 1502 #23, NGC 869 #803, and NGC 884 #2255.

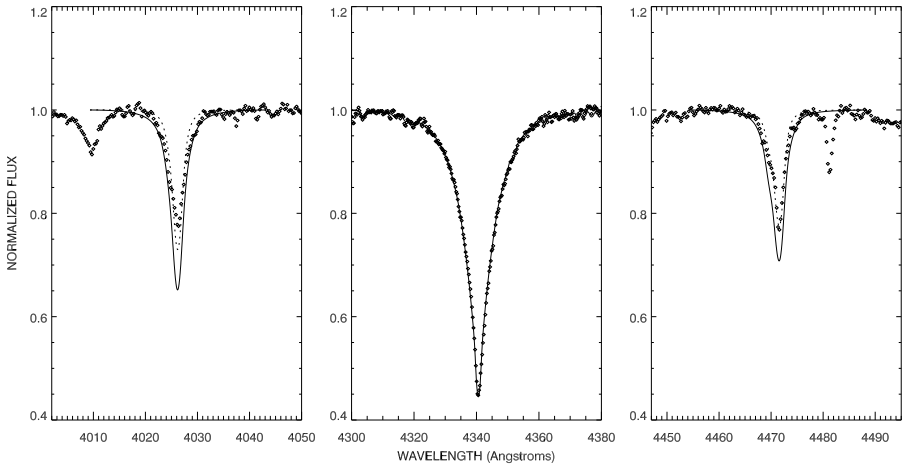

Figure 2.23: An example of a He-weak star, NGC 1502 #44. The panels from left to right: the He I λ4026 region, the Hγ region, and the He I λ4471 region. The solid lines are theoretical profiles synthesized assuming solar abundances and based upon the derived $T_{\rm eff}$, $\log g$, and $V \sin i$ for the star while the dotted lines are theoretical profiles synthesized assuming 1/4 solar abundance.

exist. They showed that the ratio of equivalent width of He I λ4026 to that of He I λ4471 decreases with increasing temperature among observed B-stars, while theoretical models predict a constant or increasing ratio between these lines among the hotter stars (and a similar trend exists between the He I λ4387 and He I λ4922 equivalent widths). The direct result of this discrepancy is that the He abundances derived from He I $\lambda\lambda 4471, 4922$ are greater than those derived from He I $\lambda\lambda 4026, 4387$. The same kind of line-to-line differences are apparently present in our analysis as well. I plot in Figure 2.25 the derived He abundance ratios $\log[\epsilon(4471)/\epsilon(4026)]$ and $\log[\epsilon(4387)/\epsilon(4026)]$ as a function of $T_{\rm eff}$. The mean value of $\log[\epsilon(4471)/\epsilon(4026)]$ increases from approx 0.0 dex at the cool end to +0.2 dex at $T_{\rm eff}$ = 26000 K. On the other hand, the differences between the abundance results from He I

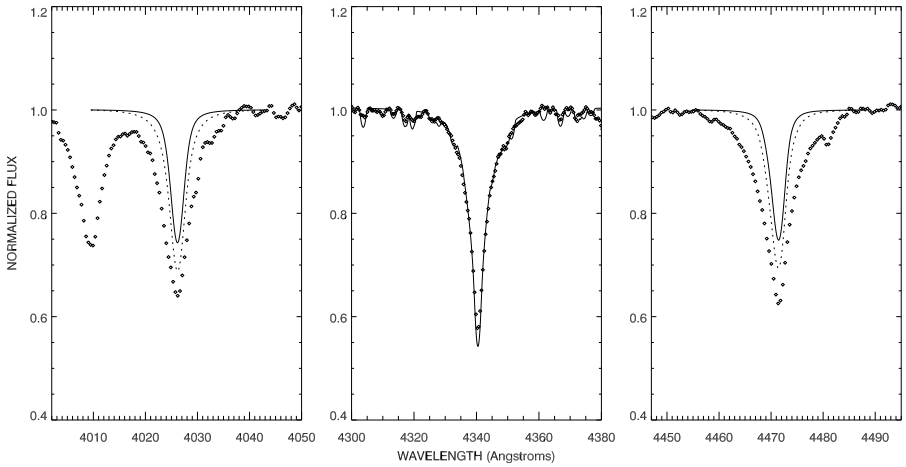

Figure 2.24: An example of a He-extremely-strong star, NGC 6193 #17. The format and legends are similar to those of Figure 2.23. The dotted lines are theoretical profiles synthesized assuming 4 times the solar abundance.

λ4026 and He I λ4387 are small except at the cool end where they differ by +0.1 dex (probably caused by line blending effects from the neglected lines of Mg II λ4385, 4391 and Fe II λ4385 that strengthen in the cooler B-stars). Lyubimkov et al. (2004) advocate the use of the He I $\lambda\lambda$4471, 4922 lines based upon their better broadening theory and their consistent results for the helium weak stars. Nevertheless, because the reasons for these inter-line differences are unknown and because our spectra have limited signal-to-noise and moderate resolution, I decided to use the average abundance based on all three He I lines in the following analysis. Since both the individual and mean line abundances are given in Table 2.5, it is straightforward to analyze the data for any subset of these lines.

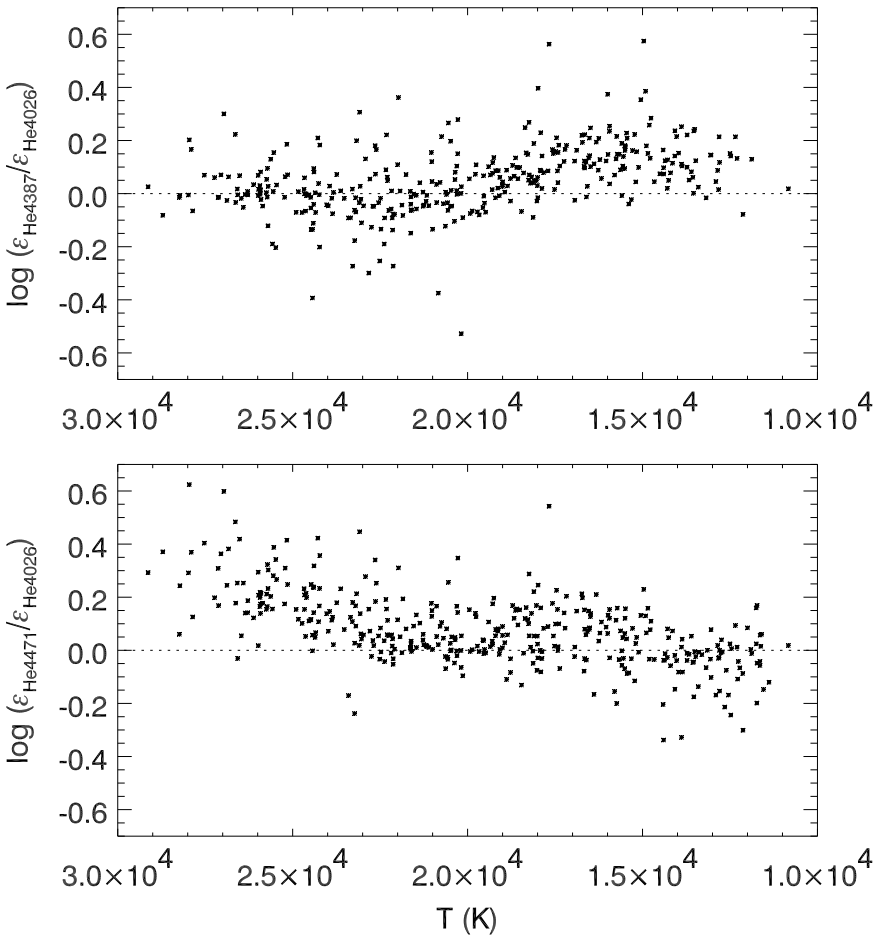

Figure 2.25: The difference in the derived He abundance from different He lines plotted against $T_{\rm eff}$. The top panel shows the differences between the results from He I λ4387 and He I λ4026 and the bottom panel shows the differences between He I λ4471 and He I λ4026.

2.7.2 Evolution of Helium Abundance

I plot in Figure 2.26 our derived He abundances for all the single stars and single-lined binaries in our sample versus $\log g_{\rm polar}$, which we suggest is a good indicator of evolutionary state (Section 2.5). The scatter in this figure is both significant (see the error bar in the upper left hand corner) and surprising. There is a concentration of data points near solar abundance that shows a possible trend of increasing He abundance with age (decreasing $\log g_{\rm polar}$), but a large fraction of the measurements are distributed over a wide range in He abundance. Our sample appears to contain a large number of helium peculiar stars, both weak and strong, in striking contrast to the sample analyzed by Lyubimkov et al. (2004) who identified only two helium weak stars out of 102 B0 - B5 field stars. Any evolutionary trend of He abundance that may exist in Figure 2.26 is lost in the large scatter introduced by the He peculiar stars.

Studies of the helium peculiar stars (Borra & Landstreet 1979; Borra et al. 1983) indicate that these stars are found only among those later than subtype B2. This distribution is clearly confirmed in our results. I plot in Figure 2.27 a diagram of He abundance versus $T_{\rm eff}$, where we see that almost all the He peculiar stars have temperatures $T_{\rm eff} < 23000$ K. In fact, in the low temperature zone ($T_{\rm eff} < 18000$ K), the helium peculiar stars are so pervasive and uniformly distributed in abundance that there are no longer any clear boundaries defining the He-weak, He-normal, and He-strong stars in our sample.

There is much evidence to suggest that both the He-strong and He-weak stars have strong magnetic fields that alter the surface abundance distribution of some chemical species (Mathys 2004). Indeed there are some helium variable stars, such as HD 125823, that

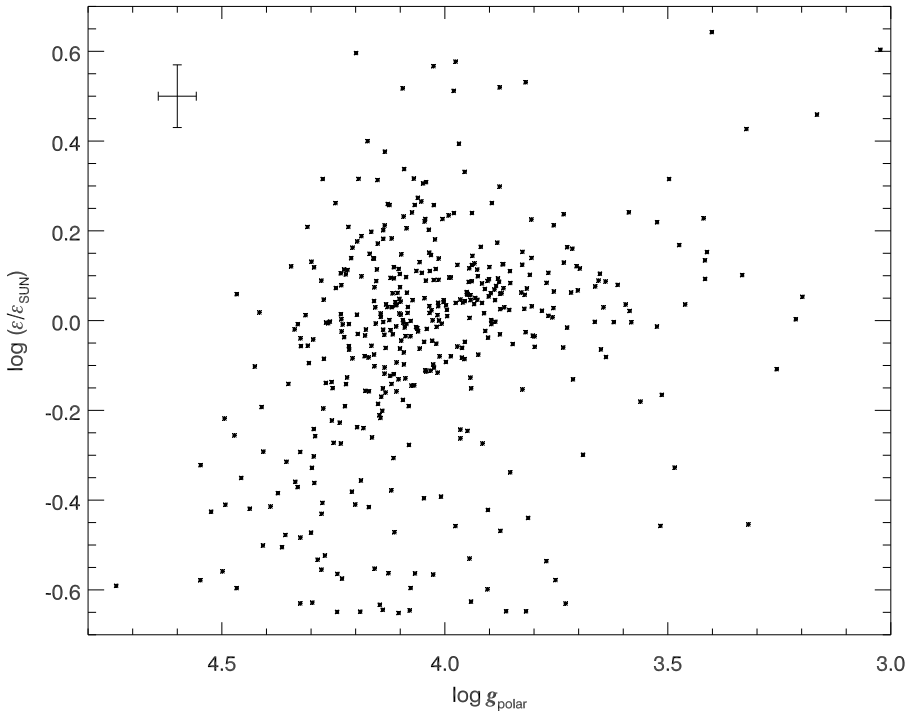

Figure 2.26: A plot of He abundance versus $\log g_{\rm polar}$ for the whole sample. The average measurement errors are indicated in the upper-left corner.

periodically vary between He-weak and He-strong over their rotation cycle (Jaschek et al. 1968). Because of the preponderance of helium peculiar stars among the cooler objects in the sample, I cannot easily differentiate between helium enrichment due to evolutionary effects or due to magnetic effects. Therefore, I will restrict our analysis of evolutionary effects to those stars with $T_{\rm eff} > 23000$ K where no He peculiar stars are found. This temperature range corresponds approximately to the high mass group of stars (138 objects) plotted in the darker shaded region of Figure 2.15.

The new diagram of He abundance versus $\log g_{\rm polar}$ for the high mass star group ($8.5 M_{\odot} < M < 16 M_{\odot}$) appears in Figure 2.28. We can clearly see in this figure that the surface helium

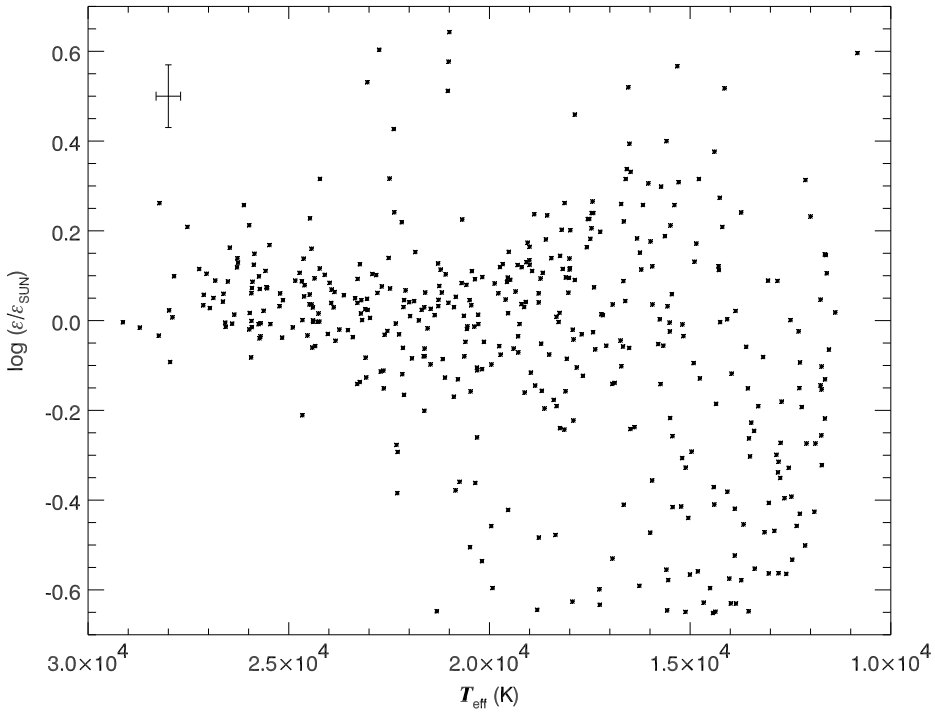

Figure 2.27: A plot of He abundance versus $T_{\rm eff}$ for the whole sample. The average measurement errors are indicated in the upper-left corner.

abundance is gradually enriched as stars evolve from ZAMS ($\log g_{\rm polar} = 4.3$) to TAMS ($\log g_{\rm polar} = 3.5$). I made a linear least squares fit to the data (shown as a dotted line)

$$\log(\epsilon/\epsilon_{\odot}) = (-0.262 \pm 0.019)\ \log g_{\rm polar}\ +\ (1.056 \pm 0.005)$$

that indicates an average He abundance increase of 0.23 ± 0.02 dex (or $70 \pm 5\%$) between ZAMS ($\log g_{\rm polar} = 4.3$) and TAMS ($\log g_{\rm polar} = 3.5$). This estimate is in reasonable agreement with the results of Lyubimkov et al. (2004) who found a ZAMS to TAMS increase in He abundance of 26% for stars in the mass range $4 - 11 M_{\odot}$ and 67% for more massive stars in the range $12 - 19 M_{\odot}$.

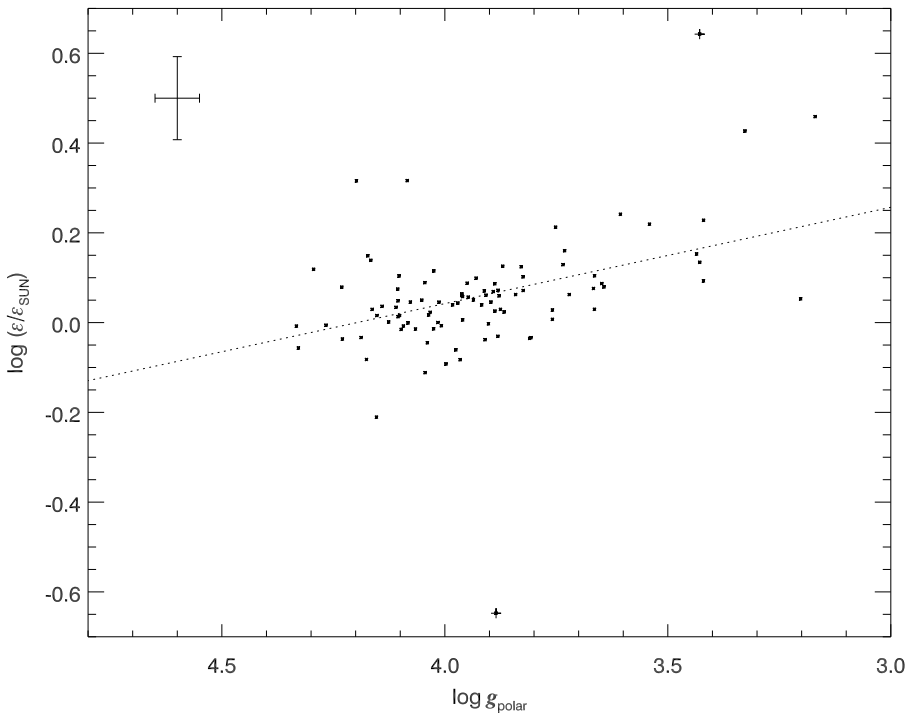

Figure 2.28: A plot of He abundance versus $\log g_{\rm polar}$ for all single stars in the high mass group (see the darker shaded area in Figure 2.15). The average measurement errors are indicated in the upper-left corner. The dotted line is the linear least squares fit. Two points marked by plus signs were not included for the fit (the He–weak star is NGC 2384 #88, the He–strong star is NGC 6193 #17).

2.7.3 Rotational Effects on the Helium Abundance

The theoretical models for mixing in rotating stars predict that the enrichment of surface helium increases with age and with rotation velocity. The faster the stars rotate, the greater will be the He enrichment as stars evolve towards the TAMS. In order to search for a correlation between He abundance and rotation ($V \sin i$), I must again restrict the sample to the hotter, more massive stars to avoid introducing the complexities of the helium peculiar stars (Section 2.7.2).

If the He abundance really does depend on both evolutionary state and rotational velocity,

then it is important to select subsamples of comparable evolutionary status in order to investigate how the He abundances may vary with rotation. I divided the high mass group into three subsamples according to their $\log g_{\rm polar}$ values, namely the young subgroup (22 stars, $4.5 > \log g_{\rm polar} > 4.1$), the mid-age subgroup (51 stars, $4.1 > \log g_{\rm polar} > 3.8$), and the old subgroup (17 stars, $3.8 > \log g_{\rm polar} > 3.4$). We plot the distribution of He abundance versus $V \sin i$ for these three subgroups in the three panels of Figure 2.29. Because each panel contains only stars having similar evolutionary status (with a narrow range in $\log g_{\rm polar}$), the differences in He abundance due to differences in evolutionary state are much reduced. Therefore, any correlation between He abundance and $V \sin i$ found in each panel will reflect mainly the influence of stellar rotation. We made least squares linear fits for each of these subgroups that are also plotted in each panel. The fit results are (from young to old) are:

$$\log(\epsilon/\epsilon_{\odot}) = (-1.3 \pm 2.3 \times 10^{-4})\ V \sin i\ +\ (0.050 \pm 0.022)$$

$$\log(\epsilon/\epsilon_{\odot}) = (0.5 \pm 1.2 \times 10^{-4})\ V \sin i\ +\ (0.029 \pm 0.012)$$

$$\log(\epsilon/\epsilon_{\odot}) = (3.8 \pm 2.0 \times 10^{-4})\ V \sin i\ +\ (0.081 \pm 0.017)$$

We can see that there is basically no dependence on rotation for the He abundances of the stars in the young subgroup (*top panel*). This situation changes slightly as stars evolve into the mid-age subgroup (*middle panel*), where the rapid rotators (with high $V \sin i$ values) appear to be more He enriched than the slow rotators. This trend continues as stars evolve into the old subgroup (*bottom panel*). Though there are fewer stars with high $V \sin i$ in the

old group (perhaps due to spin down), a positive slope is clearly seen that is larger than that of the younger subgroups.

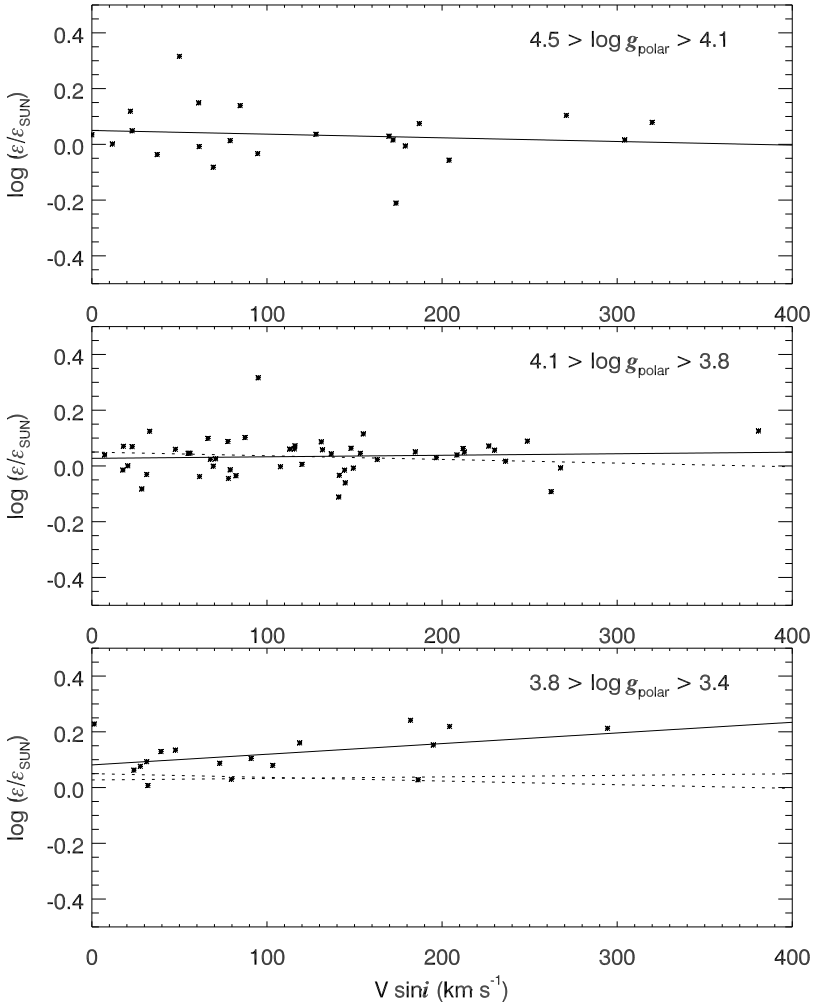

Figure 2.29: The stars shown in Figure 2.28 are divided into three subgroups by their $\log g_{\rm polar}$ values, and plotted in three panels of He abundance versus $V \sin i$. The youngest subgroup is plotted in the top panel while the oldest subgroup is in the bottom panel. The solid lines are the linear least squares fit for each subgroup. The dotted lines are the fits for the younger subgroups replotted in each older group for comparison purposes.

Our results appear to support the predictions for the evolution of rotating stars, specifically that rotationally induced mixing during the MS results in a He enrichment of the

photosphere (Figure 2.28) and that the enrichment is greater in stars that spin faster (Figure 2.29). The qualitative agreement is gratifying, but it is difficult to make a quantitative comparison with theoretical predictions because our rotation measurements contain the unknown projection factor $\sin i$ and because our samples are relatively small. However, both problems will become less significant as more observations of this kind are made.

2.8 Conclusions

Our main conclusions can be summarized as follows:

(1) Fitting the synthesized line profiles of physical models of rotating stars to observed spectra, I derived the projected rotational velocities of 496 OB stars in 19 young clusters (most of which are MS stars).

(2) I further determined average effective temperatures ($T_{\rm eff}$) and gravities ($\log g$) of 461 OB stars chosen from whole sample by fitting the Hγ profile in their spectra. The numerical tests using realistic models for rotating stars show that the measured $T_{\rm eff}$ and $\log g$ are reliable estimates of the average physical conditions in the photosphere for most of the B-type stars we observed.

(3) I used the profile synthesis results for rotating stars to develop a method to estimate the true polar gravity of a rotating star based upon its measured $T_{\rm eff}$, $\log g$, and $V \sin i$. I argue that $\log g_{\rm polar}$ is a better indicator of the evolutionary status of a rotating star than the average $\log g$ (particularly in the case of rapid rotators).

(4) A statistical analysis of the $V \sin i$ distribution as a function of evolutionary state ($\log g_{\rm polar}$) shows that all these OB stars experience a spin down during the MS phase as theories of rotating stars predict. The spin down behavior of the high mass star group in our sample ($16 M_{\odot} > M > 8.5 M_{\odot}$) quantitatively agrees with theoretical calculations that assume that the spin down is caused by rotationally-aided stellar wind mass loss. However, the spin down rates appear to be greater in the lower mass groups which have much weaker stellar winds. This surprising result suggests that other spin down processes must be active in the lower mass B-stars. I found a few relatively fast rotators among stars nearing the TAMS,

and these may be stars spun up by a short core contraction phase or by mass transfer in a close binary. I also found that close binaries experience a significant spin down around the stage where $\log g_{\rm polar} = 3.9$ that is probably the result of tidal interaction and orbital synchronization.

(5) I determined He abundances for most of the stars through a comparison of the observed and synthetic profiles of He I lines. Our non-LTE corrected data show that the He abundances measured from He I λ4026 and from He I λ4471 differ by a small amount that increases with the temperature of the star (also found by Lyubimkov et al. 2004).

(6) I was surprised to find that our sample contains many helium peculiar stars (He-weak and He-strong), which are mainly objects with $T_{\rm eff} < 23000$ K. In fact, the distribution of He abundances among stars with $T_{\rm eff} < 18000$ K is so broad and uniform that it becomes difficult to differentiate between the He-weak, He-normal, and He-strong stars. Unfortunately, this scatter makes impossible an analysis of evolutionary He abundance changes for the cooler stars.

(7) Because of the problems introduced by the large number of helium peculiar stars among the cooler stars, I limited my analysis of evolutionary changes in the He abundance to the high mass stars. I found that the He abundance does increase among stars of more advanced evolutionary state (lower $\log g_{\rm polar}$) and, within groups of common evolutionary state, among stars with larger $V \sin i$. This analysis supports the theoretical claim that rotationally induced mixing plays a key role in the surface He enrichment of rotating stars.

(8) The lower mass stars in our sample have two remarkable properties: a relatively fast spin down rate with advancing evolution and a large population of helium peculiar stars.

Many studies of the helium peculiar stars (Borra & Landstreet 1979; Borra et al. 1983; Wade et al. 1997; Shore et al. 2004) have concluded that these stars have strong magnetic fields which cause a non-uniform distribution of helium in the photosphere. If magnetic fields are a common phenomenon among the helium peculiar stars, and therefore among the late-type B-stars as a whole, then it is probable that magnetic braking is the key process in their spin down evolution.

Chapter 3

Regulus

3.1 Introduction

3.1.1 The Star Regulus

The star Regulus (α Leo, HD 87901, $m_V = 1.35$) is the second brightest B star in the sky (the brightest is Spica, α Vir, $m_V = 1.04$). Its spectral type is classified as B7 V (Johnson & Morgan 1953) or, more recently, B8 IVn (Gray et al. 2003). Compared to Spica's spectral type, B1 III-IV, Regulus has a much lower surface temperature and intrinsic luminosity. Its very high apparent brightness is due to its close distance to the Sun (Regulus is the nearest B star). According to the *Hipparcos* measurement of the parallax of Regulus (Perryman et al. 1997), 42.09 ± 0.79 mas, it is only 23.8 ± 0.45 parsec or 77.6 ± 1.5 light years distant. The projected equatorial rotational velocity $V \sin i$ derived from measurements of its spectral line widths (Slettebak et al. 1975; Abt et al. 2002) is large and implies that Regulus belongs to the category of very rapid rotators. Thus, we can expect that Regulus should exhibit all the theoretically predicted properties of rapidly rotating stars that we introduced in previous chapters, such as Roche geometry and gravitational darkening, and we could probably apply the same methods to measure $V \sin i$ and surface temperature/gravity as we did for cluster

member stars in Chapter 2.

However, we are in a much better position to analyze the rotation of Regulus, because it is close enough that its disk can be directly resolved with the Center for High Angular Resolution (CHARA) Array, an optical/IR interferometer array with the longest baselines of any in the world. With the help of the CHARA Array, we are able to "see" how the star is flattened and darkened by its rotation. Even better, we can determine the orientation of Regulus's spin axis in space from what we "see". Thus, the key parameter of stellar evolutionary status for Regulus, its polar gravity, can be firmly determined (without the need to apply a correction factor for the unknown inclination as was required for the cluster stars).

3.1.2 Interferometric Principles

An optical/IR interferometer array consists of a group of telescopes that collect stellar light, transfer optics that direct the light through pathlength delay lines, and finally a beam combiner that generates interference fringe patterns. By measuring the contrast of the fringe patterns generated by each pair of telescopes, we can obtain the key interferometric quantity, the visibility, which is defined as

$$V = \frac{I_{\max} - I_{\min}}{I_{\max} + I_{\min}} \tag{3.1}$$

where $I_{\max}$ and $I_{\min}$ are the intensities at the crests and troughs of the fringe, respectively. The visibility is related to the sky brightness distribution $F(x, y)$ of the target through a normalized Fourier transform (the van Cittert–Zernike Theorem) (Quirrenbach 2001;

Domiciano de Souza et al. 2002):

$$V(u,v)e^{i\phi(u,v)} = \frac{\iint F(x,y)e^{-2\pi i(ux+vy)}dx\,dy}{\iint F(x,y)dx\,dy} \tag{3.2}$$

where (x, y) are the coordinates in the tangent plane of the sky, and (u, v) indicates the vector in the frequency plane, determined by the length and orientation of the baseline $(= \mathbf{B}_{\rm proj}\lambda_{\rm eff}^{-1})$. The phase factor $e^{i\phi(u,v)}$ in (3.2) (corresponding to the position of the fringe) is often unmeasurable in practice due to atmospheric turbulence and/or internal fluctuations of the optical pathlength difference (OPD). Thus, the useful interferometric observables are often V or V^2. We can use theoretical models for rotating stars to predict the visibility distribution of a star, and then compare the observed and predicted visibility data to derive the star's angular size, geometric shape, and even its surface brightness distribution.

Obviously, the greater the number of visibility measurements and the better their distribution over the (u, v) plane, the more reliable are the conclusions we can draw from the comparison between the predicted and observed visibilities. An interferometer with only one pair of telescopes can obtain visibility measurements at many positions in the (u, v) plane due to the daily rotation of Earth, and observations made at different wavelengths can extend the range of (u, v) coverage. Many modern interferometers have more than two telescopes (a telescope array). An array of N-telescopes offers $N(N-1)/2$ different baseline choices. The six 1 m aperture telescopes of the CHARA Array provide 15 baselines with lengths ranging from 34 m to 331 m, which leads to an unprecedented uv coverage. The

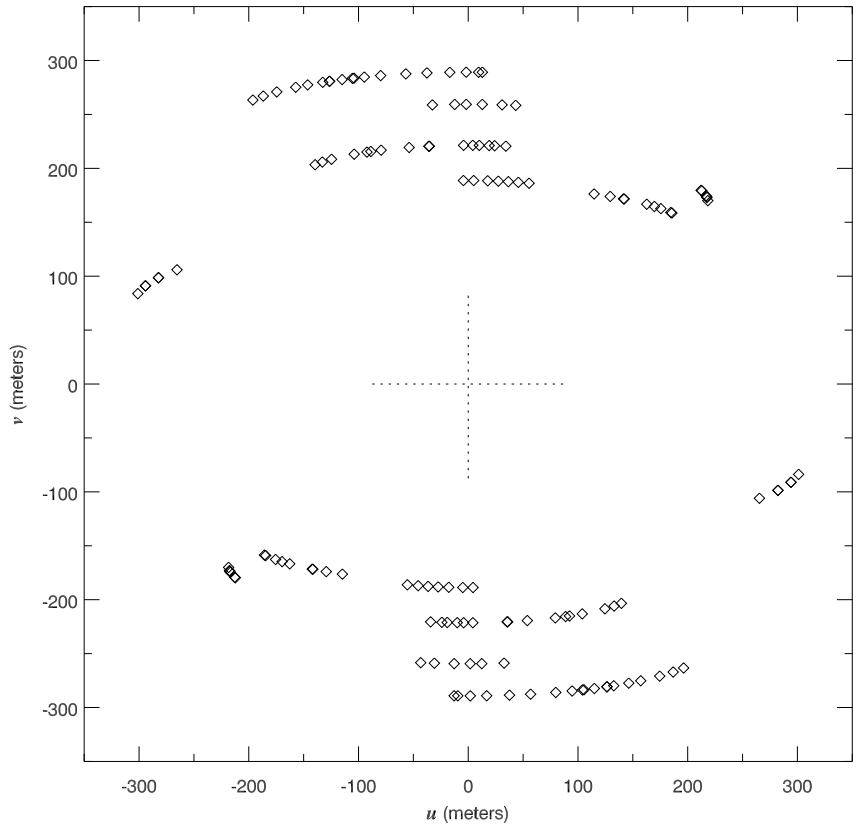

Figure 3.1: Distribution of the uv samplings of the CHARA Array in the Regulus observing run, Mar. – Apr. 2004.

details about the *uv* coverage of the CHARA Array can be found at its webpage[1]. The *uv* coverage of the Regulus observations is shown in Figure 3.1.

3.1.3 The Challenge of the Spectroscopic and Interferometric Analysis on Regulus

The observational evidence about the rotational properties of Regulus comes from two very different sources. One part consists of spectroscopic and spectrophotometric data, collected

[1]http://www.chara.gsu.edu/CHARA/Reports/appendixb.pdf

by more "traditional" methods. The other part consists of the new interferometric visibility data from the CHARA Array. The key parameters that set the physical properties of rotation in a rapid rotator like Regulus are the stellar mass M, polar radius $r_{\rm p}$, polar temperature $T_{\rm p}$, projected equatorial rotational velocity $V \sin i$, spin axis inclination angle i, gravity darkening exponent β, plus some observer related parameters, such as distance d and orientation angle of the spin axis projected on the sky α (position angle). It is very difficult to determine all these parameters from just the spectroscopic data or from just the interferometric data, and here I argue that a unique and reliable solution requires a joint analysis of both kinds of data.

We can analyze the spectroscopic data using the procedures described in the previous chapter to estimate $V \sin i$, average temperature, and average gravity. However, without a knowledge of the spin axis inclination angle, for example, it is difficult to derive other parameters, such as the polar gravity and temperature. Let us briefly review some the issues surrounding the interpretation of the spectroscopic data. The construction of synthetic profiles requires an assumed value for the gravity darkening exponent β that we must simply adopt from theoretical arguments ($\beta = 0.25$). Ideally, we would like to obtain limits on i by comparing observed profiles with synthetic profiles that properly account for the pole to equator temperature variation caused by rotation. It would be very helpful, for example, to compare the profiles of lines from different ions of the same element (in order to avoid questions about elemental abundances). Unfortunately, there are few such line pairs among the broad and shallow lines of the optical spectrum. One of the best known pairs for temperature estimation are the lines He I λ4471 and Mg II λ4481, but given the large

range in He abundance found among the late-type B stars in our cluster sample, it would be risky to assume that solar abundance models could be safely applied in our analysis of Regulus. There is no evidence that Regulus is a member of a binary system (there are no observed radial velocity variations due a close companion, nor does the *Hipparcos* parallax data exhibit the large scatter found in wider binaries), so we cannot use binary motion to measure mass. We can, however, estimate the stellar mass from $\log g$ provided we know the stellar radius, for example, from the star's apparent luminosity and distance. In turn, models of the apparent luminosity will depend on the inclination (and how much we see of the hotter polar zone), so we cannot make further progress without additional constraints.

Another set of problems confronts the use of the interferometric data alone. If the projected image of a star is circular or ellipsoidal and its surface brightness distribution can be described by well known limb darkening curves, then even a few visibility measurements scattered in a limited area of the uv plane can suffice to place good constraints on the angular size and orientation of the star. However, rapid rotators like Regulus have a more complicated shape and their surface brightness distribution is affected by gravity darkening. Later in this chapter, we will see that these rotation-induced changes have their largest impact on the visibility observed at very long baselines (beyond the first minimum in the visibility curve). Early high angular resolution studies of Regulus made using intensity interferometry and lunar occultations (Radick 1981; Berg 1970; Ridgway et al. 1982) determined that the average angular diameter of Regulus is about $1.3 \sim 1.4$ mas, which means that all the CHARA Array uv samplings made in the K-band fall into the first lobe of the visibility curve (see Figure 3.5 in Section 3.3.2). This means that even with the good uv coverage

provided by the current CHARA Array observations, it will be difficult to discern the small differences between the predictions of the rotation models for visibility in the first lobe. For example, we know that Roche geometry provides a good description of the shape of a centrally condensed rotating star, but the appearance of the projected image depends upon the polar radius, mass, rotational velocity, and inclination angle. A slightly slower rotating star may have a projected disk that appears very similar to that of a slightly faster rotating one with a lower inclination angle. It would be very difficult to distinguish between these situations in Fourier space because the subtle differences in the model predictions are smaller than the observed visibility errors.

We can overcome all these difficulties by making a combined spectroscopic – interferometric study of the nearest rapidly rotating B-star, Regulus. In following sections, I present a joint analysis that leads to the derivation of many of the basic surface parameters of Regulus, including the gravity darkening exponent that has only been measured in eclipsing binary systems before now. Because Regulus appears to be a relatively low temperature (12000 – 13000 K) MS star, we will use LTE model atmospheres generated by ATLAS9 for the spectral synthesis presented in the following sections. A full account of this work is also reported by McAlister et al. (2005).

3.2 Constraints from Spectroscopic Analysis

3.2.1 $V \sin i$ Measurements

The high resolution blue spectra ($\lambda/\Delta\lambda = 12400$) used for determining $V \sin i$ were obtained in 1989 April with the Kitt Peak National Observatory 0.9 m Coude Feed Telescope by Gies.

The final spectrum I used for fitting purposes represents the mean of 30 individual spectra that were combined to improve the S/N.

The measurement of $V \sin i$ is relatively simple and is more flexible in assuming the other physical parameters for line profile fit. Thus, measuring $V \sin i$ is often chosen as the first step of the studies of rotating stars. For rapid rotating stars, such as Regulus, stellar rotation is the dominant source of spectral line broadening, and other line broadening sources, such as thermal or presure brodening are much less important. However, if the star is not too far from the rotational breakup point, then the rotational line broadening will be affected by strong gravity darkening (Townsend et al. 2004b). Thus, when the physical parameters are assigned to the stellar models, the surface gravity (depends on the polar radius and mass) needs a very careful check, because the critical velocity (breakup velocity) is tightly connected to it. Our final values of polar radius and stellar mass were selected iteratively until the surface gravity matched with the results of the Hγ line fit (see Section 3.2.2) For rapidly rotating B stars later than B7 (like Regulus), the He I line contributions from the cool equatorial region (the most "darkened" part due to the gravity darkening effect) may become very weak or disappear altogether. Thus, we decided to use only the Mg II λ4481 line to measure $V \sin i$. Since Mg is much heavier than He, its spectral line widths contain less contributions from the thermal and collision broadening, and, thus, the line fitting of Mg II is more closely linked to the rotational broadening. The line synthesis included several nearby metallic lines (Ti II λ4468, Fe II λ4473, and Fe I λ4476) in order to account for any blending influence they have on the measurement of $V \sin i$. One example of the profile fit is plotted in Figure 3.2

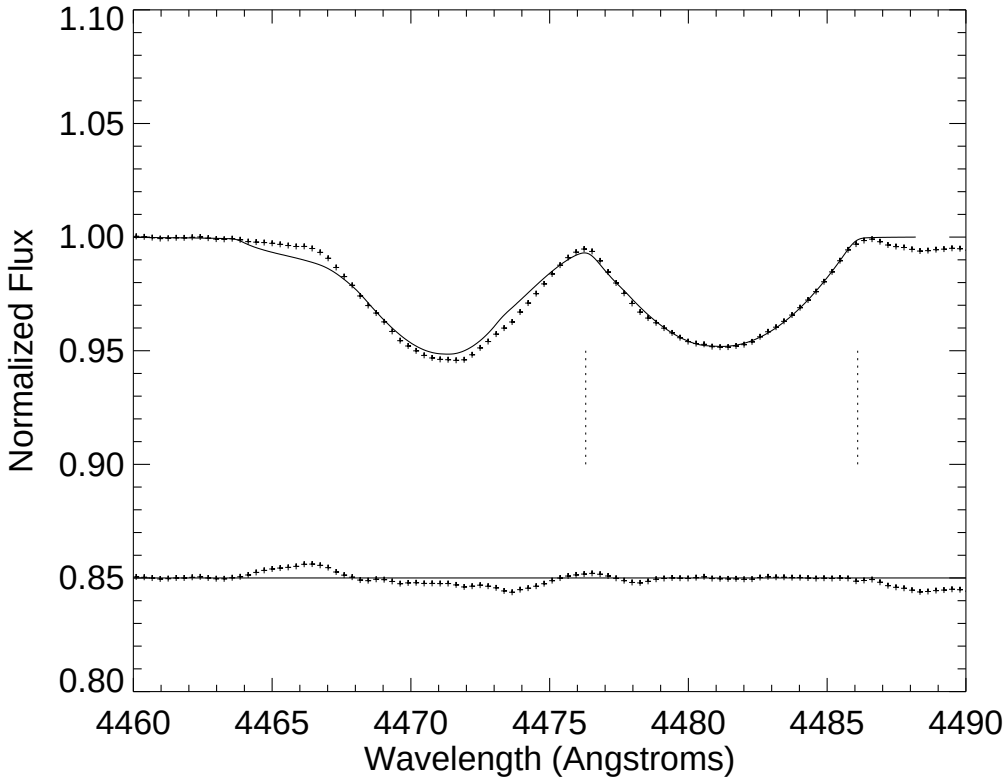

Figure 3.2: The observed (*plus signs*) and model (*solid line*) profiles for Mg II λ4481 in the spectrum of Regulus. The plot corresponds to a model with $i = 90°$ and $\beta = 0.25$. Residuals from the fit are shown below. The two vertical dashed lines indicate the wavelength range for the fit.

Ideally, we would treat the gravity darkening exponent β as an unknown parameter to be determined from observations, rather than just assuming a reasonable value ($\beta = 0.25$) as we did in the previous chapter. Different β values will influence the spectral line profiles through changes in the gravity darkening effect. Models with larger β (stronger gravity darkening) create profiles with diminished line wings, because these wings form preferentially near the equator at the approaching and receding limbs and a darker equator will lessen their contribution to the observed flux profile. Thus, a match of the observed line wings will be

made with a larger $V \sin i$ for a larger assumed β value. The final fitting results of $V \sin i$ with different β values are listed in Table 3.1 (first two columns).

β	$V \sin i$ (km s^{-1})	$< T >$ (K)	$< \log g >$
0.00	305	12280	3.600
0.05	307	12274	3.597
0.10	308	12265	3.592
0.15	310	12251	3.588
0.20	314	12190	3.570
0.25	317	12120	3.545
0.30	323	12040	3.520
0.35	326	11999	3.510

Table 3.1: $V \sin i$, $< T_{\rm eff} >$, and $< \log g >$ fit results for different β values

3.2.2 The Hγ Line and the K-Band Flux

The observed Regulus spectrum in the Hγ line region was collected from the spectral library of Valdes et al. (2004), and it has a moderate resolution of $\lambda/\Delta\lambda = 4900$. We used the derived $V \sin i$ values with the method described in the previous chapter to fit the Hγ line profile and obtain average surface temperature and gravity estimates for Regulus. The fitting results are given in Table 3.1 (last two columns). We see that Hγ fits using larger $V \sin i$ values (associated with larger β) need less pressure broadening to match the profile, so they result in lower $\log g$. However, stars with lower $\log g$ have smaller Hγ equivalent widths, and the fitting procedure compensates for this by converging on a lower temperature (since Hγ increases in strength with declining temperature at this spectral subtype). Note that the average temperatures and gravities in Table 3.1 were derived from the simplified "virtual star" models of the last chapter, which do not account for the variations in temperature and

gravity with co-latitude expected in real rotating stars. Nevertheless, I will compare these to the mean surface values for more realistic models in the next section.

The next useful constraint that also depends on stellar temperature and radius is the observed flux distribution. The optical and IR portions of the spectrum correspond to the Rayleigh-Jeans tail of the spectral energy distribution for hot stars like Regulus. Thus, the observed calibrated flux from Regulus depends directly on the product of the average temperature and the square of the angular radius of the star. With the well determined distance (from the *Hipparcos* parallax with an error $< 2\%$) and the derived average surface temperature from Hγ, the flux of Regulus measured on the Earth will put a very strict constraint on the real size of the star. The observed spectral flux distribution can be used as a target template that the synthesized spectrum of a model star must match. Once we have good estimates of temperature and radius, the value of $\log g$ from the Hγ fit will yield the mass.

For practical considerations of computation time, we restricted the spectral continuum fit to the region of the infrared K-band (which is also the band of the CHARA Array observations). Rather than rely entirely on a K-band flux estimate from IR magnitudes alone (with errors of $3-4\%$), I made a fit of the entire spectrum to set the continuum level in K-band with greater accuracy ($< 1\%$). The spectral flux data at different wave bands included the following: extreme ultraviolet fluxes from Morales et al. (2001); far- and near-ultraviolet spectra from the archive of the *International Ultraviolet Explorer (IUE) Satellite* (spectra SWP33624 and LWP10929, respectively); optical spectrophotometry from Alekseeva et al. (1996) and Le Borgne et al. (2003); and near-infrared fluxes transformed

from IR magnitudes given by Bouchet et al. (1991) using the calibration of Cohen et al. (1992). The observational fluxes were fit with a simple non-rotating star model spectrum from the LTE model atmospheres by Kurucz. The best fit parameters are $T_{\rm eff} = 12250$ K and $\log g = 3.5$ (which compare well with the averages from Hγ in Table 3.1), $E(B-V) = 0.005$ mag, and a limb-darkened angular diameter of 1.36 ± 0.06 mas. The K-band portion of this fitted model is shown below in Figure 3.3.

3.2.3 Parameters from Spectroscopy

We now have three major constraints from spectroscopic and spectrophotometric observations: (1) fits of the He I λ4471 / Mg II λ4481 profiles that lead to $V \sin i$ (dependent on β); (2) fits of the Hγ line profile that depend on the average surface temperature and gravity (which in turn depends on the stellar radius and mass); and (3) fits of the K-band flux that depend on the stellar radius and surface temperature. I constructed a series of rotating stellar models that consistently meet all of these observational constraints for a grid of assumed values of stellar inclination i and gravity darkening coefficient β. The method was an iterative approach in which we first established the projected rotational broadening from fits of the Mg II λ4481 line and then progressively approximated the polar temperature and radius to find models that met both the K-band flux and Hγ profile constraints. Note that once the temperature and radius are set, the Hγ fit provides us with the gravity ($\log g$) and hence the final parameter, stellar mass.

The results are summarized in Table 3.2 that lists the derived physical parameters over a grid of spin axis inclination ($i = 70^\circ - 90^\circ$) and gravity darkening exponent ($\beta = 0 - 0.35$).

I determined a solution for each combination of i and β (with corresponding $V \sin i$) using a successive approximation scheme. I began with a rotational model with initial guesses for mass, polar gravity, and polar temperature. I then calculated synthetic spectra in the Hγ and K-band continuum regions, and determined the average $T_{\rm eff}$ and $\log g$ over the visible hemisphere of the model star. Then I iteratively adjusted the values of the free parameters (mass, polar gravity, and polar temperature) until the I achieved good fits of the Hγ line and the K-band continuum (with hemisphere average $T_{\rm eff}$ and $\log g$ values consistent with those in Table 3.1). One example of the fitting procedure results (for $\beta = 0.25$ and $i = 90°$) is plotted in Figure 3.3.

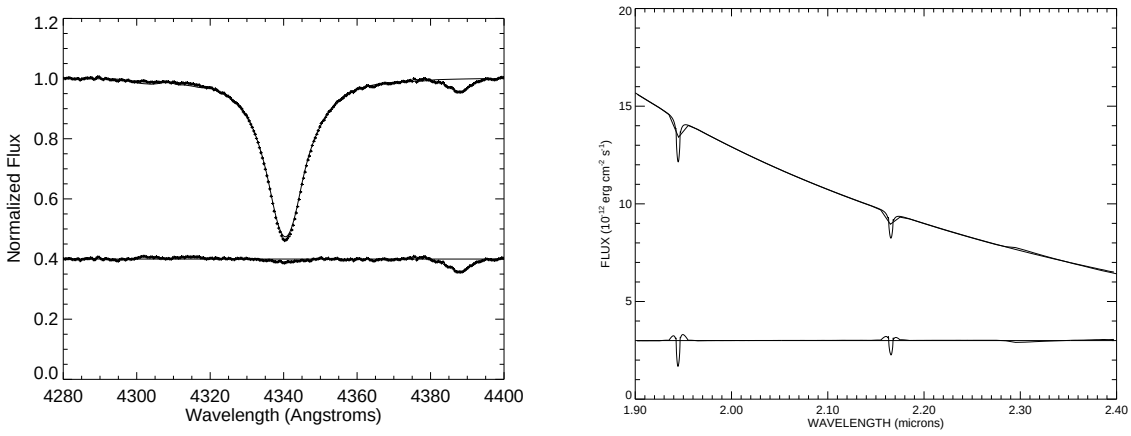

Figure 3.3: *Left*: The observed (*plus signs*) and model (*solid line*) profiles for Hγ in the spectrum of Regulus. *Right*: The adapted observational template (*thin line*) and model continuum (*thick line*) in the K–band. The plot corresponds to a model with a gravity darkening exponent $\beta = 0.25$ and an inclination $i = 90°$. The lower plots in both panels show the residuals from the fit (note that, in the *left* panel, the He I λ4387 line that was not included in the calculation).

All the solutions listed in Table 3.2 make satisfactory fits of the spectroscopic observations, and it is very difficult to determine which one of these solutions is closest to the real situation. We need additional and independent observational constraints that are more sensi-

i (deg)	β	$V \sin i$ (km s^{-1})	V_e/V_c	R_p ($R_\odot$)	R_e ($R_\odot$)	M ($M_\odot$)	T_p (K)	T_e (K)
90	0.00	305	0.82	3.15	4.05	3.45	12280	12280
90	0.05	307	0.82	3.15	4.06	3.45	12825	11968
90	0.10	309	0.83	3.14	4.07	3.45	13400	11643
90	0.15	310	0.83	3.14	4.08	3.46	14006	11309
90	0.20	314	0.84	3.14	4.12	3.43	14660	10852
90	0.25	317	0.86	3.14	4.16	3.39	15400	10314
90	0.30	323	0.87	3.15	4.22	3.39	16235	9677
90	0.35	326	0.88	3.14	4.24	3.39	17120	9155
80	0.00	305	0.83	3.13	4.05	3.45	12280	12280
80	0.05	307	0.83	3.12	4.06	3.45	12836	11943
80	0.10	309	0.84	3.12	4.07	3.45	13420	11589
80	0.15	310	0.84	3.12	4.08	3.45	14035	11220
80	0.20	314	0.85	3.12	4.12	3.44	14686	10740
80	0.25	317	0.87	3.12	4.16	3.41	15435	10191
80	0.30	323	0.88	3.12	4.22	3.40	16280	9486
75	0.00	305	0.84	3.10	4.05	3.46	12280	12280
75	0.05	307	0.85	3.10	4.07	3.46	12845	11905
75	0.10	309	0.85	3.10	4.08	3.46	13442	11516
75	0.15	310	0.85	3.10	4.09	3.46	14068	11109
75	0.20	314	0.86	3.10	4.12	3.44	14740	10581
75	0.25	317	0.88	3.10	4.17	3.40	15510	9953
70	0.00	305	0.86	3.06	4.06	3.46	12280	12280
70	0.05	307	0.86	3.06	4.07	3.47	12862	11849
70	0.10	309	0.87	3.06	4.08	3.46	13476	11401
70	0.15	310	0.87	3.06	4.09	3.47	14119	10942
70	0.20	314	0.88	3.06	4.13	3.45	14800	10336
70	0.25	317	0.90	3.06	4.17	3.41	15585	9618

Table 3.2: Spectroscopic fit results

tive to the parameters i and β, and these constraints can be determined from interferometric observations with the CHARA Array.

3.3 Parameters from Interferometry

The angular diameter of Regulus is extremely small ($\approx$ 1.4 mas), and early measurements by intensity interferometry and lunar occultation had such limited *uv* coverage that only an average angular diameter could be estimated (Brown et al. 1967; Radick 1981). Regulus was selected as the target of the first major science project for the CHARA Array, and an observing campaign in early 2004 made it possible to detect the flattened shape and equatorially darkened brightness distribution caused by rapid rotation of Regulus. The observations were carried out at the infrared K-band with a filter transmission that has an effective wavelength of $\lambda_{\rm eff} = 2.150$ μm. The final calibrated visibility data contain 69 sampling points widely scattered inside of the first lobe of the Fourier transformation of Regulus's brightness distribution. Details about the Regulus campaign and CHARA instrumentation are described in McAlister et al. (2005) and ten Brummelaar et al. (2005), respectively.

3.3.1 The Geometric Model Fits

The initial approach to modeling the visibility data from the CHARA Array was to assume that the stellar disk has a simple geometric shape (circular or ellipsoidal). Although these geometric models have no real physical meaning, they can give us a good idea about the angular size of the star in different orientations without making any complicated calculations.

There are two different methods to make such fits. The first method, used by several authors (van Belle et al. 2001; Domiciano de Souza et al. 2003), involves associating a uniform disk (UD) diameter with each visibility data point independently, plotting these

points on the tangent plane of the sky using their UD diameter, and then fitting a geometric shape with these points. The second method involves making a Fourier transform of the geometric model and then fitting it with the visibility data in frequency space. We will use the second method to do the fitting because it is mathematically more rigorous.

The program that generates the uniform brightness distributions with a regular geometric shape and the Fourier transformation program are given in Appendix A.2.1. The fitting results are listed in Table 3.3, which gives the semi-minor axis in the sky θ_b, the ratio of the semi-major to semi-minor axes θ_a/θ_b, the position angle (measured east from north) of the semi-minor axis in the sky α, and the reduced chi-squared of the fit χ^2_ν.

$\theta_{\rm b}$		α	
(mas)	$\theta_{\rm a}/\theta_{\rm b}$	(deg)	χ^2_ν
0.742	1.00	...	6.746
0.717	1.05	81.5	5.053
0.691	1.10	82.7	4.010
0.667	1.15	84.2	3.507
0.651	**1.18**	**84.9**	**3.415**
0.644	1.20	85.2	3.434
0.621	1.25	86.3	3.709
0.600	1.30	87.4	4.255

Table 3.3: Geometric model fit results

The best fit model (in bold font) in Table 3.2 has a elongated disk that strongly supports the model of Regulus's rapid rotation. The stellar surface of Regulus is deformed by a strong centrifugal force that causes the equatorial radius to be larger than the polar radius. This is an exciting result, and if the deformation caused by rotation is evident in the visibility data, are other signatures of rapid rotation also present? For example, can we "see" evidence of the gravity darkening effect? Can we determine the unknown parameters i and β left unspecified

in the spectroscopic analysis? We can answer these questions by using the physical rotation models to make predictions about the interferometric visibilities.

3.3.2 The Physical Model Fits

We saw in the previous section that the spectroscopic analysis leads to a family of solutions for the physical parameters that depend on i and β. Here we will use this grid of acceptable models (Table 3.2) to guide the parameter selection in the fits of the interferometric visibilities.

There are only two parameters to be determined in each case from the fitting procedure: the position angle of the spin axis α and a distance scaling factor $d/d(Hipparcos)$, where $d(Hipparcos)$ is the distance based on the *Hipparcos* parallax. Recall that a comparison of the model and observed flux distributions essentially sets the predicted angular size of the star. However, because of errors associated with the K-band flux, estimated stellar temperature, and the effective wavelength of interferometric observations, the angular size derived from the best fit of the visibilities cannot be guaranteed to be the same as that predicted by fits of the observed flux distribution. The use of the scaling factor $d/d(Hipparcos)$ in the fitting procedure (which scales the ratio of the model physical radii to distance to form the best match in angular size) is a simple way to account for lingering differences.

I modified the line synthesis code to create a program (see Appendix A.2.1) that uses specific intensity data from ATLAS9 and SYNSPEC43 to calculate a monochromatic K-band image of the rotating star. The image then is transformed into Fourier space to create a predicted interferometric visibility image in the uv plane. I then fit the predicted model

visibilities to the observed visibility data using two fitting parameters, the orientation angle α and the scaling factor $d/d(Hipparcos)$. I show an example of the K-band image and its Fourier transform for one of the physical models ($i = 90°, \beta = 0.25$) in Figure 3.4. All the fitting results are listed in Table 3.4 in the same order of i and β as given in Table 3.2. The columns list the inclination i, gravity darkening exponent β, projected angular radius along the minor axis (coincident with the spin axis) and along the major axis, position angle, distance scaling factor, and reduced chi-squared of the fit. The overall best fit in this grid (lowest χ^2_ν) is indicated in bold face.

Before drawing any conclusions from the fitting results, let us first inspect how different are the model predictions about the visibilities in Fourier space. Here I present the results for three physical models (**A**: $i = 90°$, $\beta = 0.25$; **B**: $i = 70°$, $\beta = 0.25$; **C**: $i = 90°$, $\beta = 0$) as examples of the influence of i and β in Fourier space. I plot in Figure 3.5 the visibility curves for each of these models in two directions (polar and equatorial). We can see that the visibility curves of all the models vary dramatically from equatorial direction to polar direction. This means that the star's orientation in the sky (position angle α) will be determined easily by a model fit to the visibility data from the baseline range of the CHARA Array observations (*gray-shaded area*). This is not unexpected for the physical models since we already found in the previous Section 3.3.1 that the fit results of simple geometric models can also lead to secure estimates of α. We see in Figure 3.5 that the CHARA Array measurements are all distributed within the first lobe of these visibility curves, and within this region the visibility differences among the models are largest at longer baselines and projected angles close to the polar direction. The sensitivity of the fits to the orientation parameter are illustrated in

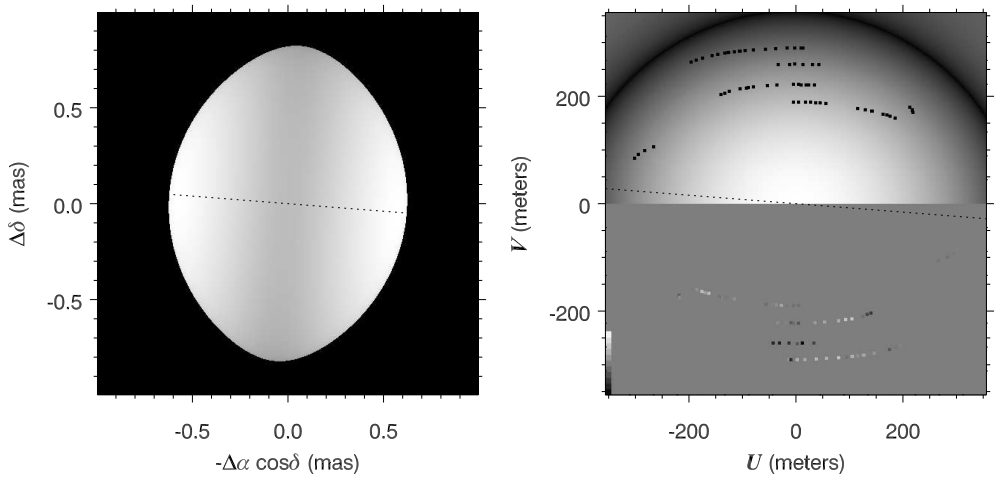

Figure 3.4: K-band image of a physical model in the sky (*left*) and its associated Fourier transform visibility pattern in the (u, v) plane (*right*). In both cases north is at the top and east is to the left. The dotted, black line indicates the direction of the rotational axis for this $i = 90°$, $\beta = 0.25$, and $\alpha = 85\overset{\circ}{.}5$ model. The upper panel of the visibility figure (*right*) shows a grayscale representation of the visibility and the positions of the CHARA measurements (*black squares*). The lower panel shows the normalized residuals from the fit as a gray scale intensity square against a gray background in a point symmetric representation of the (u, v) plane. The legend at lower left shows the intensities corresponding to normalized residuals from -5 (*black*) to $+5$ (*white*). Note that the best fit points appear gray and merge with the background.

Figure 3.6, a plot of χ^2_ν versus α for model **A**. We see clearly that the position angle α is better determined using the longer baseline data than all the data.

However, the model visibility curves in Figure 3.5 show that the differences related to different selections of β (between **A** and **C**) and i (between **A** and **B**) are much less pronounced. The minimum χ^2_ν value of the physical model fits in Table 3.4 occurs at grid values of $i = 90°$ and $\beta = 0.25$, and these probably represent the best estimates for Regulus. From

i (deg)	β	$R_{\rm minor}$ (mas)	$R_{\rm major}$ (mas)	α (deg)	$d/d(Hipparcos)$	χ^2_ν
90	0.00	0.624	0.802	87.4	0.988	3.95
90	0.05	0.624	0.806	87.2	0.987	3.76
90	0.10	0.626	0.810	86.8	0.984	3.58
90	0.15	0.625	0.811	86.1	0.984	3.45
90	0.20	0.624	0.816	86.0	0.987	3.38
90	**0.25**	**0.623**	**0.825**	**85.5**	**0.988**	**3.35**
90	0.30	0.619	0.830	85.3	0.994	3.39
90	0.35	0.620	0.836	84.6	0.993	3.55
80	0.00	0.626	0.804	87.6	0.987	3.97
80	0.05	0.627	0.807	87.2	0.985	3.78
80	0.10	0.626	0.809	86.8	0.985	3.61
80	0.15	0.628	0.814	86.6	0.982	3.48
80	0.20	0.626	0.818	86.1	0.985	3.40
80	0.25	0.625	0.825	85.9	0.987	3.36
80	0.30	0.625	0.835	85.7	0.988	3.36
75	0.00	0.626	0.803	87.7	0.988	3.98
75	0.05	0.629	0.808	87.3	0.985	3.80
75	0.10	0.629	0.810	86.9	0.985	3.64
75	0.15	0.630	0.814	86.7	0.983	3.51
75	0.20	0.630	0.821	86.5	0.983	3.43
75	0.25	0.630	0.830	86.5	0.983	3.38
70	0.00	0.628	0.804	87.6	0.987	4.02
70	0.05	0.629	0.808	87.5	0.985	3.85
70	0.10	0.630	0.813	87.3	0.982	3.70
70	0.15	0.634	0.816	86.9	0.980	3.57
70	0.20	0.635	0.825	87.1	0.979	3.50
70	0.25	0.634	0.833	87.2	0.980	3.46

Table 3.4: Interferometric fit results

the grid, I show how the chi-squared residuals of the fits vary as functions of β and i in Figure 3.7. We see that fits using all the visibility data produce quite shallow chi-squared curves that admit a significant range in possible values of β and i. However, fits based upon the subsets of longer baseline and polar direction visibility data are much more efficient in limiting the range of possible i and β.

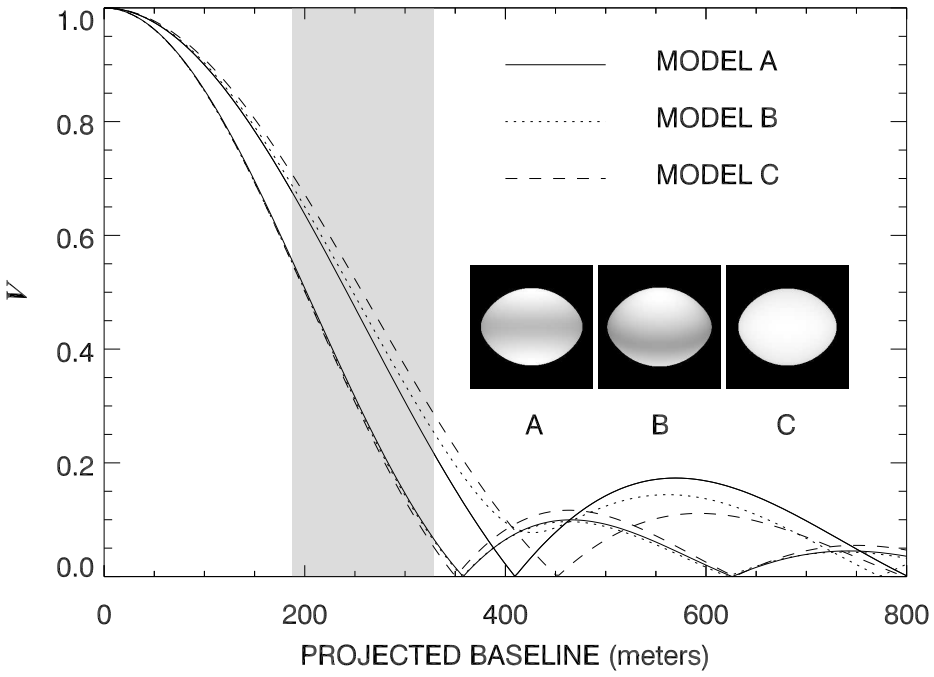

Figure 3.5: Predicted visibility variations with baseline for three rotation models and two sky orientations. The upper group correspond to a baseline parallel to the minor (rotational) axis in the sky while the lower group correspond to a baseline parallel to the major axis. The visibility curves are shown for the cases of $i = 90°, \beta = 0.25$ (**A**; *solid lines*), $i = 70°, \beta = 0.25$ (**B**; *dotted lines*), and $i = 90°, \beta = 0$ (**C**; *dashed lines*). The spatial frequency for a given baseline is shown for a filter effective wavelength of 2.1501 μm. The shaded region indicates the baseline range of the CHARA Array observations.

The interpretation of the scaling factor $d/d(Hipparcos)$ in Table 3.4 deserves some further comments. This fitting parameter is consistently about $1-2\%$ below unity, which means that the physical model needs to brought in slightly closer to match the slightly larger angular diameter found by fitting the visibility measurements. The predicted angular size comes from the ratio of observed to model flux, so there are three potential sources to explain this small discrepancy: (1) error in effective wavelength of the interferometric observations; (2) error in the K-band flux estimate; and (3) error is the assigned average temperature. Each of

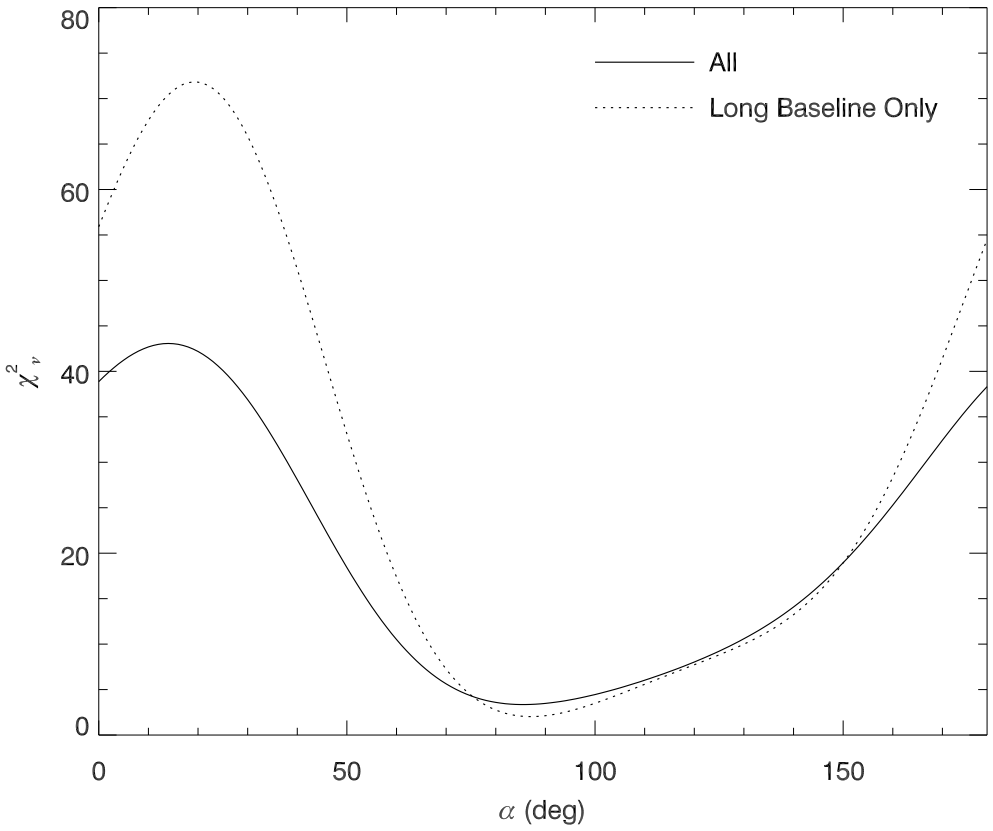

Figure 3.6: A plot of the reduced chi-square χ^2_ν of the visibility fits as a function of position angle α (for $i = 90°$ and $\beta = 0.25$). The solid line shows the reduced chi-square for whole sample while the dotted line shows the same for the long baseline data only.

these have accuracies of about 1%, so the size of the discrepancy between the predicted and observed angular dimensions is consistent with expectations. If the discrepancy is purely due to the adopted effective wavelength, then we can just assume that the *Hipparcos* distance is correct and adopt the other parameters in Table 3.2 and Table 3.4 as given. If the discrepancy is instead the result of errors in the estimate of the observed K-band flux, then we would need to increase the radii by about $0.5 - 1\%$ above the values quoted in Table 3.2. On the other hand, the discrepancy could also be explained by a decrease in temperature of $1 - 2\%$

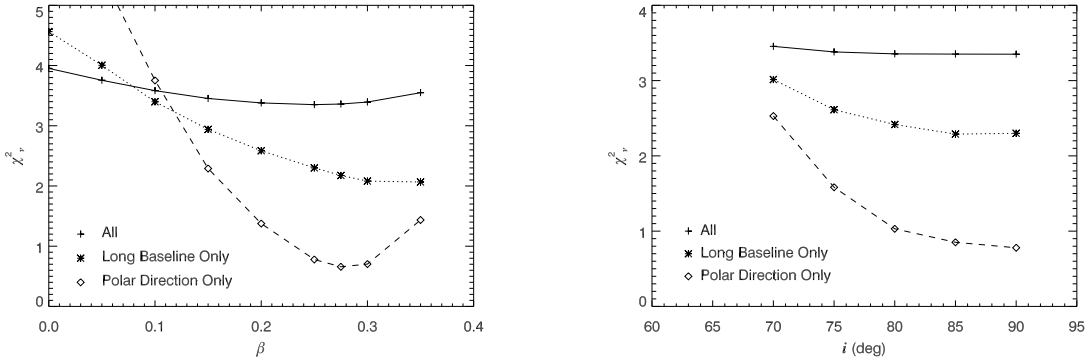

Figure 3.7: *Left*: A plot of the reduced chi-square χ^2_ν of the visibility fits as a function of gravity darkening exponent β (for $i = 90°$). *Right*: A plot of the reduced chi-square χ^2_ν of the visibility fits as a function of the rotation axis inclination angle i (for $\beta = 0.25$). In both plots, the solid line shows the reduced chi-square for whole sample (69 points). The dotted line shows the reduced chi-square of the same fits for the long baseline data only (31 points) while the dashed line shows the same for those long baseline data with a position angle near the orientation of the polar axis (the 6 points most sensitive to the selection of β).

(which would again result in slightly larger radii estimates).

3.4 Summary and Discussion

The method of combining spectroscopic and interferometric data together seems to work very successfully in the study of the rapidly rotating B-star, Regulus. Fits of the Mg II λ4481 line can provide very accurate $V \sin i$ measurements without any other prerequisites. Then the Hγ line fitting procedure combined with the K-band flux constraint lead to a restricted parameter space for possible physical models of Regulus. Finally, fits of the interferometric observations are quite sensitive to the brightness distribution and spin axis orientation, factors needed to pinpoint the correct physical model. The stellar physical properties of Regulus, such as stellar shape, space orientation, and the surface temperature distribution,

that were vague or totally unknown previously, become clear to us now. This is the first case in which we can really appreciate how different a rapidly rotating star is from a non-rotating one.

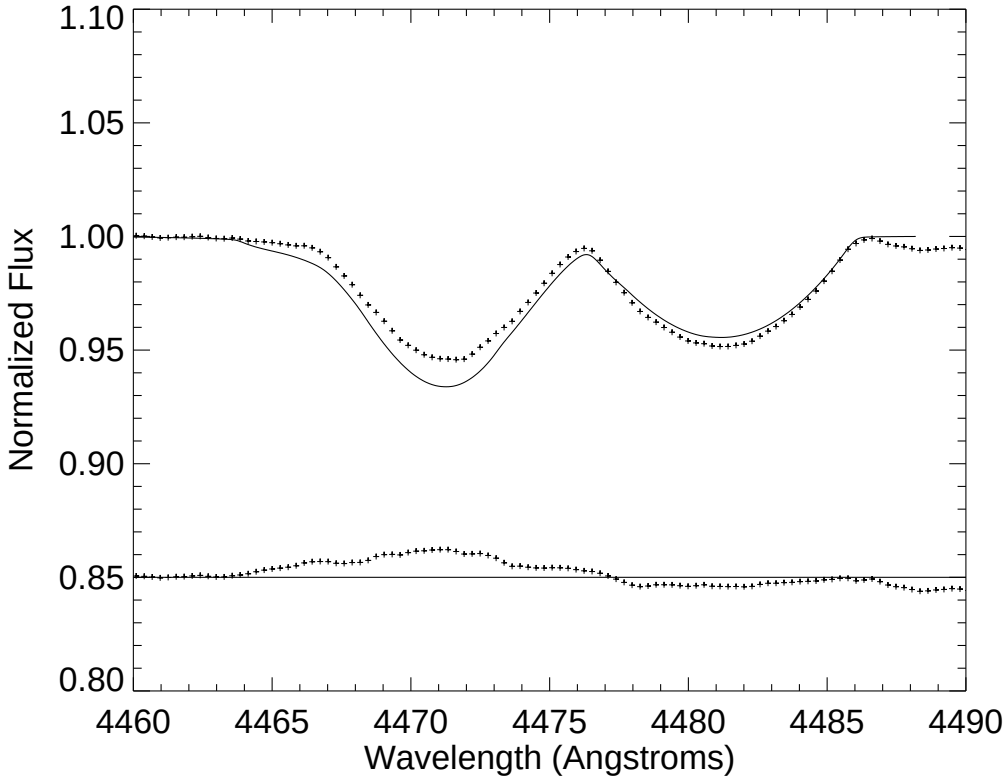

Figure 3.8: The observed spectrum (*plus signs*) and the synthesized (*solid line*) profiles of the best fit physical with solar abundance in the He I λ4471/Mg II λ4481 region. The lower plot shows the difference between them.

Rapidly rotating stars have a large pole-to-equator temperature range, which might have interesting consequences for spectral lines with differing temperature sensitivities. For example, He I lines decline with lower temperature in mid- to late-type B stars, while the Mg II λ4481 increase in strength with lower temperature. It is possible to imagine in these circumstances that the He I line will be preferentially formed in the polar regions compared

to Mg II, so their relative line widths and strengths could be different in a way that is inclination dependent (Stoeckley & Buscombe 1987). If Regulus had a smaller inclination angle, for example, we would see more of the hotter polar area and less of the cooler equatorial area, and thus observe stronger He I and weaker Mg II lines in its spectrum. However, the strength of spectral lines does not depend only on temperature, but also on the abundance of the element. Can we safely assume solar abundances for Regulus in the case of these two lines? I show in Figure 3.8 the synthesized spectrum in the He I λ4471 – Mg II λ4481 region for the best fit physical model that we derived above, made assuming solar abundances. The comparison of the model and observed spectra indicates that Regulus may be a He weak star with a Mg abundance slightly higher than the solar value. Caution is advised in such cases, since without accurate abundance data, the use of these two profiles may introduce additional uncertainties in the inclination estimate.

One surprising result from the analysis of the interferometric data is that the simple ellipsoidal model made almost as good a fit as the physical model did (minimum χ^2_ν = 3.42 and 3.35, respectively). We plot the images of two models together in Figure 3.9. Their spatial orientations are similar but their shapes and brightness distributions are very different. The radius ratio R_a/R_b is 1.18 and 1.32 for the ellipsoidal and the physical model, respectively. The figure also shows the appearance of the Fourier transforms of the two models (in a format similar to Fig. 3.5). In Fourier space, it becomes very clear that the first lobes of the Fourier transforms of these two very different models look almost identical. There is no doubt that both of them can make very good fits of the visibility data! We have to look to longer baselines (in the second lobe) to distinguish between them in Fourier space.

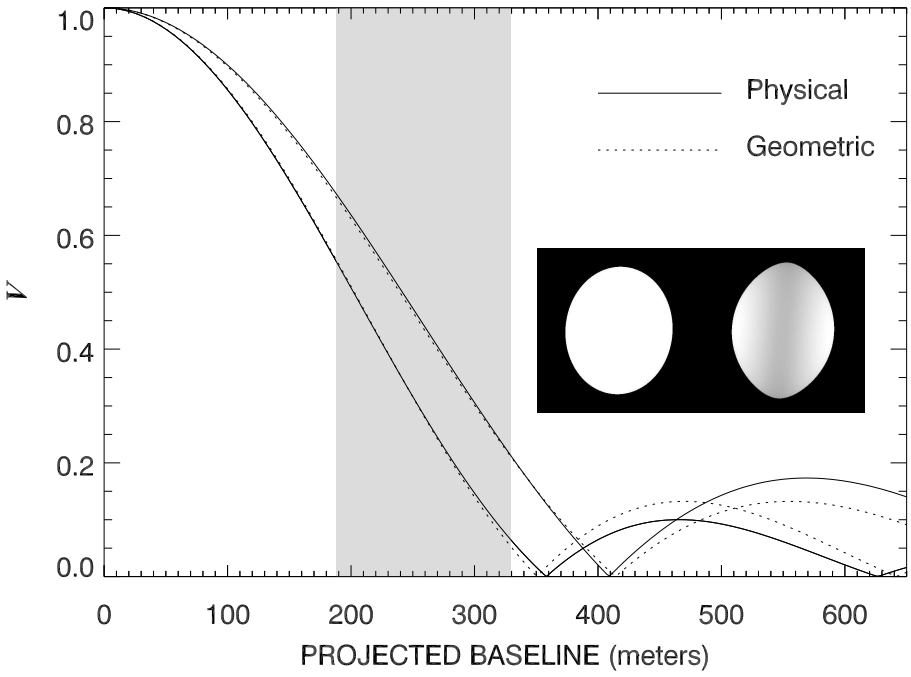

Figure 3.9: The visibility variations with baseline for the best fit geometric model and best fit physical model. The layout is similar to Figure 3.5.

The lesson here is that for rapidly rotating hot stars where strong gravity darkening exists, geometric models will not be able to recover the stellar shape accurately from visibility data with a limited uv coverage and baseline range.

Rotation may not only influence the surface conditions (Roche geometry and the gravity darkening effect), but might fundamentally change the star's evolutionary path in the Hertzsprung-Russell diagram (HRD). Rotation-induced mixing processes (Heger & Langer 2000; Meynet & Maeder 2000) are thought to bring more fresh hydrogen into the core of a rotating star, which makes it shine more luminously over a longer MS lifetime. However, even if this phenomenon does exist in rotating stars, it will be very difficult to detect in practice because it is hard to estimate the true luminosity of a rapid rotator. The observed flux

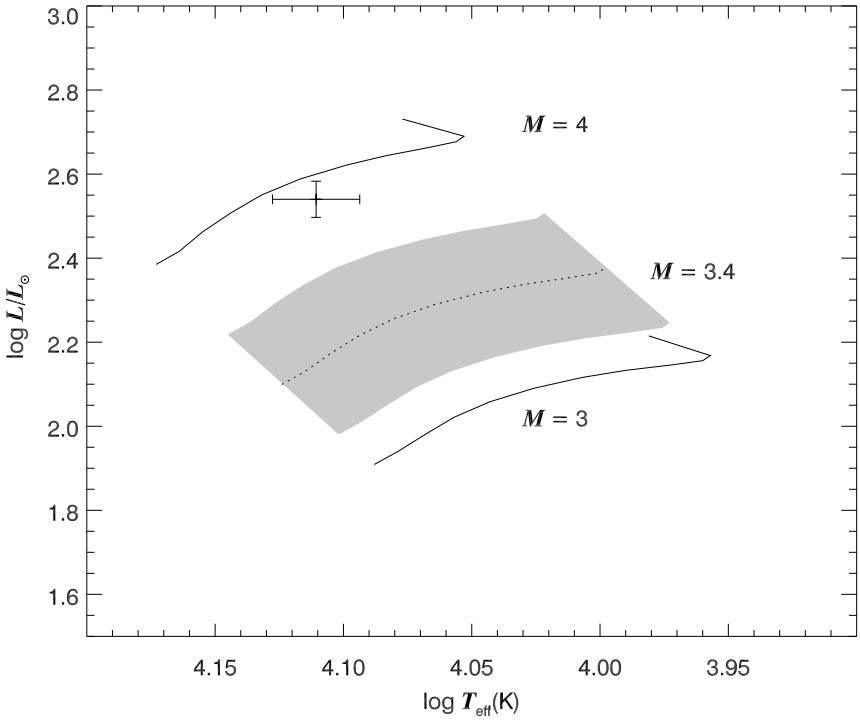

Figure 3.10: The Hertzsprung–Russell diagram for Regulus. The two solid lines show the track from zero age to terminal age main sequence (*left to right*) for non-rotating stars with initial masses of 3 and $4M_{\odot}$ (Schaller et al. 1992), while the dotted line and surrounding shaded area show the predicted region for a non-rotating star with the derived mass of Regulus and its associated error. The single point at $L/L_{\odot} = 347$ and $< T_{\rm eff} >= 12901$ K (from a surface integration of our numerical model) is well above the predicted position, indicating that the star is overluminous for its mass in comparison to models for non-rotating stars.

from a rotating star depends on its spin axis inclination, and thus the star's total luminosity remains unknown unless we know its surface temperature distribution and spin inclination angle. Regulus is the only rapidly rotating star known that meets these requirements. The evolutionary tracks for non-rotating stars with masses of 3 and $4M_{\odot}$ and the derived mass of Regulus ($3.4M_{\odot}$) are plotted in the HRD in Figure 3.10. The gray shaded area indicates the zone enclosed by the error associated with the derived mass. We obtain the total luminosity

(L) of Regulus by integrating σT^4 over the entire surface, and we then calculate an average effective temperature $T_{\rm eff}$ using the definition (Meynet & Maeder 1997),

$$L = S\sigma T_{\rm eff}^4, \tag{3.3}$$

where S is the area of the rotationally deformed stellar surface. We can see that Regulus is definitely more luminous than its non–rotating counterpart would be. Unfortunately, current model predictions for the evolutionary tracks of rotating stars have not been calculated for masses as low as that of Regulus, but its abnormally high luminosity implies that a rotation-induced mixing mechanism may operate in lower mass rapid rotators too.

Finally we note that Regulus is rotating so fast that its equatorial rotational velocity is about 86% of the critical velocity at which gravitational and centrifugal accelerations are balanced. Gas becomes so loosely bound to the photosphere in such circumstances that any number of physical processes might lead to the ejection of gas into a circumstellar disk. Indeed there is a group of B-type stars known as Be stars that appear to be rapid rotators with circumstellar disks. These Be stars are usually identified by the hydrogen Hα emission and IR excess flux from the disk. Regulus, however, shows no evidence of these disk features, and taken at face value, this suggests that a star must rotate faster than 86% of the critical velocity in order to form a disk and become a Be star. If correct, then Be stars must be exceptionally fast rotators (perhaps formed by a spin up from mass transfer in a close binary system).

Chapter 4

Non–Radial Pulsation in ϵ Per

4.1 Introduction

The study of radial and nonradial pulsations (NRP) in stars provides one of the few observational methods for testing theoretical models of stellar structure and evolution (Gautschy & Saio 1996; Aerts et al. 2002; Townsend 2005). Radial pulsations of stars are well known as the source of flux, color, and radial velocity variations, but because nonradial pulsations are more complex and may involve mutually canceling effects across the visible hemisphere of a star, it was uncertain for many years whether or not we could detect nonradial pulsations in unresolved stars. The situation changed dramatically about 20 years ago when it was realized that the Doppler broadening caused by stellar rotation could effectively redistribute the flux across a spectral line profile in a manner that would make traveling NRP waves visible through time variations in profile shape (Vogt & Penrod 1983). One of the first targets to be studied intensively for NRP spectral variability was the early-type star ϵ Persei (45 Per, HD 24760; B0.7 III). The spectral lines of ϵ Per display spectacular sequences of moving "bump" patterns that traverse the profiles from blue to red on time scales of hours (Smith 1985; Smith 1986; Smith et al. 1987; Gies & Kullavanijaya 1988; Harmanec 1989; Harmanec

& Tarasov 1990). The most intensive spectral times series investigations by Gies et al. (1999) and De Cat et al. (2000) indicate that ϵ Per is a multi-mode pulsator with periods ranging from 2 to 8 hours that have a relatively low geometric order (of degree $l = 3 - 5$). The star is also a single-lined spectroscopic binary with a possible distant third companion (Tarasov et al. 1995; De Cat et al. 2000).

Many investigators have developed codes to model these profile variations with varying degrees of sophistication. Lee & Saio (1990) and Lee et al. (1992) developed some of the first realistic models for the NRP modes in rotating stars, and Saio et al. (2000) compared these models to observations of ϵ Per with apparent success. Aerts & Waelkens (1993) developed a first-order approximation method that is applicable to slow rotators, and these methods were used to develop diagnostic procedures to determine NRP parameters from the observed profiles (Schrijvers et al. 1997; Telting & Schrijvers 1997; Schrijvers & Telting 1999). An important new code for fast rotators was developed by Townsend (1997) and it was used to model the profile variations in the rapidly rotating Be star μ Cen by Rivinius et al. (2001). Townsend (2004) presents an informative review of the physical principles that govern the kinds of NRP modes found in rapidly rotating stars.

Most of the studies to date have focused on the variations in only a few line profiles or have averaged the variations over many kinds of line transitions to increase the S/N of the observations. However, as Schrijvers & Telting (1999) and others have pointed out, lines with differing temperature sensitivity should have somewhat different patterns of temporal profile variability due to the temperature fluctuations associated with NRP. Here I present an investigation of the predicted and observed profile variations for lines in the spectrum of

ϵ Per. I discuss the assumptions behind our line profile synthesis method in Section 4.2, and I present examples of the kinds of predicted spectral variability in Section 4.3. I briefly consider in Section 4.4 the effects of multimode pulsations on the diagnostics of profile variability, and then in Section 4.5 I compare the model synthetic and observed data to find the key parameters for the dominant NRP mode in ϵ Per.

4.2 Line Synthesis Methods

I begin by describing our method of calculating synthetic line profiles. The basic idea is that the surface of the star is divided into many small patches, the specific intensity from each area element is calculated according to its local conditions (temperature, gravity, orientation to the line of sight, and net rotational and pulsational velocity along the line of sight), and then I integrate all these flux contributions over the visible part of the stellar surface to form the final line profile.

I obtain the 3-dimensional velocity field for each NRP mode using the formulae given by Schrijvers et al. (1997). Their method uses a first-order correction scheme to account for rotational effects, and this is a reasonable approximation when the rotation frequency is much lower than the frequency of the NRP mode (as is the case for the modes I will consider for ϵ Per). The velocity amplitude and phase of each NRP mode are treated as free parameters. Another important parameter is k the ratio of the horizontal to the vertical amplitude, which is determined theoretically for a mode with degree l and azimuthal order m by

$$k = k_0 + m\frac{\Omega}{\omega_0}\frac{(2+k_0)}{l(l+1)} \tag{4.1}$$

where $k_0 = GM/{\omega_0}^2 R^3$, G, M and R are the gravitational constant, the stellar mass, and radius, respectively, ω_0 is the zero-rotation angular frequency of pulsation, and Ω is the rotational angular frequency of the star. Because there is no way to measure the true value of ω_0, the angular frequency of pulsation in the co–rotating frame, $\omega_{\rm cr}$, is used instead. The relation between this two frequencies given by Schrijvers et al. (1997):

$$\omega_{\rm cr} = \omega_0 + m\Omega C_{nl}, \tag{4.2}$$

where the constant C_{nl} is very small for slow rotators, and the second term in the right hand side of the Equation (4.2) is often ignored. The value of $\omega_{\rm cr}$ can be derived from the observed angular frequencies of NRP modes using $\omega_{\rm cr} = \omega_{\rm obs} + m\Omega$.

The variation of local temperature due to NRP is another important factor for the line profile variations (LPV), because the the continuum flux level (local brightness), intensity profile shape, and line equivalent width are heavily dependent on the local temperature. Buta & Smith (1979) derived a relationship between variations of local temperature and radius,

$$\frac{dT}{T} = C\,\frac{\Gamma_2 - 1}{\Gamma_2}\left[kl(l+1) - 4 - \frac{1}{k}\right]\frac{dR}{R}e^{i\alpha} \tag{4.3}$$

where $\Gamma_2 = 5/3$ and the phase factor $e^{i\alpha}$ is added as a possible non-adiabatic phase lag α. The leading constant C is introduced here by us as an adjustment factor: $C = 0$ means I totally ignore the temperature variation while $C = 1$ means I give a full consideration to the temperature variation.

The intensity spectra for each area element were determined by interpolation in a large

grid I constructed based upon the local temperature T, gravity $\log g$, and cosine of the angle between the surface normal and line of sight μ. The were calculated by first obtaining solar abundance model atmospheres from the line blanketed LTE code ATLAS9 written by Robert Kurucz, and then intensity profiles for each transition were determined over a grid of μ values using the radiative transfer code SYNSPEC (version 43) written by Ivan Hubeny (Hubeny & Lanz 1995).

A rotating star will assume an equatorially extended shape that can be approximated by a Roche potential for a point-source mass. The temperature will vary from hot at the pole to cool at the equator, and the local flux will vary in concert (gravity darkening). The temperature distribution across the surface will vary with co-latitude θ from the pole as (Collins & Harrington 1966)

$$T(\theta) = T_{\rm pol} \left\{ \left[\frac{1}{x^2(\theta)} - \frac{8}{27}\Omega^2 x^2(\theta) \sin^2(\theta) \right]^2 + \left[\frac{8}{27}\Omega^2 x(\theta) \sin\theta\cos\theta \right]^2 \right\}^{\frac{1}{8}} \qquad (4.4)$$

where $x(\theta) = r(\theta)/R_{\rm pol}$ and $\Omega^2 = 27R_{\rm pol}^3/8GM$. For example, if I choose a projected rotational velocity of $V \sin i = 140$ km s^{-1} and an inclination between the spin axis and line of sight of $i = 70°$, then the surface temperature in our model of ϵ Per ranges from 26800 K at the equator ($R = 7.0R_\odot$) to 27600 K at the poles ($R = 6.80R_\odot$).

The integration is normally done using 20000 – 30000 areal elements to represent the surface of the star. The NRP formulation is used to estimate the local temperature, velocity, and surface normal orientation, and since the local intensity spectra are dependent on the μ angle, they accurately account for limb darkening. The visibility criterion for each areal

element is $\hat{r} \cdot \vec{s} > 0$ where $\hat{r}$ is the unit vector from the center of the element to the observer and $\vec{s}$ is the surface element normal vector. The resulting flux spectrum is rectified to a unit continuum and broadened by convolution with an instrumental broadening function for direct comparison with observations. Here I will examine blue spectra of ϵ Per obtained by Gies & Kullavanijaya (1988), for which the instrumental broadening function is a Gaussian with a width of 0.27 Å FWHM.

Once the theoretical construction of line profiles is done, I need a method to compare the results with observations. A direct comparison of model and observed profiles in observed flux versus time is difficult because the observations are made over many cycles and phases, and, in the case of ϵ Per, they represent the sum of multimode beating. A simple and appealing alternative is to examine the profile variations in Fourier transform space (Gies & Kullavanijaya 1988). This method (dubbed the Intensity Period Search or IPS method by Schrijvers et al. (1997)) involves making a Fourier transform of the temporal variations in line intensity at each wavelength position across the profile. Then the periodic component of line variability can be analyzed in terms of Fourier amplitude and phase at the signal frequency as a function of position across the profile. The amplitude and phase variations at the primary frequency and its first harmonic are very good indicators of the NRP properties (Schrijvers et al. 1997; Telting & Schrijvers 1997; Schrijvers & Telting 1999).

4.3 Variations of Local Temperature and Non-adiabatic Phase Lag

I selected five optical lines to investigate the NRP LPV properties: Si IV $\lambda\lambda 4088, 4116$, H$\delta$ $\lambda 4101$, C II $\lambda 4267$, and Si III $\lambda 4552$. All these features were recorded in the spectra of ϵ Per made by Gies & Kullavanijaya(1988) and all have interesting temperature sensitivities in the early B-type stars (see below). I calculated a grid of intensity profiles for each line and for viewing cosine $\mu = 0.1$ – 1.0 in steps of 0.1, temperature $T_{\rm eff} = 26000$ K – 28000 K in steps of 500°, and gravity $\log g = 3.5$, 3.75, and 4.0. A selection of these intensity profiles is shown in Figure 4.1 for the case of $\mu = 1$ and $\log g = 3.92$ ($\log g = 3.92$ is the average value for the model A in Table 4.1). The left column shows the profiles over the run of temperature with the hottest model profile at the top in each case (*dotted line*). The right hand column shows the net line absorption as a function of temperature. This was calculated by integrating the difference between the profile and interpolated continuum across the profile. These are similar to the equivalent width for a rectified flux profile, but they are flux weighted measurements instead. For example, the Hδ line (*middle panel*) has an equivalent width that slowly declines with increasing temperature in the early B-stars, but we see in Figure 4.1 how the flux weighted absorption increases with temperature because the continuum flux is increasing faster than the decline in line strength.

I adopted physical parameters for our model star that are close those applicable to ϵ Per (Tarasov et al. 1995; Gies et al. 1999), and these are summarized in Table 4.1. In this section I assume an inclination between the line of sight and the spin axis of $i = 70°$ (see Model A in Table 4.1), but I will explore other values in Section 4.5. The line profiles observations

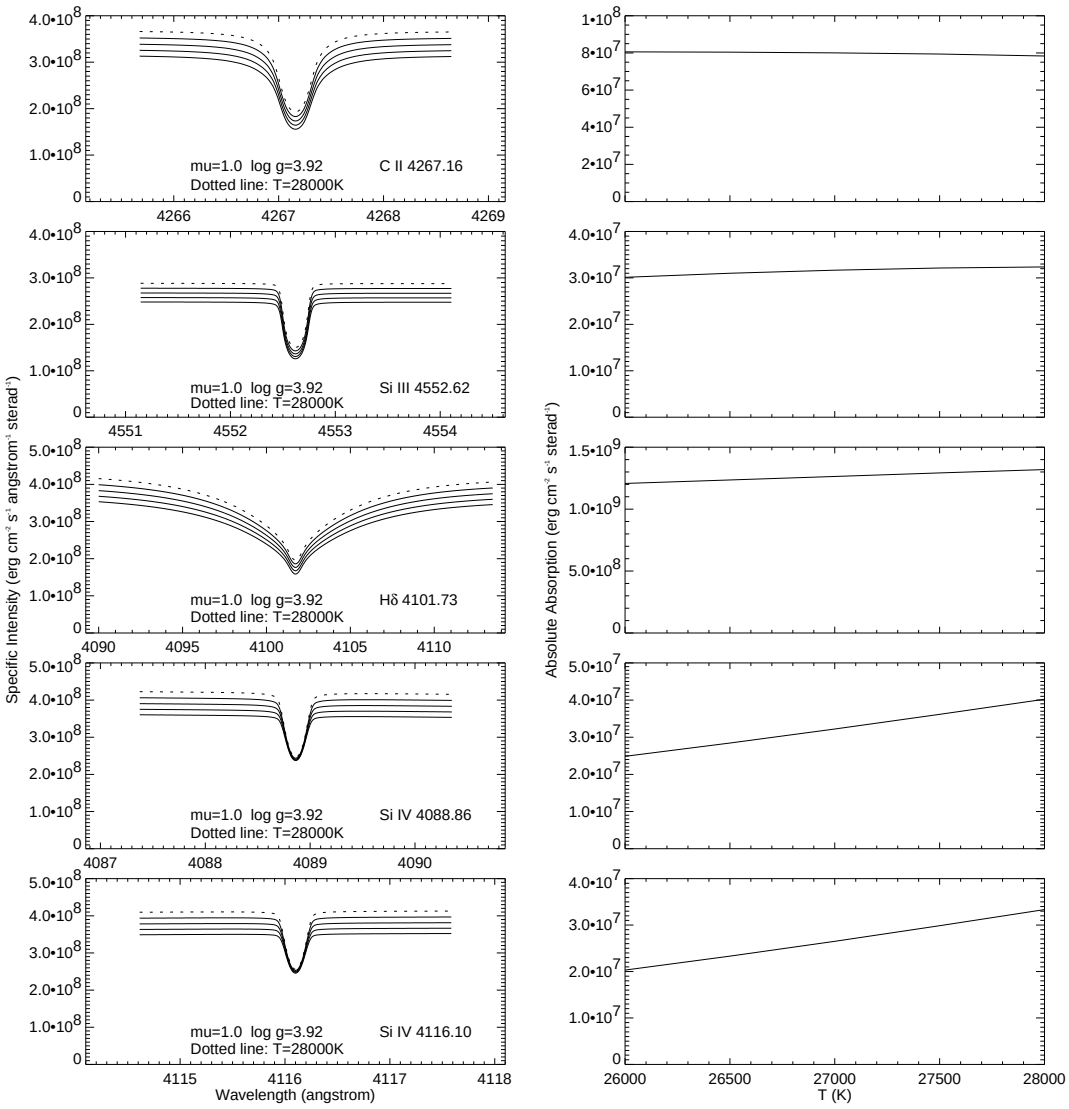

Figure 4.1: Model line profiles as a function of effective temperature. The left column shows specific intensity profiles at five temperatures (ranging from 26000 K at bottom to 28000 K at top [*dotted line*] in five panels corresponding to different lines. The right column shows the corresponding wavelength-integrated absorption strength as a function of temperature for each of the five lines.

of ϵ Per (Gies et al. 1999; De Cat et al. 2000) indicate that the NRP is dominated by one mode with degree $l = 4$, order $m = -4$, and observed period $P = 3.837$ hours, so our theoretical simulations are mainly focused on this mode. I created time sequences of models profiles for the same temporal sampling of the observations of Gies & Kullavanijaya (1988)

and then I made Fourier transforms of the line intensity time series at each wavelength point across the profile. I then isolated the Fourier amplitude and phase at both the pulsation frequency and twice the pulsation frequency (first harmonic frequency). These are plotted in a series of panels in Figure 4.2. The upper plot in each panel shows the distribution in amplitude across the line (*thick line* for the basic frequency and *thin line* for the first harmonic), while the lower plot shows the same for phase (in units of π). The five rows in Figure 4.2 correspond to the five lines I investigated, and the left column shows the results assuming no temperature variation while the right column illustrates the results with the temperature variation included (according to eq. 4.3). Note that the amplitudes have been normalized by dividing by the maximum central line depth in each case in order to inter-compare the different line results more easily.

Parameter	Model A	Model B
i (deg)	70	40
M ($M_\odot$)	14.8	14.8
$V \sin i$ (km s^{-1})	140	140
$R_{\rm polar}$ ($R_\odot$)	6.8	6.8
$R_{\rm equatorial}$ ($R_\odot$) .	7.0	7.2
$T_{\rm polar}$ (K)	27600	27600
$T_{\rm equatorial}$ (K) ..	26800	26000
$P_{\rm rotation}$ (d)	2.37	1.68

Table 4.1: Physical Parameters of ϵ Per

The amplitude plots in the case where the profile variations are caused mainly by Doppler shifts associated with NRP velocity variations (*left column* of Figure 4.2) have a rounded shape comparable to the rotational broadening function. The full span of non-zero amplitude corresponds approximately to the Doppler wavelength equivalent of 2 $V \sin i$, but note that

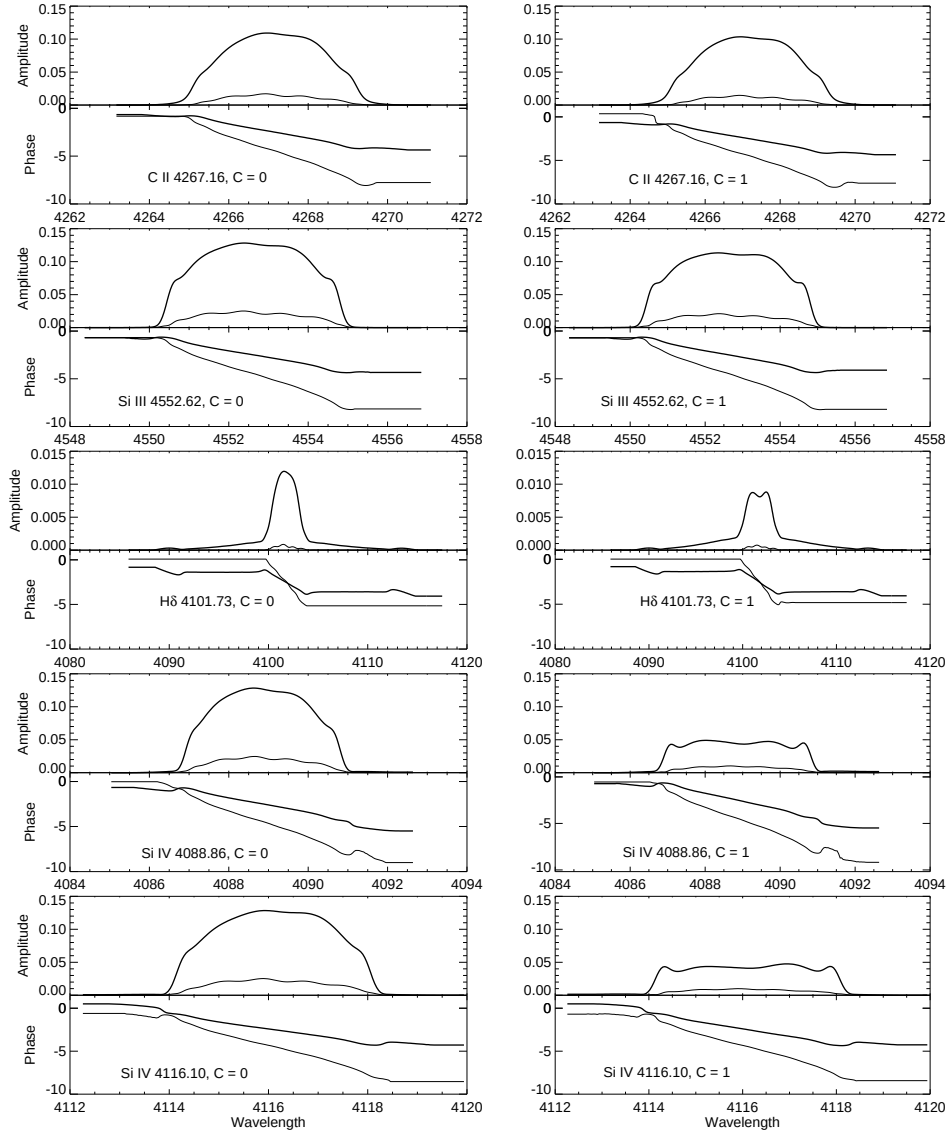

Figure 4.2: The model line profile variations for five lines, both neglecting (*left*) and including (*right*) the predicted temperature variations. The upper plot of each panel shows the distribution with wavelength across the profile of the Fourier amplitude of the line intensity variations, while the lower plot shows the variation in complex phase across the profile. Results are plotted for the basic frequency (*thick line*) and for its first harmonic (*thin line*). Amplitudes are normalized by the central depth of each line. Complex phases are expressed in unit of π. These phases extend in wavelength over the range where the amplitude is $> 5 \times 10^{-5}$, and beyond this range phases are treated as constant. The models were calculated with NRP parameters $V_{\max} = 10$ km s^{-1}, $k = 0.11$, and a non-adiabatic phase lag $\alpha = 0$.

different size wavelength intervals are plotted in each case. The amplitude in the primary frequency exceeds that in the harmonic frequency because the temporal intensity variations are almost sinusoidal in shape. The lower plots show a phase variation of approximately 2 cycles (4π) across the profile for the main frequency (and about twice that for the harmonic frequency) that corresponds to the two cycles of variation present across the visible hemisphere of the star (of the total of four cycles around the equator for this $l = -m = 4$ mode). The only striking difference between the line results based upon the NRP velocity variations alone is found for Hδ (*middle panel*). The variations in this case are spread over a much larger wavelength range because of the large intrinsic width of Hδ (caused by collisional broadening and the linear Stark effect), and consequently the normalized line intensity variations are much weaker than seen in other lines (leading to a smaller maximum amplitude in Fourier space).

The right hand column of Figure 4.2 shows the Fourier amplitudes and phases when the temperature variations from equation 4.3 are added to the model. There are no changes in the phase diagrams (since they reflect the same NRP geometry), but we see that the amplitudes have all declined by varying amounts. Lines such as C II λ4267 that are constant or decline with increasing temperature show only a modest decrease in amplitude, while lines like Si IV $\lambda\lambda 4088, 4116$ that increase in strength with temperature (Figure 4.1, right hand column) display larger amplitude reductions. These trends were also found by Schrijvers & Telting (1999) for NRP modes with small k, i.e., p-modes where the NRP velocity variations are largely vertical in direction.

We can understand why the amplitude decrease occurs by considering the relationships

between the NRP variations (velocity and temperature) and the line profile fluctuations. The $l = -m = 4$ mode in this model is a so-called sectoral mode in which the wave patterns resemble wedges cut to the spin axis. The wave patterns have nodes at both poles and attain their largest amplitude at the equator. There are 4 complete cycles of radial oscillation around the equator, and the wave patterns are moving prograde, i.e., in the direction of advancing rotation. The nodal point between radial peak and trough in the direction of rotation corresponds to the point of maximum expansion velocity, while the nodal point following the crest is the point of maximum contraction velocity. There is a one-to-one correspondence through the Doppler effect between position along the equator and wavelength position in the line profile for a rotating star, such that spectral contributions from the approaching limb appear in the blue wing, those on the star's central median appear in the line center, and those from the receding limb appear in the red wing. The NRP velocity variations redistribute the flux in the profile such that contributions from an approaching node are blue-shifted and those from a receding node are red-shifted, so that they act to strengthen the profile at a position corresponding to a radial peak.

These profile fluctuations are altered when NRP temperature variations are introduced. The coefficient in equation 4.3 is negative for the p-modes like the one we are considering, so a radial peak will correspond to a cooler zone and a radial trough to a hotter zone. The radial peak zone will now contribute less to the line profile because of the reduced flux associated with cooler temperatures, and thus, the same portion of the profile that was strengthened by the NRP velocity variations is now weakened by the temperature variation. The trend will be exacerbated in lines that also weaken in cooler gas (or strengthen with increased

temperature), so lines like the Si IV transitions are most affected by the NRP temperature variations.

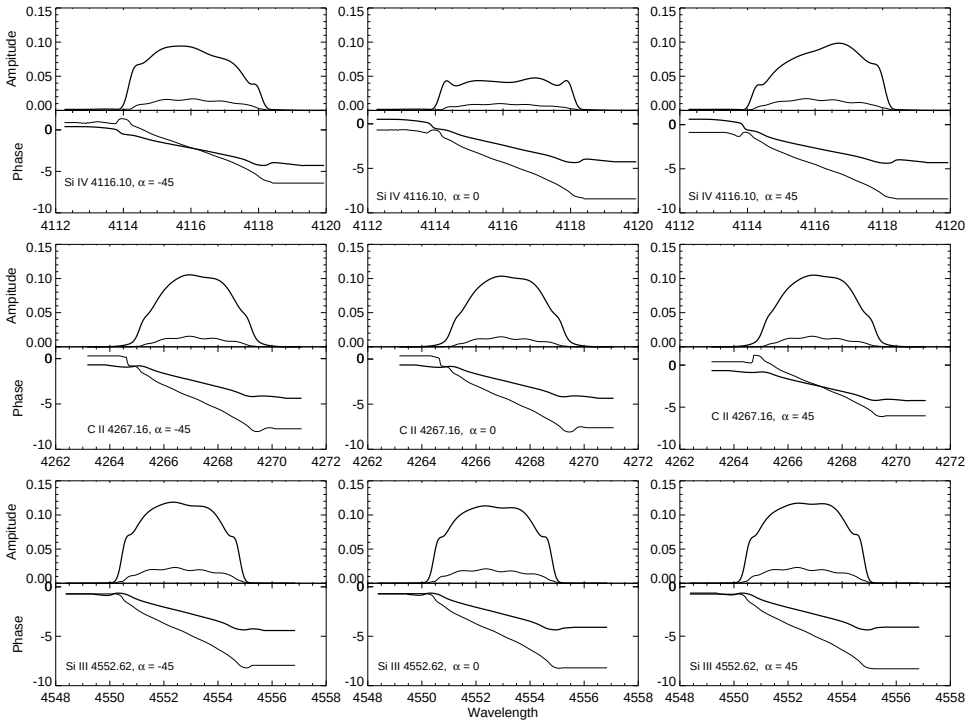

Figure 4.3: Model predictions for the LPV for three adopted values of the non-adiabatic phase lag (*left:* $\alpha = -45°$; *center:* $\alpha = 0°$; *right:* $\alpha = 45°$) and three different lines in a format similar to that of Figure 4.2. The models were calculated with NRP parameters $V_{\rm max} = 10$ km s^{-1} and $k = 0.11$, and with full consideration of temperature effects ($C = 1$).

I next consider the effects on the line profiles related to the inclusion of a non-adiabatic phase lag α in equation 4.3. We show in Figure 4.3 how the Fourier amplitudes change for phase lags of $-45°$, $0°$, and $+45°$ (in three columns) in the case of the lines Si IV λ4116, C II λ4267, and Si III λ4552 (in three rows). Once again, we see that the differences are quite subtle for lines modest temperature variations (C II, Si III), but the distribution becomes asymmetric about the line center for the Si IV line that strengthens with increasing temperature. These results generally agree with the simulations by Schrijvers & Telting

(1999). The loss of symmetry can be explained as a result of the different phase variations between LPV due to the NRP velocity field and LPV due to local temperature fluctuations across the stellar disk. For example, as the non-adiabatic phase lag shifts the hottest zone from the center of a trough to the following node where the surface is expanding, it will tend to strengthen the approaching component of velocity. Since this hot zone will have its greatest contribution to the profile when it crosses the observed central meridian, it will affect the blue side of the profile then because of the expanding NRP velocity, and the resulting Fourier amplitude will be stronger on the blue side of the profile (the sense of the asymmetry is the opposite for g-mode pulsations with $k > 1$; Schrijvers & Telting (1999)).

4.4 Multimode NRP

The models presented thus far are for a single mode, but we know that ϵ Per is a multimode pulsator (Gies et al. 1999; De Cat et al. 2000). In order to investigate how the Fourier diagnostics are affected by the presence of multimode NRP, I calculated a series of line profiles for two NRP modes for a time span of about 38 hours (about 10 times of the period of the dominant NRP mode in ϵ Per). The models used the largest amplitude mode $l = -m = 4$ considered above plus the second most important mode observed with $l = 5$, $m = -5$, and $P = 2.268$ hours. Once again I calculated the Fourier transform of the Si IV λ4116 line intensity at each wavelength point, and I show in Figure 4.4 the resulting Fourier amplitudes and phases at the primary signal frequency and its harmonic for both the single mode and multi-mode models. The differences are negligible, which indicates that, in some situations, the Fourier method can be used to investigate the NRP properties at given frequencies

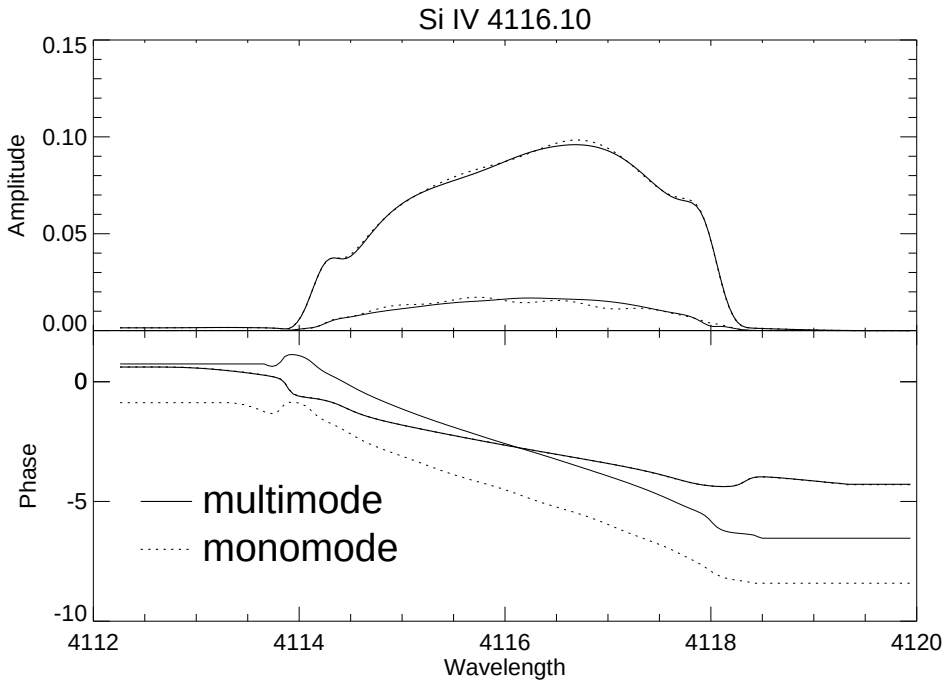

Figure 4.4: The Fourier amplitude and phase distribution across the Si IV λ4116 line in the format of Figure 4.2 for models including just one mode (*solid lines*: $l = -m = 4$, $V_{\rm max} = 10$ km s^{-1}) and two modes (*dotted lines*: $l = -m = 4$, $V_{\rm max} = 10$ km s^{-1} and $l = -m = 5$, $V_{\rm max} = 5.4$ km s^{-1}). The other model parameters are $i = 70°$ and $\alpha = 45°$. Note that phases for the primary frequency are almost identical in the one and two mode cases, and the same is true for the harmonic frequency, but in the latter case the phase curves are offset by 2π for clarity of presentation.

even in the presence of other modes. This can be easily understood mathematically. The influences from these NRP multi-modes are co–added into LPVs linearly. Thus, their Fourier transforms are little influened by each other. However, in real observations, various types of observing noise and limited and non–uniform time coverage prevent us from recovering these NRP modes in Fourier space accurately. For these cases, a full multi–mode analysis is still prefered.

I also found that the presence of multiple modes creates a much richer distribution of signals in Fourier frequency space. I plot in Figure 4.5 a gray scale image of the Fourier

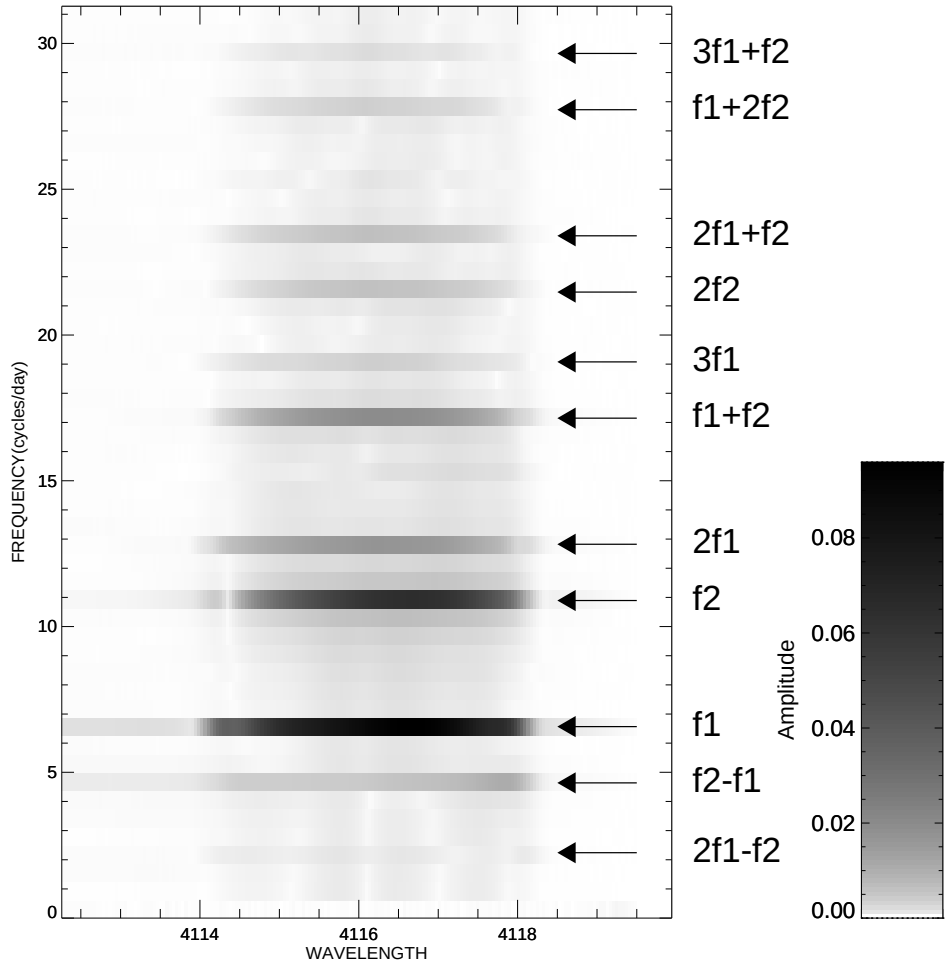

Figure 4.5: A gray scale depiction of the Fourier amplitude distribution for the two mode simulation plotted as a function of wavelength and frequency. The adopted model frequencies are $f_1 = 6.255$ cycles day^{-1} ($l = -m = 4$) and $f_2 = 10.580$ cycles day^{-1} ($l = -m = 5$), and weaker signals are found at integer combinations of these (noted at the right hand side).

amplitude as a function of wavelength across the Si IV λ4116 line and temporal frequency. We see that while the main two signal frequencies dominate, there are also many other, weaker signals present that occur at frequencies equal to a linear combination of the two basic model frequencies.

4.5 Comparison with Observations

Gies & Kullavanijaya (1988) obtained spectra of many lines during their intensive time series observations of ϵ Per, but they limited their analysis to the Si III lines. Here we will compare our model results and their observations from 1986 for the same five lines discussed above. All the profiles were first shifted to the rest frame to account for Doppler shifts from orbital motion (Tarasov et al. 1995), and then I calculated the Fourier transforms of the temporal variations of line intensity across the profile. The model synthetic profiles were constructed for the same time series as the observations, and their temporal Fourier transforms were made in the same way as for the observed profiles.

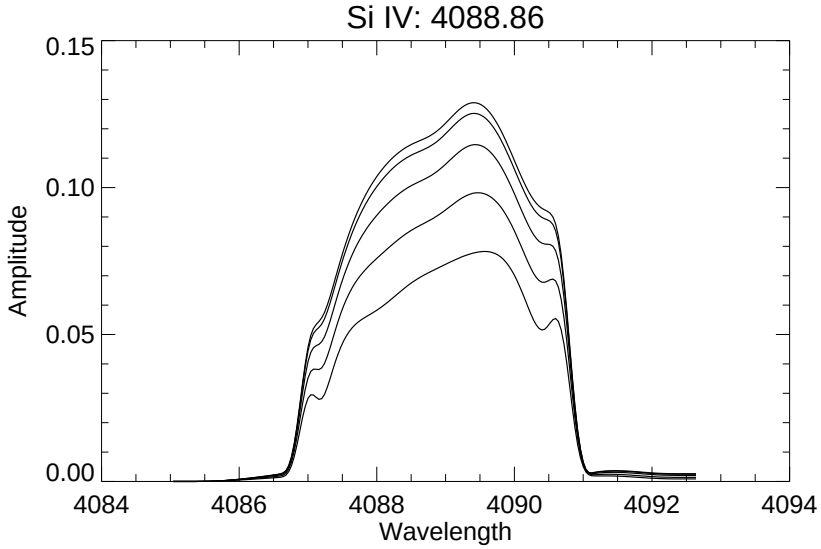

Figure 4.6: The Fourier amplitude distribution across the Si IV λ4088 line for model sequences made adopting different inclination angles (*from bottom to top:* $i = 50°$, $60°$, $70°$, $80°$, and $90°$). The other model parameters are $V_{\rm max} = 12$ km s^{-1}, $\alpha = 45°$, and $C = 1$.

Our goal is to match the observed LPV in all the lines for a unique set of NRP parameters, specifically, maximum velocity amplitude $V_{\rm max}$, temperature variation factor C,

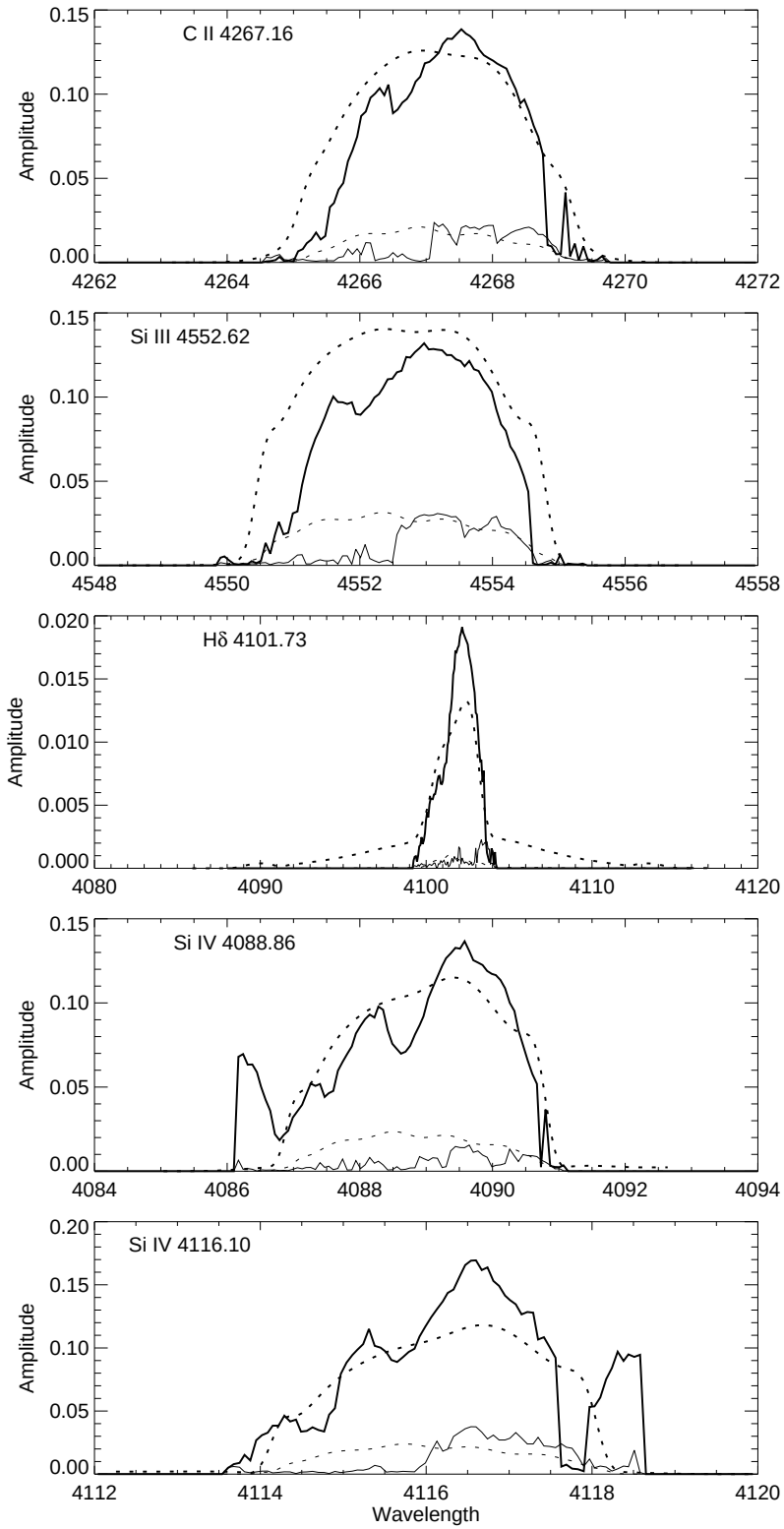

Figure 4.7: The model (*dotted line*) and observed (*solid line*) Fourier amplitude distributions for the primary (*thick*) and harmonic (*thin*) frequencies in each of the five lines discussed in the text. The parameters of NRP model A are $V_{\max} = 11$ km s^{-1}, $C = 1$, $\alpha = 45°$, and $i = 70°$.

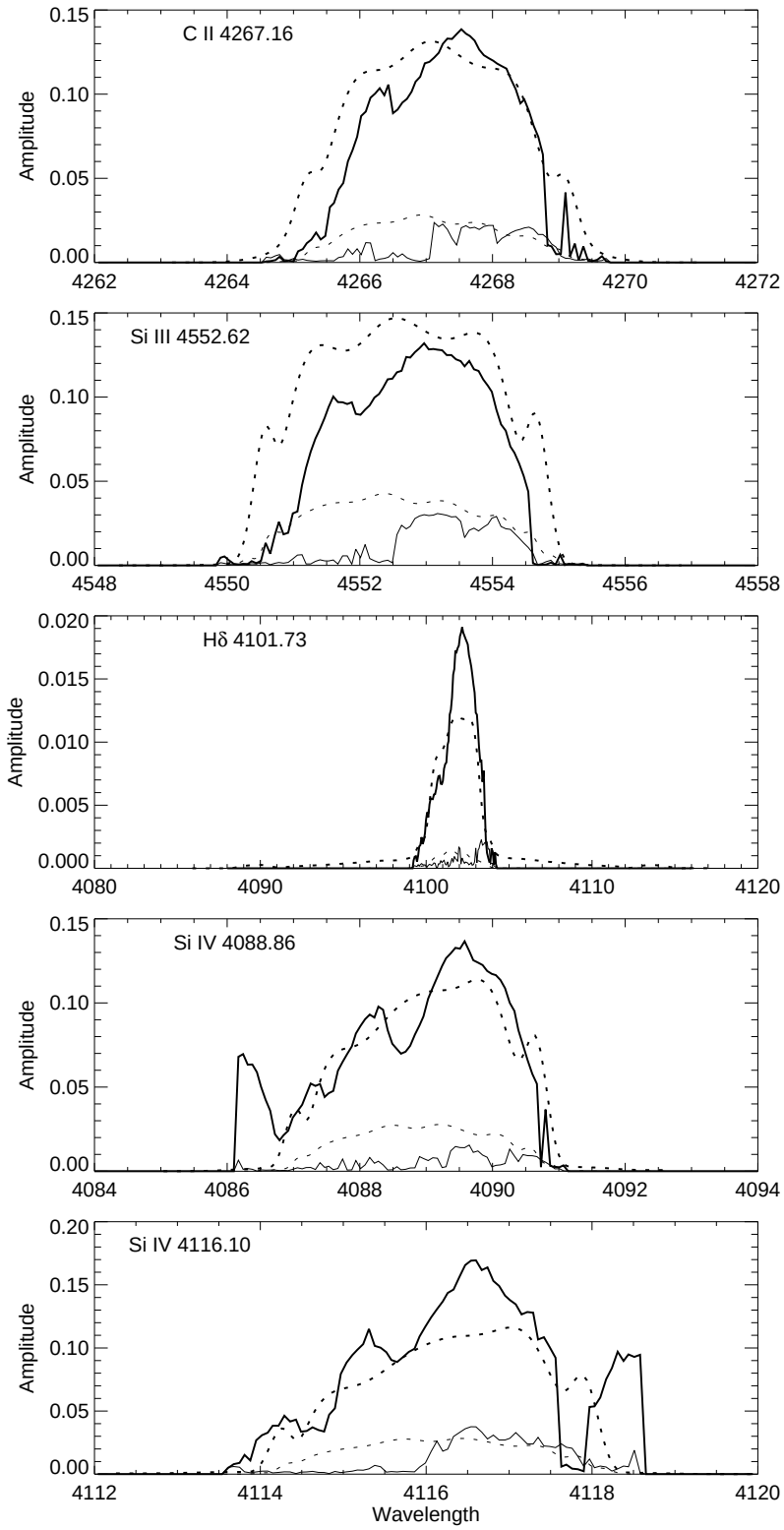

Figure 4.8: The model and observed Fourier amplitudes in the same format as Figure 4.7 for the case of the low inclination model. The NRP model B parameters are $V_{\rm max} = 24$ km s^{-1}, $C = 1$, $\alpha = 45°$, and $i = 40°$.

non-adiabatic phase lag α, and inclination angle i. I can take advantage of the results from Section 4.3 to guide our selection of these parameters. For example, the lines C II λ4267 and Si III λ4552 are not sensitive to the temperature parameters C and α, so they can be used to determine the mode amplitude $V_{\rm max}$. Once the amplitude is known, I can use the lines Si IV $\lambda\lambda 4088, 4116$ to estimate the temperature parameters C and non-adiabatic phase lag α by the relative strength and skewness, respectively, of the their Fourier amplitude distributions across the line. After I estimate $V_{\rm max}$, C and α, the last parameter that needs to be determined is inclination angle i. Since the model deals with sectoral modes that have maximum amplitude at the equator, the observed LPV amplitude will be larger the closer the inclination is to an equator-on orientation ($i = 90°$), and I show in Figure 4.6 how the observed Fourier amplitude varies with i for a fixed pulsational amplitude. However, it is not easy to obtain a unique value of i from the models in Figure 4.6, because a combination of high inclination angle i and low physical amplitude $V_{\rm max}$ can give results that appear very similar to a combination of a low i and larger $V_{\rm max}$ (with only minor differences in the amplitude distribution across the profile). The comparisons with observations of ϵ Per for two choices of inclination angle are illustrated in Figures 4.7 and 4.8. The $i = 70°$ model A shown in Figure 4.7 has a velocity amplitude of $V_{\rm max} = 11$ km s^{-1} while the $i = 40°$ model B (Figure 4.8) has a velocity amplitude of $V_{\rm max} = 24$ km s^{-1} (other parameters are listed in the captions and Table 4.1). Unfortunately, both of these representative fits make satisfactory matches of the observed Fourier representations of the LPV, so I cannot easily select between them (although we note that the low inclination model was favored by Saio et al. (2000) in order to match the rotational period with several frequency splittings between observed sig-

nals). The overall agreement between the model and observed Fourier distributions is good except in the case of Hδ (*middle panel* in Figure 4.7 and Figure 4.8), where the observed line core amplitude is stronger and the wing amplitude much weaker than predicted. This may reflect atmospheric structure changes caused by NRP that are neglected in the model and that would increase the relative importance of line formation in the upper atmospheric levels where the density is lower.

4.6 Conclusions

Our main aim in this chapter was to demonstrate how the spectral line variations observed in different line species might be used to explore the physical variations in the photosphere related to nonradial pulsations. I have used realistic model intensity profiles for these lines with a line profile synthesis code for slowly rotating stars to obtain reliable theoretical simulations of LPV in many of the optical lines that can be compared directly with the observations of pulsations in the early B-type star, ϵ Per.

I estimate that the probable amplitude of the dominant NRP mode in ϵ Per ($l = 4$, $m = -4$) is approximately $V_{\rm max} = 24$ km s^{-1} if ϵ Per has a low inclination angle of $i = 40°$ (or a smaller amplitude if the inclination is larger). This result agrees with a previous analysis by Saio et al. (2000) that was based upon ultraviolet spectroscopy. However, a more reliable estimate of $V_{\rm max}$ will require a better estimate of i and more detailed studies of the LPV in specific lines.

Our results for the most temperature sensitive lines in the optical spectrum of ϵ Per indicate that NRP related temperature fluctuations do exist in the photosphere and that

there is a phase lag between the radial and temperature variations caused by NRP. These fluctuations can influence the LPV in some spectral lines and alter the distribution of the Fourier amplitude of the line intensity variations across the profile. It is possible that the temperature phase lag results from non-adiabatic effects for the dominant mode (Cugier et al. 1994), but the temperature shifts may also reflect the results of wave leakage in the outer atmosphere (Townsend 2000).

However, there are still many features visible in observational data that are not well replicated in the synthetic models. For example, most of the lines I considered show a trough near line center in the distribution of Fourier amplitude across the line that is not present in the Fourier amplitude curves for the model sequences. Furthermore, there are a number of discrepancies peculiar to specific lines, such as a weaker than predicted amplitude for Si III λ4552 and a stronger than predicted variation in the core of Hδ. These differences may be the result of line blending problems, the need for a full non-LTE treatment of line formation in some cases, and/or other approximations made in the model (for example, the slow-rotator assumption may be poor if the inclination angle of ϵ Per is $< 40°$). Nevertheless, I regard these shortcomings as opportunities to probe more deeply into the physical origins of NRP in hot stars.

Chapter 5

Conclusions

5.1 Methodology

All the spectroscopic analysis methods used in this dissertation are based on spectrum synthesis. It is more and more clear that in order to simulate properly the stellar spectra of massive rotating stars, the spectrum synthesis calculations must be based upon realistic stellar models that include the two most important features associated with rapid rotation, a distorted shape (given by Roche geometry) and gravity darkening. Today's powerful personal computers allow us to run the synthesis codes even with a dense sampling of representative points on the stellar surface, and new model atmosphere programs offer us a very solid basis for spectrum synthesis. All these practical considerations make it possible to use the synthesis codes to create very reliable model spectra for late O- and all B-type stars.

My general procedure of spectroscopic analysis for a rotating star with an OB spectral type can be summarized in following steps:

(1) Measure $V \sin i$ by fitting the He I $\lambda\lambda 4026, 4387, 4471$ and Mg II $\lambda 4481$ lines.

(2) Use the measured $V \sin i$ and the observed Hγ profile to determine both the surface average temperature and gravity.

(3) The results from steps (1) and (2) can then be used to estimate the polar gravity of the star, and this parameter is a good indicator of stellar evolutionary status. If the spin inclination angle of a star is independently determined, then its polar gravity and evolutionary status can be accurately determined.

(4) The combination of results from above provide the basis for a realistic rotation model for the star that can be used to predict line strengths for any assumed chemical abundance, so that reliable abundance estimates can be obtained by line fits.

This procedure has proved to be very successful in analyzing the spectra of OB members of young Galactic clusters. One convenient aspect of this observational program is that all the spectral features used are nicely concentrated in a relatively narrow waveband (4000 Å–4500 Å) which can be easily recorded with a single spectrogram in most moderate dispersion spectrographs.

5.2 Stellar Physics

I present here reliable data on the stellar surface properties of more than 400 cluster OB stars, and the results make it very clear that these massive rotating stars experience a spin down during their MS phase. The lower mass stars appear to slow down more quickly than more massive stars do when considered on time scales normalized to their main sequence lifetimes. This partially confirms the theoretical predictions about evolution of stellar rotation. However, rotation theories (Meynet & Maeder 2000; Heger & Langer 2000) predict a faster spin down for more massive stars due to their larger mass loss rates (stronger stellar winds), which does not seem to be the case in our sample. The lowest mass considered in

these theoretical models is $\approx 8M_{\odot}$, and I suspect that the spin down mechanism may be more complicated in the lower mass stars of the my sample.

The surface He abundance data present a complicated picture. I find that in the high mass group ($M > 8.5M_{\odot}$), the He abundance gradually increases as stars evolve through the MS phase, and the increase seems related to stellar rotation in the sense that the more rapidly stars rotate, the more He is found in their atmosphere. This discovery agrees very well with theoretical predictions. However, I find a huge range in the measured He abundance for the low mass group (with $T_{\rm eff} < 23000$ K). A lot of helium peculiar stars (both He-strong and He-weak) are present in this group, and the large scatter in He abundance makes the search for evolutionary trends impossible. The stars of the lower mass group have two striking properties: they appear to spin down more quickly than predicted, and they include large numbers of helium peculiar stars. One possible explanation is that these stars may have strong magnetic fields that could alter the surface helium abundance and slow them down by transfer of their angular momentum to their surroundings.

I also applied spectral synthesis methods to the interferometric observations of a nearby rapidly rotating B star, Regulus. By combining the results from both spectroscopic and interferometric analyses, the shape, space orientation, mass, and surface temperature distribution of Regulus are firmly determined. For first time, the gravity darkening phenomenon is confirmed in a single-star system. The unusually high luminosity found in Regulus seems to agree with the theoretical prediction that rapidly rotating stars can become more luminous as rotationally-induced mixing brings more hydrogen down into core.

Finally, I demonstrated that the synthesis code can also be used to simulate the surface

oscillations caused by nonradial pulsation (NRP), and I compared the predicted line profile variations (LPVs) with those observed in the spectra of the variable star ϵ Per (B0.7 III) The analysis indicates that the NRPs of ϵ Per do indeed cause associated local temperature variations that are not synchronized with the radial oscillation (non-adiabatic phase lag).

5.3 Future Work

The spectrum synthesis and spectroscopic methods discussed here have led to many fruitful results in several related research areas. These examples demonstrate the power of these techniques to address many new questions in stellar astrophysics.

The methods themselves are always open to improvements. It is possible to consider numerical schemes that will converge faster to find the best fit temperature, gravity, and projected rotational velocity. There are obvious advantages to extending the methods to the hotter O-type stars and cooler A-type stars. However, work on the hotter stars will require the use of fully line-blanketed non–LTE model atmospheres for the input grid. Furthermore, grids for different line transitions will need to explored for application in these hotter and cooler temperature regimes where many of the lines examined here disappear. The abundance work could also be greatly improved by considering many other spectral lines. For example, the microturbulent velocity could be measured rather than just adopted by studying the line strengths of very strong and weak metallic lines (Gies & Lambert 1992; Gummersbach et al. 1998).

It would be very interesting to try to verify our results on stars where we have independent estimates of their radius and mass. This could be accomplished by obtaining similar

kinds of spectra of detached eclipsing binary stars for which we know masses, radii, and temperatures from studies of their orbital radial velocity and light curves. The Doppler tomography algorithm could be used to make a clean separation of the spectral features of both components, which in turn could be studied by line synthesis methods.

Many interesting objects turned up in my cluster survey, and it would be very exciting to get additional spectra to study these cases. We found several fast rotators near the TAMS, and the origin of their fast rotation is a puzzle. Were these stars spun up during the core shrinking phase as rotation theories predict or were they spun up by mass exchange in close binaries? A radial velocity program of observations on these targets could decide the issue by searching for the orbital Doppler shifts that would be present if the stars are members of close binary systems. The extreme He-strong and He-weak stars identified in the survey are almost certainly magnetic stars, and it will be important to search for the abundance anomalies in other elements that are often found in such He-peculiar stars.

The cluster survey as a whole is a large sample, but for many clusters the total number of stars is insufficient for statistical analyses. The results are naturally concentrated on the brightest stars in these young clusters, and it will be very important to pursue similar investigations of the fainter and lower mass cluster stars to test theories of spin evolution with cluster age.

The detailed studies of individual stars like Regulus and ϵ Per show that they offer many opportunities to explore the nature of rotation and pulsation in massive stars. The models for chemical mixing in rotating stars also predict changes in the CNO abundances. These metallic lines are generally weaker and become exceptionally shallow and broad in the rapidly

rotating stars, so it is very difficult to measure their abundances. However, spectrum synthesis models could accurately predict the shapes and strengths of these often blended features, and a comparison of the synthetic spectra with high S/N observations would provide an exciting test of the CNO abundances. The case of Regulus demonstrates the remarkable opportunities that exist to combine spectrum synthesis work with new interferometric observations of the angularly resolved stars. The analysis of Regulus resolved the issue of its spin inclination and gravity darkening, so that we could estimate the star's actual rotational velocity and placement in the Hertzsprung-Russell diagram. These kinds of investigations offer us the means to test for the first time the evolutionary models for rapidly rotating stars. It will be especially informative to launch new spectroscopic and interferometric programs of observations on the fastest rotating stars, in particular the Be stars. Such observations will help us solve the age old question of how close to critical rotation a star must be in order to eject gas into a circumstellar disk. This combination of spectroscopic and interferometric work will allow us to tackle questions that until now have been the stuff of dreams.

Appendix A

Programs

A.1 Spectral Line Synthesis

A.1.1 Associated Programs

The first IDL program attached here calculates the Roche geometry $x(\theta)$ $(= r(\theta)/r_p)$. I do not follow the formal solution (1.3) given in Section 1.3.1. Instead, a Newton-Raphson iterative algorithm is used in the program, which often reachs very high accuracy in just two or three iterations.

```
FUNCTION roche, accuracy, beta, stheta ; Roche Geometry

;;;;;;;;;;;;;;;;;;;;;;;;;;;;;;;;;;;;;;;;;;;;;;;;;;;;;;;;;;;;;;;;;;;;;;;;;;;
; Revised by Wenjin Huang      06/22/05
;-------------------------------------------------------------------
; This function returns the radius in a rapidly rotating star
; with a shape defined by the Roche potential.
; The returned value is given as a fractional of the polar radius.
; beta= 0.5 omega^2 rpstar^3 / ( G mass )
; stheta= sin (theta) for theta = polar angle (spherical coords.)
; A Newton-Raphson iterative method is used to solve:
;    1/x + beta * stheta^2 * x^2 - 1 = 0

a=beta*stheta*stheta
x=(1.-2.*a)/(1.-3.*a)
eps=1.
repeat begin ; Iterate for solution
   xnew=(x + (x-1.5)/(3.*a*x*x-1.))/1.5
   eps=abs(xnew-x)
   x=xnew
   endrep until (eps lt accuracy)

return,x
end
```

The second IDL program handles convolution calculations which are required when the instrumental broadening is considered (see Section 1.4).

```
PRO line_convol, wave, line, d_wave, gauss_n, gauss_a
;;;;;;;;;;;;;;;;;;;;;;;;;;;;;;;;;;;;;;;;;;;;;;;;;;;;;;;;;;;;;;;;;;;;;;;;;;;
```

```
; Written by Wenjin Huang      06/22/05
;-----------------------------------------------------------------
; line ---- the input line profile, and the output convolved profile
; wave ---- uniformly spaced wavelength grid
; d_wave ---- wave(1)-wave(0)
; gauss_n ---- 5 or bigger integer (5 is big enough for good
;              numerical accuracy)
; gauss_a ---- Gaussian f(x)~exp((x-x0)/a^2)
;-----------------------------------------------------------------

pi=3.1415926536

n=(size(wave))(1)
line_conv=fltarr(n)

if gauss_a gt 0. then begin
  ;temp=' '
  hf_n=fix(gauss_n*gauss_a/d_wave)
  full_n=2*hf_n+1

  gauss=fltarr(full_n)
  c1=1./sqrt(pi)/gauss_a
  c2=d_wave/gauss_a
  x=indgen(full_n)
  x=(x-hf_n)*(x-hf_n)*c2*c2
  gauss=c1*exp(-x)

  for iw=0, n-1 do begin
    for icn=iw-hf_n, iw+hf_n do begin
      ig=iw+hf_n-icn
      itmp=icn
      itmp=(itmp > 0)
      itmp=(itmp < (n-1))
      line_conv(iw)=line_conv(iw)+line(itmp)*gauss(ig)
      endfor
    endfor
  line=line_conv*d_wave
  endif
;plot,wave,line
;oplot,wave,line_conv
;read,' Enter to continue ',temp

return
end
```

A.1.2 Synthesis Programs

It is definitely not an exaggeration to say that this IDL program is the representative of core programs used throughout the entire work. All synthesized spectra of rotating model stars presented in this work are calculated by this or similar programs. Most of the differences of these core programs are trivial, mainly due to slightly different formats of input specific intensity data prepared from other programs.

```
PRO prof_rotation,box,line_name,star_type,inclin_org,vsini,wav,line
;;;;;;;;;;;;;;;;;;;;;;;;;;;;;;;;;;;;;;;;;;;;;;;;;;;;;;;;;;;;;;;;;;;;;;;;
; Written by Wenjin Huang      06/22/05
;---------------------------------------------------------------
; Calculate rotational-broadening line profile with Roche geometry
; and gravity darkening effect (beta = 0.25, coded in program)
; box --- box(nt, ngrav, nmupts, nwavpts), storing specific
; intensity data.
; star_type ---- program gets all stellar parameters through it
; vsini (km s^(-1))
; inclin_org ---- inclination angle in deg
; wav, line ---- output wavelength grid and line profile
; Note: if inclin_org=0, then vsini will be used as veq
;;;;;;;;;;;;;;;;;;;;;;;;;;;;;;;;;;;;;;;;;;;;;;;;;;;;;;;;;;;;;;;;;;;;;;;;

pi=3.141592654
pi_hf=pi/2.
convert=pi/180.
c=2.997925E+05  ; in km/s
rsun=695990.    ; solar radius in km
sft_factor=vsini/c

dir_startype='~/Regulus/idl/star_prm/'
name_type=' '

;*********************************************************
openr, 1, '~/Regulus/idl/synspec/'+line_name+'/trimmed/prm.dat'
readf, 1, ntemp, ngrav, nmupts, nwavpts
readf, 1, tunit, lgunit, muunit, wavgridunit
readf, 1, temp0, logg0, mu0, wav0
close, 1

delwav=0.04 ; output wavelength unit in \AA

; wavelength grid for box
boxwav=wav0+wavgridunit*indgen(nwavpts)
nwav=fix((boxwav(nwavpts-1)*(1.-sft_factor)  $
       -boxwav(0)*(1.+sft_factor))/delwav)
wav=boxwav(0)*(1.+sft_factor)+delwav*indgen(nwav)
line=fltarr(nwav)
;*********************************************************


;*********************************************************
; Parameters Related to Numerical Calculation
;*********************************************************
nsurf=40000
accur_roche=0.00001
;*********************************************************


;*********************************************************
; Determine grid points for surface integration
; Use spherical coordinates (r, theta, phi)
; Choose elements of approximately equal area
```

```
;*********************************************************
; ntheta= no. of theta points
ntheta=2*fix(sqrt(pi*nsurf)/4.+0.5)
print, ' Number of theta points = ', ntheta
; theta= array of theta points
dtheta=pi/ntheta
theta=dtheta*(indgen(ntheta)+0.5)
; Calculate sin and cos of theta
stheta=sin(theta)
ctheta=cos(theta)
ss_theta=stheta*stheta
sc_theta=stheta*ctheta
; nphi= no. of phi points (depends on theta)
nphimax=2*ntheta
print,' Number of phi points < ', nphimax
phi=fltarr(nphimax,ntheta)
nphi=fix(stheta*nphimax+0.5)
dphi=2.*pi/nphi
for it=0,ntheta-1 do begin
   for ip=0,nphi(it)-1 do phi(ip,it)=dphi(it)*(ip+0.5)
   endfor
sphi=sin(phi)
cphi=cos(phi)
ds=stheta*dtheta*dphi
;*********************************************************


;*********************************************************
; Input Basic Stellar Parameters
;*********************************************************
openr,1, dir_startype+star_type+'.dat'
readf,1,name_type
readf,1,rpstar,mass,tpeff ; rpstar, mass in solar units
close,1

const1=1.270135E+6*rpstar^3/mass
lg_fact=4.437723+alog10(mass/(rpstar*rpstar))
;*********************************************************


;*********************************************************
;*********************************************************
  inclin=convert*inclin_org
  nadir=inclin+pi_hf
  sincl=sin(inclin)
  cincl=cos(inclin)

  ; Determine radius and dr/dtheta as a function of theta
  r=fltarr(ntheta)
  xr=fltarr(ntheta)
  slp=fltarr(ntheta)

  print,' '
  print,'-------------------------------------------------------------'
  print,' V-critical = ', 356.55*sqrt(mass/rpstar), '  km/s'
```

```
; Calculate Roche geometry for a rotating star
if (inclin gt 0.) then veq=vsini/sincl else begin
  veq=vsini
  vsini=0.
  endelse

print,' i =',inclin_org,'  Vsini =',vsini,'  Veq =',veq
xeq=1./(1.-3.767392E-12*veq*veq*rsun*rpstar/mass)
requator=rpstar*xeq
print, ' R(eq.), R(pole) = ', requator, rpstar

omega=veq/rsun/requator
beta=const1*omega*omega
const2=2.*beta
const3=3.*beta

for it=0, ntheta-1 do begin
  xr(it)=roche(accur_roche,beta,stheta(it))
  r(it)=xr(it)*rpstar
  slp(it)=const2*sc_theta(it)/(1./xr(it)/xr(it)-const3*ss_theta(it))
  endfor

; Form theta constants used in determining mu
ang1=theta-atan(slp) ; angle between normal and spin axis
sang1=sin(ang1)
cang1=cos(ang1)

; find the top theta value for the integration
ang2=nadir-ang1

ittop=ntheta/2                  ; ittop always >= ntheta/2
ittop0=ittop
while (ittop lt ntheta and ang2(ittop0) gt 0. ) do begin
  ittop=ittop+1
  ittop0=(ittop < (ntheta-1))
  endwhile
ittop=ittop-1

; Rotational velocity:
vrot=omega*r*rsun*stheta

; Area element
areael=r*r*ds*sqrt(1.+slp*slp)

; Calculate the temperature as a function of theta due
; to gravity darkening.  See Collins and Harrington 1966,
; Ap J, 146, 152 (a typo on this page, corrected below),
; for derivation of g(theta).
; Assume von Zeipel law: T(theta)=T(pole) (g(theta)/g(pole))^0.25
temp=fltarr(ntheta)

gn=1./(xr*xr)-const2*xr*stheta*stheta
gn=gn*gn
gn=gn+(const2*xr*stheta*ctheta)^2
temp=tpeff*gn^0.125 ; ^(beta/2)
```

```
tmin=temp(ntheta/2)
tmax=tpeff
print,' Temperature range: ', tmin,tmax

log_g=lg_fact+.5*alog10(gn)
loggmin=log_g(ntheta/2)
loggmax=lg_fact
print,' Log (g) range: ', loggmin, loggmax

tmp_3=vrot*sincl/c ; saving time

ss=0.
avr_t=0.
avr_logg=0.

; Next loop - for each theta angle
for it=0,ittop do begin

  tf=(temp(it)-temp0)/tunit
  ti=fix(tf)
  ti=(ti > 0)
  ti=(ti < (ntemp-2))
  tf=tf-ti
  i_t=1.-tf

  lgf=(log_g(it)-logg0)/lgunit
  lgi=fix(lgf)
  lgi=(lgi > 0)
  lgi=(lgi < (ngrav-2))
  lgf=lgf-lgi
  i_lg=1.-lgf

  tmp_1=sincl*sang1(it)
  tmp_2=cincl*cang1(it)

  red_box1=i_t*(i_lg*box(*,*,ti,lgi)+lgf*box(*,*,ti,lgi+1))+  $
          tf*(i_lg*box(*,*,ti+1,lgi)+lgf*box(*,*,ti+1,lgi+1))
  for ip=0,nphi(it)-1 do begin
    mu=tmp_1*cphi(ip,it)+tmp_2
    ; if mu > 0 then surface element is visible
    if (mu gt 0.) then begin   ; Include element in integration

      ; Calculate projected surface area
      area=mu*areael(it)

      muf=(mu-mu0)/muunit
      mui=fix(muf)
      mui=(mui > 0)
      mui=(mui < (nmupts-2))
      muf=muf-mui
      i_mu=1.-muf

      red_box2=i_mu*red_box1(*,mui)+muf*red_box1(*,mui+1)

      ; Calculate Doppler shift to correct position
```

```
        wavshift=boxwav*(1.+tmp_3(it)*sphi(ip,it))

        ; calculate the contribution of the element area
        ploc=interpol(red_box2, wavshift, wav)
        line=line+ploc*area

        wgt=area*ploc(0)
        ss=ss+wgt
        avr_t=avr_t+temp(it)*wgt
        avr_logg=avr_logg+log_g(it)*wgt

        endif ; for mu > 0
      endfor ; end of phi loop
    endfor ; end of theta loop

  print, ' Average     T = ', avr_t/ss      ; flux-wighted avr
  print, ' Average Log g = ', avr_logg/ss   ; flux-wighted avr

  ; Normalize line profile to a unit continuum
  normal=line(0)+indgen(nwav)*(line(nwav-1)-line(0))/(nwav-1.)
  line=line/normal

  eqw=total(1.-line)*delwav
  print, ' E.W. = ', eqw    ; equivalent width

return
end
```

The second program is also for spectrum synthesis. It is much simplified because it is designed for the "virtual star" model only (see Section 2.4).

```
PRO virtual_star_h1, box, t, logg, vsini, wav, line, eqw
;;;;;;;;;;;;;;;;;;;;;;;;;;;;;;;;;;;;;;;;;;;;;;;;;;;;;;;;;;;;;;;;;;;;;;;;
; Written by Wenjin Huang      06/22/05
;---------------------------------------------------------------
; spectrum synthesis for a "virtual star"
; no roche geometry. no grav. darkening
; only 3 parameters for the model: t, logg, and vsini
; see section 2.4 in dissertation.
; box --- storing the intrinsic line profile data of H-gamma
; wav, line --- output line profile
;;;;;;;;;;;;;;;;;;;;;;;;;;;;;;;;;;;;;;;;;;;;;;;;;;;;;;;;;;;;;;;;;;;;;;;;

pi=3.141592654
pi_hf=pi/2.
convert=pi/180.
c=2.997925E+05  ; in km/s

sft_factor=vsini/c

ntemp=11
ngrav=10
nmupts=20
nwavpts=5941

tunit=2000.
lgunit=0.2
muunit=0.05
boxwav=4281.1+0.02*indgen(nwavpts)

temp0=10000.
logg0=2.6
mu0=0.05

delwav=0.04

nwav=fix((boxwav(nwavpts-1)*(1.-sft_factor)  $
       -boxwav(0)*(1.+sft_factor))/delwav)
wav=boxwav(0)*(1.+sft_factor)+delwav*indgen(nwav)
line=fltarr(nwav)

;lg0, lgn, accuml_n help define the data structure in 'box'
lg0=[2.6, 2.6, 2.6, 2.6, 2.6, 2.6, 2.6, 2.8, 3., 3.2, 3.4]
lgn=[10,10,10,10,10,10,10,9,8,7,6]
accuml_n=[0,10,20,30,40,50,60,70,79,87,94]

total_n=100 ;lgn(ntemp-1)+accuml_n(ntemp-1)

t_index=indgen(ntemp)
logt=alog10(temp0+tunit*t_index)
;*******************************************************
```

```
;*********************************************************
; Parameters Related to Numerical Calculation
;*********************************************************
nsurf = 20000
;*********************************************************

;*********************************************************
; Determine grid points for surface integration
; Use spherical coordinates (r, theta, phi)
; Choose elements of approximately equal area
;*********************************************************
; ntheta= no. of theta points
ntheta=2*fix(sqrt(pi*nsurf)/4.+0.5)
; print, ' Number of theta points = ', ntheta
; theta= array of theta points
dtheta=pi/ntheta
theta=dtheta*(indgen(ntheta)+0.5)
; Calculate sin and cos of theta
stheta=sin(theta)
ctheta=cos(theta)
; nphi= no. of phi points (depends on theta)
nphimax=2*ntheta
; print,' Number of phi points < ', nphimax
phi=fltarr(nphimax,ntheta)
nphi=fix(stheta*nphimax+0.5)
dphi=2.*pi/nphi
for it=0,ntheta-1 do begin
   for ip=0,nphi(it)-1 do phi(ip,it)=dphi(it)*(ip+0.5)
   endfor
sphi=sin(phi)
cphi=cos(phi)
ds=stheta*dtheta*dphi
;*********************************************************


;*********************************************************
  print,'-------------------------------------------------------------'
  print,' Vsini =',vsini, ' km/s'

  print,' Temperature: ', t
  print,' Log (g): ', logg

  log_temp=alog10(t)
  tf=interpol(t_index,logt,log_temp) ; (t-temp0)/tunit -- linear interpolation
  ti=fix(tf)
  ti=(ti > 0)
  ti=(ti < (ntemp-2))
  tf=tf-ti
  i_t=1.-tf

  lgf0=(logg-lg0(ti))/lgunit
  lgi=fix(lgf0)
  lgi=(lgi > 0)
  lgi=(lgi < (lgn(ti)-2))
  lgf0=lgf0-lgi
```

```
i_lg0=1.-lgf0

t0g0=accuml_n(ti)+lgi
t0g1=t0g0+1

lgf1=(logg-lg0(ti+1))/lgunit
lgi=fix(lgf1)
lgi=(lgi > 0)
lgi=(lgi < (lgn(ti+1)-2))
lgf1=lgf1-lgi
i_lg1=1.-lgf1

t1g0=accuml_n(ti+1)+lgi
t1g1=t1g0+1

a_t0g0=i_t*i_lg0
a_t0g1=i_t*lgf0
a_t1g0=tf*i_lg1
a_t1g1=tf*lgf1

red_box1=a_t0g0*box(*,*,t0g0)+a_t0g1*box(*,*,t0g1)+ $
  a_t1g0*box(*,*,t1g0)+a_t1g1*box(*,*,t1g1)

; Next loop - for each theta angle
for it=0, ntheta-1 do begin

  tmp_3=sft_factor*stheta(it)

  for ip=0,nphi(it)-1 do begin
    mu=stheta(it)*cphi(ip,it)
    ; if mu > 0 then surface element is visible
    if (mu gt 0.) then begin   ; Include element in integration

      ; Calculate projected surface area
      area=mu*ds(it)

      muf=(mu-mu0)/muunit
      mui=fix(muf)
      mui=(mui > 0)
      mui=(mui < (nmupts-2))
      muf=muf-mui
      i_mu=1.-muf

      red_box2=i_mu*red_box1(*,mui)+muf*red_box1(*,mui+1)

      ; Calculate Doppler shift to correct position
      wavshift=boxwav*(1.+tmp_3*sphi(ip,it))

      ; calculate the contribution of the element area
      ploc=interpol(red_box2, wavshift, wav)
      line=line+ploc*area

      endif ; for mu > 0
    endfor ; end of phi loop
  endfor ; end of theta loop
```

```
  ; Normalize line profile to a unit continuum
  normal=line(0)+indgen(nwav)*(line(nwav-1)-line(0))/(nwav-1.)
  line=line/normal

  eqw=total(1.-line)*delwav
  print, ' E.W. = ', eqw
return
end
```

A.2 Interferometric Related Programs

A.2.1 Make Images

The first program generates a uniform disk (UD) image with an ellipsoidal shape. The input parameter (the minor axis) and the size of the output image are given in solar radius to ensure that the output images are compatible with the visibility computing code in Appendix A.2.2

```
PRO make_elp, rpstar,ratio, ra,fpic
;;;;;;;;;;;;;;;;;;;;;;;;;;;;;;;;;;;;;;;;;;;;;;;;;;;;;;;;;;;;;;;;;;;;;;;;
; Written by Wenjin Huang      06/22/05
;-----------------------------------------------------------------
; This Program make Uniform Disk (UD) Image with elliptical or
; circular shape.
; rpstar --- minor axis
; ratio ---- major axis/minor axis
; ra ------- the position angle of the minor axis
;            from north trough east in degrees
; fpic ----- output image, a 2D array with a default size 513X513
;            (resol=512 in the program). the true size of the output
;            image is coded by r_range = 1.6*rpstar in program
;;;;;;;;;;;;;;;;;;;;;;;;;;;;;;;;;;;;;;;;;;;;;;;;;;;;;;;;;;;;;;;;;;;;;;;;

pi=3.14159265
re=rpstar*ratio

resol=513
center=fix(resol/2.)
x=long(indgen(resol)-center)
y=x
x2=x^2
y2=y^2
ra=ra*pi/180.
fpic=fltarr(resol,resol)

;*************************************************************
r_range=1.6*rpstar
px_size=r_range*2./resol
;*************************************************************

for i=0,resol-1 do begin
  for j=0, resol-1 do begin
```

```
    r=sqrt(x2(i)+y2(j))*px_size
    theta=atan(y(j),x(i))-ra
    r0=re*rpstar/sqrt((rpstar*cos(theta))^2+(re*sin(theta))^2)
    fpic(i,j)=0
    if r le r0 then fpic(i,j)=255
    endfor
  endfor

tvscl,fpic

return
end
```

The second program prepares a projected disk image of a phyisical model of a rotating star at a given wavelength, which is defined by the input specific intensity data.

```
PRO star_image, box, mass, rpstar, tpeff, vsini, inclin_org, bt, fpic
;;;;;;;;;;;;;;;;;;;;;;;;;;;;;;;;;;;;;;;;;;;;;;;;;;;;;;;;;;;;;;;;;;;;;;;;
; Written by Wenjin Huang      06/22/05
;-------------------------------------------------------------------
; box --- box(t_n, lg_n, mu_n), 3D array storing specific intensity
;         data
; mass, rpstar, tpeff ---- stellar mass, polar radius (in solar units)
;                          and polar temperature (K)
; vsini (km s^(-1))
; inclin_org ---- inclination angle in degree
; bt ---- gravity darkening exponent, for ex. bt=0.25 for radiative
;         envelope
; fpic ---- output image, a 2D array with a default size 513X513
;           (resol+1=513 in the program). The true size of the output
;           image is coded by r_range = 1.6*rpstar in program
;;;;;;;;;;;;;;;;;;;;;;;;;;;;;;;;;;;;;;;;;;;;;;;;;;;;;;;;;;;;;;;;;;;;;;;;

pi=3.141592654
pi_hf=pi/2.
convert=pi/180.
c=2.997925E+05  ; in km/s
rsun=695990.    ; solar radius in km

resol=512.

;---------------------------------
; Following based on box
t_n=8
lg_n=10
mu_n=20

t_unit=2000.
lg_unit=0.2
mu_unit=0.05

t_grid=8000.+t_unit*indgen(t_n)
lg_grid=2.6+lg_unit*indgen(lg_n)
mu_grid=mu_unit*indgen(mu_n)+0.05
```

```
;---------------------------------

red_box=fltarr(mu_n)

print,'-------------------------------------------------------------'
print,' V-critical = ', 356.55*sqrt(mass/rpstar), '  km/s'

;*********************************************************
; Parameters Related to Numerical Calculation
;*********************************************************
nsurf = 20000
accur_roche = 0.00001
;*********************************************************

;*********************************************************
; Determine grid points for surface integration
; Use spherical coordinates (r, theta, phi)
; Choose elements of approximately equal area
;*********************************************************
; ntheta= no. of theta points
ntheta=2*fix(sqrt(pi*nsurf)/4.+0.5)
print, ' Number of theta points = ', ntheta
; theta= array of theta points
dtheta=pi/ntheta
theta=dtheta*(indgen(ntheta)+0.5)
; Calculate sin and cos of theta
stheta=sin(theta)
ctheta=cos(theta)
ss_theta=stheta*stheta
sc_theta=stheta*ctheta
; nphi= no. of phi points (depends on theta)
nphimax=2*ntheta
print,' Number of phi points < ', nphimax
phi=fltarr(nphimax,ntheta)
nphi=fix(stheta*nphimax+0.5)
dphi=2.*pi/nphi
for it=0,ntheta-1 do begin
   for ip=0,nphi(it)-1 do phi(ip,it)=dphi(it)*(ip+0.5)
   endfor
sphi=sin(phi)
cphi=cos(phi)
ds=stheta*dtheta*dphi
;*********************************************************


;*********************************************************
; Pre-calculated constants
;*********************************************************
const1=1.270135E+6*rpstar^3/mass ; const1=Rp^3/(2GM)
lg_fact=4.437723+alog10(mass/(rpstar*rpstar))
;*********************************************************

;*********************************************************
r_range=1.6*rpstar ; real size of the output image
px_size=r_range*2./resol
```

```
;***********************************************************

;***********************************************************
; Read Vsini and Inclination Angles in a Task File, which
; is only for the stellar type refered to "star_type" and
; the spetral line located by "cwav"
;***********************************************************
  inclin=convert*inclin_org
  nadir=inclin+pi_hf
  sincl=sin(inclin)
  cincl=cos(inclin)

  ; Determine radius and dr/dtheta as a function of theta
  r=fltarr(ntheta)
  xr=fltarr(ntheta)
  slp=fltarr(ntheta)

  print,'-------------------------------------------------------------'
  ; Calculate Roche geometry for a rotating star
  if (inclin gt 0.) then veq=vsini/sincl else $
    read, ' Inclination angle is 0, please input Veq: ', veq
  print,' i =',inclin_org,'  Vsini =',vsini,'  Veq =',veq
  xeq=1./(1.-3.767392E-12*veq*veq*rsun*rpstar/mass)
  requator=rpstar*xeq
  print, ' R(eq.), R(pole) = ', requator, rpstar

  omega=veq/rsun/requator
  beta=const1*omega*omega
  const2=2.*beta
  const3=3.*beta

  for it=0, ntheta-1 do begin
    xr(it)=roche(accur_roche,beta,stheta(it))
    r(it)=xr(it)*rpstar
    slp(it)=const2*sc_theta(it)/(1./xr(it)/xr(it)-const3*ss_theta(it))
    endfor

  ; Form theta constants used in determining mu
  ang1=theta-atan(slp)
  sang1=sin(ang1)
  cang1=cos(ang1)

  ; find the top theta value for the integration
  ang2=nadir-ang1

  ittop=ntheta/2                  ; ittop always >= ntheta/2
  ittop0=ittop
  while (ittop lt ntheta and ang2(ittop0) gt 0. ) do begin
    ittop=ittop+1
    ittop0=(ittop < (ntheta-1))
    endwhile
  ittop=ittop-1
  print, ' Rx, Ry (Steller Disk) = ', requator, r(ittop)

  ; Rotational velocity:
```

```
vrot=omega*r*rsun*stheta

; Area element
areael=r*r*ds*sqrt(1.+slp*slp)

; Calculate the temperature as a function of theta due
; to gravity darkening. See Collins and Harrington 1966
; Ap J, 146, 152 (a typo on this page, corrected below)
; for derivation of g(theta).
; Assume von Zeipol law: T(theta)=T(pole)*(g(theta)/g(pole))^0.25

temp=fltarr(ntheta)

gn=1./(xr*xr)-const2*xr*stheta*stheta
gn=gn*gn
gn=gn+(const2*xr*stheta*ctheta)^2
temp=tpeff*gn^(bt/2) ;0.125
tmin=temp(ntheta/2)
tmax=tpeff
print,' Temperature range: ', tmin, tmax

log_g=lg_fact+0.5*alog10(gn)
loggmin=log_g(ntheta/2)
loggmax=lg_fact
print,' Log(g) range: ', loggmin, loggmax

tmp_3=vrot*sincl

iproj=-1
xproj=fltarr(fix(0.6*nsurf))
yproj=fltarr(fix(0.6*nsurf))
fproj=fltarr(fix(0.6*nsurf))

ss=0.
t_avr=0.
lgg_avr=0.
total_f=0.

for it=0,ittop do begin
  tf=(temp(it)-t_grid(0))/t_unit
  ti=fix(tf)
  ti=(ti > 0)
  ti=(ti < (t_n-2))
  tf=tf-ti
  i_t=1.-tf

  lgf=(log_g(it)-lg_grid(0))/lg_unit
  lgi=fix(lgf)
  lgi=(lgi > 0)
  lgi=(lgi < (lg_n-2))
  lgf=lgf-lgi
  i_lg=1.-lgf

  red_box(*)=i_t*(i_lg*box(ti,lgi,*)       $
                  +lgf*box(ti,lgi+1,*))    $
```

```
              +tf*(i_lg*box(ti+1,lgi,*)     $
                   +lgf*box(ti+1,lgi+1,*))

    tmp_1=sincl*sang1(it)
    tmp_2=cincl*cang1(it)

    for ip=0,nphi(it)-1 do begin
      mu=tmp_1*cphi(ip,it)+tmp_2
      ; if mu > 0 then surface element is visible
      if (mu gt 0.) then begin   ; Include element in integration
        area=mu*areael(it)

        iproj=iproj+1
        xproj(iproj)=r(it)*stheta(it)*sphi(ip,it)
        yproj(iproj)=r(it)*(ctheta(it)*sincl-stheta(it)*cphi(ip,it)*cincl)

        fproj(iproj)=interpol(red_box,mu_grid,mu)

        ss=ss+area
        total_f=total_f+fproj(iproj)*area
        t_avr=t_avr+temp(it)*area
        lgg_avr=lgg_avr+log_g(it)*area

        endif ; for mu > 0
      endfor ; end of phi loop
    endfor ; end of theta loop

  print, ' Average T = ', t_avr/ss, ' K'
  print, ' Average log g = ', lgg_avr/ss
  print,'------------------------------------------------------------'

  xproj=xproj(0:iproj)
  yproj=yproj(0:iproj)
  fproj=fproj(0:iproj)

  f_max=max(fproj)
  triangulate, xproj, yproj, tr

  lowleft=-r_range
  upright=r_range-px_size

  fpic=trigrid(xproj,yproj,fproj,tr,[px_size,px_size],  $
    [lowleft,lowleft,upright,upright])

  tvscl,fpic

return
end
```

A.2.2 2D Fourier Transformation (Not FFT)

This program takes a input image created by the programs listed in Appendix A.2.1 and generates its visibility distribution in the *uv* plane (i.e. Fourier space).

```
PRO vis,fq_range_factor,img_size,prl,wavelength,fpic,bproj,vs
;;;;;;;;;;;;;;;;;;;;;;;;;;;;;;;;;;;;;;;;;;;;;;;;;;;;;;;;;;;;;;;;;;;;;;;;
; Written by Wenjin Huang      06/22/05
;-------------------------------------------------------------------
; fq_range_factor: control the output range, 2-3 is good for start
; img_size ----- the size of input image in solar redius
; prl ---------- parallax in milliarcseconds
; wavelength --- in Angstroms
; fpic --------- the input image (2D array)
; bproj -------- in meters, output
; vs ----------- normalized visibility in uv plane
;;;;;;;;;;;;;;;;;;;;;;;;;;;;;;;;;;;;;;;;;;;;;;;;;;;;;;;;;;;;;;;;;;;;;;;;
pi=3.141592654

m=301 ; output size
n=(size(fpic))(1) ; input size
work1=fltarr(n)
work2=fltarr(n)
vs=fltarr(2*m-1,m)
re_vs=vs
im_vs=vs

bproj_unit=4.43358*fq_range_factor*wavelength/(m-1.)/img_size/prl
bproj=bproj_unit*indgen(m)
n_100=max(where(bproj le 100.))+1

dtheta=2.*pi/(m-1.)/(n-1.)*fq_range_factor
x=indgen(n)*dtheta

cos_vl=fltarr(n,2*m-1)
sin_vl=fltarr(n,2*m-1)
for i=0,2*m-2 do begin
  cos_vl(*,i)=cos(x*(i-m+1))
  sin_vl(*,i)=sin(x*(i-m+1))
  endfor

; 2d integration
for i=0, 2*m-2 do begin
  for k=0,n-1 do begin
    work1(k)=total(fpic(*,k)*cos_vl(*,i))
    work2(k)=total(fpic(*,k)*sin_vl(*,i))
    endfor    ;k
  for j=0, m-1 do begin
    re_vs(i,j)=total(work1(*)*cos_vl(*,m-1+j)) $
      -total(work2(*)*sin_vl(*,m-1+j))
    im_vs(i,j)=total(work2(*)*cos_vl(*,m-1+j))      $
      +total(work1(*)*sin_vl(*,m-1+j))
    endfor ;j
  endfor ;i

vs=sqrt(re_vs*re_vs+im_vs*im_vs)
vs=vs/max(vs)

vs0=fix(vs^0.5*255)
vs0(30:(29+n_100),m-51)=255
```

```
vs0(30,(m-51):(m-46))=255
vs0((29+n_100),(m-51):(m-46))=255

tv, vs0

return
end
```

Appendix B

Data Tables

B.1 $V \sin i$ Measurements

Table: Projected Rotational Velocities of B Stars in 19 open clusters

Byte-by-byte Description of file:

Bytes	Format	Units	Label	Explanations
1- 7	A		Name of cluster	
8- 13	I6	---	WEBDA index	Id of stars at http://obswww.unige.ch/web
14- 19	I6	km/s	vsini	Derived projected rotational velocity
20- 24	I5	km/s	dvsini	RMS of residuals of vsini (1)
25- 32	F8.1	km/s	Vr(N1)	Radial velocity of first night(2)
33- 40	F8.1	km/s	Vr(N2)	Radial velocity of second night if available
41- 48	F8.1	km/s	Vr(N3)	Radial velocity of third night if available
49- 55	F7.1	---	Spectral type	Index number of estimated spectral type(3)
56-	A	---	Notes	

Note (1): here "..." means that there is no RMS calculation available

Note (2): The HJD of each night for clusters

	HJD(N1)	HJD(N2)	HJD(N3)
Ber86	2451862.642	2451864.584	...
IC1805	2451861.825	2451863.820	...
IC2395	2451950.677	2451952.586	...
IC2944	2451949.873	2451951.752	2451952.845
NGC457	2451862.722	2451864.755	...
NGC869	2451861.686	2451863.734	...
NGC884	2451862.828	2451864.824	...
NGC1502	2451862.973	2451864.928	...
NGC2244	2451861.950	2451863.938	2451865.007
NGC2362	2451949.558	2451951.563	...
NGC2384	2451949.615	2451951.613	...
NGC2422	2451862.030	2451864.017	...
NGC2467	2451949.683	2451952.538	...
NGC3293	2451950.744	2451952.637	...
NGC4755	2451951.850	2451952.793	...
NGC6193	2451951.894	2451952.882	...
NGC7160	2451861.606	2451864.657	...
TR14	2451950.861	...	...
TR16	2451949.774	...	...

Note (3): The index table for subspectral types is

0 -- O95V, 1 -- O98V

```
          2  -- B0V,   3  -- B03V,  4  -- B05V, 5  -- B1V
          6  -- B15V   7  -- B2V,   8  -- B25V, 9  -- B3V
          10 -- B35V,  11 -- B4V,   12 -- B45V, 13 -- B5V
          14 -- B55V,  15 -- B6V,   16 -- B65V, 17 -- B7V
          18 -- B75V,  19 -- B8V,   20 -- B85V, 21 -- B9V
================================================================================

Ber86       1   184    1    30.3    30.8     ...    1.3
Ber86       3   192    9   -24.6     7.5     ...    4.0   SB2
Ber86       4   178   10    17.2    45.2     ...    1.0   SB2
Ber86       9   362    3    -7.6   -15.7     ...    3.3
Ber86      12   309   23    -6.8     8.0     ...   10.0
Ber86      13   182   28    49.9    48.3     ...    0.7
Ber86      14   133    5  -131.7  -142.5     ...    1.3   SB2
Ber86      15    23    8   -13.9   -15.8     ...    5.0
Ber86      17    79    4   -41.4   -43.2     ...    2.0
Ber86      30   103   15    -7.7    -7.7     ...    6.3
Ber86      34   241    4     4.1    20.7     ...    3.0   strong em. at H1 4340
Ber86     149   181    9   -17.7   -48.9     ...    2.7   SB1
Ber86     214   276    3   -10.5    -9.8     ...   11.0
Ber86     235   325   13   -25.1   -23.1     ...    4.7
Ber86     261   251    1   -22.2   -25.7     ...    5.7
Ber86     288   184    7   -12.1   -11.8     ...    8.0
Ber86     291    87    7   -16.8   -15.3     ...    7.0
IC1805     72   266   23   -62.7   -58.8     ...    8.0
IC1805     82   191    5     4.4   -41.4     ...    4.3   SB1, He I LP varying a bit
                                                          night to night
IC1805    103   179    4    55.8   -52.8     ...    2.0   SB2
IC1805    111   160   11    -1.1   -98.2     ...    4.3   SB1
IC1805    113   218   18   -20.2   -12.5     ...    0.3   strong em. at H1 4340. P Cyg.
                                                          He I profiles
IC1805    118    18    3   -66.0   -41.3     ...    2.0
IC1805    121    61    8   -27.5   -15.0     ...    3.0
IC1805    130   133   10   -32.3   -60.9     ...    9.0   SB1
IC1805    143   320    3   -53.8   -59.9     ...    3.0
IC1805    149    86   14   -21.9   -39.7     ...    4.0
IC1805    157    51   18    -8.3   -10.3     ...   10.3
IC1805    158   162    5   -69.9   -41.3     ...    4.0
IC1805    161   178    4   -81.6   -51.6     ...    2.3
IC1805    166   107    9   -67.9   -60.8     ...    5.0
IC1805    167   247   24    -0.1   -54.1     ...    6.0   SB1
IC1805    169    76   10   -60.4   -48.7     ...    5.0
IC1805    174   190    5    23.7   -10.7     ...    9.0   SB1
IC1805    188    28    5   -51.1   -40.0     ...    7.0
IC1805    260   102   13   -45.6   -23.4     ...    6.0   SB2? unusual LP
IC1805    277   156    6   -19.3   -53.7     ...    9.0   SB1 (SB2?)
IC1805    288   204    3   -41.9   -58.5     ...    4.0
IC1805   1309   172    2   -32.9   -38.5     ...    4.0
IC1805   1329    68    5   -14.7   -48.4     ...   13.0   SB1
IC1805   1406   295   17   -37.7   -46.1     ...   11.0
IC1805   1433    26    2   -30.0    -7.8     ...   16.0
IC1805   1824   289   14     0.1   -50.1     ...    3.0   SB1
IC1805   1924   229   17   -30.9   -18.3     ...    4.0
IC1805   1930    35   22   -31.6   -40.0     ...    8.7
IC1805   1939    41   15   -38.6   -32.9     ...    5.0
```

IC1805	1984	47	1	-49.2	-40.9	...	5.0	
IC2395	2	247	17	23.1	97.5	...	11.0	SB1 (SB2?)
IC2395	4	97	31	-14.1	-9.5	...	10.7	Mg II 4481 disappeared in one spectrum
IC2395	6	169	6	36.9	29.3	...	4.0	
IC2395	7	136	15	20.2	29.7	...	10.3	
IC2395	9	105	1	-0.5	17.8	...	17.0	
IC2395	10	91	5	23.6	31.9	...	2.0	
IC2395	14	49	...	13.4	18.8	...	20.0	
IC2395	15	79	...	20.1	22.8	...	20.0	
IC2395	16	146	...	-1.3	2.7	...	20.0	
IC2395	21	108	19	48.0	20.0	...	14.0	SB1
IC2395	55	50	39	28.5	24.1	...	12.7	
IC2395	56	20	1	14.2	11.5	...	4.0	
IC2395	57	249	11	10.0	11.0	...	13.3	
IC2395	67	60	50	13.4	44.4	...	17.0	
IC2395	219	115	22	8.8	32.6	...	15.0	
IC2395	...	24	...	9.4	37.5	...	19.0	GSC 081550286 08:40:47.39 -48:01:40.3 (2000.0)
IC2944	5	135	6	-4.1	12.9	4.7	9.0	
IC2944	13	63	9	-20.3	-7.5	-18.3	4.0	
IC2944	14	31	26	1.2	-1.6	0.8	1.7	
IC2944	16	214	13	-8.8	-4.8	-9.5	3.0	
IC2944	19	82	10	-3.9	-3.8	-4.3	1.3	
IC2944	20	149	11	-20.6	-14.5	-18.3	2.3	
IC2944	...	231	23	-60.5	51.8	-9.0	10.7	SB1, CD-62 549C, 11:38:09.2 -63:12:00 (2000.0), weak emission at H1 4340
IC2944	23	179	21	-13.4	-19.3	-17.5	1.3	
IC2944	25	133	12	4.2	-16.9	6.8	12.5	weak emission at H1 4340? varying night to night
IC2944	27	52	5	-14.1	-32.7	-14.9	17.0	
IC2944	29	84	7	-14.6	-7.5	-17.8	3.0	
IC2944	33	0	1	-17.3	-6.0	-10.9	2.0	
IC2944	34	70	12	-3.4	2.0	14.2	5.0	
IC2944	36	196	6	21.9	-13.4	-17.6	1.3	SB1
IC2944	41	251	16	-15.8	-68.4	-36.2	11.3	SB1, weak emission at H1 4340
IC2944	48	225	8	-13.5	-7.5	-10.9	3.0	
IC2944	71	153	6	-6.1	-6.8	6.1	13.0	very weak emission at H1 4340
IC2944	83	285	46	-115.6	-15.7	-14.4	13.7	SB1, narrow and deep absorp. at H1_4340
IC2944	88	122	16	-13.9	-27.7	-27.1	4.7	
IC2944	90	195	6	2.8	-4.7	-0.0	9.0	
IC2944	91	187	1	-21.0	-9.4	-14.9	2.0	
IC2944	93	92	5	-19.0	-11.6	-10.9	14.0	
IC2944	96	55	23	-18.0	-20.3	-16.0	3.0	
IC2944	98	1	1	-12.8	-3.8	-10.8	2.0	
IC2944	102	93	13	-37.6	-28.1	-20.5	13.3	
IC2944	105	86	25	-20.3	-15.6	-13.5	1.5	
IC2944	106	99	...	-36.2	-20.1	-18.8	9.0	
IC2944	109	79	9	6.1	1.4	2.7	3.0	
IC2944	110	181	10	-14.3	-40.8	-12.7	12.7	very weak emission at H1 4340
IC2944	112	316	18	-19.7	-1.0	3.2	9.0	emission at H1 4340
IC2944	115	311	20	-27.9	-94.0	-13.5	10.5	SB1, emission at H1 4340
IC2944	119	118	8	-22.4	-33.2	-22.4	2.5	very weak emission at H1 4340
IC2944	120	22	5	-12.2	-11.5	-11.5	4.0	
IC2944	122	271	1	-25.0	-7.3	-13.5	3.0	very weak emission at H1 4340

IC2944	134	198	13	3.7	13.2	-14.1	2.7	
IC2944	178	155	8	-22.3	-27.8	-18.9	2.0	
IC2944	...	28	12	-4.7	-7.4	-5.4	12.0	HD 308805, 11:39:26.103 -63:07:32.01 (2000.0), strong emission at H1 4340
IC2944	...	32	1	10.2	-2.0	0.7	9.0	11:37:43.20 -63:13:07.40 (2000.0)
NGC457	19	15	2	19.1	-58.6	...	9.3	SB1
NGC457	33	103	4	-37.3	-28.9	...	3.7	
NGC457	37	103	4	64.6	-117.6	...	2.0	SB1
NGC457	43	389	7	18.3	-32.9	...	8.0	SB1
NGC457	54	129	1	-34.4	-59.5	...	3.0	SB2?
NGC457	85	159	1	-19.0	-144.1	...	1.0	SB2?
NGC457	109	78	...	5.4	-30.8	...	20.0	
NGC457	120	22	4	-25.1	-31.6	...	3.3	
NGC457	128	204	10	-34.1	-32.5	...	10.0	
NGC457	129	99	8	-10.5	-79.7	...	12.0	SB1
NGC457	135	113	9	-22.2	-33.8	...	8.3	
NGC457	140	165	5	-68.2	-60.6	...	17.0	
NGC457	143	279	16	31.5	6.6	...	15.0	
NGC457	149	242	8	-17.7	-27.3	...	9.0	
NGC457	151	58	5	-88.0	22.2	...	9.7	SB1
NGC457	153	173	14	-11.8	-29.3	...	0.7	strong double peak em. at H1 4340, H-gamma almost disappears
NGC457	174	49	18	-24.9	-33.2	...	17.0	SB2?
NGC457	198	182	4	-43.9	-29.4	...	9.3	
NGC457	215	292	15	3.6	-33.5	...	5.0	
NGC869	49	200	21	-42.3	-39.6	...	1.0	strong double line em. at H1 4340, He I P Cyg. prof.
NGC869	63	153	2	19.3	-40.5	...	3.0	SB1
NGC869	90	31	4	-61.3	-51.2	...	3.3	
NGC869	133	327	5	-80.0	-44.6	...	1.0	SB1
NGC869	260	163	7	-58.1	-44.0	...	1.0	
NGC869	289	47	9	-51.9	-31.3	...	7.0	
NGC869	323	5	5	-71.9	-18.5	...	8.0	SB1
NGC869	339	47	2	-19.6	-16.2	...	2.3	
NGC869	350	152	5	-58.4	-41.5	...	5.0	
NGC869	487	110	1	-9.7	-37.4	...	5.0	
NGC869	496	31	11	19.2	28.3	...	2.0	SB2
NGC869	517	168	28	-29.6	-35.7	...	9.3	
NGC869	530	51	13	-90.4	-61.9	...	3.0	SB1
NGC869	551	228	1	-72.9	-43.3	...	5.0	SB1
NGC869	566	295	4	-4.3	-61.5	...	1.0	SB1
NGC869	572	80	6	-13.4	-29.3	...	5.0	
NGC869	590	120	5	-51.6	-35.3	...	4.0	
NGC869	622	45	8	-56.9	-41.4	...	5.0	
NGC869	670	96	5	-35.7	-45.2	...	5.0	
NGC869	678	67	4	-59.5	-47.5	...	3.0	
NGC869	717	69	11	2.5	-29.3	...	2.7	
NGC869	731	163	4	6.4	-58.3	...	4.0	SB1
NGC869	748	276	4	6.1	-16.8	...	15.0	
NGC869	768	9	6	-61.8	-56.4	...	7.7	
NGC869	782	27	4	-68.7	-43.3	...	3.0	
NGC869	789	185	10	-8.0	-31.7	...	3.0	strange LP
NGC869	803	248	7	-31.7	-56.0	...	2.0	
NGC869	834	110	13	-8.8	-4.2	...	3.7	
NGC869	839	27	5	-90.2	-27.5	...	4.0	SB1

NGC869	843	100	2	-2.9	-37.7	...	3.0	SB1
NGC869	847	66	8	-31.9	-37.6	...	2.0	
NGC869	864	144	19	-26.4	-52.2	...	2.3	strange LP
NGC869	922	267	4	-66.2	-56.5	...	1.0	
NGC869	980	24	4	-52.0	-47.9	...	4.0	
NGC869	1015	45	...	-12.7	-5.2	...	17.0	
NGC869	1067	32	8	-65.3	-37.7	...	3.7	SB1
NGC869	1078	196	11	-36.0	-53.0	...	2.0	
NGC869	1085	70	4	-40.0	-64.3	...	3.7	
NGC869	1116	118	3	-36.6	-44.4	...	2.3	
NGC869	1141	226	10	-56.8	-52.2	...	9.0	
NGC869	1196	123	3	-42.4	-39.6	...	4.0	
NGC869	1226	54	2	-40.5	-38.3	...	5.0	
NGC869	1252	21	9	-24.0	-51.2	...	9.0	
NGC869	1261	308	62	-8.8	-28.8	...	0.0	extremely strong double peak em. at H1 4340, He I P Cyg. prof.
NGC869	1268	131	1	-32.9	-49.7	...	2.3	
NGC869	1352	146	3	4.7	-32.6	...	4.0	SB1
NGC869	1364	212	9	-62.3	-49.3	...	3.0	
NGC869	1387	47	15	-64.6	-54.4	...	5.0	
NGC869	1391	153	2	-15.7	-45.6	...	3.7	
NGC869	1439	40	8	-4.6	-50.8	...	5.0	SB1
NGC869	1516	153	6	29.9	103.7	...	3.0	SB2
NGC869	1539	12	2	7.5	-59.1	...	7.0	SB1
NGC869	1566	136	1	-14.3	-47.6	...	5.0	
NGC869	1586	236	1	-33.6	-49.7	...	9.3	
NGC869	1590	34	25	-44.1	-46.0	...	6.7	
NGC884	1702	87	9	-78.1	-37.6	...	0.3	SB1, strong emission at H1 4340 (double peaks)
NGC884	1770	221	3	-31.7	-37.7	...	4.7	
NGC884	1772	191	24	-79.5	-80.7	...	10.0	unusual He I LP, narrow and deep absorp. at H1 4340
NGC884	1873	168	4	-73.5	-19.0	...	5.0	SB1
NGC884	1901	69	3	-61.0	-46.0	...	2.3	
NGC884	1924	58	1	-5.6	-56.3	...	3.3	SB1
NGC884	1926	102	13	-11.4	-47.0	...	0.5	SB1, very strong emission at H1 4340
NGC884	1960	96	4	-0.4	-39.6	...	5.0	SB1
NGC884	1983	56	9	-31.7	-44.7	...	5.0	
NGC884	2014	272	3	-1.9	-42.8	...	4.7	SB1
NGC884	2048	125	5	-40.1	-53.6	...	6.0	
NGC884	2049	380	3	-7.3	-13.2	...	0.7	
NGC884	2051	20	1	-51.7	-42.3	...	7.0	
NGC884	2085	269	3	-47.4	-36.8	...	5.0	
NGC884	2088	169	15	-38.5	-38.1	...	0.7	SB1, unusual He LP, double emission peaks at H1 4340
NGC884	2091	229	12	14.2	-89.4	...	9.7	SB1
NGC884	2112	73	5	-53.9	-49.8	...	4.0	
NGC884	2138	94	...	-39.6	-36.9	...	0.0	weak He lines, unusual weak H1 4340 (emission?)
NGC884	2139	136	4	-43.7	-40.9	...	5.3	
NGC884	2140	164	1	-54.8	-65.9	...	10.5	
NGC884	2165	79	13	-48.9	-41.4	...	2.3	emission at H1 4340
NGC884	2185	194	1	-52.7	-51.6	...	3.0	
NGC884	2190	304	4	-53.4	-52.8	...	2.0	
NGC884	2191	269	11	-36.7	-50.4	...	5.0	

NGC884	2232	111	7	-41.0	-42.8	...	5.3	
NGC884	2255	318	5	-51.1	-42.1	...	8.0	
NGC884	2299	115	1	-58.6	-38.5	...	2.3	
NGC884	2336	171	11	-108.0	-45.1	...	3.0	SB1
NGC884	2392	54	4	-7.5	-35.9	...	5.0	
NGC884	2402	141	6	-47.9	-43.7	...	1.0	
NGC884	2433	44	10	-20.6	-18.0	...	4.3	
NGC884	2444	144	5	-89.8	-86.9	...	2.0	
NGC884	2468	182	...	-58.1	-41.7	...	19.0	
NGC884	2488	131	3	-51.1	-48.0	...	3.0	
NGC884	2513	52	9	-16.3	-45.2	...	4.7	
NGC884	2540	244	5	-16.3	-44.7	...	4.0	
NGC884	2541	67	6	-3.7	-45.1	...	3.0	SB1
NGC884	2563	275	3	-8.3	-38.6	...	1.0	strong double peak emission at H1 4340
NGC884	2601	78	8	-59.6	-43.3	...	3.3	
NGC884	2603	89	5	16.8	-16.3	...	7.0	
NGC884	2605	17	4	-23.6	-40.4	...	2.3	
NGC884	2612	69	2	-31.2	-37.3	...	6.0	
NGC884	2622	360	4	-12.8	-45.4	...	4.0	He lines->fast rotation, H1 4340-> slow rotation
NGC884	2628	150	1	-6.6	-16.3	...	16.0	SB2
NGC884	2656	34	3	-42.8	-41.4	...	7.0	
NGC884	2716	181	3	-4.8	-49.0	...	4.7	SB1
NGC884	2729	247	3	-57.4	-39.1	...	16.0	
NGC884	2731	165	2	-24.2	-46.6	...	4.3	
NGC884	2759	187	12	-13.4	-30.9	...	0.0	strong emission at H1 4340
NGC884	2794	79	4	-26.4	-40.0	...	3.0	
NGC884	2809	36	9	-66.9	-22.9	...	4.0	SB1
NGC884	2826	221	7	-37.5	-39.5	...	6.0	
NGC884	2837	183	5	-5.3	-47.2	...	5.0	SB1
NGC884	2851	65	15	61.7	-26.6	...	4.0	SB2
NGC884	2907	228	6	20.4	13.2	...	12.0	
NGC884	2910	23	1	12.6	-74.4	...	2.3	SB1
NGC884	2949	168	1	-38.1	-36.8	...	5.0	
NGC1502	7	54	20	-65.9	-36.6	...	16.3	
NGC1502	10	123	6	3.3	-8.2	...	7.0	
NGC1502	12	169	1	-33.9	-9.2	...	4.0	
NGC1502	16	124	8	-11.2	-6.3	...	16.0	
NGC1502	23	149	4	-18.6	4.3	...	9.0	
NGC1502	26	174	4	27.4	-7.1	...	3.7	SB1
NGC1502	30	128	3	-14.9	-7.4	...	4.0	
NGC1502	33	180	30	-10.7	-32.8	...	14.0	SB1
NGC1502	37	37	6	1.4	14.3	...	4.0	
NGC1502	40	195	1	-21.4	-5.6	...	8.0	
NGC1502	43	203	2	92.2	-8.3	...	9.0	SB1
NGC1502	44	69	22	-32.2	-13.6	...	13.0	
NGC1502	49	195	3	-14.0	-4.3	...	7.0	
NGC1502	61	307	17	70.1	-8.4	...	5.0	SB1
NGC1502	70	142	8	-4.7	-11.8	...	18.0	2 nights different, SB2?
NGC1502	74	332	...	-70.0	-67.0	...	17.0	
NGC1502	78	296	10	36.1	-7.2	...	8.0	SB1
NGC1502	1233	212	6	-17.6	-9.7	...	9.0	
NGC2244	59	67	12	48.5	5.4	18.2	19.5	SB1
NGC2244	62	11	4	94.2	79.8	107.0	7.0	
NGC2244	80	247	10	90.9	36.2	81.4	9.0	SB1

NGC2244	88	43	16	-9.6	-17.2	-13.5	18.0	
NGC2244	116	302	...	34.9	30.8	25.5	16.0	
NGC2244	119	4	7	21.5	62.5	72.0	12.7	SB1
NGC2244	123	175	5	42.1	33.1	36.4	9.0	
NGC2244	128	187	3	108.2	33.1	110.4	4.0	SB1
NGC2244	130	77	5	37.9	35.3	25.2	7.3	
NGC2244	133	183	5	36.8	7.4	-8.0	16.0	SB1
NGC2244	167	119	2	51.2	33.5	41.4	7.0	
NGC2244	172	260	7	24.9	32.0	29.3	5.3	
NGC2244	192	70	6	17.0	47.1	51.7	14.5	
NGC2244	193	66	12	43.8	27.0	36.8	7.0	
NGC2244	194	343	9	90.5	33.5	95.5	1.0	SB1
NGC2244	201	25	6	103.9	31.6	112.7	3.7	SB1
NGC2244	206	305	7	25.8	30.7	23.5	10.0	
NGC2244	231	165	20	23.9	37.2	52.1	17.0	
NGC2244	241	214	22	33.0	61.3	36.5	17.0	unusual He I LP
NGC2244	253	167	2	27.1	35.5	-0.2	10.0	
NGC2244	260	198	8	16.3	10.7	33.1	17.0	very weak em. at H1 4340
NGC2244	274	71	13	34.5	35.9	35.0	12.0	
NGC2244	298	134	...	70.0	14.9	26.8	19.0	SB1
NGC2244	319	286	12	118.0	63.2	36.3	13.5	SB1, very narrow and deep absorp. at the cen. of H1 4340
NGC2244	331	298	3	51.9	71.1	38.4	15.0	
NGC2244	337	321	13	24.9	21.2	24.9	15.0	very weak em. at H1 4340
NGC2244	345	227	15	74.8	3.5	34.3	14.0	SB1
NGC2244	353	222	3	33.6	40.5	35.0	3.7	
NGC2244	376	26	4	50.4	34.4	53.1	2.0	
NGC2244	391	349	12	11.3	32.7	26.5	1.0	
NGC2244	392	136	4	38.6	59.0	50.2	6.0	
NGC2244	1006	165	7	82.8	44.1	102.0	10.7	SB1, unusual He I LP, very strong em. at H1 4340
NGC2244	1034	3	4	78.2	15.3	87.8	14.0	SB1
NGC2244	1134	257	5	14.4	41.3	42.9	14.0	unusual He I LP, similar to #241
NGC2244	1147	256	3	31.4	34.5	32.0	4.0	
NGC2244	1209	40	10	60.7	4.2	74.5	20.0	SB1
NGC2244	1254	282	1	64.4	25.4	63.2	14.0	SB1
NGC2244	1259	170	25	37.8	17.3	44.4	18.0	
NGC2244	1262	108	2	110.7	44.3	118.7	14.0	SB1
NGC2244	1607	136	14	54.5	103.8	37.7	3.0	SB2
NGC2244	1616	192	8	34.4	40.5	39.5	15.0	
NGC2362	1	310	28	41.5	37.5	...	13.0	
NGC2362	2	126	3	33.4	29.1	...	15.0	
NGC2362	3	173	...	-10.7	-10.7	...	18.0	
NGC2362	5	107	8	28.8	29.8	...	11.0	
NGC2362	12	229	13	29.9	29.3	...	8.7	
NGC2362	14	101	9	43.1	38.9	...	7.0	
NGC2362	20	50	34	37.5	33.3	...	6.3	
NGC2362	25	72	27	46.8	31.8	...	19.5	
NGC2362	26	201	17	27.6	25.2	...	10.0	
NGC2362	27	87	7	25.8	30.1	...	4.7	
NGC2362	31	157	6	27.3	30.3	...	5.7	
NGC2362	34	197	25	-57.4	-37.6	...	11.0	
NGC2362	39	73	16	27.8	31.5	...	7.0	
NGC2362	42	135	3	-1.6	27.3	...	17.0	
NGC2362	48	193	15	42.6	40.8	...	5.0	

NGC2362	56	247	30	-133.5	-86.1	...	17.0	SB1
NGC2362	67	293	4	41.3	45.6	...	5.0	
NGC2362	68	95	11	31.8	31.1	...	6.0	
NGC2362	69	224	5	33.3	32.8	...	5.0	
NGC2362	73	93	6	40.5	26.0	...	19.0	
NGC2362	76	213	23	38.5	33.9	...	10.7	
NGC2362	...	47	22	40.8	42.2	...	8.7	CD-24 5190, 07:19:20.82 -24:41:15.1 (2000.0)
NGC2362	...	189	6	-24.4	13.4	...	16.0	SB1, 7:18:56.11 -24:43:38.10 (2000.0)
NGC2362	...	35	29	15.1	17.5	...	10.3	CD-24 5189 07:19:15.08 -25:05:48.8 (2000.0)
NGC2362	...	216	...	56.3	18.8	...	15.0	SB1, 7:19:52.28 -24:57:29.50 (2000.0)
NGC2362	...	187	...	5.4	0.0	...	19.0	7:18:48.86 -25:12:41.70 (2000.0)
NGC2362	...	199	...	12.1	38.9	...	19.0	7:19:43.99 -24:51:35.80 (2000.0)
NGC2362	...	245	29	20.2	-33.6	...	14.0	SB1,GSC 0654102724,07:18:41.56 -25:08:50.7 (2000.0)
NGC2384	3	9	9	37.9	12.9	...	11.5	spectrum very noisy, vsini not reliable
NGC2384	4	105	11	56.3	102.2	...	2.0	SB1
NGC2384	5	70	23	43.2	43.3	...	0.0	
NGC2384	12	66	61	61.5	55.2	...	11.0	
NGC2384	17	7	6	45.0	34.3	...	3.3	
NGC2384	23	77	3	55.4	47.8	...	3.3	
NGC2384	37	11	11	51.6	51.5	...	5.0	
NGC2384	44	157	1	44.1	41.4	...	3.3	
NGC2384	62	151	8	67.2	53.2	...	4.3	
NGC2384	77	262	10	50.9	48.2	...	10.0	
NGC2384	88	99	31	52.1	52.8	...	14.0	
NGC2384	102	31	...	14.8	13.4	...	19.0	
NGC2384	126	36	37	53.5	55.5	...	10.0	
NGC2384	160	25	35	37.1	35.4	...	13.0	
NGC2384	...	260	...	5.4	2.7	...	14.0	7:25:28.08 -21:01:34.60 (2000.0), H1 4340 very weak
NGC2422	32	113	17	40.1	-13.8	...	18.0	SB1
NGC2422	42	44	3	27.0	37.2	...	15.0	weak em. at H1 4340
NGC2422	65	107	...	32.8	32.8	...	18.0	
NGC2422	67	241	6	44.1	30.2	...	15.0	
NGC2422	70	181	2	-4.3	24.2	...	19.0	
NGC2422	77	220	...	23.8	41.4	...	18.0	
NGC2422	78	108	7	26.1	36.8	...	18.0	
NGC2422	89	94	7	19.1	31.8	...	18.5	
NGC2422	123	3	3	29.4	34.0	...	13.0	
NGC2422	125	205	1	74.8	61.1	...	15.0	
NGC2422	180	316	...	29.0	42.4	...	15.0	
NGC2422	...	244	8	69.6	43.0	...	8.7	SB1, HD 60855, double peak at cen. of H1 4340, He I with P Cyg. profile
NGC2422	...	9	6	-1.0	23.3	...	14.3	7 36 36.34 -14 27 40.4 (J2000.0)
NGC2422	...	176	2	29.9	43.3	...	15.0	HD 61017
NGC2422	...	73	4	12.6	30.2	...	14.0	HD 60997/8
NGC2467	2	77	...	25.5	22.8	...	19.0	
NGC2467	15	191	...	-7.2	-6.9	...	20.0	
NGC2467	16	113	1	15.1	11.8	...	19.0	
NGC2467	21	163	4	44.0	54.8	...	5.0	
NGC2467	30	163	30	36.4	72.9	...	12.0	SB1
NGC2467	33	111	8	38.9	61.7	...	17.0	
NGC2467	39	173	24	61.2	62.2	...	10.7	weak emission at H1 4340

NGC2467	43	195	7	91.1	87.8	...	1.3	
NGC2467	47	31	23	22.0	29.2	...	16.0	
NGC2467	54	319	6	62.7	67.0	...	10.0	narrow and deep absorp. at H1 4340
NGC2467	59	228	29	75.7	73.5	...	12.0	narrow and deep absorp. at H1 4340
NGC2467	61	166	12	27.1	29.5	...	16.0	
NGC2467	65	136	13	43.2	105.6	...	2.3	SB1
NGC2467	...	23	16	57.1	54.0	...	13.3	CD-26 5020, 07:52:48.2 -26:29:37 (2000.0)
NGC3293	5	102	13	-20.2	-71.1	...	1.7	SB1
NGC3293	7	116	...	-6.7	-1.3	...	3.0	
NGC3293	8	32	37	-23.4	-20.0	...	2.0	
NGC3293	9	141	1	-27.1	-21.1	...	3.0	
NGC3293	10	107	15	-19.6	-25.8	...	2.7	
NGC3293	13	28	13	-6.1	-7.5	...	4.0	
NGC3293	14	113	3	-30.8	-18.3	...	2.7	
NGC3293	16	18	5	-33.2	-15.6	...	3.0	
NGC3293	19	294	14	-53.5	-22.2	...	1.0	emission at H1 4340
NGC3293	20	73	3	-25.7	-19.6	...	2.5	
NGC3293	25	186	14	-22.1	-24.2	...	1.0	
NGC3293	27	61	1	-40.6	-21.6	...	3.0	
NGC3293	28	358	7	-38.5	-46.9	...	1.0	
NGC3293	29	359	5	-25.7	-23.8	...	2.5	
NGC3293	65	230	1	-33.1	-33.2	...	2.5	
NGC3293	79	361	3	-17.5	-2.7	...	1.0	
NGC3293	83	320	...	-29.5	-61.7	...	10.0	SB1
NGC3293	85	265	4	-27.8	-26.4	...	3.5	
NGC3293	89	80	6	-18.3	-11.4	...	5.0	
NGC3293	92	56	15	-0.7	4.8	...	3.5	
NGC3293	117	279	...	24.1	21.5	...	11.0	emission at H1 4340
NGC3293	299	376	25	-47.5	-58.9	...	9.0	emission at H1 4340
NGC3293	534	262	7	-44.0	-24.9	...	0.7	emission at H1 4340
NGC4755	5	39	4	-23.7	-26.4	...	10.0	
NGC4755	6	87	1	-29.8	-27.1	...	3.0	
NGC4755	7	23	5	-31.1	-25.7	...	3.0	
NGC4755	10	150	1	-22.3	-21.0	...	5.0	
NGC4755	106	6	6	-25.8	-25.7	...	10.0	very narrow H1 4340, giant?
NGC4755	115	117	4	-16.9	-23.1	...	5.5	
NGC4755	122	64	7	-29.1	-23.0	...	13.0	
NGC4755	129	216	...	-21.5	-53.6	...	18.0	SB1
NGC4755	136	190	9	-11.3	-37.1	...	12.0	
NGC4755	137	178	...	-42.9	0.0	...	16.0	SB1
NGC4755	139	371	1	-44.7	-27.9	...	3.0	
NGC4755	150	150	...	-10.7	-16.1	...	19.0	
NGC4755	152	136	24	-32.4	-18.3	...	12.0	He I LP varying greatly night to night
NGC4755	157	55	9	-38.6	-35.9	...	5.0	
NGC4755	202	278	10	-21.0	-11.6	...	3.0	
NGC4755	209	89	1	-29.8	-29.1	...	9.0	
NGC4755	210	298	3	-33.1	-29.1	...	4.0	
NGC4755	238	67	7	-25.1	-21.7	...	8.0	
NGC4755	270	33	1	-36.5	-37.9	...	3.0	
NGC4755	332	107	10	-136.8	-14.9	...	10.0	SB2
NGC4755	403	158	...	-56.3	-56.3	...	17.0	noisy, emission at H1 4340? not reliable
NGC4755	408	260	22	-31.8	-40.0	...	2.0	
NGC4755	414	26	26	-27.8	-28.4	...	10.0	
NGC4755	418	208	8	-49.4	-31.1	...	3.0	

NGC4755	433	157	6	-29.8	-28.5	...	11.0	
NGC4755	449	19	8	-23.7	-23.7	...	7.0	
NGC4755	452	120	4	-19.6	-21.0	...	5.0	
NGC4755	462	221	1	-42.0	-37.3	...	2.0	
NGC4755	1309	212	6	-31.1	-29.7	...	4.0	
NGC4755	1621	279	5	-0.5	-10.0	...	1.0	strong emission at H1 4340
NGC4755	1804	109	17	-37.2	-38.0	...	14.0	
NGC4755	3312	219	...	-24.1	-10.7	...	14.0	
NGC4755	3602	15	5	-31.1	-21.7	...	12.0	
NGC6193	...	64	6	-10.1	-18.9	...	8.0	at 16:41:11.02 -48:46:55.60, the closest star: GSC 08333-01215?
NGC6193	4	8	8	-32.5	-31.8	...	8.5	
NGC6193	6	296	8	-33.5	-42.0	...	7.0	
NGC6193	8	61	11	-5.4	-8.1	...	4.0	
NGC6193	16	74	9	-24.4	-16.9	...	8.0	
NGC6193	17	83	36	-29.1	-26.4	...	7.0	Extremely strong He I lines
NGC6193	18	129	6	-49.4	-13.5	...	8.0	
NGC6193	20	226	...	-2.7	-52.3	...	10.0	SB1
NGC6193	21	320	...	-69.7	-30.8	...	10.0	
NGC6193	25	274	16	-38.9	-30.4	...	8.7	
NGC6193	26	175	15	-86.7	46.1	...	9.0	SB1 (SB2?)
NGC6193	27	89	1	-19.0	-15.6	...	8.0	
NGC6193	1175	132	...	-2.7	5.4	...	19.0	
NGC6193	1291	63	8	-43.3	-20.3	...	8.0	
NGC6193	1614	148	...	-20.1	-20.1	...	19.0	
NGC6193	1620	259	7	-78.7	-17.2	...	15.0	SB1
NGC6193	1648	305	32	-37.1	-15.4	...	6.3	
NGC6193	1695	138	8	-53.5	-56.2	...	9.0	
NGC6193	1696	216	28	-9.7	-40.5	...	9.0	SB1
NGC6193	1702	30	11	-36.5	-18.9	...	8.0	
NGC7160	3	94	7	6.1	2.4	...	4.0	
NGC7160	4	143	2	-41.0	-15.7	...	6.0	
NGC7160	5	219	5	-30.2	-27.9	...	7.0	
NGC7160	7	66	9	18.6	-25.6	...	14.0	SB1, unusual He I LP (SB2?)
NGC7160	9	225	7	28.9	-28.1	...	13.0	SB1
NGC7160	13	191	...	-44.9	-27.1	...	15.0	
NGC7160	18	203	...	-31.2	-68.6	...	18.5	SB1
NGC7160	32	120	2	-30.2	-16.2	...	12.0	
NGC7160	424	83	...	-20.1	-30.8	...	20.0	
NGC7160	436	282	...	62.1	-37.2	...	17.0	SB1
NGC7160	513	100	9	-20.4	-21.9	...	11.5	
NGC7160	529	145	...	-1.6	-19.4	...	18.0	
NGC7160	741	316	10	-50.6	-24.4	...	13.0	
NGC7160	903	282	8	-6.3	-27.0	...	9.0	
NGC7160	940	312	...	-5.5	-11.2	...	15.0	
NGC7160	955	148	11	-12.5	-18.6	...	9.3	
TR14	29	78	-1	-10.9	...	...	11.0	very strong emission at H1_4340
TR14	118	207	4	-19.6	...	...	5.5	strong emission at H1_4340
TR14	149	73	25	2.0	...	...	10.5	emission at H1_4340
TR14	...	149	7	21.7	...	...	9.0	10:44:17.91 -59:25:20.70 (2000.0), emission at H1_4340
TR14	1200	9	9	-3.4	...	...	12.0	very stron emission at H1_4340
TR16	2	228	18	-28.2	...	...	1.7	emission at H1 4340
TR16	3	21	19	-15.9	...	...	1.3	
TR16	4	96	13	-21.5	...	...	3.0	

TR16	5	349	1	-31.4	...	...	1.0	emission at H1 4340, weak emission at He lines
TR16	9	93	18	13.5	...	...	1.3	
TR16	10	152	7	-15.7	...	...	2.0	weak emission at H1 4340
TR16	11	292	14	-50.3	...	...	2.7	strong emission at H1 4340
TR16	12	55	26	-12.1	...	...	4.0	strong emission at H1 4340
TR16	14	106	23	1.8	...	...	2.3	strong emission at H1 4340
TR16	15	0	1	-14.4	...	...	2.3	emission at H1 4340
TR16	16	133	12	-36.7	...	...	3.3	weak emission at H1 4340
TR16	17	233	21	-26.9	...	...	2.7	emission at H1 4340
TR16	20	51	13	-19.2	...	...	9.7	
TR16	21	90	8	-2.9	...	...	1.7	
TR16	23	233	10	-22.7	...	...	0.0	very weak emission at H1 4340
TR16	24	198	18	-23.3	...	...	7.0	weak emission at H1 4340
TR16	25	156	18	-15.2	...	...	9.0	weak emission at H1 4340
TR16	28	46	16	-14.3	...	...	4.7	weak emission at H1 4340
TR16	29	24	30	-28.4	...	...	5.3	emission at H1 4340
TR16	47	371	25	-32.2	...	...	3.0	strong emission at H1 4340, weak emission at He lines
TR16	48	203	27	-20.8	...	...	8.0	strong emission at H1 4340, weak emission at He lines
TR16	80	204	8	-88.5	...	...	9.3	emission at H1 4340
TR16	94	118	10	-48.0	...	...	9.5	very strong emission at H1 4340
TR16	138	141	30	-8.8	...	...	5.0	strong emission at H1 4340
TR16	158	107	14	-14.0	...	...	1.3	
TR16	242	134	...	-44.8	...	...	19.0	emission at H1 4340
TR16	246	120	13	-17.4	...	...	1.3	emission at H1 4340
TR16	258	138	28	-15.2	...	...	14.0	
TR16	283	113	8	-18.1	...	...	2.7	weak emission at H1 4340
TR16	1075	5	7	-7.1	...	...	11.3	
TR16	1400	117	26	-38.9	...	...	10.0	strong emission at H1 4340
TR16	1462	69	12	-7.3	...	...	9.0	
TR16	1591	133	5	-0.4	...	...	18.0	
TR16	1641	55	39	-39.0	...	...	19.0	
TR16	1657	37	...	-20.1	...	...	19.0	weak emission at H1 4340
TR16	1658	212	7	-27.1	...	...	3.3	very weak emission at H1 4340 and He lines

B.2 Physical Parameters of Cluster Stars

Table: Physical Parameters of B Stars in 19 open clusters

Byte-by-byte Description of file:

Bytes	Format	Units	Label	Explanations
1- 7	A		Name of cluster	
8- 13	I6	---	WEBDA index	Id of stars at http://obswww.unige.ch/web
14- 21	I8	K	T_eff	Effective Temperature
22- 26	I5	K	dT	Measuring error of T_eff
27- 34	F8.3	dex	log g	
35- 41	F7.3	dex	dlog g	Measuring error of log g
42- 46	I5	km/s	Vsini	Projected equatorial velocity
47- 53	F7.3	dex	log g_polar	
54- 61	F8.3	dex	log(e/e_solar)[He4026]	Helium abundance from the He I 4026 line (1)
62- 69	F8.3	dex	log(e/e_solar)[He4387]	Helium abundance from the He I 4387 line (1)
70- 77	F8.3	dex	log(e/e_solar)[He4471]	Helium abundance from the He I 4471 line (1)
78- 85	F8.3	dex	<log(e/e_solar)>	Average of Helium abundance from 3 He lines
86- 92	F7.3	dex	d<log(e/e_solar)>	Measuring error of Helium abundance

Note (1): "..." means that it is not measurable or measurements are not reliable

Ber86	1	26878	406	3.841	0.035	185	3.936	-0.023	-0.048	0.222	0.050	0.122
Ber86	12	15440	232	4.048	0.040	309	4.291	-0.298	-0.089	-0.386	-0.258	0.124
Ber86	13	28711	191	3.590	0.023	183	3.723	-0.112	-0.194	0.259	-0.016	0.197
Ber86	15	23049	316	4.099	0.034	23	4.105	0.035	0.014	0.097	0.048	0.035
Ber86	17	26357	415	4.084	0.038	79	4.105	-0.032	-0.036	0.108	0.013	0.067
Ber86	30	16513	322	3.922	0.053	104	3.998	0.318	0.461	0.403	0.394	0.059
Ber86	149	20354	241	4.207	0.032	181	4.302	-0.402	-0.321	-0.362	-0.362	0.033
Ber86	214	15737	405	4.003	0.064	276	4.225	-0.147	0.069	-0.347	-0.142	0.170
Ber86	235	17487	310	3.831	0.042	325	4.137	0.096	0.255	0.195	0.182	0.065
Ber86	261	17241	250	3.970	0.037	251	4.171	0.111	0.232	0.251	0.198	0.062
Ber86	288	17393	232	4.038	0.032	184	4.172	-0.020	0.163	0.080	0.074	0.075
Ber86	291	18561	251	3.961	0.035	87	4.013	0.184	0.240	0.279	0.234	0.039
IC1805	72	21999	607	3.930	0.074	266	4.114	-0.034	0.075	0.081	0.041	0.053
IC1805	82	21759	584	3.911	0.057	191	4.037	-0.050	0.021	0.030	0.000	0.036
IC1805	111	24630	388	4.093	0.041	160	4.166	0.142	0.077	0.195	0.138	0.048
IC1805	118	20838	531	3.193	0.062	19	3.202	0.171	-0.204	0.192	0.053	0.182
IC1805	121	25750	510	4.323	0.048	61	4.333	-0.061	-0.057	0.094	-0.008	0.072
IC1805	130	16250	272	3.958	0.046	134	4.060	0.070	0.278	0.105	0.151	0.091
IC1805	143	24605	392	4.044	0.038	320	4.231	0.015	0.007	0.214	0.079	0.095
IC1805	149	21930	248	4.187	0.029	87	4.219	-0.104	-0.095	-0.054	-0.084	0.022
IC1805	157	18134	424	3.954	0.068	51	3.977	-0.255	-0.215	-0.259	-0.243	0.020
IC1805	158	22142	565	4.049	0.073	162	4.139	0.062	-0.076	0.105	0.030	0.077
IC1805	161	22297	280	4.307	0.035	178	4.381	-0.425	-0.363	-0.366	-0.385	0.028
IC1805	166	19398	384	4.060	0.049	108	4.120	-0.132	-0.030	-0.025	-0.062	0.049
IC1805	167	18459	398	4.040	0.056	247	4.216	0.205	0.138	0.074	0.139	0.053
IC1805	169	21638	297	4.162	0.029	76	4.191	-0.086	-0.077	-0.075	-0.079	0.004
IC1805	174	22286	240	4.245	0.031	190	4.332	-0.347	-0.298	-0.234	-0.293	0.046
IC1805	188	19196	441	4.109	0.056	29	4.120	0.064	0.150	0.142	0.119	0.039
IC1805	260	17873	274	3.984	0.036	102	4.050	0.094	0.114	0.063	0.090	0.021

IC1805	277	16217	389	4.145	0.074	157	4.242	0.049	0.177	0.114	0.114	0.052
IC1805	288	24342	312	4.242	0.034	204	4.328	-0.055	-0.126	0.011	-0.057	0.056
IC1805	1309	23202	357	4.062	0.039	172	4.152	-0.035	-0.051	0.133	0.016	0.083
IC1805	1329	17364	438	3.619	0.059	68	3.673	-0.076	0.028	-0.145	-0.064	0.071
IC1805	1406	13059	111	4.025	0.029	295	4.281	0.052	0.197	0.018	0.089	0.078
IC1805	1433	13406	72	3.942	0.015	26	3.956	-0.208	-0.184	-0.345	-0.246	0.071
IC1805	1824	17905	568	4.100	0.075	289	4.296	-0.043	0.042	-0.125	-0.042	0.068
IC1805	1924	18772	429	3.763	0.056	229	3.970	0.078	0.049	-0.006	0.040	0.035
IC1805	1930	18326	240	4.075	0.036	35	4.089	-0.295	-0.142	-0.134	-0.191	0.074
IC1805	1939	19286	484	4.070	0.061	41	4.085	-0.068	0.009	-0.046	-0.035	0.032
IC1805	1984	19349	426	3.744	0.048	48	3.766	0.037	0.107	0.051	0.065	0.030
IC2395	4	15563	96	3.753	0.014	97	3.839	-0.019	0.085	0.029	0.032	0.042
IC2395	6	16322	143	4.013	0.026	169	4.138	0.048	0.242	0.258	0.183	0.095
IC2395	7	15756	176	4.169	0.029	137	4.251	-0.078	0.052	0.035	0.003	0.058
IC2395	9	13507	48	4.253	0.010	106	4.322	-0.382	-0.140	-0.387	-0.303	0.115
IC2395	10	27049	625	3.621	0.055	91	3.664	-0.040	0.030	0.323	0.104	0.157
IC2395	14	12797	90	4.115	0.024	49	4.137	-0.602	-0.485	-0.602	-0.563	0.055
IC2395	15	11731	65	4.448	0.022	80	4.493	-0.157	...	-0.355	-0.256	0.099
IC2395	16	11719	66	4.508	0.023	147	4.554	...	...	-0.322	-0.322	...
IC2395	21	18811	439	4.098	0.060	109	4.159	...	-0.644	...	-0.644	...
IC2395	55	14253	57	3.604	0.012	51	3.642	-0.036	0.014	0.012	-0.003	0.023
IC2395	56	24397	431	4.010	0.046	21	4.016	-0.110	-0.016	0.126	0.000	0.097
IC2395	57	12745	20	4.062	0.005	250	4.255	-0.292	...	-0.253	-0.272	0.020
IC2395	67	17260	220	3.886	0.030	60	3.921	-0.599	...	...	-0.599	...
IC2395	219	21591	1325	4.424	0.133	115	4.457	...	...	...	...	...
IC2395	...	18998	894	4.387	0.116	25	4.395	...	...	...	...	...
IC2944	5	17700	427	4.044	0.053	135	4.136	-0.089	-0.003	0.000	-0.031	0.041
IC2944	13	23070	289	4.208	0.030	64	4.226	-0.182	-0.154	-0.044	-0.127	0.059
IC2944	14	23284	462	3.410	0.044	31	3.420	0.124	-0.150	0.304	0.093	0.186
IC2944	16	20883	283	3.984	0.031	215	4.127	0.024	-0.010	0.076	0.030	0.035
IC2944	19	25704	724	3.774	0.059	82	3.810	-0.072	-0.194	0.160	-0.035	0.147
IC2944	20	25459	229	4.027	0.021	149	4.093	-0.107	-0.075	0.159	-0.008	0.119
IC2944	...	23230	819	4.139	0.074	232	4.258	-0.037	-0.099	-0.275	-0.137	0.101
IC2944	23	25700	404	4.196	0.035	179	4.266	-0.116	-0.089	0.187	-0.006	0.137
IC2944	25	19956	373	3.902	0.045	133	3.995	...	-0.374	-0.542	-0.458	0.084
IC2944	27	12851	30	3.671	0.007	53	3.713	-0.334	-0.247	-0.316	-0.299	0.038
IC2944	29	26280	303	4.145	0.029	85	4.166	0.078	0.073	0.265	0.139	0.089
IC2944	33	27130	622	4.109	0.051	0	4.109	-0.064	-0.079	0.245	0.034	0.149
IC2944	34	22334	423	4.141	0.052	70	4.165	-0.100	-0.011	0.091	-0.007	0.078
IC2944	36	24229	166	3.535	0.016	196	3.706	0.106	-0.096	0.338	0.116	0.177
IC2944	41	18356	304	4.216	0.044	251	4.362	-0.600	-0.352	-0.481	-0.478	0.101
IC2944	48	18511	201	4.003	0.028	225	4.168	-0.159	-0.061	-0.007	-0.076	0.063
IC2944	71	15223	130	4.332	0.023	153	4.402	-0.450	-0.227	-0.565	-0.414	0.140
IC2944	88	17909	151	4.204	0.023	123	4.270	-0.352	-0.123	-0.193	-0.223	0.096
IC2944	90	16617	206	4.030	0.033	196	4.174	-0.015	0.103	0.043	0.044	0.049
IC2944	91	25555	552	4.016	0.047	187	4.106	-0.022	-0.014	0.259	0.074	0.131
IC2944	93	15592	189	4.247	0.033	92	4.299	-0.617	-0.428	-0.619	-0.555	0.090
IC2944	96	25144	274	4.064	0.026	55	4.077	-0.061	0.010	0.187	0.046	0.104
IC2944	98	24471	453	3.420	0.040	1	3.420	0.190	0.055	0.438	0.228	0.159
IC2944	102	14077	201	3.122	0.040	93	3.258	-0.038	0.104	-0.057	0.003	0.072
IC2944	105	29132	375	3.556	0.039	86	3.589	-0.110	-0.084	0.183	-0.004	0.132
IC2944	106	18712	278	3.983	0.036	99	4.043	-0.143	-0.037	0.025	-0.052	0.070
IC2944	109	20308	357	4.143	0.047	80	4.177	-0.350	-0.247	-0.184	-0.260	0.068
IC2944	110	14964	181	4.335	0.035	181	4.413	-0.560	0.014	-0.331	-0.292	0.236
IC2944	112	15506	140	3.958	0.022	316	4.231	-0.105	0.075	-0.042	-0.024	0.075

IC2944	115	15995	190	4.062	0.030	311	4.300	-0.618	-0.244	-0.555	-0.473	0.164
IC2944	119	16881	238	4.221	0.037	118	4.285	-0.243	-0.079	-0.095	-0.139	0.073
IC2944	120	26288	555	4.292	0.056	22	4.294	0.069	0.077	0.210	0.119	0.065
IC2944	122	22919	364	3.921	0.037	271	4.103	-0.032	0.098	0.245	0.104	0.113
IC2944	134	15490	150	4.004	0.026	199	4.151	0.101	0.277	0.257	0.212	0.079
IC2944	178	27232	611	3.961	0.046	155	4.025	0.029	0.089	0.227	0.115	0.083
IC2944	...	15946	128	4.183	0.018	29	4.194	-0.475	-0.240	-0.354	-0.356	0.096
IC2944	...	18104	330	4.165	0.050	33	4.177	-0.294	-0.105	-0.073	-0.158	0.097
NGC457	19	23982	570	3.770	0.067	15	3.773	0.076	0.029	0.147	0.084	0.049
NGC457	33	20575	202	3.556	0.010	103	3.643	0.100	0.065	0.073	0.079	0.015
NGC457	37	20376	236	3.464	0.030	103	3.558	0.037	-0.067	-0.011	-0.013	0.043
NGC457	54	20636	332	3.690	0.041	130	3.792	0.059	-0.063	0.036	0.011	0.053
NGC457	109	10253	13	3.895	0.007	79	3.964	...	...	...	...	...
NGC457	120	22384	333	3.319	0.038	22	3.327	0.478	0.288	0.514	0.427	0.099
NGC457	128	22184	366	3.321	0.031	204	3.541	0.242	0.184	0.232	0.219	0.025
NGC457	129	14199	161	4.273	0.038	100	4.335	0.202	0.280	0.144	0.209	0.056
NGC457	135	15589	294	4.126	0.049	113	4.198	0.421	0.414	0.365	0.400	0.025
NGC457	140	14663	237	4.221	0.047	165	4.311	-0.632	-0.587	-0.667	-0.629	0.032
NGC457	143	12606	48	4.003	0.012	279	4.246	-0.527	...	-0.602	-0.564	0.038
NGC457	149	14394	60	3.940	0.012	242	4.144	0.364	0.438	0.327	0.376	0.046
NGC457	151	16940	214	4.340	0.031	58	4.361	-0.174	-0.052	-0.198	-0.141	0.064
NGC457	174	15547	313	3.738	0.048	49	3.768	-0.615	-0.475	-0.645	-0.578	0.074
NGC457	198	22371	158	3.430	0.049	182	3.606	0.286	0.194	0.243	0.241	0.038
NGC457	215	17413	262	3.685	0.035	292	3.981	0.184	0.338	0.197	0.240	0.070
NGC869	63	21623	173	4.067	0.017	153	4.152	-0.189	-0.229	-0.185	-0.201	0.020
NGC869	90	22251	232	3.871	0.029	31	3.881	-0.028	-0.091	0.028	-0.031	0.049
NGC869	133	15511	195	3.989	0.032	327	4.265	-0.013	0.081	-0.082	-0.005	0.067
NGC869	260	27980	394	3.969	0.056	163	4.033	-0.073	-0.078	0.219	0.023	0.139
NGC869	289	18127	204	3.884	0.029	48	3.906	0.308	0.218	0.259	0.262	0.037
NGC869	323	19536	180	3.911	0.020	5	3.913	0.024	0.014	0.011	0.016	0.005
NGC869	339	26627	443	3.871	0.040	48	3.878	0.012	-0.022	0.189	0.060	0.093
NGC869	350	17925	319	4.050	0.044	152	4.155	-0.050	0.039	-0.050	-0.020	0.042
NGC869	487	19870	176	3.865	0.020	111	3.940	0.104	0.038	0.106	0.083	0.031
NGC869	496	23295	341	4.115	0.036	31	4.123	-0.183	-0.166	-0.075	-0.141	0.047
NGC869	530	22707	299	4.034	0.033	51	4.049	-0.110	-0.157	-0.074	-0.114	0.034
NGC869	551	19562	324	3.757	0.037	228	3.957	0.091	0.038	0.130	0.086	0.038
NGC869	566	25229	332	3.817	0.028	295	4.015	-0.022	-0.035	0.153	0.032	0.086
NGC869	572	21542	216	4.041	0.021	80	4.076	-0.047	-0.049	0.044	-0.017	0.043
NGC869	590	22975	206	3.892	0.021	120	3.960	0.002	-0.044	0.060	0.006	0.042
NGC869	622	20303	175	4.036	0.022	45	4.052	-0.103	-0.106	-0.123	-0.111	0.009
NGC869	670	21270	241	3.893	0.024	96	3.948	0.042	-0.005	0.102	0.046	0.044
NGC869	678	23033	284	3.838	0.031	68	3.867	0.046	-0.064	0.088	0.024	0.064
NGC869	717	25929	344	4.064	0.034	69	4.083	-0.068	-0.066	0.131	-0.001	0.093
NGC869	731	20561	328	3.944	0.040	163	4.054	0.014	-0.049	-0.020	-0.019	0.026
NGC869	748	11040	22	3.735	0.008	277	4.014	...	...	...	...	...
NGC869	768	16605	138	3.494	0.020	10	3.501	0.332	0.319	0.295	0.315	0.015
NGC869	782	22681	377	3.658	0.043	28	3.667	0.086	0.038	0.104	0.076	0.028
NGC869	789	15392	204	4.005	0.035	185	4.142	0.299	0.260	0.214	0.257	0.035
NGC869	803	24838	354	3.891	0.033	249	4.045	0.048	0.055	0.164	0.089	0.053
NGC869	834	18860	283	4.029	0.039	110	4.096	-0.174	-0.145	-0.116	-0.145	0.024
NGC869	839	26117	644	4.022	0.063	27	4.027	0.205	0.239	0.327	0.257	0.051
NGC869	843	22090	207	3.657	0.025	100	3.727	0.092	0.013	0.096	0.067	0.038
NGC869	847	27857	375	3.914	0.039	66	3.930	0.079	0.013	0.204	0.099	0.079
NGC869	864	22155	370	3.882	0.047	145	3.975	-0.036	-0.127	-0.019	-0.061	0.047
NGC869	922	26411	435	3.846	0.042	268	4.008	-0.074	-0.126	0.179	-0.007	0.133

NGC869	980	21600	257	3.712	0.025	24	3.721	0.085	0.021	0.081	0.062	0.029
NGC869	1015	12500	54	4.083	0.015	46	4.104	-0.057	0.093	-0.033	0.001	0.066
NGC869	1067	21107	254	3.937	0.028	33	3.948	-0.116	-0.161	-0.105	-0.127	0.025
NGC869	1078	23881	219	3.736	0.022	197	3.875	-0.002	-0.020	0.111	0.029	0.058
NGC869	1085	23096	280	3.856	0.029	71	3.888	0.031	-0.003	0.049	0.025	0.022
NGC869	1116	24433	469	3.652	0.045	119	3.731	0.186	0.051	0.243	0.160	0.081
NGC869	1141	22475	157	3.626	0.017	227	3.824	0.118	-0.016	0.112	0.071	0.062
NGC869	1196	21615	185	3.930	0.017	123	4.003	-0.071	-0.132	-0.036	-0.080	0.040
NGC869	1226	20692	372	3.841	0.046	54	3.864	0.081	0.043	0.127	0.084	0.034
NGC869	1252	17418	131	3.813	0.016	21	3.825	-0.039	0.002	-0.040	-0.026	0.020
NGC869	1268	25904	418	3.819	0.043	131	3.888	0.022	-0.000	0.237	0.086	0.107
NGC869	1352	23525	224	4.059	0.021	147	4.131	-0.041	-0.059	0.037	-0.021	0.042
NGC869	1364	21186	280	3.658	0.031	212	3.841	0.066	0.037	0.084	0.062	0.019
NGC869	1387	19202	296	3.925	0.035	47	3.944	0.024	0.008	0.078	0.037	0.030
NGC869	1391	23193	244	3.924	0.025	153	4.013	0.038	-0.031	0.129	0.045	0.066
NGC869	1439	20312	186	4.017	0.024	41	4.032	-0.108	-0.097	-0.110	-0.105	0.006
NGC869	1516	20886	234	4.066	0.026	153	4.155	-0.237	-0.202	-0.071	-0.170	0.072
NGC869	1539	19518	322	3.823	0.037	12	3.829	0.164	0.128	0.167	0.153	0.018
NGC869	1566	21876	296	3.883	0.032	137	3.971	0.061	0.018	0.052	0.043	0.019
NGC869	1586	25972	344	3.903	0.035	236	4.036	-0.058	-0.041	0.150	0.017	0.094
NGC869	1590	18884	304	3.725	0.037	34	3.742	0.244	0.332	0.134	0.237	0.081
NGC884	1770	16652	119	3.859	0.018	221	4.058	0.162	0.259	0.242	0.221	0.042
NGC884	1873	20599	140	3.946	0.016	168	4.060	-0.073	-0.076	0.007	-0.047	0.039
NGC884	1901	25937	401	4.160	0.041	69	4.176	-0.147	-0.117	0.018	-0.082	0.072
NGC884	1924	22544	249	3.897	0.030	58	3.919	-0.030	-0.064	0.024	-0.023	0.036
NGC884	1960	21617	197	4.028	0.019	97	4.073	-0.067	-0.079	-0.041	-0.062	0.016
NGC884	1983	22127	192	3.875	0.022	56	3.897	0.082	0.005	0.050	0.046	0.031
NGC884	2014	19078	298	3.828	0.037	273	4.060	0.109	0.170	0.112	0.130	0.028
NGC884	2048	18007	198	3.944	0.027	126	4.036	0.110	0.140	0.164	0.138	0.022
NGC884	2049	23227	256	3.405	0.024	381	3.870	0.176	-0.002	0.203	0.126	0.091
NGC884	2051	19000	195	3.968	0.024	20	3.976	0.091	0.135	0.147	0.124	0.024
NGC884	2085	19135	123	3.865	0.014	269	4.086	-0.001	0.020	0.071	0.030	0.030
NGC884	2112	22172	216	4.097	0.025	74	4.125	-0.142	-0.132	-0.084	-0.119	0.025
NGC884	2139	19297	248	3.858	0.028	136	3.961	0.107	0.122	0.142	0.124	0.014
NGC884	2140	14912	324	4.230	0.053	164	4.318	-0.266	0.119	-0.137	-0.095	0.160
NGC884	2165	26571	485	4.003	0.038	79	4.025	-0.002	-0.007	-0.033	-0.014	0.014
NGC884	2185	16520	176	4.001	0.030	195	4.149	-0.157	0.052	-0.078	-0.061	0.086
NGC884	2190	24259	239	3.901	0.024	304	4.102	-0.033	0.005	0.075	0.016	0.044
NGC884	2191	16041	116	3.793	0.020	269	4.054	0.236	0.358	0.323	0.306	0.052
NGC884	2232	21023	250	3.970	0.027	112	4.033	-0.043	0.077	0.085	0.040	0.059
NGC884	2255	20360	178	3.560	0.022	318	3.901	0.059	0.111	0.107	0.092	0.024
NGC884	2299	25931	419	3.853	0.045	116	3.908	-0.011	-0.014	0.208	0.061	0.104
NGC884	2336	18399	222	3.984	0.033	172	4.109	-0.199	-0.121	-0.210	-0.177	0.040
NGC884	2392	20494	228	3.931	0.029	54	3.953	0.053	0.005	0.079	0.046	0.031
NGC884	2402	28238	449	3.730	0.069	141	3.807	-0.049	-0.063	0.011	-0.034	0.032
NGC884	2433	20469	221	4.102	0.027	44	4.116	-0.162	-0.150	-0.161	-0.158	0.005
NGC884	2444	24900	362	4.032	0.035	144	4.098	-0.043	-0.114	0.111	-0.015	0.094
NGC884	2468	10305	15	4.076	0.008	183	4.185	...	...	...	...	...
NGC884	2488	24478	256	3.890	0.026	132	3.960	0.037	-0.017	0.154	0.058	0.071
NGC884	2513	21163	206	3.946	0.021	52	3.965	-0.088	-0.095	-0.074	-0.086	0.009
NGC884	2540	20453	264	3.803	0.033	244	4.003	0.033	-0.014	0.083	0.034	0.040
NGC884	2541	24729	580	3.750	0.055	67	3.777	0.096	0.025	0.198	0.106	0.071
NGC884	2601	23836	243	4.010	0.024	78	4.039	-0.053	-0.049	-0.032	-0.045	0.009
NGC884	2603	19002	187	3.885	0.023	89	3.943	0.125	0.152	0.215	0.164	0.037
NGC884	2605	25920	511	4.062	0.052	18	4.066	-0.065	-0.052	0.073	-0.015	0.062

NGC884	2612	16482	168	3.932	0.029	69	3.975	0.251	0.353	0.390	0.331	0.059
NGC884	2622	19250	393	3.900	0.048	360	4.212	-0.118	0.017	0.078	-0.008	0.082
NGC884	2628	12297	64	3.974	0.020	150	4.089	-0.072	0.060	-0.060	-0.024	0.060
NGC884	2656	16540	148	3.868	0.023	34	3.886	0.426	0.560	0.574	0.520	0.067
NGC884	2716	19483	291	3.891	0.033	181	4.029	0.117	0.047	0.108	0.091	0.031
NGC884	2729	10639	55	4.028	0.026	248	4.227	...	...	...	...	...
NGC884	2731	21251	290	3.776	0.030	165	3.901	0.084	0.041	0.106	0.077	0.027
NGC884	2794	21624	291	3.611	0.027	80	3.664	0.075	-0.073	0.087	0.030	0.073
NGC884	2809	21463	368	3.815	0.038	36	3.828	0.042	-0.016	0.052	0.026	0.030
NGC884	2826	19669	378	3.680	0.041	222	3.882	0.154	0.074	0.149	0.126	0.037
NGC884	2837	19094	320	3.874	0.041	183	4.017	0.049	0.041	0.034	0.041	0.006
NGC884	2851	16663	228	4.136	0.038	66	4.169	-0.004	0.119	0.148	0.088	0.066
NGC884	2907	13968	40	3.963	0.008	229	4.147	-0.142	0.011	-0.224	-0.118	0.097
NGC884	2910	27117	781	3.819	0.062	23	3.822	0.006	-0.007	0.174	0.057	0.083
NGC884	2949	18240	308	3.816	0.048	169	3.959	0.103	0.173	0.157	0.144	0.030
NGC1502	7	14411	174	4.320	0.040	55	4.340	-0.358	-0.193	-0.562	-0.371	0.151
NGC1502	10	17514	278	3.979	0.038	124	4.067	0.216	0.231	0.232	0.226	0.007
NGC1502	12	24398	230	4.082	0.025	170	4.163	-0.004	-0.045	0.137	0.029	0.078
NGC1502	16	14073	133	4.153	0.031	125	4.233	-0.411	-0.175	-0.558	-0.381	0.158
NGC1502	23	15286	113	3.951	0.019	149	4.067	0.227	0.389	0.309	0.308	0.066
NGC1502	26	24026	230	4.120	0.024	175	4.202	-0.062	-0.104	0.076	-0.030	0.077
NGC1502	30	24481	218	4.087	0.023	128	4.141	0.003	-0.011	0.117	0.036	0.058
NGC1502	33	12128	139	4.053	0.046	181	4.170	0.440	0.361	0.138	0.313	0.128
NGC1502	37	23403	823	4.221	0.083	37	4.230	0.051	-0.041	-0.120	-0.037	0.070
NGC1502	40	16175	144	3.925	0.027	195	4.085	0.203	0.260	0.310	0.258	0.043
NGC1502	43	15628	201	4.060	0.035	203	4.201	0.134	0.223	0.207	0.188	0.039
NGC1502	44	16935	154	3.921	0.023	69	3.964	-0.526	-0.551	-0.514	-0.530	0.015
NGC1502	49	18199	210	3.893	0.033	195	4.051	0.185	0.224	0.197	0.202	0.016
NGC1502	61	20282	250	3.974	0.032	307	4.196	-0.084	0.066	0.058	0.013	0.069
NGC1502	70	13041	100	3.987	0.024	142	4.096	-0.638	-0.492	-0.560	-0.563	0.059
NGC1502	74	10832	40	3.907	0.017	332	4.201	0.584	0.602	0.602	0.596	0.009
NGC1502	78	15986	133	3.947	0.024	297	4.197	0.083	0.230	0.215	0.176	0.066
NGC1502	1233	23347	356	3.921	0.038	213	4.052	0.039	-0.053	0.163	0.050	0.089
NGC2244	59	13263	81	4.032	0.018	67	4.075	...	...	...	...	...
NGC2244	62	17872	514	3.161	0.065	11	3.170	0.413	0.555	0.408	0.459	0.068
NGC2244	80	25727	188	4.222	0.016	248	4.326	-0.090	-0.103	0.075	-0.040	0.081
NGC2244	88	12902	79	3.862	0.019	43	3.889	-0.427	-0.382	-0.596	-0.469	0.092
NGC2244	116	12797	95	4.109	0.025	302	4.361	-0.238	...	-0.391	-0.315	0.077
NGC2244	119	14284	111	4.218	0.025	5	4.219	0.044	0.171	0.124	0.113	0.052
NGC2244	123	14142	106	3.986	0.033	175	4.116	0.455	0.570	0.528	0.517	0.047
NGC2244	128	24239	164	4.181	0.018	188	4.264	-0.057	-0.061	0.110	-0.002	0.080
NGC2244	130	16578	183	4.066	0.024	78	4.111	0.305	0.333	0.375	0.338	0.029
NGC2244	133	12219	90	4.347	0.032	183	4.411	-0.160	...	-0.226	-0.193	0.033
NGC2244	167	20179	115	4.036	0.014	119	4.104	0.070	0.096	0.124	0.097	0.022
NGC2244	172	18001	196	3.951	0.031	260	4.157	0.086	0.146	0.109	0.114	0.025
NGC2244	192	13533	134	3.938	0.029	70	3.988	-0.283	-0.047	-0.458	-0.262	0.169
NGC2244	193	18937	186	4.016	0.025	66	4.049	0.099	0.105	0.127	0.110	0.012
NGC2244	194	15669	191	4.022	0.032	344	4.304	-0.093	0.054	-0.129	-0.056	0.079
NGC2244	201	25742	408	4.185	0.037	25	4.189	0.010	0.064	0.222	0.099	0.090
NGC2244	206	16386	226	3.935	0.039	306	4.196	-0.219	-0.108	-0.386	-0.238	0.114
NGC2244	231	12649	56	3.946	0.022	165	4.074	-0.289	...	-0.503	-0.396	0.107
NGC2244	241	14024	80	4.099	0.016	214	4.240	-0.634	-0.419	-0.673	-0.575	0.112
NGC2244	253	14781	244	4.194	0.018	167	4.288	0.245	0.378	0.323	0.315	0.054
NGC2244	260	13146	8	3.991	0.024	198	4.131	-0.472	...	-0.472	-0.472	0.000
NGC2244	274	19922	120	4.058	0.014	71	4.091	-0.570	-0.644	-0.574	-0.596	0.034

NGC2244	298	14305	228	4.276	0.042	135	4.348	...	...	...	...	...
NGC2244	319	13886	131	4.239	0.026	286	4.443	-0.347	-0.236	-0.675	-0.419	0.186
NGC2244	331	12279	113	3.983	0.041	299	4.255	-0.096	...	-0.205	-0.151	0.054
NGC2244	337	12543	57	4.035	0.015	321	4.300	-0.244	...	-0.412	-0.328	0.084
NGC2244	345	14398	172	4.042	0.036	228	4.210	-0.330	-0.232	-0.668	-0.410	0.187
NGC2244	353	20626	310	3.850	0.038	222	4.020	-0.058	-0.053	-0.128	-0.080	0.034
NGC2244	391	16671	133	3.530	0.022	349	3.972	-0.066	0.036	-0.144	-0.058	0.074
NGC2244	392	18276	219	4.068	0.036	137	4.156	-0.091	0.057	0.025	-0.003	0.063
NGC2244	1034	13604	59	3.797	0.012	3	3.800	-0.104	-0.021	-0.050	-0.059	0.034
NGC2244	1134	13039	45	4.080	0.011	257	4.280	-0.355	...	-0.457	-0.406	0.051
NGC2244	1147	18773	211	3.621	0.030	257	3.881	0.053	0.109	0.020	0.061	0.037
NGC2244	1209	10561	17	4.050	0.008	41	4.071	...	...	...	...	...
NGC2244	1254	12262	60	3.840	0.019	283	4.112	-0.072	...	-0.114	-0.093	0.021
NGC2244	1259	12477	162	3.917	0.047	151	4.040	-0.358	-0.217	-0.602	-0.392	0.159
NGC2244	1262	14354	92	4.103	0.019	109	4.179	-0.222	-0.099	-0.235	-0.186	0.061
NGC2244	1607	17213	216	4.169	0.033	137	4.250	-0.069	0.097	0.014	0.014	0.068
NGC2244	1616	12001	82	3.977	0.031	193	4.113	0.190	...	0.274	0.232	0.042
NGC2362	1	14503	138	4.266	0.029	310	4.470	-0.633	-0.559	...	-0.596	0.037
NGC2362	2	13478	58	4.180	0.012	127	4.260	-0.261	-0.137	-0.285	-0.228	0.065
NGC2362	3	11726	117	4.369	0.040	173	4.428	-0.078	...	-0.126	-0.102	0.024
NGC2362	5	15192	156	4.188	0.030	107	4.254	-0.032	0.012	-0.006	-0.009	0.018
NGC2362	12	15943	208	4.211	0.036	229	4.351	-0.015	0.239	0.139	0.121	0.104
NGC2362	14	18593	197	3.984	0.028	101	4.046	0.096	0.195	0.252	0.181	0.064
NGC2362	20	24223	343	4.188	0.040	50	4.198	0.136	0.319	0.492	0.316	0.146
NGC2362	25	13986	105	4.305	0.025	72	4.341	...	-0.630	...	-0.630	...
NGC2362	26	14846	89	4.022	0.017	202	4.165	0.068	0.220	0.227	0.171	0.073
NGC2362	27	17174	117	4.289	0.017	87	4.329	-0.116	0.065	0.087	0.012	0.091
NGC2362	31	19778	267	4.030	0.031	157	4.131	-0.010	0.063	0.129	0.061	0.057
NGC2362	34	16654	160	4.419	0.028	197	4.496	-0.474	-0.252	-0.505	-0.410	0.113
NGC2362	39	17431	218	4.030	0.030	73	4.071	0.186	0.271	0.340	0.265	0.063
NGC2362	42	13887	48	4.210	0.011	136	4.290	-0.611	-0.360	-0.599	-0.524	0.116
NGC2362	48	17457	252	3.947	0.035	194	4.101	0.060	0.270	0.286	0.206	0.103
NGC2362	67	18671	222	3.793	0.030	293	4.052	0.044	0.110	0.165	0.106	0.049
NGC2362	68	22489	210	4.043	0.025	95	4.084	0.294	0.276	0.378	0.316	0.044
NGC2362	69	16719	211	3.954	0.034	225	4.140	0.130	0.322	0.327	0.260	0.092
NGC2362	73	15026	151	3.977	0.027	94	4.046	...	...	...	...	...
NGC2362	76	15455	172	4.376	0.031	213	4.468	-0.031	0.197	0.011	0.059	0.099
NGC2362	...	19006	386	3.401	0.047	48	3.428	0.120	0.154	0.129	0.134	0.014
NGC2362	...	11751	76	4.187	0.024	190	4.280	-0.033	...	0.126	0.047	0.080
NGC2362	...	15939	75	3.449	0.011	35	3.476	0.033	0.070	0.005	0.036	0.027
NGC2362	...	16266	232	4.692	0.045	217	4.731	-0.635	-0.547	...	-0.591	0.044
NGC2362	...	11641	104	4.444	0.036	187	4.485	-0.190	...	-0.247	-0.218	0.029
NGC2362	...	11905	81	4.476	0.028	200	4.509	-0.427	...	-0.424	-0.426	0.002
NGC2362	...	14807	149	4.372	0.031	245	4.500	-0.634	-0.376	-0.667	-0.559	0.130
NGC2384	3	21549	2123	3.254	0.191	9	3.258	...	...	...	...	...
NGC2384	4	26832	560	3.612	0.050	105	3.669	-0.059	0.004	0.323	0.089	0.167
NGC2384	12	23848	2713	3.903	0.373	67	3.928	...	...	...	...	...
NGC2384	17	23943	330	3.915	0.035	7	3.917	-0.019	0.009	0.127	0.039	0.063
NGC2384	23	24673	316	3.920	0.032	78	3.950	0.005	0.021	0.237	0.088	0.106
NGC2384	37	23173	398	4.123	0.041	12	4.126	-0.136	0.063	0.077	0.001	0.097
NGC2384	44	20786	311	4.019	0.036	158	4.117	-0.175	-0.133	-0.084	-0.131	0.037
NGC2384	62	19951	368	3.938	0.044	151	4.042	-0.167	-0.112	-0.015	-0.098	0.063
NGC2384	77	15167	87	3.853	0.014	262	4.095	-0.103	0.054	-0.055	-0.035	0.066
NGC2384	88	21311	519	3.824	0.056	99	3.885	...	-0.648	...	-0.648	...
NGC2384	102	11726	89	3.816	0.027	31	3.838	-0.238	...	-0.069	-0.154	0.084

NGC2384	126	20137	367	3.948	0.050	37	3.962	0.015	-0.076	-0.081	-0.047	0.044
NGC2384	160	15499	236	4.140	0.040	25	4.150	-0.312	-0.149	-0.191	-0.217	0.069
NGC2422	32	11257	122	3.895	0.045	114	3.997	...	...	...	...	...
NGC2422	42	12826	60	3.891	0.011	45	3.917	0.093	0.108	0.063	0.088	0.019
NGC2422	65	11618	50	3.978	0.016	107	4.070	0.138	...	0.154	0.146	0.008
NGC2422	67	11541	24	4.035	0.009	241	4.222	0.009	...	-0.138	-0.065	0.074
NGC2422	70	10689	21	4.055	0.005	181	4.168	...	...	...	...	...
NGC2422	77	11280	81	3.951	0.014	221	4.122	...	...	...	...	...
NGC2422	78	11644	28	4.047	0.009	108	4.134	0.169	...	0.126	0.148	0.021
NGC2422	89	13542	53	3.764	0.016	94	3.854	-0.634	-0.632	-0.677	-0.648	0.021
NGC2422	123	13868	95	3.585	0.018	4	3.587	-0.027	0.077	0.015	0.021	0.043
NGC2422	125	13858	262	3.514	0.051	205	3.755	-0.590	...	-0.672	-0.631	0.041
NGC2422	180	11750	54	3.746	0.016	316	4.069	-0.157	...	-0.132	-0.144	0.012
NGC2422	...	13560	19	3.938	0.014	9	3.944	-0.156	-0.095	-0.202	-0.151	0.044
NGC2422	...	12720	62	3.336	0.016	176	3.594	-0.178	...	-0.184	-0.181	0.003
NGC2422	...	13182	81	3.595	0.009	74	3.670	-0.054	-0.070	-0.119	-0.081	0.028
NGC2467	2	11878	60	3.879	0.019	78	3.944	-0.313	-0.184	-0.325	-0.274	0.064
NGC2467	15	10731	20	4.229	0.009	192	4.309	...	...	...	...	...
NGC2467	16	12345	84	3.398	0.025	114	3.558	-0.560	-0.346	-0.467	-0.458	0.087
NGC2467	21	17993	218	3.829	0.031	163	3.966	0.131	0.116	0.103	0.117	0.012
NGC2467	30	14757	222	3.989	0.044	164	4.111	-0.260	0.024	-0.151	-0.129	0.117
NGC2467	33	12811	70	3.781	0.017	112	3.890	-0.400	-0.187	-0.427	-0.338	0.108
NGC2467	39	24662	843	4.071	0.081	174	4.153	-0.282	-0.223	-0.128	-0.211	0.063
NGC2467	43	21848	379	3.212	0.034	195	3.435	0.116	0.033	0.309	0.153	0.116
NGC2467	47	13669	76	3.307	0.013	32	3.339	-0.466	-0.415	-0.481	-0.454	0.028
NGC2467	54	20483	550	4.179	0.061	319	4.363	-0.570	-0.373	-0.572	-0.505	0.093
NGC2467	59	20186	538	3.560	0.060	229	3.786	-0.536	-0.535	-0.537	-0.536	0.001
NGC2467	61	13391	44	4.067	0.009	166	4.178	-0.549	...	-0.556	-0.553	0.003
NGC2467	65	24660	448	3.829	0.046	136	3.908	-0.068	-0.069	0.140	0.001	0.099
NGC2467	...	15111	137	3.477	0.022	23	3.495	-0.358	-0.259	-0.365	-0.328	0.048
NGC3293	5	26584	600	4.070	0.054	102	4.101	-0.095	-0.078	0.158	-0.005	0.116
NGC3293	7	25538	623	3.822	0.052	116	3.881	-0.109	0.046	0.279	0.072	0.159
NGC3293	8	27898	490	3.756	0.064	32	3.759	-0.171	-0.005	0.198	0.007	0.151
NGC3293	9	22643	356	3.964	0.041	141	4.044	-0.285	-0.105	0.055	-0.112	0.139
NGC3293	10	24279	276	3.846	0.029	108	3.902	-0.213	-0.004	0.209	-0.003	0.172
NGC3293	13	23085	297	3.957	0.031	29	3.966	-0.334	-0.027	0.113	-0.083	0.186
NGC3293	14	25214	482	3.910	0.037	113	3.962	-0.064	-0.000	0.246	0.060	0.134
NGC3293	16	25721	700	3.908	0.063	18	3.911	-0.069	0.026	0.254	0.070	0.135
NGC3293	19	25986	654	3.489	0.105	295	3.752	0.091	0.160	0.386	0.212	0.126
NGC3293	20	26516	480	3.618	0.048	73	3.648	-0.075	-0.008	0.344	0.087	0.184
NGC3293	25	26965	545	3.623	0.047	186	3.759	-0.272	0.028	0.327	0.028	0.244
NGC3293	27	25165	561	3.891	0.052	62	3.910	-0.238	-0.052	0.176	-0.038	0.170
NGC3293	28	21279	415	3.524	0.041	358	3.933	...	0.131	0.123	0.127	0.004
NGC3293	29	20550	320	3.770	0.036	360	4.108	-0.187	0.079	0.069	-0.013	0.123
NGC3293	65	23626	402	3.783	0.039	230	3.948	-0.024	-0.014	0.207	0.057	0.107
NGC3293	79	22610	398	3.833	0.046	362	4.134	-0.171	-0.006	0.082	-0.032	0.105
NGC3293	83	18331	299	3.859	0.044	320	4.143	...	0.035	-0.018	0.008	0.026
NGC3293	85	17671	312	3.905	0.041	265	4.127	-0.492	0.071	0.051	-0.123	0.261
NGC3293	89	20277	374	3.868	0.049	81	3.914	-0.217	0.062	0.131	-0.008	0.150
NGC3293	92	18243	241	4.171	0.045	57	4.194	-0.425	-0.157	-0.137	-0.240	0.131
NGC3293	299	18769	571	4.030	0.072	376	4.318	...	-0.371	-0.596	-0.484	0.113
NGC3293	534	27956	662	3.854	0.069	262	3.997	-0.368	-0.165	0.256	-0.092	0.260
NGC4755	5	26264	447	3.728	0.047	40	3.735	...	0.008	0.250	0.129	0.121
NGC4755	6	24103	403	3.780	0.044	88	3.825	...	-0.007	0.211	0.102	0.109
NGC4755	7	23932	390	3.885	0.039	23	3.891	...	0.017	0.121	0.069	0.052

NGC4755	10	19050	372	3.783	0.045	150	3.905	...	0.134	0.213	0.173	0.040
NGC4755	106	22747	790	3.022	0.071	6	3.024	0.653	0.526	0.630	0.603	0.055
NGC4755	115	20678	279	3.743	0.030	118	3.830	...	0.161	0.289	0.225	0.064
NGC4755	122	17932	437	3.922	0.061	64	3.958	...	-0.645	-0.607	-0.626	0.019
NGC4755	129	12267	136	4.153	0.043	216	4.282	...	...	-0.430	-0.430	...
NGC4755	136	15199	254	3.991	0.044	190	4.133	...	-0.309	-0.304	-0.306	0.003
NGC4755	137	15005	304	3.902	0.055	178	4.049	...	-0.475	-0.657	-0.566	0.091
NGC4755	139	18072	317	3.948	0.042	372	4.266	...	-0.067	-0.103	-0.085	0.018
NGC4755	150	12101	89	4.164	0.028	150	4.254	...	-0.030	-0.518	-0.274	0.244
NGC4755	157	21687	384	3.985	0.035	55	4.005	...	0.010	0.037	0.024	0.013
NGC4755	202	20437	232	3.579	0.023	278	3.857	...	0.111	0.109	0.110	0.001
NGC4755	209	18968	288	3.986	0.035	90	4.037	...	-0.136	-0.096	-0.116	0.020
NGC4755	210	21216	331	3.654	0.032	299	3.927	...	0.034	0.193	0.114	0.080
NGC4755	238	17451	260	3.917	0.035	68	3.957	...	0.228	0.251	0.240	0.012
NGC4755	270	25870	566	3.822	0.058	33	3.829	...	-0.004	0.253	0.124	0.128
NGC4755	332	16930	186	4.064	0.026	108	4.132	...	0.007	0.065	0.036	0.029
NGC4755	408	17090	320	3.958	0.045	261	4.170	...	-0.000	-0.112	-0.056	0.056
NGC4755	414	19722	316	3.920	0.038	27	3.931	-0.058	-0.127	-0.042	-0.076	0.037
NGC4755	418	23290	468	3.845	0.049	209	3.983	...	-0.076	0.155	0.039	0.116
NGC4755	433	14262	130	3.965	0.028	157	4.086	...	0.307	0.240	0.274	0.033
NGC4755	449	19737	338	3.897	0.033	19	3.904	...	0.032	0.206	0.119	0.087
NGC4755	452	18726	232	3.814	0.030	121	3.907	...	0.053	0.135	0.094	0.041
NGC4755	462	16714	179	3.995	0.030	222	4.169	...	-0.096	-0.108	-0.102	0.006
NGC4755	1309	19597	396	3.800	0.041	212	3.977	...	-0.025	0.119	0.047	0.072
NGC4755	1804	15436	262	4.126	0.044	109	4.196	...	-0.366	-0.465	-0.416	0.050
NGC4755	3312	17251	457	3.986	0.063	219	4.157	...	-0.644	-0.622	-0.633	0.011
NGC4755	3602	19535	1306	3.900	0.137	16	3.907	...	-0.555	-0.289	-0.422	0.133
NGC6193	...	19757	365	4.202	0.041	65	4.226	-0.135	-0.027	-0.009	-0.057	0.056
NGC6193	4	19281	221	4.091	0.026	8	4.094	-0.168	-0.051	0.007	-0.071	0.073
NGC6193	6	21036	295	3.723	0.031	296	3.980	0.401	0.556	0.578	0.512	0.079
NGC6193	8	25856	511	4.160	0.049	61	4.173	0.105	0.058	0.283	0.149	0.097
NGC6193	16	21275	330	4.015	0.036	74	4.049	0.017	0.023	0.056	0.032	0.017
NGC6193	17	20999	431	3.356	0.043	84	3.429	0.686	0.552	0.690	0.643	0.064
NGC6193	18	18173	222	4.037	0.034	129	4.123	0.048	0.111	0.187	0.115	0.057
NGC6193	20	15320	229	3.833	0.033	226	4.040	0.585	0.562	0.553	0.567	0.013
NGC6193	21	16488	250	4.042	0.042	320	4.292	-0.366	-0.119	-0.240	-0.242	0.101
NGC6193	25	17825	232	3.911	0.029	275	4.138	-0.158	-0.079	-0.076	-0.105	0.038
NGC6193	26	18628	340	4.182	0.045	175	4.284	-0.291	-0.156	-0.140	-0.196	0.067
NGC6193	27	18254	183	4.054	0.028	89	4.104	-0.033	0.018	0.067	0.017	0.041
NGC6193	1175	15116	338	4.182	0.063	133	4.262	...	-0.638	-0.660	-0.649	0.011
NGC6193	1291	18097	296	3.973	0.044	63	4.005	0.062	0.110	0.116	0.096	0.024
NGC6193	1614	14430	142	4.020	0.031	149	4.128	...	-0.636	-0.667	-0.652	0.015
NGC6193	1620	14370	270	3.980	0.047	259	4.196	-0.630	...	-0.667	-0.649	0.019
NGC6193	1648	17985	408	3.876	0.053	306	4.138	-0.013	0.384	0.233	0.201	0.163
NGC6193	1695	16734	175	4.021	0.025	138	4.119	-0.189	0.031	0.024	-0.045	0.102
NGC6193	1696	21467	246	3.955	0.023	216	4.099	-0.140	-0.146	-0.007	-0.098	0.064
NGC6193	1702	18034	261	4.079	0.041	31	4.092	-0.011	0.039	0.158	0.062	0.071
NGC7160	3	24534	198	4.159	0.021	95	4.188	-0.069	-0.073	0.042	-0.033	0.053
NGC7160	4	18018	226	4.042	0.032	143	4.139	0.130	0.102	0.054	0.095	0.031
NGC7160	5	17549	192	3.821	0.025	219	4.018	0.158	0.309	0.212	0.226	0.062
NGC7160	7	15797	107	3.822	0.017	67	3.869	-0.024	0.046	-0.179	-0.052	0.094
NGC7160	9	13303	33	4.073	0.007	226	4.233	-0.182	...	-0.199	-0.191	0.008
NGC7160	13	11596	43	4.142	0.015	192	4.244	0.075	...	0.135	0.105	0.030
NGC7160	18	10654	24	4.062	0.011	203	4.183	...	...	...	...	...
NGC7160	32	13728	54	4.013	0.011	121	4.104	0.211	0.311	0.200	0.241	0.050

NGC7160	424	12134	45	4.381	0.014	83	4.431	-0.458	...	-0.545	-0.501	0.044
NGC7160	436	11384	23	4.191	0.009	283	4.423	0.078	...	-0.042	0.018	0.060
NGC7160	513	14292	40	3.639	0.008	100	3.743	0.124	0.144	0.096	0.121	0.019
NGC7160	529	12457	27	4.223	0.007	145	4.305	-0.536	...	-0.530	-0.533	0.003
NGC7160	741	12756	25	4.236	0.007	316	4.461	-0.346	...	-0.355	-0.351	0.005
NGC7160	903	14891	82	4.085	0.017	282	4.303	0.049	0.229	0.115	0.131	0.074
NGC7160	940	11638	28	3.272	0.007	313	3.714	-0.160	...	-0.102	-0.131	0.029
NGC7160	955	23859	219	3.875	0.021	148	3.962	0.047	-0.028	0.172	0.064	0.083
TR14	118	23042	716	3.663	0.067	207	3.829	...	0.499	0.563	0.531	0.032
TR14	149	20844	2098	4.102	0.213	73	4.133	...	-0.370	-0.386	-0.378	0.008
TR14	...	18695	771	4.100	0.097	150	4.193	...	-0.103	-0.210	-0.157	0.054
TR16	2	26639	891	3.989	0.069	228	4.102	-0.193	0.030	0.290	0.042	0.198
TR16	3	22822	609	3.328	0.063	21	3.336	0.149	-0.150	0.304	0.101	0.188
TR16	4	27526	848	4.201	0.061	96	4.220	0.051	0.120	0.455	0.209	0.176
TR16	5	25917	613	4.037	0.059	350	4.243	-0.013	0.069	0.162	0.072	0.071
TR16	9	24412	790	3.700	0.073	93	3.752	-0.102	-0.214	0.136	-0.060	0.146
TR16	10	24617	369	3.819	0.031	153	3.911	-0.017	-0.018	0.197	0.054	0.101
TR16	11	22791	376	3.905	0.032	293	4.107	0.019	0.074	0.091	0.062	0.031
TR16	12	26468	639	4.201	0.050	55	4.210	0.150	0.132	0.205	0.162	0.031
TR16	14	25983	762	4.318	0.071	106	4.340	-0.023	-0.030	-0.006	-0.020	0.010
TR16	15	25626	771	3.782	0.056	0	3.782	-0.089	0.041	0.114	0.022	0.084
TR16	16	23739	468	4.128	0.040	133	4.186	-0.104	-0.032	0.075	-0.020	0.074
TR16	17	25579	592	3.936	0.044	234	4.067	0.122	-0.068	0.277	0.111	0.141
TR16	20	17574	237	3.711	0.029	51	3.740	0.049	0.215	0.226	0.163	0.081
TR16	21	24434	680	3.557	0.066	90	3.613	0.168	-0.226	0.165	0.036	0.185
TR16	23	20183	258	2.935	0.028	234	3.277	0.089	-0.439	0.025	-0.108	0.235
TR16	24	21018	362	3.840	0.033	199	3.987	0.512	0.557	0.661	0.577	0.063
TR16	25	19123	389	4.046	0.046	156	4.148	-0.216	-0.130	-0.135	-0.160	0.039
TR16	28	24357	553	4.108	0.056	47	4.119	0.077	0.080	0.125	0.094	0.022
TR16	29	21364	590	4.012	0.055	25	4.021	-0.036	0.005	0.067	0.012	0.042
TR16	47	21090	1010	3.919	0.096	371	4.219	...	0.168	0.038	0.103	0.065
TR16	48	19544	610	3.838	0.058	203	4.000	0.061	0.128	0.097	0.096	0.027
TR16	80	22633	689	4.029	0.069	205	4.146	-0.237	-0.163	-0.053	-0.151	0.075
TR16	94	22317	665	4.035	0.070	119	4.094	-0.402	-0.181	-0.247	-0.277	0.093
TR16	138	21977	676	3.922	0.071	141	4.009	-0.214	0.148	0.096	0.010	0.160
TR16	158	25481	492	3.415	0.034	107	3.494	0.122	-0.081	0.464	0.168	0.225
TR16	242	11061	103	3.664	0.034	134	3.824	...	...	...	...	...
TR16	246	24390	598	3.596	0.050	120	3.682	-0.136	-0.054	0.182	-0.003	0.135
TR16	258	15047	178	3.710	0.028	138	3.845	-0.601	-0.248	-0.470	-0.440	0.146
TR16	283	28222	474	4.223	0.054	113	4.247	0.183	0.176	0.426	0.262	0.116
TR16	1075	22128	1113	3.512	0.132	5	3.514	-0.057	-0.330	-0.110	-0.165	0.118
TR16	1400	20744	943	4.301	0.100	117	4.346	-0.466	-0.251	-0.361	-0.359	0.088
TR16	1462	15723	156	3.851	0.023	69	3.899	0.196	0.344	0.355	0.298	0.073
TR16	1591	15572	330	4.006	0.055	133	4.104	...	-0.641	-0.651	-0.646	0.005
TR16	1641	13726	202	4.543	0.039	55	4.556	-0.639	-0.419	-0.678	-0.579	0.114
TR16	1657	10749	121	3.432	0.045	37	3.474	...	...	...	...	...
TR16	1658	22510	517	3.636	0.052	212	3.816	0.235	-0.019	0.202	0.140	0.113

REFERENCES

Abt, H. A., Levato, H., & Grosso, M., (2002) ApJ, **573**, 359.

Aerts, C., Bedding, T. R., & Christensen-Dalsgaard, J., (2002) *Radial and Nonradial Pulsations as Probes of Stellar Physics* (ASP: San Francisco).

Aerts, C., & Waelkens, C., (1993) A&A, **273**, 135.

Alekseeva, G. A., Arkharov, A. A., Galkin, V. D., Hagen–Thorn, E. I., Nikanorova, I. N., Novikov, V. V., Novopashenny, V. B., Pakhomov, V. P., Ruban, E. V., & Shchegolev, D. E., (1996) Baltic Astron., **5**, 603.

Arnal, M., Morrell, N., Garcia, B., & Levato, H., (1988) PASP, **100**, 1076.

Auer, L. H., & Mihalas, D., (1973) ApJS, **25**, 433.

Balona, L. A., (1975a) Mem. Roy. Astron. Soc., **78**, 51.

Balona, L. A., (1975b) MNRAS, **173**, 449.

Barai, P., Gies, D. R., Choi, E., Das, V., Deo, R., Huang, W., Marshall, K., McSwain, M. V., Ogden, C., Osterman, M. A., Riddle, R. L., Seymour, Jr., J. L., Wingert, D. W., Kaye, A. B., & Peters, G. J., (2004) ApJ, **608**, 989.

Barden, S. C., & Armandroff, T., (1995) *Fiber Optics in Astronomical Applications*, eds: Barden, S. C., (Proc. SPIE: Bellingham, WA), Vol. 2476, p. 56.

Berg, R. A., (1970) *Stellar Diameters from Occultations*, Ph.D. dissertation, University of Virginia.

Borra, E. F., & Landstreet, J. D., (1979) ApJ, **228**, 809.

Borra, E. F., Landstreet, J. D., & Thompson, I., (1983) ApJS, **53**, 151.

Bouchet, P., Schmider, F. X., & Manfroid, J., (1991) A&AS, **131**, 395.

Brown, A. G. A., & Verschueren, W., (1997) A&A, **319**, 811.

Brown, R. H., Davis, J., Allen, L. R., & Rome, J. M., (1967) MNRAS, **137**, 393.

Buta, R. J., & Smith, M. A., (1979) ApJ, **232**, 213.

Claret, A., (1998) A&AS, **131**, 395.

Claret, A., (2000) A&A, **359**, 289.

Claret, A., (2003) A&A, **406**, 623.

Cohen, M., Walker, R. G., Barlow, M. J., & Deacon, J. R., (1992) AJ, **104**, 1650.

Collins, G. W., II, (1963) ApJ, **138**, 1134.

Collins , G. W., II, & Harrington, J. P., (1966) ApJ, **146**, 152.

Collins, G. W., II, & Sonneborn, G. H., (1977) ApJS, **34**, 41.

Collins, G. W., II, Truax, R. J., & Cranmer, S. R., (1991) ApJS, **77**, 541.

Cugier, H., Dziembowski, W. A., & Pamyatnykh, A. A., (1994) A&A, **291**, 143.

De Cat, P., Telting, J., Aerts, C., & Mathias, P., (2000) A&A, **359**, 539.

Domiciano de Souza, A., Kervella, P., Jankov, S., Abe, L., Vakili, F., di Folco, E., & Paresce, F., (2003) A&A, **407**, 47.

Domiciano de Souza, A., Vakili, F., Jankov, S., Janot-Pacheco, & Abe, L. 2002, (2002) A&A, **393**, 345.

Dworetsky, M. M., (1975) AJ, **80**, 131.

Etzel, P. B., & Olson, E. C., (1993) AJ, **106**, 1200.

Fabregat, J., & Torrejón, J. M., (2000) A&A, **357**, 451.

Forbes, D., English, D., & de Robertis, M. M., (1992) AJ, **103**, 916.

Gautschy, A., & Saio, H., (1996) ARA&A, **34**, 551.

Gies, D. R., Bagnuolo, W. G., Jr., Ferrara, E. C., Kaye, A. B., Thaller, M. L., Penny, L. R., & Peters, G. J., (1998) ApJ, **493**, 440.

Gies, D. R., Kambe, E., Josephs, T. S., Bagnuolo, W. G., Jr., Choi, Y. J., Gudehus, D., Guyton, K. M., Hartkopf, W. I., Hildebrand, J. L., Kaye, A. B., Mason, B. D., Riddle, R. L., Sowers, J. W., Turner, N. H., Wilson, J. W., & Xiong, Y., (1999) ApJ, **525**, 420.

Gies, D. R., & Kullavanijaya, A., (1988) ApJ, **326**, 813.

Gies, D. R., & Lambert, D. L., (1992) ApJ, **387**, 673.

Gray, D. F., (1992) *The Observation and Analysis of Stellar Photospheres, 2*$^{\rm nd}$ *ed.* (Cambridge University Press: New York).

Gray, R. O., Corbally, C. J., Garrison, R. F., McFadden, F. T., & Robinson, P. E., (2003) AJ, **126**, 2048.

Griem, H. R., (1974) *Spectral Line Broadening by Plasmas* (Academic Press: New York).

Gummersbach, C. A., Kaufer, A., Schaefer, D. R., Szeifert, T., & Wolf, B., (1998) A&A, **338**, 881.

Hanson, M. M., Howarth, I. D., & Conti, P. S., (1997) ApJ, **489**, 698.

Harmanec, P., (1989) Bull. Astron. Inst. Czech., **40**, 201.

Harmanec, P., & Tarasov, A. E., (1990) Bull. Astron. Inst. Czech., **41**, 273.

Heger, A., & Langer, N., (2000) ApJ, **544**, 1016.

Hill, G., (1967) ApJS, **14**, 263.

Howarth, I. D., Siebert, K. W., Hussain, G. A. J., & Prinja, R. K., (1997) MNRAS, **284**, 265.

Howarth, I. D., & Smith, K. C., (2001) MNRAS, **327**, 353.

Hubeny, I., Harmanec, P., & Stefl, S., (1986) Bull. Astron. Inst. Czech., **37**, 370.

Hubeny, I., & Lanz, T., (1995) ApJ, **439**, 875.

Jackson, S., MacGregor, K. B., & Skumanich, A., (2005) ApJS, **156**, 245.

Jaschek, C., Jaschek, M., Morgan, W. W., & Slettebak, A., (1968) ApJ, **153**, L87.

Johnson, H. L., & Morgan, W. W., (1953) ApJ, **117**, 313.

Kurucz, R. L., (1979) ApJS, **40**, 1.

Langer, N., Yoon, S.-C., Petrovic, J., & Heger, A., (2004) *in Proc. IAU Symp. 215, Stellar Rotation*, eds: A. Maeder & P. Eenens, (ASP: San Francisco), 535.

Lanz, T., & Hubeny, I., (2003) ApJS, **146**, 417.

Le Borgne, J.–F., Bruzual, G., Pelló, R., Lançon, A., Rocca–Volmerange, B., Sanahuja, B., Schaerer, D., Soubiran, C., & Vílchez–Gómez, R., (2003) A&A, **402**, 433.

Lee, U., Jeffery, C. S., & Saio, H., (1992) MNRAS, **254**, 185.

Lee, U., & Saio, H., (1990) ApJ, **349**, 570.

Leone, F., & Manfre, M., (1997) A&A, **320**, 257.

Lucy, L. B., (1967) Zeitschrift *für* astrophysik, **65**, 89.

Lucy, L. B., (1974) AJ, **79**, 745.

Lyubimkov, L. S., Rostopchin, S. I., & Lambert, D. L., (2004) MNRAS, **351**, 745.

Maeder, A., Grebel, E. K., & Mermilliod, J.C., (1999) A&A, **346**, 459.

Massey, P., Johnson, K. E., & DeGioia-Eastwood, K., (1995) ApJ, **454**, 151.

Mathys, G., (2004) *in Proc. IAU Symp. 215, Stellar Rotation*, eds: A. Maeder & P. Eenens, (ASP: San Francisco), 270.

Mathys, G., Andrievsky, S. M., Barbuy, B., Cunha, K., & Korotin, S.A., (2002) A&A, **387**, 890.

McAlister, H. A., ten Brummelaar, T. A., Gies, D. R., Huang, W., Bagnuolo, W. G., Jr., Shure, M. A., Sturmann, J., Sturmann, L., Turner, N. H., Taylor, S. F., Berger, D. H., Grundstrom, E., Ogden, C., Ridgway, S. T., & van Belle, G., (2005) ApJ, **628**, 439.

McSwain, M. V., & Gies, D. R., (2005) ApJS, **161**, in press.

Mermilliod, J.C., (1982) A&A, **109**, 48.

Mermilliod, J.C., & Paunzen, E., (2003) A&A, **410**, 511.

Meynet, G., & Maeder, A., (1997) A&A, **321**, 465.

Meynet, G., & Maeder, A., (2000) A&A, **361**, 101.

Morales, C., Orozco, V., Gómez, J. F., Trapero, J., Talavera, A., Bowyer, S., Edelstein, J., Korpela, E., Lampton, M., & Drake, J. J., (2001) ApJ, **552**, 278.

Penny, L. R., (1996) ApJ, **463**, 747.

Perryman, M. A. C., Lindegren, L., Kovalevsky, J., Hoeg, E., Bastian, U., Bernacca, P. L., Crz, M., Donati, F., Grenon, M., van Leeuwen, F., van der Marel, H., Mignard, F., Murray, C. A., Le Poole, R. S., Schrijver, H., Turon, C., Arenou, F., Froeschl, M., Petersen, C. S., (1997) A&A, **323**, 49.

Pols, O. R., Coté, J., Waters, L. B. F. M., & Heise, J., (1991) A&A, **241**, 419.

Quirrenbach, A., (2001) ARA&A, **39**, 353.

Radick, R., (1981) AJ, **86**, 1685.

Ridgway, S. T., Jacoby, G. H., Joyce, R. R., Seigel, M. J., & Wells, D. C., (1982) AJ, **87**, 680.

Rivinius, Th., Baade, D., Štefl, S., Townsend, R. H. D., Stahl, O., Wolf, B., & Kaufer, A., (2001) A&A, **369**, 1058.

Sackmann, I.-J., & Anand, S. P. S., (1970) ApJ, **162**, 105.

Saio, H., Kambe, E., & Lee, U., (2000) ApJ, **543**, 359.

Schaller, G., Schaerer, D., Meynet, G., & Maeder, A., (1992) A&AS, **96**, 269.

Schrijvers, C., & Telting, J. H., (1999) A&A, **342**, 453.

Schrijvers, C., Telting, J. H., Aerts, C., Ruymaekers, E., & Henrichs, H. F., (1997) A&AS, **121**, 343.

Shore, S. N., Bohlender, D. A., Bolton, C. T., North, P., & Hill, G. M., (2004) A&A, **421**, 203.

Šimon, V., (1999) A&AS, **134**, 1.

Slettebak, A., (1965) ApJ, **145**, 121.

Slettebak, A., (1968) ApJ, **154**, 933.

Slettebak, A., (1970) *in Proc. IAU Coll. 4, Stellar Rotation*, eds: A. Slettebak, (Reidel: Dordrecht), 3.

Slettebak, A., (1985) ApJS, **59**, 769.

Slettebak, A., Collins, G. W., Parkinson, T. D., Boyce, P. B., & White, N. M., (1975) ApJS, **29**, 137.

Smith, M. A., (1985) ApJ, **288**, 266.

Smith, M. A., (1986) ApJ, **307**, 213.

Smith, M. A., Fullerton, A. W., & Percy, J. R., (1987) ApJ, **320**, 768.

Stoeckley, T. R., & Buscombe, W., (1987) MNRAS, **227**, 801.

Tarasov, A. E., et al., (1995) A&AS, **110**, 59.

Telting, J. H., & Schrijvers, C., (1997) A&A, **317**, 723.

ten Brummelaar, T. A., McAlister, H. A., Ridgway, S. T., Bagnuolo Jr, W. G., Turner, N. H., Sturmann, L., Sturmann, J., Berger, D. H., Ogden, C. E., Cadman, R., Hopper, C. H., Shure, M. A., (2005) ApJ, **628**, 453.

Townsend, R. H. D., (1997) MNRAS, **284**, 839.

Townsend, R. H. D., (2000) *in IAU Coll. 175, The Be Phenomenon in Early-Type Stars*, eds: M. A. Smith, H. F. Henrichs, & J. Fabregat, (ASP: San Francisco), 214.

Townsend, R. H. D., (2004a) *in Proc. IAU Symp. 215, Stellar Rotation*, eds: A. Maeder & Eenens, P., (ASP: San Francisco), 404.

Townsend, R. H. D., (2005) MNRAS, **360**, 465.

Townsend, R. H. D., Owocki, S. P., & Howarth, I. D., (2004b) MNRAS, **350**, 189.

Turner, D. G., Grieve, G. R., Herbst, W., & Harris, W. E., (1980) AJ, **85**, 1193.

Valdes, F., (1995) *Guide to the HYDRA Reduction Task DOHYDRA* (NOAO: Tucson).

Valdes, F., Gupta, R., Rose, J. A., Singh, H. P., & Bell, D. J., (2004) ApJS, **152**, 251.

van Belle, G. T., Ciardi, D. R., Thompson, R. R., Akeson, R. L., & Lada, E. A., (2001) ApJ, **559**, 1155.

Van Bever, J., & Vanbeveren, D., (1997) A&A, **332**, 116.

van den Heuvel, E. P. J., (1970) *in Proc. IAU Coll. 4, Stellar Rotation*, eds: A. Slettebak, (Reidel: Dordrecht), 178.

Verschueren, W., (1991), Ph.D. thesis, Vrije Universite Brussels.

Vogt, S. S., & Penrod, G. D., (1983) ApJ, **275**, 661.

von Zeipel, H., (1924) MNRAS, **84**, 665.

Wade, G. A., Bohlender, D. A., Brown, D. N., Elkin, V. G., Landstreet, J. D., & Romanyuk, I. I., (1997) A&A, **320**, 172.

Wolff, S. C., (1981) ApJ, **244**, 221.

Wolff, S. C., Edwards, S., & Preston, G. W., (1982) ApJ, **252**, 322.

Zorec, J., (2004) *in Proc. IAU Symp. 215, Stellar Rotation*, eds: A. Maeder & P. Eenens, (ASP: San Francisco), 73.